A NONINTRUSIVE DIAGNOSTICS TECHNIQUE FOR FLAME SOOT BASED ON NEAR-INFRARED EMISSION SPECTROMETRY

A THESIS SUBMITTED TO
THE GRADUATE SCHOOL OF NATURAL AND APPLIED SCIENCES
OF
MIDDLE EAST TECHNICAL UNIVERSITY

BY

IŞIL AYRANCI KILINÇ

IN PARTIAL FULFILLMENT OF THE REQUIREMENTS
FOR
THE DEGREE OF DOCTOR OF PHILOSOPHY
IN
CHEMICAL ENGINEERING

JUNE 2007

This thesis was prepared within the frame of a joint doctoral program between
Department of Chemical Engineering , Middle East Technical University and
Centre de Thermique de Lyon (CETHIL), Institut National des Sciences Appliquées (INSA) de Lyon, France.

N° d'ordre 2007-ISAL-0037 Année 2007

Thèse en co-tutelle

A nonintrusive diagnostics technique for flame soot based on near-infrared emission spectrometry

présentée devant
L'Institut National des Sciences Appliquées de Lyon

et
L'Université Technique du Moyen-Orient, Ankara

pour obtenir
le grade de docteur

Ecole doctorale : MEGA - Mécanique, Énergétique, Génie civil, Acoustique
Spécialité : Thermique et Energétique

par
Işıl AYRANCI KILINÇ
Soutenue le 17 juin 2007 devant la Commission d'examen

Jury

M[r]	F. ARINÇ	Professeur, METU, ME	Président
M[r]	J.-P. VANTELON	Directeur de Recherche au CNRS	Rapporteur
M[me]	G. GÜRÜZ	Professeur, METU, CHE	Rapporteur
M[me]	N. SELÇUK	Professeur, METU, CHE	Directrice de thèse
M[r]	R. VAILLON	Chargé de Recherche au CNRS	Directeur de thèse
M[r]	J.-F. SACADURA	Professeur Emérite, INSA de Lyon	Directeur de thèse

Cette thèse a été préparée dans le cadre d'un programme de formation doctorale en cotutelle entre le Centre de Thermique de Lyon (CETHIL) de l'Institut National des Sciences Appliquées (INSA) de Lyon, France et le Département de Génie Chimique de l'Université Technique du Moyen-Orient (METU), Ankara, Turquie.

Approval of the Graduate School of Natural and Applied Sciences

_____

Prof. Dr. Canan Özgen
Director

I certify that this thesis satisfies all the requirements as a thesis for the degree of Doctor of Philosophy.

_____

Prof. Dr. Nurcan Baç
Head of the Department of
Chemical Engineering

This is to certify that we have read this thesis and that in our opinion it is fully adequate, in scope and quality, as a thesis for the degree of Doctor of Philosophy.

Dr. Rodolphe Vaillon Supervisor	Prof. Dr. Jean-François Sacadura Supervisor	Prof. Dr. Nevin Selçuk Supervisor

Examining Committee Members

Prof. Dr. Faruk Arınç	(METU, ME)	_____
Prof. Dr. Nevin Selçuk	(METU, CHE)	_____
Dr. Rodolphe Vaillon	(INSA-Lyon, France)	_____
Prof. Dr. Jean-François Sacadura	(INSA-Lyon, France)	_____
Prof. Dr. Güniz Gürüz	(METU, CHE)	_____
Dr. Jean-Pierre Vantelon	(ENSMA, France)	_____

I hereby declare that all information in this document has been obtained and presented in accordance with academic rules and ethical conduct. I also declare that, as required by these rules and conduct, I have fully cited and referenced all material and results that are not original to this work.

Işıl Ayrancı Kılınç

ABSTRACT

A NONINTRUSIVE DIAGNOSTICS TECHNIQUE FOR FLAME SOOT BASED ON NEAR-INFRARED EMISSION SPECTROMETRY

Ayrancı Kılınç, Işıl
Ph.D., Department of Chemical Engineering, METU
CETHIL, INSA-Lyon

Supervisors: Prof. Dr. Nevin Selçuk, Dept. Chemical Engineering, METU
Dr. Rodolphe Vaillon, CETHIL, INSA-Lyon
Prof. Dr. Jean-François Sacadura, CETHIL, INSA-Lyon

June 2007, 194 pages

A novel nonintrusive soot diagnostics methodology was developed, validated and applied for *in-situ* determination of temperature, volume fraction and refractive index of soot aggregates formed inside flames by using near-infrared emission spectrometry. Research was conducted in three main parts, first one addressing development and validation of a comprehensive "direct" model for simulation of line-of-sight radiative emission from axisymmetric sooty flames by coupling sub-models for radiative transfer, radiative properties and optical constants. Radiative property estimation for soot agglomerates was investigated by experimentally validating discrete dipole approximation against microwave measurements and using it as reference to assess applicability of simpler Rayleigh-Debye-Gans approximation for fractal aggregates (RDG-FA). Comparisons between predictions of two methods for soot-like model aggregates demonstrated that radiative property predictions of RDG-FA are acceptably accurate for relatively small soot aggregates encountered in small-scale flames.

Part two concerns experimental investigation of an axisymmetric ethylene/air diffusion flame by Fourier Transform Near-Infrared spectroscopy. Measurement of line-of-sight emission intensity spectra was performed along with analyses on calibration, noise, uncertainty and reproducibility. A noise characterization approach was introduced to account for spatial fluctuations which were found to dominate over spectral noise.

Final part focuses on development, evaluation and application of an inversion methodology that inputs spectral emission intensity measurements from optically thin flames, removes noise, identifies soot refractive index from spectral gradients and retrieves soot temperature and volume fraction fields by tomographic reconstruction. Validation with simulated data and favorable application to measurements indicate that proposed methodology is a promising option for nonintrusive soot diagnostics in flames.

Keywords: Combustion diagnostics, radiative property, tomography, diffusion flame, soot aggregates

ÖZ

ALEV İSİ İÇİN YAKIN-KIZILÖTESİ IŞIMA SPEKTROMETRİSİNE DAYALI GİRİŞİMSİZ TANILAMA YÖNTEMİ

Ayrancı Kılınç, Işıl
Doktora, Kimya Mühendisliği Bölümü, ODTÜ
CETHIL, INSA-Lyon

Tez Danışmanları : Prof. Dr. Nevin Selçuk, Kimya Mühendisliği Bölümü, ODTÜ
Dr. Rodolphe Vaillon, CETHIL, INSA-Lyon
Prof. Dr. Jean-François Sacadura, CETHIL, INSA-Lyon

Haziran 2007, 194 sayfa

Alev içinde oluşan is taneciklerine ilişkin kırılma indisi, sıcaklık dağılımı ve hacim oranı gibi özelliklerin yerinde saptanması için yakın-kızılötesi ışıma spektrometrisine dayanan yeni bir girişimsiz is tanılama yöntemi geliştirilmiş, doğrulanmış ve uygulanmıştır. Üç temel kısımdan oluşan araştırmanın birinci bölümü is içeren eksenel simetrik alevlerde görüş hattı boyunca yayılan ışınım şiddetinin benzetimine ayrılmıştır. Işınım aktarımı, isin ışınım özellikleri ve optik sabitlerinin hesaplanması için geliştirilen yan modeller birleştirilerek kapsamlı bir "düz" model oluşturulmuştur. Alevde agregalar halinde bulunan is taneciklerinin ışınım özelliklerinin tahmini için iki yöntem ele alınmıştır. Hesaplanan ışınımsal özelliklerin mikrodalga ölçümleriyle karşılaştırılması sonucu doğrulanan ayrık çiftucay yaklaşımı referans alınarak daha sade bir tahmin yolu olan fraktal agregalar için Rayleigh-Debye-Gans yaklaşımının (RDG-FA) amaca uygunluğu değerlendirilmiştir. İs benzeri model agregalar için bu iki yöntemle elde edilen ışınımsal özelliklerin karşılaştırılması sonucunda RDG-FA yönteminin küçük ölçekli alevlerde rastlanan, nispeten daha ufak is taneleri için kabul edilebilir doğrulukta sonuçlar verdiği belirlenmiştir.

Çalışmanın ikinci kısmında bir eksenel simetrik etilen/hava difüzyon alevinin Fourier dönüşümü yakın-kızılötesi spektroskopisi (FTIR) ile deneysel olarak incelenmesi ele alınmıştır. Görüş hattı ışıma şiddeti tayf ölçümü ve kalibrasyonu gerçekleştirilmiş, deneydeki gürültü miktarı ve belirsizlik düzeyi incelenmiş, ölçümlerin tekrarlanabilirliği sınanmıştır. Spektral gürültüye nazaran daha baskın etkisi olduğu belirlenen konumsal dalgalanmaların nicelik tayini için yeni bir gürültü tanımlama yöntemi önerilmiştir.

Araştırmanın son bölümü ölçülen değerlerden alev isine ilişkin özelliklerin elde edilmesi için bir "ters analiz" yönteminin geliştirilmesi, doğrulanması ve uygulanmasını kapsamaktadır. Optikçe ince alevlerde ölçümlenen ışıma şiddeti tayflarının, gürültüden arındırılması, spektral düşümlerinden kırınım indisi belirlenmesi ve is parçacıklarına dair sıcaklık ve hacim oranı dağılımlarının tomografik geriçatımla elde edilmesi esasına dayanan bir ters algoritma sunulmuştur. Deney simülasyonları ve ölçülmüş ışınım tayfları kullanılarak yapılan doğrulama ve uygulama çalışmalarında elde edilen olumlu sonuçlar, önerilen yöntemin alev isi karakterizasyonu için gelecek vaat eden bir seçenek olduğunu göstermişir.

Anahtar Kelimeler: Yanma tanılaması, ışınımsal özellikler, tomografi, difüzyon alevi, is agregaları

.: to Memet :.

ACKNOWLEDGEMENTS

This thesis was prepared within the frame of a joint doctoral program between Chemical Engineering Department of Middle East Technical University and Centre de Thermique de Lyon (CETHIL), Institut National des Sciences Appliquées de Lyon and was supported by a French Government Scholarship granted by the Embassy of France in Turkey, which is gratefully acknowledged. The research was partially supported by Turkish Scientific and Technical Research Council (TÜBİTAK) with project no. MİSAG-263 (103M037) and French Ministry of Research (Réseau de Recherche et d'Innovation Technologique: "Recherche Aéronautique sur le Supersonique", décision no. 03T233).

I would like to express my deepest gratitude to my supervisors Prof. Dr. Nevin Selçuk and Dr. Rodolphe Vaillon, for all the guidance and support they provided throughout this study. I am profoundly thankful to them for giving me the opportunity to pursue this challenge, believing in my capacity and embellishing it with their counsel. Also many thanks for the entire administrative difficulties they overcame to realize this joint doctoral program. I wish to voice my heartfelt thanks to Emeritus Prof. Dr. Jean-François Sacadura who honored this thesis with his support, supervision and contributions.

Dr. Dany Escudié, director of CETHIL, is gratefully acknowledged for her valuable support at many stages throughout the research project. I would like to gratefully acknowledge Prof. Dr. Ural Akbulut, President of METU and Mr. Zouheir Hamrouni, former University Cooperation Attache of Embassy of France in Turkey, who favored this collaboration and provided concrete contributions to its realization by resolving dreadlocks of financial and administrative problems that emerged along the way. I would also like to express my thanks to respected members of the thesis examination committee, Prof. Dr. Güniz Gürüz, Prof. Dr. Faruk Arınç, Dr. Jean-Pierre Vantelon for their evaluations and for allocating their valuable time to travel all the way to attend the jury meeting.

Publicly available DDSCAT code was very instrumental for this research. The authors of the code, Prof. Dr. Bruce T. Draine and Prof. Dr. Piotr J. Flatau are gratefully acknowledged for granting worldwide access to this excellent tool for DDA implementations. Special thanks to our research partners from Institut Fresnel Marseille, Dr. Pierre Sabouroux, Dr. Brian Stout,

Dr. Jean Michel Geffrin and Dr. Christelle Eyraud who provided the experimental data from microwave measurements and T-Matrix model predictions presented in section 2.2.5.2.

I am deeply thankful to Dr. Dany Escudié and Dr. Rodolphe Vaillon for their close concern and sympathy during my stay in France which was a privilege of great value for me. I would like to thank Dr. Frédéric André, Dr. Dominique Baillis, Dr. Guillaume Pinguet and Dr. Jaona Harifidy Randrianalisoa for their experienced collaboration during experimental studies and fruitful discussions. I am also thankful to Prof. Dr. Martin Raynaud who kindly bothered to share his office at CETHIL with me. Bernard Lacroix, technical staff member of CETHIL is thankfully acknowledged for his efforts to improve our set-up. I would like to thank all other members of the friendly and helpful community of CETHIL, including Dr. Severine Gomes, Dr. Laurent David and Guillaume Chareyre, for their warm welcome.

Sincere thanks are addressed to my valuable friends and colleagues from METU, Dr. İsmail Doğan, Zeynep Serinyel, Mehmet Moralı, Nilüfer Sultan Aybar, Aykan Batu, Dr. Ahmet Bilge Uygur, Nihan Çayan and Ertan Karaismail.

I owe my warmest gratitude to my parents Özsevim and Mustafa Ayrancı and my sister Işık who maintained constant encouragement, tolerance and all means of support during the years. My final words are for my beloved husband Mehmet Kılınç who was always nearby to ease frustrating moments and to rejoice achievements during the course of my work. I am grateful to him for his sincere belief in my goals, for his patience, endurance and for always being so close despite long distances.

TABLE OF CONTENTS

LIST OF TABLES

LIST OF FIGURES

NOMENCLATURE

a	particle characteristic length
a_{eq}	radius of volume equivalent sphere
A_A	aperture cross-section of diaphragm A
B_0	constant (= $12\pi hc_0^2$)
B_1	constant (= hc_0 / k)
C_a	absorption cross-section
C_s	scattering cross-section
c_0	speed of light in vacuum (= 2.9979×10^8 m/s)
d	diameter, interdipole separation
d_b	beam diameter
d_{eq}	diameter of volume equivalent sphere
D_f	fractal dimension
d_x	lateral scanning increment
D_0	nozzle diameter of the burner
e	charge of an electron (=1.6022×10^{-19} C)
$\hat{\mathbf{e}}$	unit basis vectors
E	complex electric field vector
E	complex electric field component
E_m	refractive index function (Eq. 2.41)
F	axisymmetric property field
f	complex forward scattering amplitude matrix (Eq. 2.20)
$f(q.R_g)$	form factor (Eq. 2.48-49)
F_m	refractive index function (Eq. 2.41)
f_v	soot volume fraction
g	aggregate scattering factor, (Eq. 2.53-54)
G_η	raw background spectrum [IU]
h	Planck's constant (= 6.6261×10^{-34} Js)
H_η	local emission source term
I_η	spectral intensity per unit wavenumber [W/ (m^2 sr cm^{-1})]
k	Boltzmann's constant (= 1.3807×10^{-23} J/K) , wavenumber (Ch.2)

k	absorptive index in complex index of refraction
k_f	fractal prefactor
m	complex index of refraction (m = n+ik)
M	amplitude of scattered wave
m_e	electron rest mass (= 9.1096×10^{-31} kg)
m_f	free electron mass [kg]
n	refractive index in complex index of refraction
$\hat{\mathbf{n}}$	unit vector in scattering direction
$\bar{N}$	particle number density [m^{-3}]
N_e	electron number density
N_d	total number of dipoles
N_p	number of primary particles per aggregate
NS	total number of slices
NW	total number of wavenumbers
NX	total number of lateral nodes
P	property field along lateral axis
$\mathbf{P}_j$	instantaneous complex dipole moment vector of dipole j
q	modulus of scattering vector [=$2k.\sin(\theta/2)$]
Q_a	absorption efficiency (Eq. 2.57)
Q_s	scattering efficiency (Eq. 2.58)
r	radial coordinate
$\mathbf{r}$	position vector
R	radius of axisymmetric medium
Re	Reynolds number
R_g	radius of gyration
R_η	spectrometer response function [IU W^{-1} sr m^{-1}]
s	line-of-sight coordinate
s_f	medium exit location
S_η	raw spectrum [IU]
S_1, S_2, S_3, S_4	complex amplitude scattering matrix elements
S_{11}	Mueller Matrix element
T	temperature [K]
u_0	fuel velocity at burner exit
x	position axis; lateral position alongside the flame; size parameter (=$\pi d/\lambda$)

x_0	lateral distance from origin
X_i	% ratio of two consecutive measurements at spectral index i
$\bar{X}$	mean X averaged over wavenumber range
y	position axis
Y_i	difference between two consecutive measurements at spectral index i
$\bar{Y}$	mean Y averaged over wavenumber range
z	position axis, height

Symbols

α	polarizability tensor
β	extinction coefficient [m^{-1}], differential scattering parameter Eq.(2.55)
δ_C	argument of complex number C
$\Delta\eta$	spectral resolution
ε	relative permittivity
ε_0	dielectric constant [$=8.8542\times10^{-12}$ $C^2N^{-1}m^{-2}$]
$\in$	complex dielectric function ($= m^2$)
ϕ	azimuthal scattering angle, phase difference [rad]
Φ	intermediate function (Eq. 4.18)
Γ	differential operator defined in (Eq. 4.14)
γ	intermediate function (Eq. 4.11), damping constant [rad/s]
η	wavenumber [cm^{-1}]
κ	absorption coefficient [m^{-1}]
λ	wavelength [m]
θ	polar scattering angle
Θ	scattering phase function
σ_s	scattering coefficient [m^{-1}] , sample standard deviation for flame spectrum
σ_{sb}	sample standard deviation for blackbody spectrum [IU]
τ	optical thickness
ω	angular frequency ($= 2\pi c_0\eta$) [rad/s]
ω_p	plasma frequency [rad/s]
ω_r	resonant frequency [rad/s]
Ω	solid angle [sr]
Ψ	refractive index indicator function (Eqs. 4.13,4.15,4.17) [m^2]

Subscripts and superscripts

a	aggregate, absorption
abs	absorption
b	blackbody, bulk material
eq	volume equivalent sphere
es	equivalent sphere
ext	external
f	free electron
hh	horizontal polarization
i	radial node index, incident field, spectral index
inc	incident
io	incident field at origin
j	lateral node index, dipole index, bound electron index
k	oscillating dipole index, slice index
l	index for incident polarization state
p	primary particle
ref	reference
s	scattered field
sca	scattering
vv	vertical polarization
η	per unit wavenumber
0	incident
01, *02*	orthogonal polarization states in DDSCAT formulation
$\|\|$	parallel polarization
$\perp$	perpendicular polarization
$'$	$\partial/\partial\eta$
$''$	$\partial^2/\partial\eta^2$

Abbreviations

ASM	Amplitude Scattering Matrix
bb	blackbody
DDA	Discrete Dipole Approximation
DL	Drude-Lorenz
FFT	fast Fourier transform

FT	Fourier transform
FT-VisIR	Fourier transform – visible, infrared
HAB	height above burner
IR	infrared
NEP	noise equivalent power
NIR	near-infrared
SNR	signal-to-noise ratio
SOR	signal-to-offset ratio
SSE	sum of squared errors
RDG	Rayleigh-Debye-Gans
RDG-FA	Rayleigh-Debye-Gans approximation for Fractal Aggregates
RMS	root mean square
UV	ultraviolet
Vis	visible

CHAPTER 1

INTRODUCTION

Soot is composed of nanoscale, carbonaceous particles produced in fuel-rich parts of flames as a result of incomplete combustion of hydrocarbons. Flame luminosity, which is associated with the radiation emitted by soot particles, is a typical way to observe soot within the flame. Another evidence of soot formation is smoke, which can be observed when the soot escapes the flame envelope.

Physically, soot appears as grape-like clusters of small spheres (spherules) as shown in Figure 1.1. Primary soot particles are generally small and spherical, ranging in size between 10-60 nm. As formation of soot progresses, the primary soot particles agglomerate to become random clusters that may have a fractal-like or chainlike morphology owing to electrical charging and random collision. Coagulation among these agglomerates leads to more complex morphology which leads to significantly different radiative properties from those of spheres [1-6].

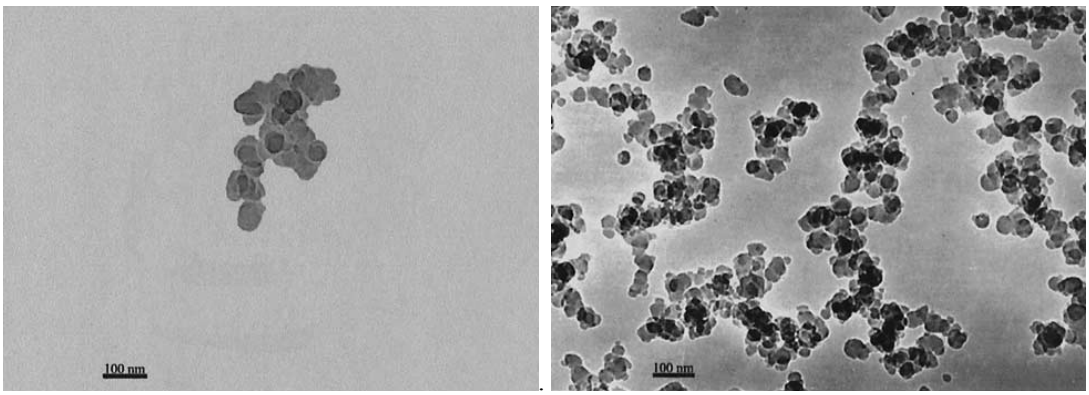

(a) (b)

Figure 1.1. Typical Transmission Electron Microscopy (TEM) photographs of soot aggregates along the axis of an ethylene-fuelled laminar jet diffusion flame [7]
(a) photograph near start of soot formation
(b) photograph near the maximum soot concentration condition.

In combustion processes, soot is an undesirable end product. Higher temperatures and pressures such as in Diesel engines, lead to increased amounts of soot which may be carcinogenic itself or absorbs other carcinogenic polycyclic aromatic hydrocarbons (PAHs) [8]. Correlation between pulmonary diseases and small size (5-300nm) particles has been proved by recent epidemiological studies [9]. Hence, soot emissions from stacks and tailpipes need to be controlled. On the other hand, in engines which derive their power from expansion, soot causes additional heat loss and reduces efficiency [10]. However, soot is a desired intermediate in furnaces, because it contributes a great deal to the heat transfer. Experiments have shown that soot emission is often considerably stronger than the emission from the combustion gases [11], it can even double or triple the heat that would be radiated by gaseous products alone [12]. This is because soot particles are generally at the same temperature as the flame, therefore, strongly emit thermal radiation in a continuous spectrum over the infrared (IR) region.

The strategy to find a compromise between the advantages and disadvantages of soot formation is to generate soot early in the flame, have it radiate and then have it oxidized before leaving the furnace [8]. In order to have such a control over soot formation and oxidation, it is essential to establish an understanding on these subtle processes. The present level of knowledge on the reactive and physical processes of soot in flame environments is quite limited, affecting progress toward developing reliable predictions of flame radiation properties, predictions of flame pollutant emission properties and computational models for combustion [7]. Considerable uncertainties associated with current diagnostic tools for *in-situ* observation of soot particle properties in combustion systems is an important obstacle that hampers further understanding about soot formation and oxidation mechanisms.

Characterization of soot in flame environments is a particularly challenging task. Strong sensitivity of soot mechanisms to temperature and flow gradients implies the necessity to acquire *in-situ*, nonintrusive measurement techniques. Electromagnetic radiation, particularly in UV, visible and infrared spectra serves as a suitable diagnostic tool due to the following advantages: *i*) the emission and transmission behavior of soot particles in these particular spectral ranges is sensitive to soot characteristics, *ii*) it is possible to identify spectral windows where radiation activity of soot does not interfere considerably with other constituents in the flame environment, *iii*) optical access enables probing hostile combustion environments. Presently existing widely used characterization techniques are intrusive techniques and/or techniques requiring complementary ex-situ measurements i.e.

transmission electron microscopy etc and/or they rely on external empirical inputs such as soot optical constants [13-18]. Reliability of existing *in-situ* techniques are questionable as they are either based on over-simplified approximations or suffer from strong dependence on external data for unknown physical parameters, which are introducing serious uncertainties. A fully independent, nonintrusive technique for complete *in-situ* characterization of soot is not available to date.

Most important limitation of optical soot characterization techniques is the uncertainty in refractive index (optical constants) of soot [5, 19]. Previous attempts on determination of wavelength dependent refractive index of soot by measurements or dispersion relations show considerable variations which point out the sensitivity of this critical parameter to flame conditions [20, 21]. Local variations of refractive index within a flame, its dependence on temperature, fuel type and H/C ratio are among reported findings [21-23]. These results about soot refractive index reveal that *in-situ* characterization of refractive index simultaneously with other soot properties is the most reliable approach.

Soot particles which appear as nanoscale spherules or fractal agglomerates of such spherules in flame environments can be characterized by determination of its temperature, volume fraction, optical constants and its morphological parameters such as size of primary spherules, fractal parameters, number distribution of monomers per aggregate, etc. This long list of unknowns can be retrieved at the same time only if the information obtained from experiments is adequate in quantity and quality. Use of spectrally resolved measurements for soot diagnostics is a promising approach in this sense, as it provides numerous data from the same location simultaneously.

In high-temperature environments such as flames, soot particles are strong emitters of thermal radiation with a continuous spectrum over the infrared. This emission can be a useful tool to extract characteristic information on soot particles such as their temperature, volume fraction and refractive index.

Near-infrared (NIR) range emission from soot particles is a suitable source of information for implementation of emission based soot property reconstruction methods as this range harbors wide spectral windows where other species are transparent and continuum soot radiation can be isolated. As soot particles attain smaller size parameters in NIR range when compared to visible range, the equations that govern radiative transfer can be simplified

considerably by neglecting scattering and eliminating effects of complex shape of soot agglomerates. Another potential advantage of this range is due to significant spectral dependence of soot refractive index when compared to visible range which introduces the possibility to extract characteristic information on soot optical constants from spectral variation of observed emission intensities. Utilization of NIR range spectral emission for soot property reconstruction is relatively less examined in the literature when compared with the existing applications in the visible and infrared ranges (reviewed in section 3.1.3). Therefore investigation of NIR range emission for soot property reconstruction deserves attention.

Motivated with the above considerations, the objective of the thesis is development and application of a nonintrusive optical methodology based on FTIR flame emission spectrometry in the near-infrared range, which can provide access to temperature, volume fraction and refractive index of soot particles formed inside flames, with minimal dependence on external data.

The methodology followed to achieve this objective relies on common basic principles of particle characterization techniques that make use of radiative transfer of electromagnetic waves emitted by or interacting with the particulate medium under investigation. How particles emit, absorb and scatter electromagnetic radiation depends on their physical and chemical properties such as the material they are made of (determines its complex index of refraction), its temperature, size with respect to the incident radiation, wavelength and its shape. Particle characterization by optical/IR methods is basically determination of physical and chemical properties of target particles from experimental information on how they emit, absorb and scatter radiation. This is an inverse problem as equations governing radiative transfer enable calculation of radiative parameters from physical properties of the medium as illustrated in Figure 1.2. A reliable inverse analysis of an accurate direct model enables inferring physical and optical properties from measured radiative parameters. Therefore, the main components of a radiative transfer based particle characterization technique can be outlined as:

- a reliable theoretical model for prediction of relation between desired particle properties and information on radiative parameters transmitted by those particles,
- a suitable measurement technique to observe the radiative parameters sensitive to particle characteristics and
- an inversion technique to infer particle properties from measurements.

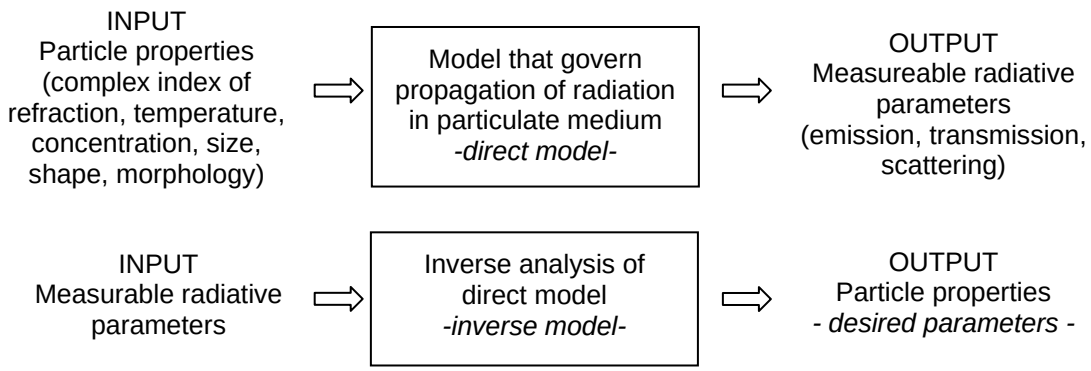

Figure 1.2. Principle of radiative transfer based nonintrusive particle characterization

In the present study, these three components were individually studied and then integrated to develop, apply and evaluate a novel nonintrusive soot characterization methodology based on NIR emission spectrometry that can provide access to temperature, volume fraction and refractive index of soot particles formed inside flames.

In Chapter 2, radiative transfer in soot laden-media, radiative properties of soot agglomerates were investigated and a direct model was developed to simulate line-of-sight radiative emission from axisymmetric sooty flames. In Chapter 3 measurement of line-of-sight flame emission intensities was performed by Fourier Transform Infrared (FTIR) spectroscopy on an axisymmetric, laboratory grade, ethylene/air diffusion flame within 1.1-1.7 μm spectral range and calibration, noise characterization, uncertainty assessment and reproducibility tests were elaborated. Then in Chapter 4 an inversion algorithm based on tomographic reconstruction of spectral line-of-sight intensities for inferring soot temperature, volume fraction and refractive index in small-scale flames was derived and its performance was evaluated by using the intensities simulated by the direct model. A set of data conditioning steps were developed to accommodate noisy data commonly encountered in practical soot diagnostics. Use was made of simulated noisy intensities to demonstrate effectiveness of the data conditioning procedure. Finally application of the proposed soot diagnostics methodology on the experimentally investigated ethylene diffusion flame was realized by inferring soot properties from measured intensities. Reconstructed properties are found to be in reasonable agreement with properties reported in literature for similar flames, indicating applicability of the present methodology for nonintrusive soot diagnostics in flames.

CHAPTER 2

RADIATIVE TRANSFER IN SOOT-LADEN MEDIA

The principle behind radiative transfer based diagnostics techniques is analysis of electromagnetic waves emitted by and/or interacting with a participating medium to extract the characteristic information about this medium. This is why a theoretical model that simulates the physics of radiative transfer from the specimen to the detecting equipment is the backbone of any optical characterization technique. In the present section the theoretical aspects on which the reconstruction methodology is built are explained and a comprehensive forward model is developed in order to assess the reconstruction capabilities of the inverse model.

Generation and propagation of radiative energy emitted by soot particles from the high-temperature, non-homogeneous, sooty combustion environment to the measuring equipment is governed mainly by three physical phenomena, *i*) radiative transfer along the participating medium *ii*) radiative properties of soot agglomerates, and *iii*) optical constants of soot bulk material. The first necessitates solution of line-of-sight radiative transfer equation for given system geometry, temperature profiles and radiative properties of particulate medium. The second phenomenon is at particle scale and deals with evaluation of radiative properties of soot aggregates of given optical constants, particle shape and size by using approximate methods. Determination of spectral optical constants requires use of a dispersion model that provides the relation between molecular properties and optical constants.

In the present chapter, these three models are first analyzed individually from the viewpoint of soot radiation in combustion systems and then their integration is demonstrated for simulation of spectrometry measurements. Presentation of the theoretical aspects behind each model is followed by their implementation to sooty media and validation of the models on ideal test cases. Last section involves description of the global forward model obtained by coupling these sub-models, application of the forward model to an experimentally characterized flame from literature and presentation of simulated line-of-sight intensities in this problem.

2.1. RADIATIVE TRANSFER MODEL

2.1.1. Problem definition and assumptions

Let us consider a physical situation where an optically thin, small-scale, soot-laden flame is monitored nonintrusively from its side, by measuring spectral intensity of radiative energy emitted by the cloud of soot particles, observed along a line-of-sight as depicted in Figure 2.1. The spectral range under consideration is near-infrared range spectral windows for soot, where radiative contributions due to all other combustion species are negligible. Soot particle cloud within such a flame is approximated as an absorbing, emitting medium with transparent, cold boundaries. Scattering due to soot particles is considered to be negligible as optically thin small-scale flames are expected to contain relatively small soot agglomerates that have size parameters less than unity in the near-infrared range. This approximation introduces considerable simplification to the problem by reducing the governing equation from integro-differential radiative transfer equation that needs to be solved simultaneously for all directions at all locations within the medium, to a line integral along the path, decoupled from the properties of rest of the medium. Justification for this approximation is provided in section 2.2.5.4.

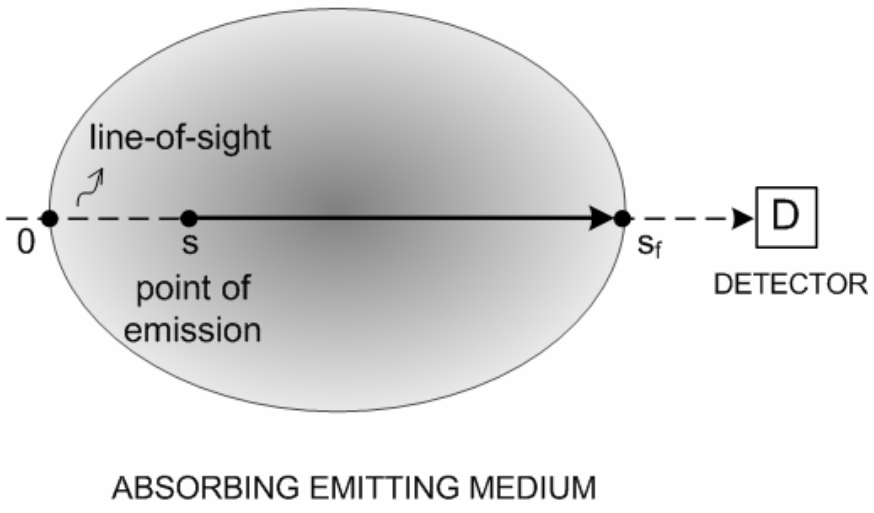

Figure 2.1. Line-of-sight radiative transfer from absorbing emitting medium to detector

2.1.2. Line-of-sight radiative transfer equation

Intensity of radiative energy emanating from the medium, impinging on the detecting equipment as shown in Figure 2.1 is governed by the line-of-sight radiative transfer equation which is based on radiative energy balance along a chord, s, crossing through the medium under analysis. Line-of-sight spectral emission intensity exiting the medium under local thermodynamic equilibrium is formulated as

$$I_{\eta,f} = \int_0^{s_f} \left[\kappa(\eta,s)\cdot I_{\eta,b}(\eta,s)\right]\cdot \exp\left[-\int_s^{s_f} \kappa(\eta,s')ds'\right] ds \tag{2.1}$$

where η and κ are wavenumber and position dependent absorption coefficient of the medium, respectively. $I_{\eta,b}$ is the blackbody intensity per unit wavenumber given by Planck function for a blackbody temperature T_b as [24]

$$I_{\eta,\mathrm{b}} = 2n^2hc_0^2 \frac{\eta^3}{\left[\exp\left(hc_0\eta/nkT_\mathrm{b}\right)-1\right]} \tag{2.2}$$

where h, k and c_0 are Planck's constant, Boltzmann's constant and speed of light in vacuum, respectively and n is the refractive index of the surrounding medium which can be taken as unity for air and combustion gases.

In Eq. (2.1) radiative intensity emitted at point s given in the first brackets undergoes extinction due to absorption along its path towards s_f, as expressed in the exponential term which represents transmittance of this path. Outermost integration sums up the transmitted parts of the emitted intensities along the line-of-sight.

Once the spatial and spectral variation of absorption coefficient and temperature along the line-of-sight are known, $I_{\eta,b}$ can directly be evaluated from Eq. (2.1) by numerical integration.

2.1.3. Numerical solution method for axisymmetric media

The geometric configuration selected for implementation of the nonintrusive technique in the present study is that of an axisymmetric open flame. The treatment is limited to this configuration because of its particular suitability to 1-D tomographic reconstruction which will be explained section 4.2.1. In order to simulate line-of sight flame emission experiments, lateral positions are first specified relative to the medium and hypothetical chords are placed as shown in Figure 2.2. Line-of-sight emission intensity at lateral position x_j is calculated by performing the line integrals as the chord j crosses the medium as given by Eq. (2.1). Evaluating the inner and outer integrals requires knowledge of temperature and absorption coefficient profiles along the path s, where radial profiles are available by specifications. Radial profiles are converted to profiles along the path length, by using Eq. (2.3) which gives functional relation between r and s for a given chord j at lateral position x_j.

$$r(s) = \sqrt{x_j^2 + \left(s - \sqrt{R^2 - x_j^2}\right)^2} \tag{2.3}$$

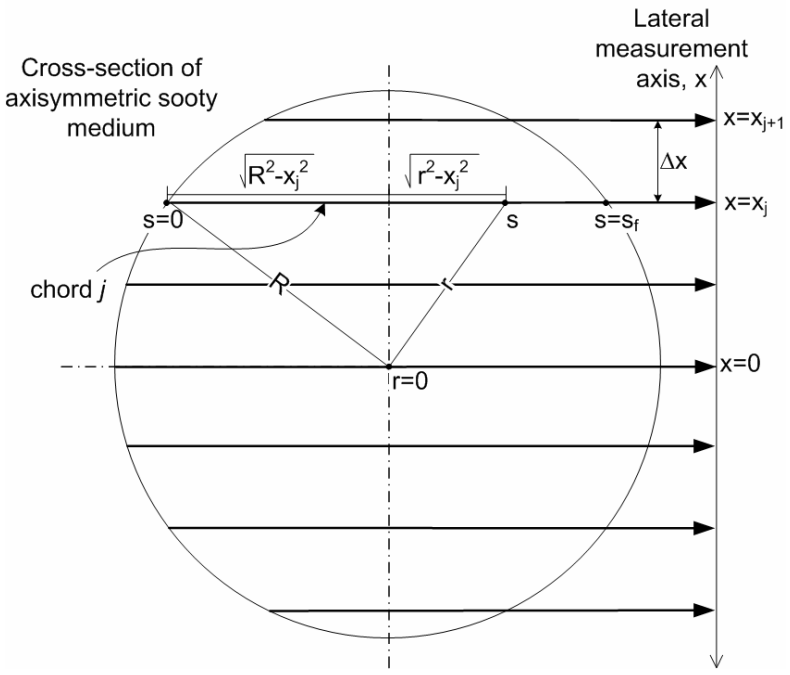

Figure 2.2. Coordinate system and geometrical configuration for modeling line-of-sight radiative transfer in axisymmetric medium

The total path length of line-of-sight chord *j* through the medium, which is required for determination of integration limits in Eq. (2.1) can be geometrically evaluated from

$$s_{f,j} = 2\sqrt{R^2 - x_j^2} \tag{2.4}$$

Now that the functional expressions of the integrands in Eq. (2.1) are available, numerical quadratures can be used to evaluate the integrals accurately. In the present simulation, IMSL library routine QDAGS [25] which is an implementation of QAGS algorithm by Piessens *et* al. [26] was utilized. This algorithm is based on a 21-point Gauss-Kronrod rule to estimate the integral and uses a globally adaptive scheme to reduce the absolute error estimated by comparison with the 10-point Gauss quadrature rule. A relative error tolerance of 1% was imposed for present simulations.

2.1.4. Validation

Prediction of projected emission intensities at given lateral positions from given radial distribution of temperature and absorption coefficient is carried out by means of a FORTRAN code which implements the numerical solution method described above. The code was validated on a hypothetical test problem of uniform temperature and radiative properties. Homogeneous case is a suitable test case as its exact solution can be evaluated analytically, and it still tests the accuracy of the numerical integration routine as integrands in Eq.(2.1) are exponentially varying functions. The medium specifications which are summarized in Table 2.1 were selected so as to be close to flame conditions. Wavelength is specified within the near-infrared range.

In homogeneous media, the inner integral for optical thickness can be directly evaluated as

$$\tau(s,\eta) = \exp\left[-\int_{s}^{s_f} \kappa(\eta)ds\right] = \exp\left[-\kappa\cdot(s_{f,j} - s)\right] \tag{2.5}$$

Substituting Eq. (2.5) in Eq. (2.1) and evaluating the outermost line integral gives the exact expression for line-of-sight emission intensity for each projection chord as

Table 2.1. Physical specifications of homogeneous test problem

Radius of axisymmetric medium, R	3.5 mm
Temperature, T	1500 K
Wavelength, η	1.25 μm (8000 cm^{-1})
Refractive index function, E_m at 1.25μm [(a)]	0.3104
Soot volume fraction, f_v	3 ppm
Absorption coefficient [(b)], κ	14.04 m^{-1}

[(a)] Calculated from Drude-Lorenz model (explained in section 2.3.2) by using dispersion constants from Dalzell and Sarofim [27]

[(b)] Evaluated by RDG-FA method from f_v and E_m (see section 2.2.4)

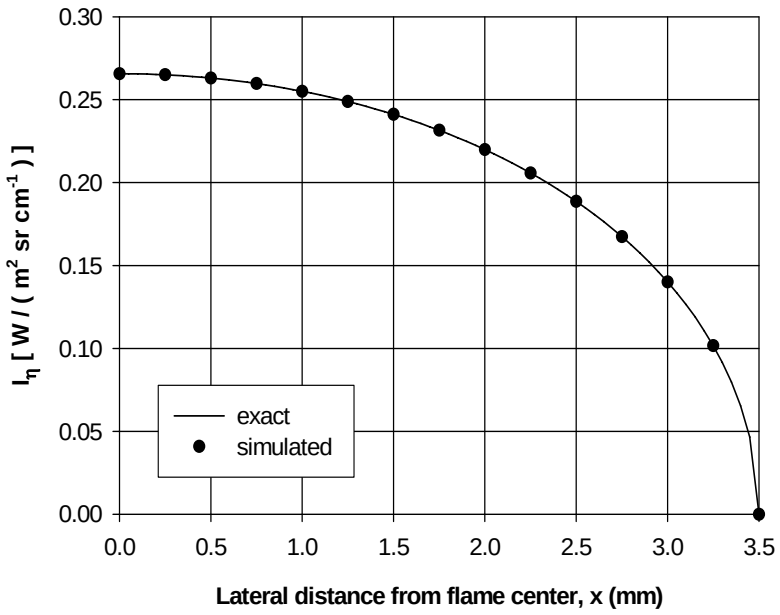

Figure 2.3. Comparison between simulated line-of-sight emission intensities and exact solutions

$$I_{\eta,j} = \kappa I_{b\eta}(T) \int_0^{s_{f,j}} \exp\left[-\kappa \cdot (s_{f,j} - s)\right] ds = I_{b\eta}(T).\left[1 - \exp(-\kappa \cdot s_{f,j})\right] \quad (2.6)$$

which can readily be evaluated from radiative properties and path length s_{fj}. Comparison between the intensities simulated by the code and exact solutions evaluated from Eq. (2.6) is displayed in Figure 2.3. Excellent agreement between the two solutions demonstrates the validity of the radiative transfer code.

This sub-model evaluates line-of-sight radiative emission intensity from given temperature and radiative property distributions. Coupling it with the radiative property sub-models described in the next two sections will form the forward model that enables simulation of measurements.

2.2. RADIATIVE PROPERTY MODEL

2.2.1. Interaction of electromagnetic waves with agglomerated particles

Optical techniques which enable nonintrusive characterization are based on determination of particle properties from their interaction with electromagnetic radiation. As soot is found in agglomerates of nanoscale spheres [2, 4], such a complex structure should be taken into consideration while studying radiative properties of soot.

When an electromagnetic wave interacts with a medium containing small particles, the radiative intensity is altered due to absorption and/or scattering phenomena. These interactions are governed by Maxwell's equations which is the mathematical expression for interaction between light and matter. How much and into which direction a particle scatters an electromagnetic wave passing through its vicinity depends on the shape of the particle, its material (i.e. complex index of refraction, m = n + ik), its size relative to wavelength (i.e. size parameter, $x = \pi d/\lambda$) and clearance between the particles.

As exact solution of Maxwell's equations is not possible for realistic complex shaped particles such as aggregates, many numerical approaches have been developed for solving the electromagnetic interaction problem approximately. Recent reviews on these techniques [28, 29] indicate that no single method can be identified as the best approach for all

problems. Each method has a different applicability range in terms of size parameters, refractive indices and geometries. Availability of the code, ease of implementation, setup time and computational load are other factors that affect the selection of solution technique.

Ku and Shim [30] presented a comparison between Jones, Purcell and Pennypacker and Iskander-Chen-Penner (I-C-P) formulations for prediction of radiative properties of aggregates. I-C-P method which is based on volume-integral equation formulation was found to be the most accurate approach. Comberg and Wriedt [31] evaluated Discrete Dipole Approximation (DDA) and Multiple Multipole (MMP) methods for densely packed clusters against Order of Scattering Mie approach (OS-Mie). Both methods were found to yield accurate solutions but DDA method was found to be memory intensive. Another comparative study was carried out by Kimura [32] who applied DDA and superposition T-Matrix methods to simulated fractal aggregates and compared the solutions with eachother. The solutions were in agreement but T-Matrix method was reported to be computationally expensive especially for large numbers of spheres.

The numerical methods that are most commonly used in literature for modeling radiative properties of soot aggregates can be listed as Rayleigh-Debye-Gans approximation for Fractal Aggregates (RDG-FA) [33-52], Discrete Dipole Approximation (DDA) [35, 42, 53-56] and Iskander-Chen-Penner (ICP) approach [57-62], the latter two being physically equivalent methods [63, 64] for rather comprehensive modeling of arbitrarily shaped particles. RDG approximation has received considerable interest as it accommodates complicated irregular particle shape and population effects with relatively simple expressions and this feature poses a critical advantage from the viewpoint of inversion for diagnostics applications [50, 65]. Also its simplicity enables efficient computations in coupled heat transfer models [37]. However, as will be discussed later in more detail, validity of RDG theory for soot is questionable especially towards the infrared due to its large refractive index. Therefore, its use for beyond its validity conditions needs to be carried out cautiously, in close comparison with a more rigorous model, which is selected as DDA in this study.

The objective of this chapter is to determine limits of applicability of RDG-FA by comparing its predictions against those of DDA at the wavelength range under consideration and corresponding refractive index values proposed in the literature for soot. To realize this objective first the DDA method is experimentally validated within the frame of a

collaborative study on a model aggregate against microwave measurements of amplitude and phase of scattered field [66]. In order to enable comparisons in terms of amplitude and phase, publicly available DDA code, DDSCAT was modified for accurate prediction of these primary parameters that provide complete description of the scattered field [67]. RDG-FA and DDA methods were then compared on an idealized sphere-like aggregate against exact solutions for absorption and scattering efficiencies and phase function. Finally the RDG model predictions were compared against DDA solutions on a soot-like fractal aggregate model.

2.2.2. Electromagnetic scattering-absorption problem

The physical situation under consideration is depicted in Figure 2.4. An arbitrary particle surrounded by a homogeneous, isotropic and non-conducting medium is subjected to an incident electromagnetic radiation which is scattered by the particle in all directions. The problem is determination of the electromagnetic field scattered by the target particle of known shape, size and optical constants, in response to incident monochromatic beam of known wavelength and polarization state.

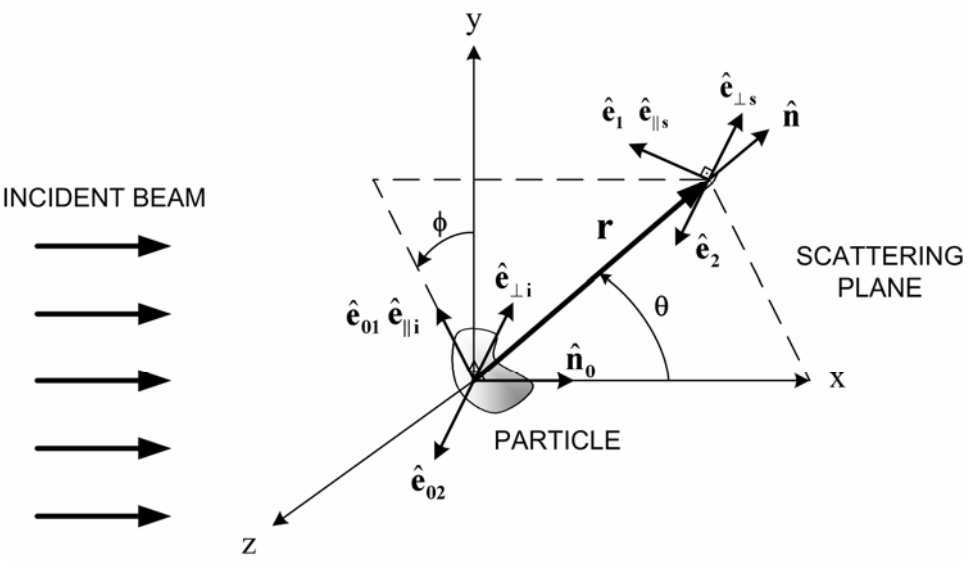

Figure 2.4. Coordinate system and basis vectors for the scattering problem.

The incident wave of wavenumber k (=$2\pi/\lambda$) propagating in $\hat{\mathbf{n}}_0$ direction and scattered wave propagating along $\hat{\mathbf{n}}$ detected at position $\mathbf{r}$ (= $r\hat{\mathbf{n}}$) in the far field, where kr >>1, are represented in terms of their parallel and perpendicular components as follows [68]

$$\mathbf{E}_i = E_{\|,i} \cdot \hat{\mathbf{e}}_{\|\mathrm{i}} + E_{\perp,i} \cdot \hat{\mathbf{e}}_{\perp\mathrm{i}} \tag{2.7}$$

$$\mathbf{E}_s = E_{\|,s} \cdot \hat{\mathbf{e}}_{\|\mathrm{s}} + E_{\perp,s} \cdot \hat{\mathbf{e}}_{\perp\mathrm{s}} \tag{2.8}$$

where $\hat{\mathbf{e}}_{\perp\mathrm{i}}$, $\hat{\mathbf{e}}_{\|\mathrm{i}}$, $\hat{\mathbf{e}}_{\perp\mathrm{s}}$, $\hat{\mathbf{e}}_{\|\mathrm{s}}$ are basis vectors for orthogonal polarization states of incident and scattered fields parallel and perpendicular to the scattering plane, that is the plane formed by $\hat{\mathbf{n}}_0$ and $\hat{\mathbf{n}}$. The origin for the position vector $\mathbf{r}$ is located at an arbitrary point within the particle boundary and it coincides with the origin of the scattering plane, i.e., pivot point for the scattering angle θ.

Scattered wave in the far-field can be represented in terms of the incident field via *amplitude scattering matrix* (ASM) as follows

$$\begin{pmatrix} E_{\|,s} \\ E_{\perp,s} \end{pmatrix} = \frac{\exp\left[ik(r - \mathbf{r}\cdot\hat{\mathbf{n}}_0)\right]}{-ikr} \begin{pmatrix} S_2 & S_3 \\ S_4 & S_1 \end{pmatrix} \begin{pmatrix} E_{\|,i} \\ E_{\perp,i} \end{pmatrix} \tag{2.9}$$

where $E_{\|,i}$, $E_{\perp,i}$ and $E_{\|,s}$, $E_{\perp,s}$ are complex parallel and perpendicular components of the incident and scattered electric fields, respectively. The elements of the ASM are also complex variables. Any complex variable C can be expressed in terms of magnitude |C| and phase δ_C as follows

$$C = |C| \cdot \exp(i\delta_C) \tag{2.10}$$

Eq. (2.9) implies that the amplitude of the scattered field and its polarization state depend on the amplitude and polarization of the incident field, scattering distance, wavenumber and the magnitudes of complex ASM elements. On the other hand, the phase of the scattered field depends on the phase and polarization state of the incident field and the phases of the ASM elements. The origins of the phases of incident field and ASM elements must be coincident with the origin of the scattering plane for meaningful phase analysis.

A radiative property model that solves the above scattering problem may have a variety of output parameters that characterize the response of the particle to incident radiation. A complete solution to the scattering problem requires determination of the ASM elements which can be regarded as primary variables as all other auxiliary scattering parameters are derived from ASM elements. Commonly analyzed scattering parameters such as absorption, scattering cross-sections, Mueller matrix elements, intensities etc. are secondary parameters that characterize the polarization state and amplitude of the scattered field and hence partially describe scattering phenomena. In the present study the parameters of interest for experimental validation of DDA are complex ASM elements which provide complete description of the relation between incident and scattered wave fields.

On the other hand, comparisons with RDG-FA approximations on hypothetical test problems are based on secondary radiative properties such as absorption and scattering efficiencies and S_{11} element of the Mueller matrix. Absorption and scattering efficiencies are obtained by normalizing corresponding optical cross-sections with physical cross-sectional areas of the particles. Physical significance of these parameters is as follows. Total scattered power by a particle is proportional to the incident intensity and the proportionality constant having dimension of area is termed *scattering cross-section*, C_s. Similarly, *absorption cross-section*, C_a is the ratio of total absorbed power to incident intensity. When these optical cross-sections are normalized with physical cross-sectional area of the particle, the resulting property is termed *scattering/absorption efficiency* and gives the ratio of scattered power to incident power. S_{11} element of the Mueller matrix is an angle dependent property and is directly related to the scattering phase function as follows

$$\Theta(\theta,\phi) = \frac{4\pi}{k^2 C_s} S_{11}(\theta,\phi) \tag{2.11}$$

where θ and ϕ denote scattering direction. The phase function expresses the probability that irradiance on the particle from the direction of incidence will be scattered in (θ,ϕ) direction. The phase function is defined in normalized form as follows

$$\frac{1}{4\pi}\int_0^{2\pi}\int_0^{\pi}\Theta(\theta,\phi)\ \sin\theta\ d\theta\ d\phi = 1 \tag{2.12}$$

For practical utilization of particle radiative property model in combination with the direct and inverse methods, the parameters that characterize the radiative properties of the particulate medium are required to provide input to the radiative transfer model. These medium properties are the scattering phase function, absorption and scattering coefficients. Absorption and scattering coefficients depend on local properties of the particle population (size, shape, refractive index) and wavelength. The scattering phase function depends on scattering angle as well as local particle properties and wavelength. Once single particle properties (absorption – scattering cross-sections, phase function) are determined from the radiative property model, they are ensemble averaged based on prespecified particle number-property distribution information to evaluate effective radiative properties of the particle cloud. For a particle cloud with uniform size, shape and refractive index, medium absorption and scattering coefficients are directly proportional to the local number density of particles as given below and the medium phase function is equivalent to that of a single particle.

$$\kappa = \bar{N} C_a \tag{2.13}$$

$$\sigma_s = \bar{N} C_s \tag{2.14}$$

The extinction coefficient is expressed as

$$\beta = \kappa + \sigma_s \tag{2.15}$$

To take the polydisperse nature of particles into consideration, the particle population is subdivided into sub-classes of uniform physical properties such as spherule size, number of spherules per aggregate etc. and number averaged properties are calculated by using associated number distribution function. In the present study the particles are considered to be of uniform size, shape and refractive index at a given location.

2.2.3. Discrete dipole approximation

Discrete dipole approximation (DDA), which is also referred to as coupled dipole approximation, is a well-established approach for estimation of scattering and absorption of electromagnetic radiation by arbitrarily shaped particles of size comparable to incident wavelength. This approach is categorized as one of the volume-integral equation methods for

numerical modeling of electromagnetic scattering [69]. This approach, classified as one of the volume integral equation techniques for discretization of Maxwell's equations, was pioneered by Purcell and Pennypacker [70] and developed by Draine, Flatau and co-workers [71-77], Singham and Bohren [78-80], Mulholland *et* al. [42] and Hoekstra *et* al. [81, 82]. Recent reviews on this method and further details can be found from [71] and [73].

The approximation is based on replacement of a continuum real scatterer by a finite array of interacting discrete dipoles positioned at the sites of a lattice such that the lattice spacing is small compared to wavelength. The oscillating polarizations (dipole moments) induced on each dipole due to the incident wave and the electric fields of the other oscillating dipoles in the system can be expressed by linear relations depending on polarizability of the dipole, incident electric field, positions and polarizations of other dipoles. The resulting system of $3N_d$ coupled linear equations, N_d being the total number of dipoles, represents a discrete analog of the integral equation that governs the scattering problem. Once the system of complex linear equations is solved for polarizations, the scattered electric fields at desired scattering planes and directions can be readily evaluated. The associated formulations for evaluation of polarizations, forward scattering amplitude matrix elements, ASM elements, absorption emission and scattering cross-sections were extensively documented previously [74].

The principal advantage of the DDA is that it is completely flexible regarding the geometry of the target, being limited only by the need to use an interdipole separation, d, small compared to the structural lengths in the target and the wavelength, λ. Numerical studies with the DDSCAT code indicated that the second criterion is adequately satisfied for calculations of total cross-sections if $|m|kd<1$ where $k=2\pi/\lambda$. More accurate calculations of scattering cross sections necessitates a more conservative criterion, $|m|kd<0.5$. It is therefore clear that DDA is not suitable for very large values of the equivalent sphere size parameter, x_{eq}, or very large values of refractive index, m. The primary utility of the DDA is for scattering by dielectric targets with sizes comparable to the wavelength.

2.2.3.1. Description of the method

The scattering problem described in the previous section is governed by Maxwell's equations, analytical solution of which is restricted to specific simple situations [68].

Discrete Dipole Approximation (DDA) is a flexible approach for simulation of scattering by arbitrarily shaped particles. Derivation of DDA equations from Maxwell's monochromatic curl equations can be found in Lakhtakia and Mulholland [63].

DDA is based on representation of the scatterer by an array of dipoles. Each dipole is characterized by a polarizability tensor, α_j , that depends on the number density of dipoles, wavenumber of the incident wave and the optical constants of the target material with respect to the surrounding media [72, 83]. Once the array of dipoles together with corresponding array of dipole polarizabilities is constructed, the next task is to solve for the dipole moments of the dipoles. Each dipole subjected to an external electric field oscillates with a dipole moment $\mathbf{P}_j = \alpha_j.\mathbf{E}_{ext,j}$ where $\mathbf{P}_j$ stands for the instantaneous complex dipole moment vector of dipole j. The external electric field at position j, $\mathbf{E}_{ext,j}$, is the superposition of the electric fields radiated by the rest of the oscillating dipoles together with the incident electric field. Therefore the dipole moment vector for dipole j can be expressed as

$$\mathbf{P}_j = \alpha_j \left(\mathbf{E}_{inc,j} - \sum_{k \neq j} \mathbf{A}_{jk} \cdot \mathbf{P}_k \right) \tag{2.16}$$

where $\mathbf{E}_{inc,j}$ is the instantaneous electric field due to the incident wave at dipole position $\mathbf{r}_j$ and $(-\mathbf{A}_{jk}\cdot\mathbf{P}_k)$ is the electric field at dipole location $\mathbf{r}_j$ caused by the oscillating dipole k located at $\mathbf{r}_k$. 3×3 matrix $\mathbf{A}_{jk}$ is given by

$$\mathbf{A}_{jk} = \frac{\exp(ikr_{jk})}{r_{jk}} \left[k^2(\hat{\mathbf{r}}_{jk}\hat{\mathbf{r}}_{jk} - \tilde{\mathbf{1}}_3) + \frac{ikr_{jk} - 1}{r_{jk}^2}(3\hat{\mathbf{r}}_{jk}\hat{\mathbf{r}}_{jk} - \tilde{\mathbf{1}}_3) \right] \text{ for } j \neq k \tag{2.17}$$

where $r_{jk} \equiv |\, \mathbf{r}_j - \mathbf{r}_k \,|$ is the distance between two dipoles and $\hat{\mathbf{r}}_{jk} \equiv (\, \mathbf{r}_j - \mathbf{r}_k \,) / r_{jk}$ is the unit vector along the direction from source dipole to target dipole and $\tilde{\mathbf{1}}_3$ is 3×3 identity matrix. The first term in the brackets above, accounts for the far-field effects and the second term accounts for the near-field effects of oscillating dipole. Assigning $\mathbf{A}_{jj} = \alpha_j^{-1}$ enables representation of the coupled dipole problem as a system of $3N_d$ complex linear equations as follows

$$\mathbf{E}_{inc,j} = \sum_{k=1}^{N} \mathbf{A}_{jk} \cdot \mathbf{P}_k \quad j = 1,2,3,..,N_d \tag{2.18}$$

The above equation which is the fundamental equation for DDA, can be solved for the unknown dipole moment vectors by various matrix inversion techniques in small scale problems or some iterative methods in large scale problems. Once the dipole moments are obtained, scattered field at position **r** can be evaluated from

$$\mathbf{E}_s = \frac{k^2 \exp(ikr)}{r} \sum_{j=1}^{N} \exp(-ik\hat{\mathbf{r}} \cdot \mathbf{r}_j)(\hat{\mathbf{r}}\hat{\mathbf{r}} - \tilde{\mathbf{1}}_3) \cdot \mathbf{P}_j \tag{2.19}$$

The above description summarizes the basic principles of DDA. In practice, DDA implementations show variations due to different applications associated with: *i*) dipole array configuration, *ii*) physical models to relate dipole polarizabilities to complex dielectric constant, *iii*) use of fast-Fourier transform (FFT) algorithms utilized for efficient evaluation of matrix-vector products and *iv*) numerical methods for accurate and computationally efficient solution of complex linear system of equations. Usually the particle is framed in a cubic lattice and occupied cells are treated as dipoles. Reviews and discussions on different prescriptions for dipole polarizabilities, FFT algorithms, and iterative linear system solvers can be found in [73] and references cited therein. Specific features of the present DDA implementation are given in Table 2.2.

Table 2.2. Specific features of the present DDA implementation

Feature	**Present practice**	**Source**	**DDSCAT acronym [84]**
Dipole geometry	Cubic lattice		
Dipole polarizability model	Lattice dispersion relation	Developed by Draine and Goodman [72], improved by Gutkowicz-Krusin and Draine [83]	GKDLDR
FFT	Generalized prime factor algorithm for FFT	Temperton [85]	GPFAFT
Linear system solver	Preconditioned bi-conjugate gradient method with stabilization	Developed by van der Vorst [86], implemented in Parallel Iterative Methods (PIM) package by da Cunha and Hopkins [87].	PBCGST

2.2.3.2. DDSCAT code and its adaptation of for prediction of amplitude scattering matrix elements

Publicly available DDSCAT code [84] developed by Draine and Flatau provides a flexible means for implementation of DDA and serves for different applications in earlier studies by various researchers. Its accuracy was previously demonstrated by comparing its predictions for absorption and scattering cross sections, some Mueller Matrix elements against Mie theory solutions for spheres and against solutions of other methods or measurements [73, 84].

Experimental validation of DDSCAT presented in the next section is based on comparisons of ASM elements as microwave measurements can provide these primary variables. Current DDSCAT software package was designed to calculate DDA predictions for secondary radiative properties such as absorption and scattering efficiency factors, Mueller scattering intensity matrix. Its accuracy and limitations for prediction of these parameters was demonstrated extensively. However, in its original form, the complex ASM elements computed at intermediate stages within the code are inaccurate. Predictions of the original DDSCAT v.6.1 code for ASM elements of a single sphere of size parameter 3 and refractive index m = 2+i is presented in Figure 2.5 and compared with Mie theory solutions obtained via Bohren and Huffmann's BHMIE code [68]. This test case was previously analyzed in [72, 74, 84] to demonstrate accuracy of DDSCAT predictions for efficiency factors and differential scattering cross section which are all quantities dependent on the magnitude of the ASM elements. As can be seen from Figure 2.5, magnitudes of the elements are correctly predicted, however the phase predictions are not accurate. To correct this error which does not affect efficiency factors and Mueller matrix elements, it is necessary to analyze how ASM elements are computed within the code.

The DDSCAT code is based on the formulations outlined in [74] in which scattered electric field is expressed in terms of the incident field as follows

$$\begin{pmatrix} E_{1,s} \\ E_{2,s} \end{pmatrix} = \frac{\exp\left[ik(r-\mathbf{r}\cdot\hat{\mathbf{n}}_0)\right]}{kr} \begin{pmatrix} f_{11} & f_{12} \\ f_{21} & f_{22} \end{pmatrix} \begin{pmatrix} E_{01,0} \\ E_{02,0} \end{pmatrix} \tag{2.20}$$

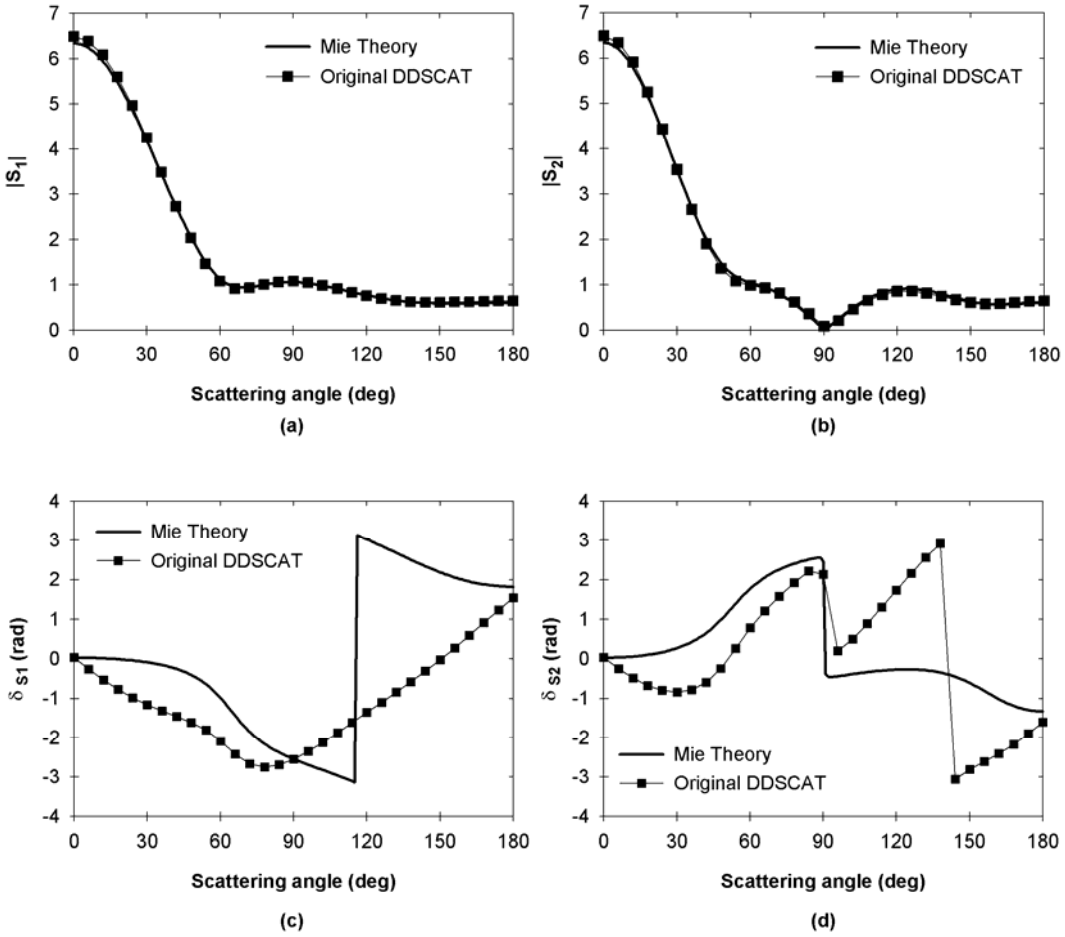

Figure 2.5. Comparison between predictions of the original DDSCAT v.6.1 code and Mie theory solutions for magnitudes and arguments of the complex ASM elements (x=3, m = 2+i).

$$\mathbf{E}_0 = E_{01,0} \cdot \hat{\mathbf{e}}_{01} + E_{02,0} \cdot \hat{\mathbf{e}}_{02} \tag{2.21}$$

$$\mathbf{E}_s = E_{1,s} \cdot \hat{\mathbf{e}}_1 + E_{2,s} \cdot \hat{\mathbf{e}}_2 \tag{2.22}$$

where **f** is the "forward scattering amplitude matrix" defined in terms of parallel and perpendicular components of $\mathbf{P}_j = \mathbf{P}_j^{01} \cdot \hat{\mathbf{e}}_{01} + \mathbf{P}_j^{02} \cdot \hat{\mathbf{e}}_{02}$ which are computed separately for two orthogonal polarization states of linearly polarized incident field. For incident polarization state *l* and scattered field polarization state *m* the elements of the matrix are evaluated from

$$f_{ml} = \frac{k^3}{E_0} \sum_{j=1}^{N} \exp\left(-ik\hat{\mathbf{n}}.\mathbf{r}_j\right) \mathbf{P}_j^{(l)} \cdot \hat{\mathbf{e}}_m \tag{2.23}$$

Eq. (2.20) is equivalent to Eq. (2.9) but based on the basis vectors $\hat{\mathbf{e}}_{01}, \hat{\mathbf{e}}_{02}, \hat{\mathbf{e}}_1, \hat{\mathbf{e}}_2$ with opposite sign convention such that $\hat{\mathbf{e}}_{01} \times \hat{\mathbf{e}}_{02} = \hat{\mathbf{n}}_0$ and $\hat{\mathbf{e}}_1 \times \hat{\mathbf{e}}_2 = \hat{\mathbf{n}}$ when polarization states $\hat{\mathbf{e}}_{01}$ and $\hat{\mathbf{e}}_1$ are selected to lay on the scattering plane. The relation between the two sets of basis vectors in Eqs. (2.20) and (2.9) is demonstrated in Figure 2.4. In this configuration, the relation between the ASM elements which is the parameter of interest in the present study and **f** matrix can be obtained by equating RHSs of two equations

$$\begin{pmatrix} S_2 & S_3 \\ S_4 & S_1 \end{pmatrix} = i \begin{pmatrix} -f_{11} & -f_{12} \\ f_{21} & f_{22} \end{pmatrix} \tag{2.24}$$

The above relation implies that the phase of the complex ASM elements which are inaccurately computed in the direct code is directly dependent on phase of the corresponding elements of the **f** matrix. From Eq. (2.23) the phase of f_{ml} depends on the position vectors of each dipole ($\mathbf{r}_j$) and phase of the dipole moment ($\mathbf{P}_j$). At this point it is evident that the origin for the position vectors needs to be coincident with the origin selected within the target. Inspection of the code revealed that the positions assigned to the dipoles at target generation stage is in coherence with input target origin but the origin is then shifted to the centre of a corner cell of the cubic lattice at an intermediate stage. This problem can be fixed by using initial correct positions for $\mathbf{r}_j$ term in f_{ml} computation (Eq. (2.23)). The second incompatibility in phase arises during the computation of dipole moments ($\mathbf{P}_j$) where origin is shifted to the lattice corner to avoid negative positions which is apparently a convenient

practice for the fast Fourier transform (FFT) application. The phase error in dipole moment vector caused by shifting the origin to the corner can be eliminated by adding a correction to the phase of the variable defined as incident field at origin as follows

$$\mathbf{E}_{\mathbf{io,modified}} = \mathbf{E}_{\mathbf{io}} \cdot \exp(ik\hat{\mathbf{n}}_{\mathbf{0}} \cdot \mathbf{r}_{\mathbf{oc}}) \tag{2.25}$$

where $\mathbf{r}_{\mathbf{oc}}$ is the position vector from target corner to origin.

The modifications implemented on the original source code are provided in Appendix A.

2.2.3.3. Evaluation of radiative properties of interest

The parameter of interest for experimental validation of DDA (section 2.2.5.2) is relative amplitude of the scattered wave with respect to incident field and phase difference of scattered wave from the incident wave for identically polarized scattering and incidence. Variations of these parameters along the scattering angle provide a complete description of the scattered field. Amplitude of scattered wave in the far field relative to that of incident wave can be obtained from ASM elements as presented in Eqs. (2.26) and (2.27) for parallel and perpendicularly polarized incident fields, respectively. In this test case the scattering plane is horizontal so subscripts *hh* (horizontal) and *vv* (vertical) correspond to parallel and perpendicularly polarized incident and scattered waves, respectively.

$$M_{hh} = \frac{\left|E_{\parallel,s}\right|}{\left|E_{\parallel,i}\right|} = \frac{\left|S_2\right|}{kr} \tag{2.26}$$

$$M_{vv} = \frac{\left|E_{\perp,s}\right|}{\left|E_{\perp,i}\right|} = \frac{\left|S_1\right|}{kr} \tag{2.27}$$

Phase differences between the scattered and incident fields are given by Eqs. (2.28) and (2.29) for parallel and perpendicularly polarized incidence, respectively.

$$\Delta\phi_{hh} = -\left[\delta_{S2} - \frac{\pi}{2}\right] \tag{2.28}$$

$$\Delta\phi_{vv} = -\left[\delta_{S1} - \frac{\pi}{2}\right] \tag{2.29}$$

Comparison of DDA with RDG-FA predictions in sections 2.2.5.3 and 2.2.5.4 were carried out in terms of secondary radiative properties. DDA predictions for absorption and scattering cross-sections are calculated as follows from dipole polarizabilities [74].

$$C_a = \frac{4\pi k}{\left|\mathbf{E_0}\right|^2}\sum_{j=1}^{N}\left\{\mathrm{Im}\left[\mathbf{P}_j\cdot\left(\alpha_j^{-1}\right)^*\mathbf{P}_j^*\right] - \frac{2}{3}k^3\mathbf{P}_j\cdot\mathbf{P}_j^*\right\} \tag{2.30}$$

$$C_s = \frac{k^4}{\left|\mathbf{E_0}\right|^2}\int_{4\pi}\left|\sum_{j=1}^{N}\left[\mathbf{P}_j - \hat{\mathbf{n}}\left(\hat{\mathbf{n}}\cdot\mathbf{P}_j\right)\right]\exp\left(-ik\hat{\mathbf{n}}\cdot\mathbf{r}_j\right)\right|^2 d\Omega \tag{2.31}$$

Once cross sections are evaluated, they are normalized with volume equivalent sphere cross-section to yield absorption and scattering efficiencies as follows

$$Q_a = \frac{C_a}{\pi a_{eq}^2} \tag{2.32}$$

$$Q_s = \frac{C_s}{\pi a_{eq}^2} \tag{2.33}$$

where a_{eq} is the radius of the sphere of volume equal to the total volume of occupied dipoles in the target. Predictions for S_{11} element of the Mueller scattering matrix is computed from ASM elements as given below [68].

$$S_{11}(\theta,\phi) = \frac{\left|S_1(\theta,\phi)\right|^2 + \left|S_2(\theta,\phi)\right|^2 + \left|S_3(\theta,\phi)\right|^2 + \left|S_4(\theta,\phi)\right|^2}{2} \tag{2.34}$$

2.2.4. Rayleigh-Debye-Gans approximation for fractal aggregates

Rayleigh-Debye-Gans approximation (also referred to as Rayleigh-Gans-Debye, Rayleigh-Gans or first Born approximation) provides relatively simple expressions for modelling

radiative properties of small, arbitrarily shaped particles. It is based on approximating the field inside the particle with the incident field and neglection of self-interaction and multiple-scattering effects. Conditions of validity of this approximation are [65, 68, 88, 89]

$$| m - 1 | << 1 \tag{2.35}$$

$$ka| m - 1 | <<1 \tag{2.36}$$

where a is the characteristic length of the particle (radius for a sphere) and $k=2\pi/\lambda$. The first condition ensures reflection of incident field at particle-medium interface is very small, i.e., the particle is composed of "soft" or "tenuous" material according to light scattering terminology [65]. The second condition checks that the phase or amplitude shift inside the particle is very small. Under these constraints, the internal field inside the particle is approximately the same as the field that would be induced by the incident beam, in the absence of the particle. This approximation decouples the dipole effects from eachother and converts the formulation to a scalar form instead of a vectorial form such as the DDA formulation explained in the previous section. This substantial simplification frequently lead to utilization of this approximation beyond its conditions of validity [88].

It is suitable to utilize RDG approximation for prediction of optical properties of loose aggregates of Rayleigh particles as such a physical structure supports the approximation that incident wave propagates with little change. Implementation of RDG approximation to fractal aggregates was first demonstrated in various forms by Forrest and Witten [90], Martin and Hurd [91] and Jullien and Botet [92]. It was later developed and evaluated by Dobbins and Megaridis [93], Sorensen and co-workers [94-97] and Köylü, Farias and co-workers [37, 43, 49, 98, 99] who used the term RDG-FA for this technique. Extensive reviews on the topic are available by Sorensen [37], Köylü [44] and Jones [65].

In RDG-FA method aggregates are modelled as a cluster of N_p identical spherules (primary particles), each of which has a diameter d_p and a complex index of refraction m. These clusters are considered as mass fractal objects which implies that cluster radius is scaled with mass [100]. When primary particles have identical mass, the relation between the number of particles in a fractal aggregate and its radius of gyration R_g is expressed as [92]

$$N_p = k_f (R_g / d_p)^{D_f} \tag{2.37}$$

where D_f and k_f stand for fractal dimension and fractal prefactor that characterize the fractal structure of the aggregate. Radius of gyration is root mean square distance between spherules and it represents a physical dimension for cluster size. The spherules are assumed to be arranged so that they contact eachother and do not overlap.

Rayleigh-Debye-Gans implementation for fractal aggregates is based on the absorption and scattering cross sections of primary spherules which can be evaluated as follows from Rayleigh scattering theory [68, 88, 89] as their size parameter x_p<<1 ($x_p \leq 0.14$ for $d_p \leq$ 50nm, $\lambda \geq 1.18\mu m$, $\eta \leq 8500 cm^{-1}$)

$$C_a^p = \frac{4\pi x_p E_m}{k^2} \tag{2.38}$$

$$C_s^p = \frac{8\pi x_p^6 F_m}{3k^2} \tag{2.39}$$

where E_m and F_m are functions of complex index of refraction of the particle material at given wavelength as follows

$$G(m) = \frac{m^2 - 1}{m^2 + 2} \tag{2.40}$$

$$E_m = \mathrm{Im}\left[G(m)\right] \tag{2.41}$$

$$F_m = \left|G(m)\right|^2 \tag{2.42}$$

Polarized scattering cross-sections for Rayleigh scatterers are given as

$$C_{vv}^p = \frac{x_p^6 F_m}{k^2} \tag{2.43}$$

$$C_{hh}^p(\theta) = C_{vv}^p \cos^2\theta \tag{2.44}$$

$$C_{hv}^{p} = C_{vh}^{p} \approx 0 \tag{2.45}$$

where θ stands for the scattering angle.

Based on RDG approximation, scattering cross-sections for fractal aggregates can be evaluated from [89]

$$C_{vv}^{a}(\theta) = N_{p}^{2} C_{vv}^{p} f\left(qR_{g}\right) \tag{2.46}$$

$$C_{hh}^{a}(\theta) = C_{vv}^{a} \cos^{2}\theta \tag{2.47}$$

where $f(q.R_g)$ is termed as the form factor that depends on q [=$2k.\sin(\theta/2)$], modulus of scattering vector and radius of gyration. For small aggregates and/or small scattering angles form factor follows Guinier (small-angle) regime relations and for larger aggregates and large scattering angles, power law (large-angle) regime expressions are used to evaluate the form factor [91-93]. The boundary between the two regimes is taken as $(qR_g)^2 = 1.5\ D_f$ [49]

$$f\left(qR_{g}\right) = \exp\left(\frac{-\left(qR_{g}\right)^{2}}{3}\right), \text{ Guinier regime for } \left(qR_{g}\right)^{2} \le 1.5D_{f} \tag{2.48}$$

$$f\left(qR_{g}\right) = \left(qR_{g}\right)^{-D_{f}}, \text{ power-law regime for } \left(qR_{g}\right)^{2} > 1.5D_{f} \tag{2.49}$$

As cross-polarized scattering cross sections are negligible under the present assumptions, differential scattering cross-section for unpolarized light can be evaluated from

$$\frac{dC_{s}^{a}(\theta)}{d\Omega} = \frac{C_{vv}^{a}(\theta) + C_{hh}^{a}(\theta)}{2} \tag{2.50}$$

S_{11} element of Mueller scattering matrix, which is one of the parameters of interest in the present study, is obtained from the differential scattering cross-section as follows [68]

$$S_{11}(\theta) = \frac{1}{k^2}\frac{dC_s^a(\theta)}{d\Omega} \tag{2.51}$$

Integrating differential scattering cross-section over the whole 4π solid angle gives the total scattering cross section of the aggregate as follows [49]

$$C_s^a = N_p^2 C_s^p \cdot g(kR_g, D_f) \tag{2.52}$$

where g is the aggregate scattering factor that is expressed in different forms given below depending on whether Guinier regime prevails or power-law regime is reached until θ=π, q=2k. For $(2kR_g)^2 \leq 1.5D_f$ aggregate scattering factor is independent of fractal dimension and is evaluated from [49]

$$g(kR_g) = 1 - \frac{2\left(kR_g\right)^2}{3} \tag{2.53}$$

and corresponding expression for $(2kR_g)^2 > 1.5D_f$ is

$$g(kR_g, D_f) = \frac{\beta\left(3 - 3\beta + 2\beta^2\right)}{2} - \frac{\left(kR_g\beta\right)^2\left(3 - 4\beta + 3\beta^2\right)}{3} + \left(2kR_g\right)^{-D_f} \times \left[\frac{3}{2 - D_f} - \frac{12}{(6 - D_f)(4 - D_f)} - 3\beta^{\left(1 - D_f/2\right)}\left(\frac{1}{2 - D_f} - \frac{2\beta}{4 - D_f} + \frac{2\beta^2}{6 - D_f}\right)\right] \tag{2.54}$$

where β is the aggregate scattering parameter given by

$$\beta = \frac{3D_f}{8k^2R_g^2} \tag{2.55}$$

Several other approaches on determination of structure factors and limiting conditions for Guinier and power law regimes can be found from the reviews of Sorensen [50] and Jones [65].

Following previous practice by Dobbins and Megaridis [93], Köylü *et* al. [49] and based on the previous reportings by Nelson [101] and Chen *et* al. [102] effect of aggregation on absorption is considered to be insignificant for small aggregates under consideration in the

present study and cross-section of the aggregate is considered to be sum of that of the spherules that are Rayleigh monomers [49]

$$C_a^a = N_p C_a^p \tag{2.56}$$

Once aggregate cross sections are evaluated, they are normalized as follows to yield absorption and scattering efficiencies

$$Q_a = \frac{C_a^a}{\pi a_{eq}^2} \tag{2.57}$$

$$Q_s = \frac{C_s^a}{\pi a_{eq}^2} \tag{2.58}$$

where a_{eq} is the radius of the sphere of volume equal to the total volume of spherules in the aggregate and related to spherule radius as follows.

$$a_{eq} = a_p \sqrt[3]{N_p} \tag{2.59}$$

In particular, the RDG-FA approximation is suitable for practical applications as it enables computationally efficient treatment of complex populations of soot aggregates having widely varying numbers of primary particles per aggregate [103, 104]. RDG-FA model was initially applied to estimate soot scattering properties and to interpret scattering measurements in order to infer soot structure properties [105, 106]. However, there have been a significant number of uncertainties about implementation of this theory for soot aggregates. In particular, the RDG approximation requires that both $|m - 1| \ll 1$ and $x|m - 1| \ll 1$ which is questionable due to the large refractive indices of soot. Moreover, RDG approximation neglects the effects of multiple scattering which were shown be significant especially for large soot aggregates [30, 101, 102, 107, 108]. Despite these uncertainties, recent experimental evaluations of the RDG-FA theory [35, 97, 98, 103] and theoretical evaluations [37, 109] have shown good efficiency for this approach. Therefore the suitability of this technique for soot characterization is still a controversial issue and its validity needs to be assessed for specific conditions of application.

In this study, a computer code was developed for determination of optical cross sections and S_{11} function for a given fractal aggregate layout, fractal dimension, equivalent diameter,

wavelength and refractive index. The formulation of the code was validated by reproducing RDG-FA solutions reported by Farias *et* al. [43].

2.2.5. Results and discussion: Evaluation of radiative property models

2.2.5.1. Modification of DDSCAT for prediction of amplitude and phase

2.2.5.1.1. Comparison between predictions of original and modified codes

Performances of the original and modified codes for the prediction of magnitudes and phases of ASM elements with respect to Mie theory solutions are displayed in Figure 2.6. As can be seen from the figures Figure 2.6 (c) and (d), the proposed modifications result in phase predictions in complete agreement with Mie Theory. Now that the code is applicable to prediction of ASM elements, it can now be utilized to evaluate the performance of DDA in predicting amplitude and phase of scattered field.

2.2.5.1.2. Validation of modified DDSCAT against Mie theory

Although primary utility of DDA is for irregularly shaped particles, the first stage in validation of such models is always carried out on single spheres as exact solutions are available through Mie theory. In an attempt to evaluate the accuracy of ASM elements predicted by the modified DDSCAT code, simulations were validated against exact Mie theory solutions on single sphere test problems with 2 size parameters, $x = 2$ and $x = 8$ and 2 refractive indices, m=1.75+i0.5 and m=2.5+i0.1. Figure 2.7 and Figure 2.8 display the comparisons for magnitudes and phases of ASM elements, respectively. Predictions are in excellent agreement except S_2 predictions for the larger m and x values. This is because this case is a more demanding problem and finer dipole discretization is necessary to improve accuracy. The resolution requirement for accurate DDA predictions depends on the target properties and is covered in the next section.

2.2.5.1.3. Applicability conditions of DDA for prediction of ASM elements

Modification of the DDSCAT code for accurate prediction of amplitude and phase of scattered electromagnetic field has enabled assessment of dipole subdivision requirement for accurate DDA predictions and determination of applicability conditions of DDA for prediction of ASM elements. Detailed investigation on this topic was carried within the frame of our publication [67] and is given in detail in Appendix B.

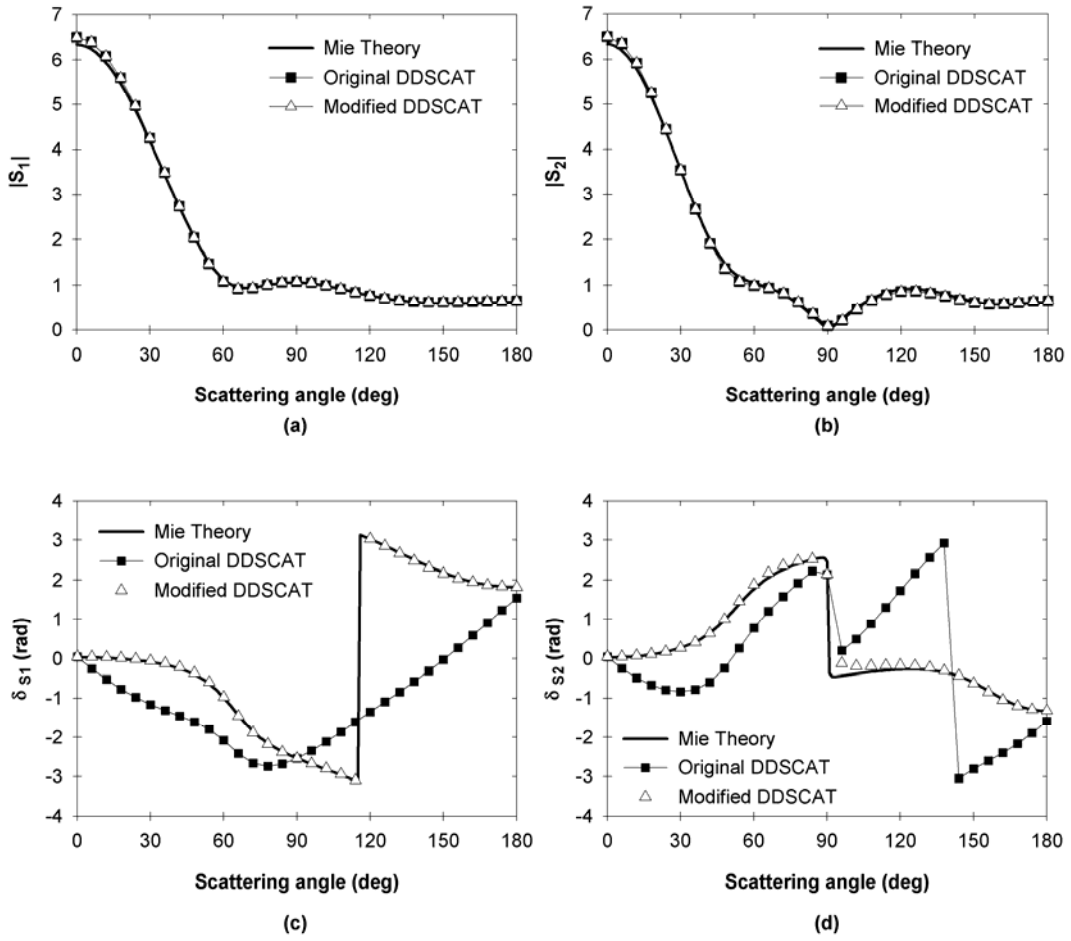

Figure 2.6. Comparison between predictions of the original DDSCAT v.6.1 and modified code against Mie theory solutions for magnitudes and arguments of the complex ASM elements ($x = 3$, $m = 2 + i$).

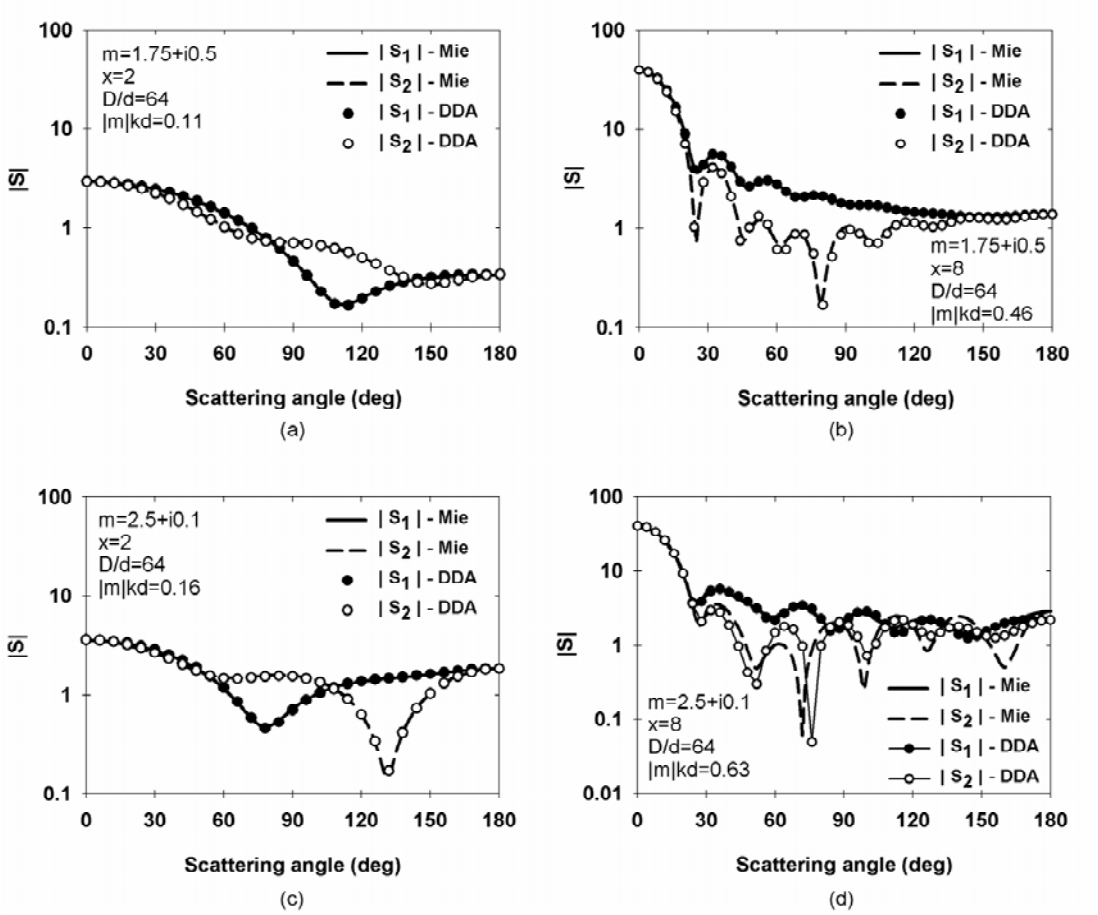

Figure 2.7. Comparison between predictions of modified DDSCAT code for magnitudes of ASM elements and exact Mie theory solutions

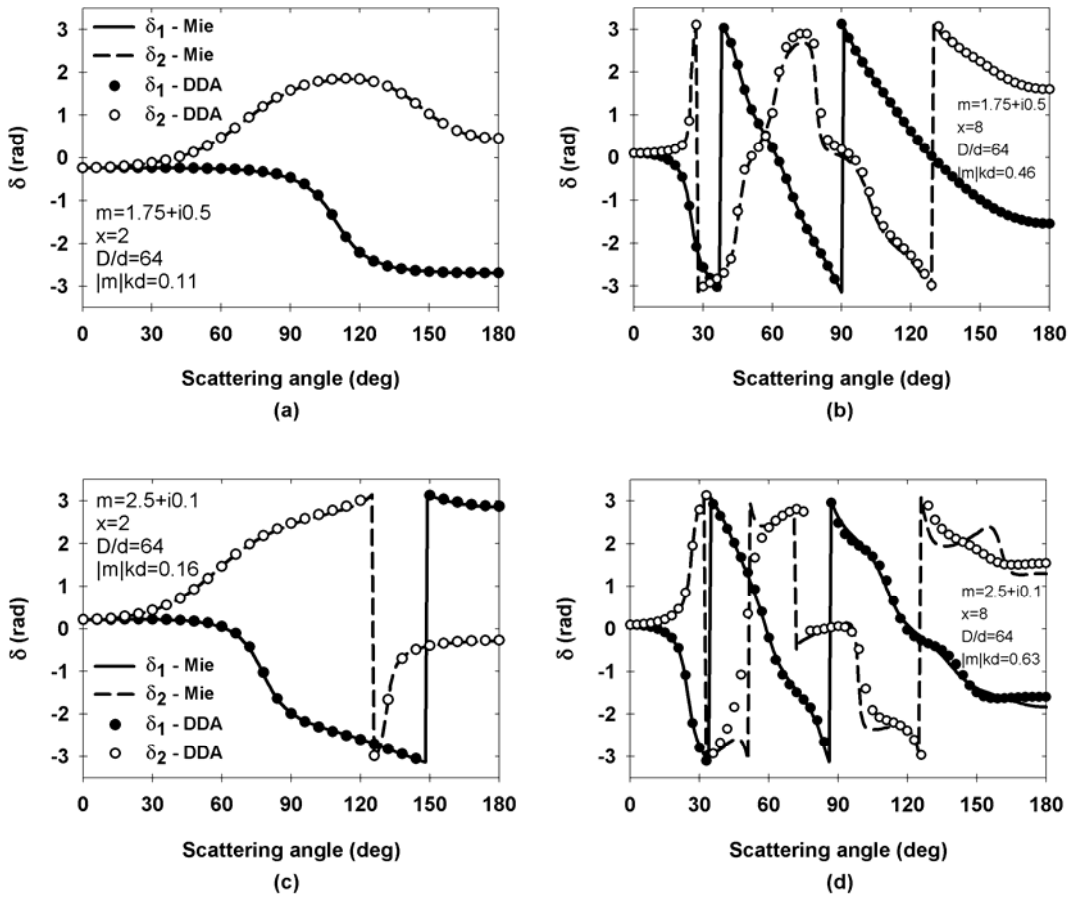

Figure 2.8. Comparison between predictions of modified DDSCAT code for phases of ASM elements and exact Mie theory solutions

2.2.5.2. Experimental validation of DDA

Comparison between amplitude scattering matrix element predictions of the present DDSCAT code and microwave measurements were carried out within the frame of a collaborative study with Fresnel Institute[1] that has led to a publication in Journal of Quantitative Spectroscopy and Radiative Transfer [66]. Microwave experiments carried out by Fresnel Institute were modeled via the T-Matrix code by the same partners and modified DDSCAT code by CETHIL[2] and METU[3]. Predictions of these two models were compared against measurements. The study aimed to cross-validate the experimental method as well as the models.

2.2.5.2.1. Description of test problem: Cubical aggregate

A 27-sphere cube-like aggregate shown in Figure 2.9 was built for electromagnetic wave scattering pattern analysis by microwave experiments. Identical spheres of 15.9 mm diameter are composed of Polymethyl Methacrylate (PMMA) which is a dielectric polymeric material of measured relative permittivity ε=2.5, refractive index, m=1.58 [66]. The edge of the cubical frame is 47.7 mm long. Detailed explanations about the experimental setup and measurement procedure are available from [66]. Actually this is the first target in a planned course of future research which involves analysis of targets that approach soot aggregates, improving experimental practices for microwave measurements step by step.

Experiments were performed at several configurations as demonstrated in Figure 2.10. Two incident field directions were investigated: a “face incidence” for which the propagation direction is perpendicular to one of the faces of the cube (case 0°), and an “edge incidence” for which the beam is oriented at an angle of 45° with respect to the normal (case 45). Furthermore, two incident field polarizations were studied with respect to the scattering plane. In vertical (or perpendicular) polarization state the electric field is normal to the scattering plane and in horizontal (or parallel) polarization state the electric field is parallel to the scattering plane.

---

[1] Institut Fresnel, UMR CNRS 6613, Université de Provence, Aix-Marseille 1, France

[2] Centre de Thermique de Lyon (CETHIL, UMR CNRS 5008 – INSA Lyon – UCBL)

[3] Department of Chemical Engineering, Middle East Technical University, Ankara

Figure 2.9. 27-sphere cubical aggregate [66]

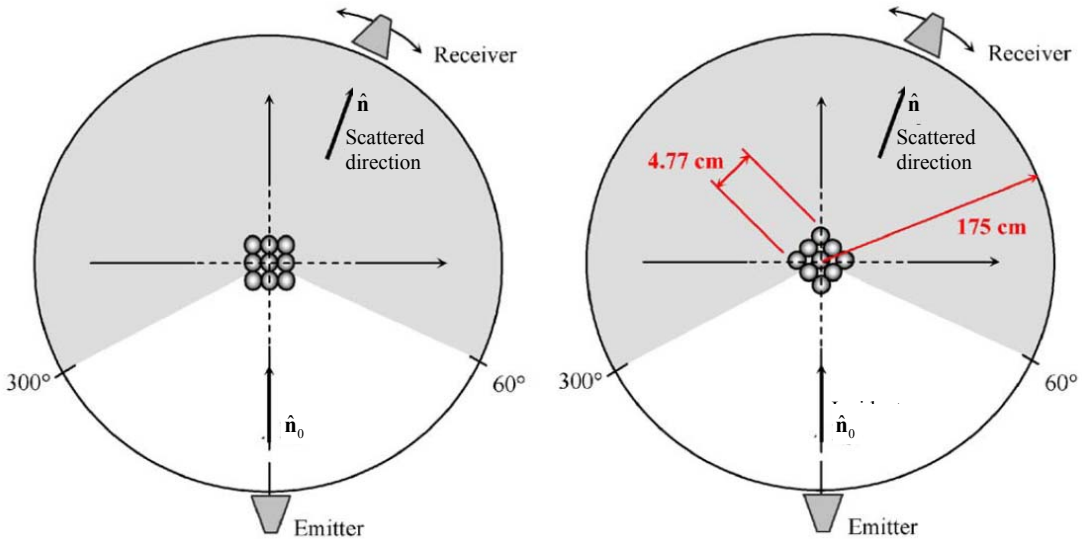

(a) 0° case (b) 45° case

Figure 2.10. Schematic layout of two target orientations with respect to the incident field [66]

Experiments were carried out at two microwave frequencies, 8 GHz and 14 GHz, which correspond to wavelengths of 3.75 cm and 2.14 cm and primary sphere size parameters of 1.33 and 2.33, respectively. The size parameters of aggregates based on aggregate edge is 4 and 7, respectively. Large size parameters were selected to test the DDA method as effects of self-interaction and multiple-scattering are quite pronounceable and once the method performs well in this case, its performance for smaller size parameters is also assured.

2.2.5.2.2. Comparison between DDA predictions and measurements

The target of 27-sphere cubic agglomerate under consideration was framed in a 48×48×48 cubic lattice in which the number of occupied lattice sites amount to 56781 dipoles. This discretization with $|m|kd$ = 0.27 for 8 GHz case and $|m|kd$ = 0.47 for 14 GHz case was checked to satisfy applicability criterion of DDSCAT which was reported as $|m|kd$ should be less than 0.5 where m represents the complex index of refraction and d stands for the lattice spacing [73, 84]. DDSCAT code modified for phase computations [67] was run by using the specifications summarized in Table 2.2. More detailed coverage on this test problem can be obtained from our joint publication [66].

Figure 2.11 to Figure 2.14 and Figure 2.15 to Figure 2.18 display comparisons between measurements, T-Matrix predictions and DDA solutions for variation of amplitude and phase difference along the receiver angle at 8 GHz and 14 GHz with vertical and horizontal polarizations for Case 0° and Case 45° orientations, respectively. Excellent agreement among the measurements and models in all cases validate both the models and experimental procedure.

The strong peaks at 180° scattering angle in relative magnitude plots indicate that the 27-sphere aggregate under investigation is a strong forward scatterer for each combination of orientations and wavelengths. As frequency is increased from 8 GHz to 14 GHz while keeping other variables constant the aggregate size parameter increases from 4 to 7. As the size parameter gets larger, the forward scattering peaks in relative magnitude plots get narrower and both relative magnitude and phase difference attain more detailed patterns along scattering angle. These trends are in line with typical effects of increased size parameter for dielectric scatterers. The parameter that is most sensitive to orientation appears to be the vertically polarized relative magnitude at large scattering angles which increase when the orientation is shifted from 0° to 45°.

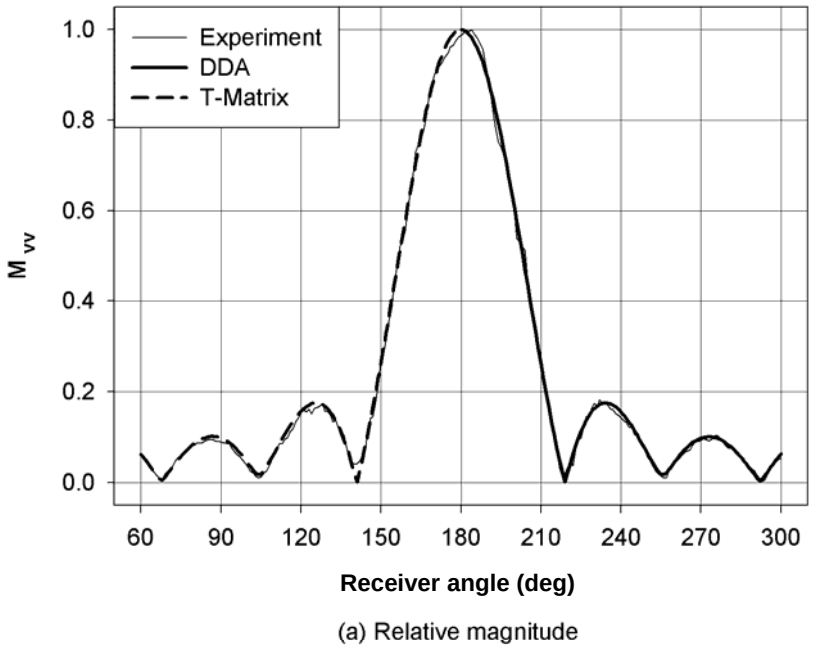

(a) Relative magnitude

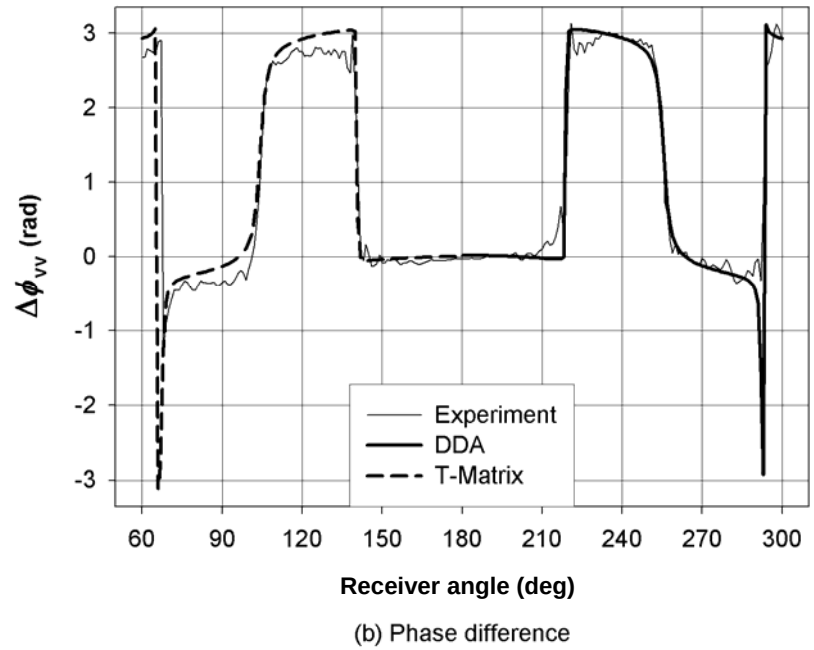

(b) Phase difference

Figure 2.11. Comparison between measurements, DDA and T-Matrix predictions for vertical polarization at 8 GHz, Case 0° [66] .

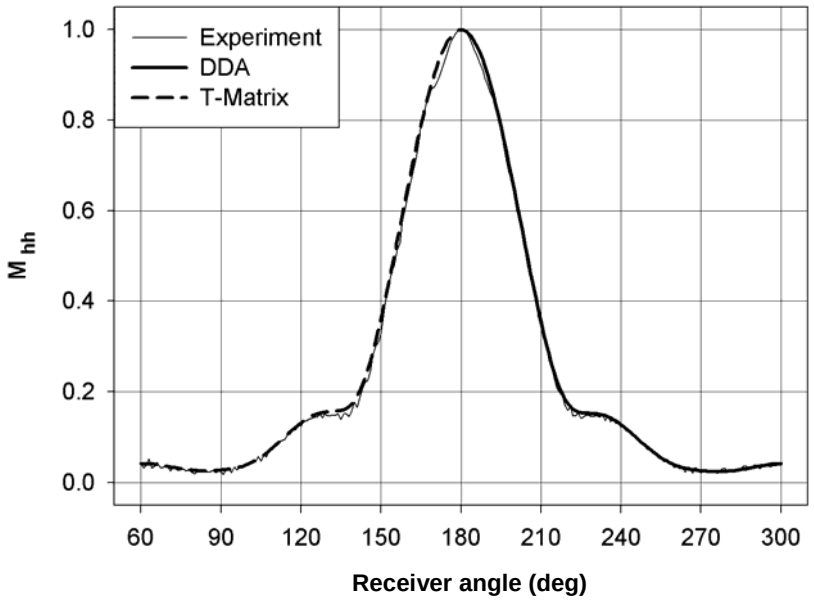

(a) Relative magnitude

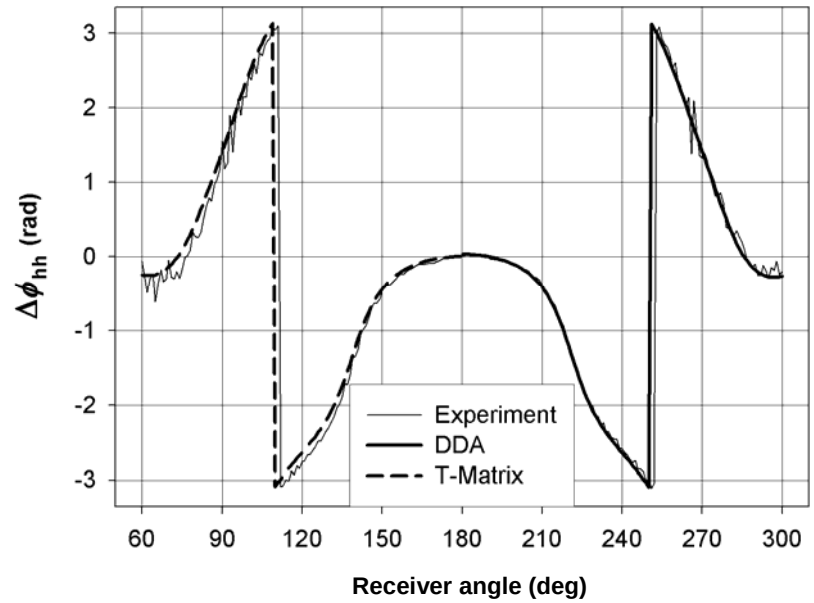

(b) Phase difference

Figure 2.12. Comparison between measurements, DDA and T-Matrix predictions for horizontal polarization at 8 GHz, Case 0° [66].

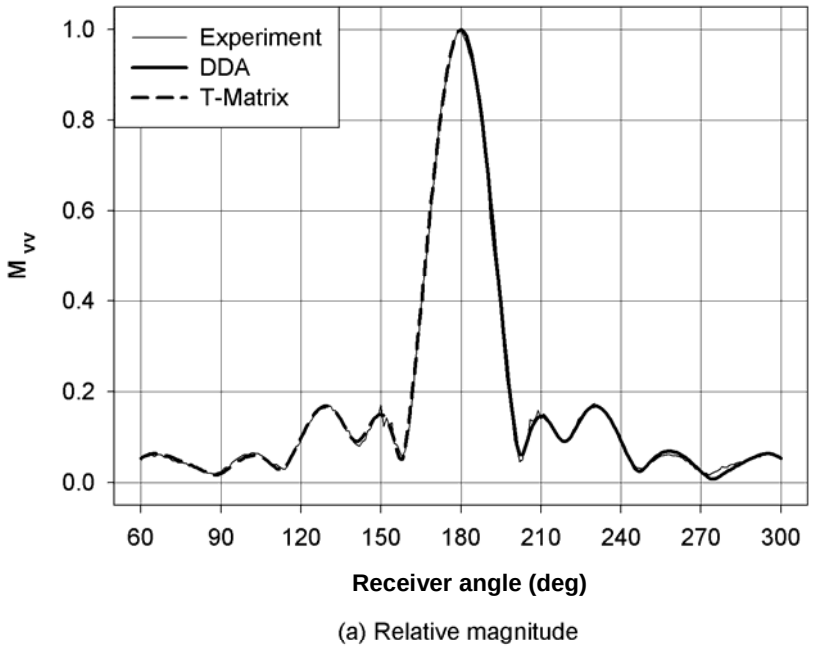

(a) Relative magnitude

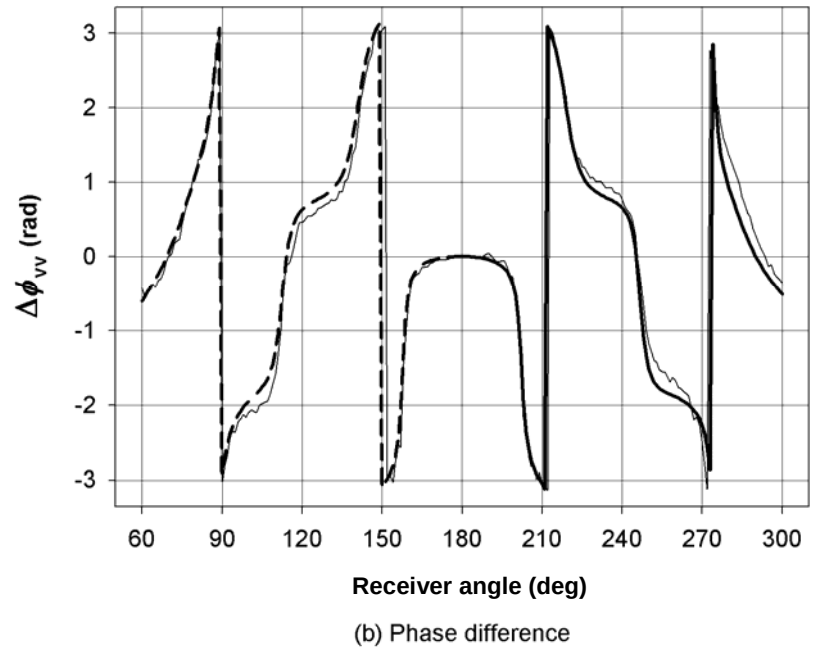

(b) Phase difference

Figure 2.13. Comparison between measurements, DDA and T-Matrix predictions for vertical polarization at 14 GHz, Case 0° [66].

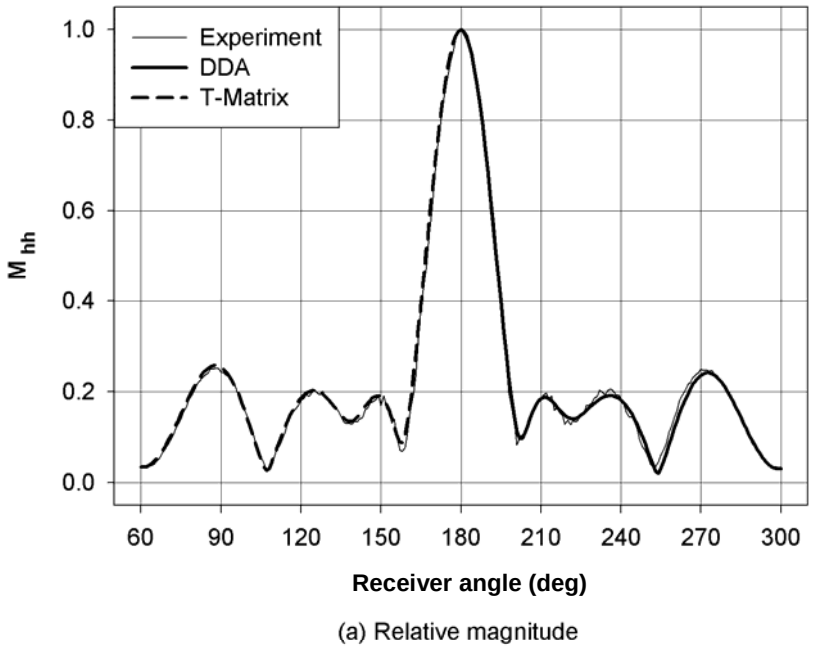

(a) Relative magnitude

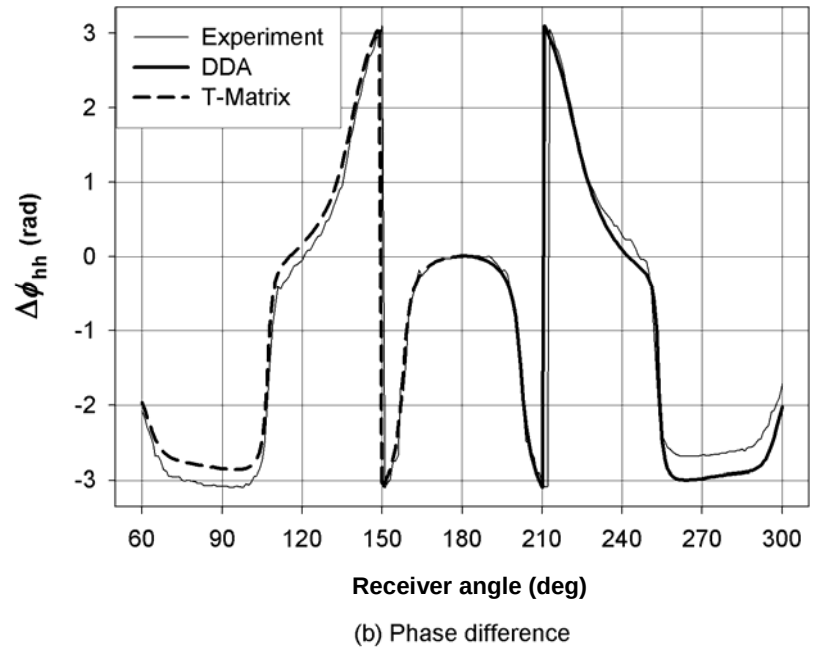

(b) Phase difference

Figure 2.14. Comparison between measurements, DDA and T-Matrix predictions for horizontal polarization at 14 GHz, Case 0° [66].

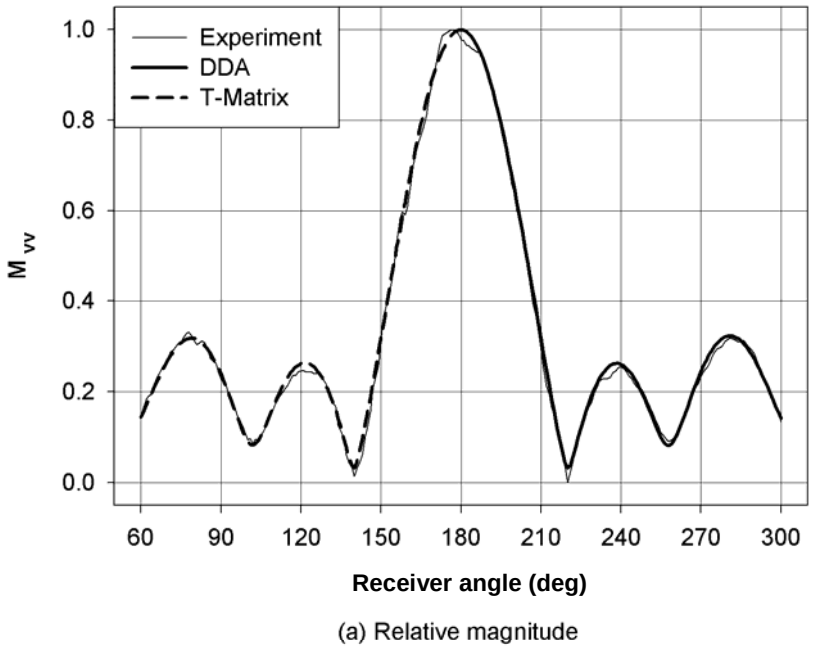

(a) Relative magnitude

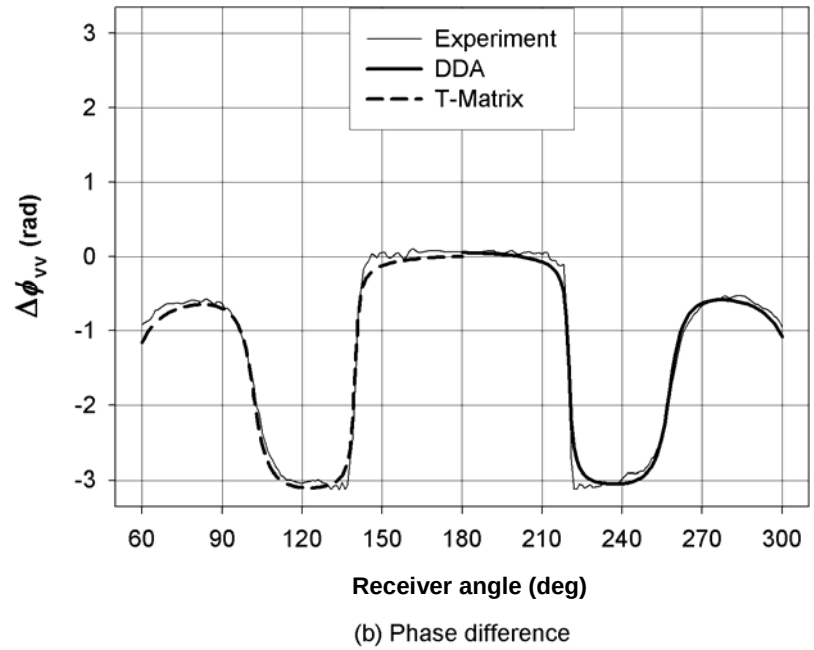

(b) Phase difference

Figure 2.15. Comparison between measurements, DDA and T-Matrix predictions for vertical polarization at 8 GHz, Case 45° [66].

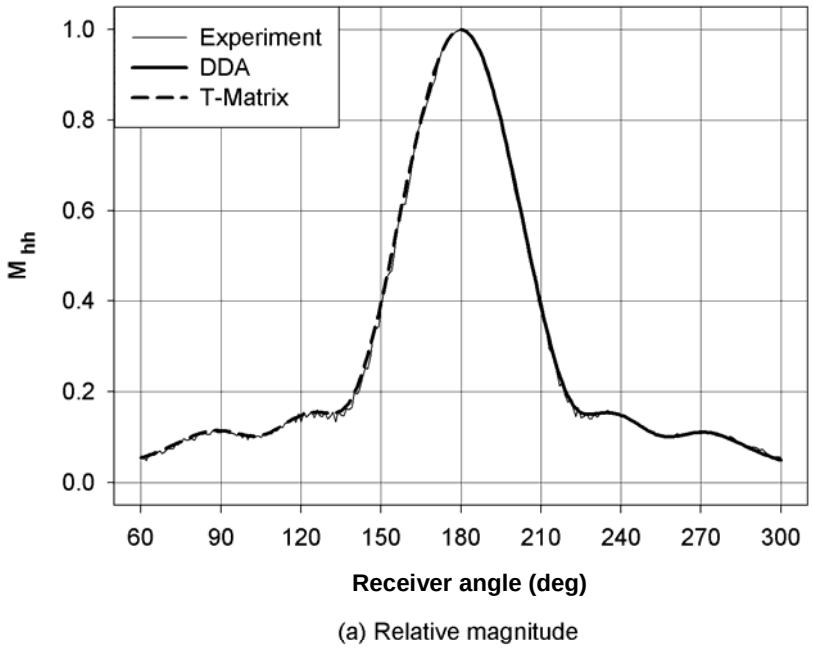

(a) Relative magnitude

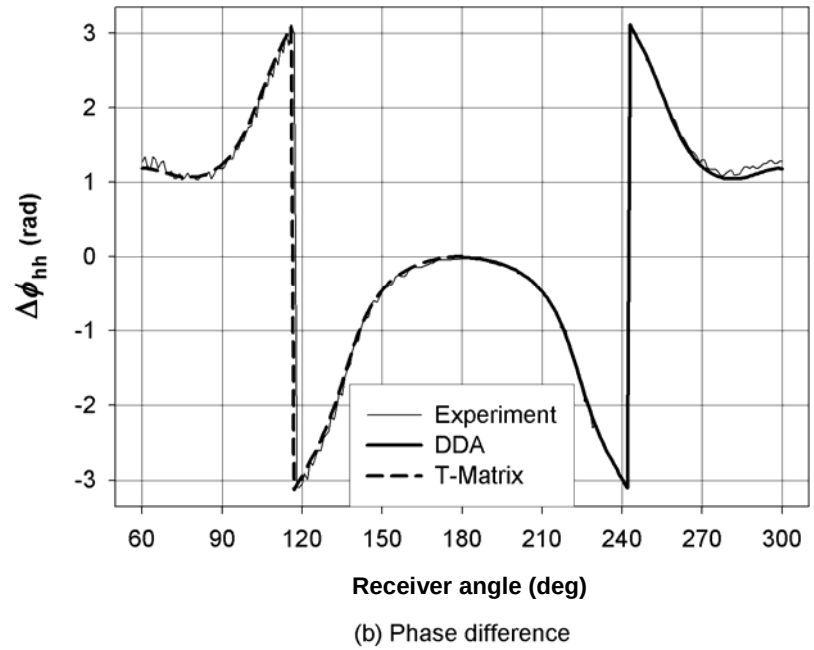

(b) Phase difference

Figure 2.16. Comparison between measurements, DDA and T-Matrix predictions for horizontal polarization at 8 GHz, Case 45° [66].

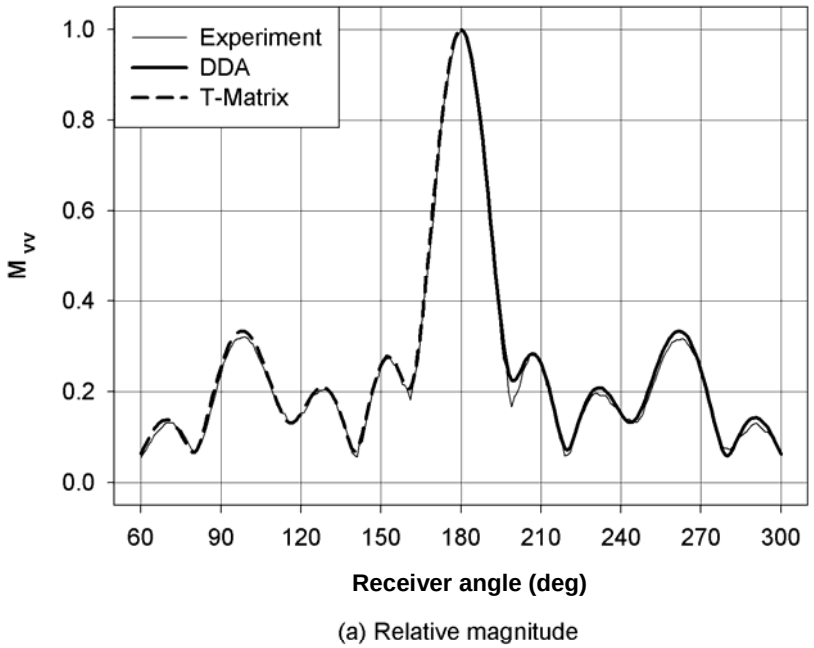

(a) Relative magnitude

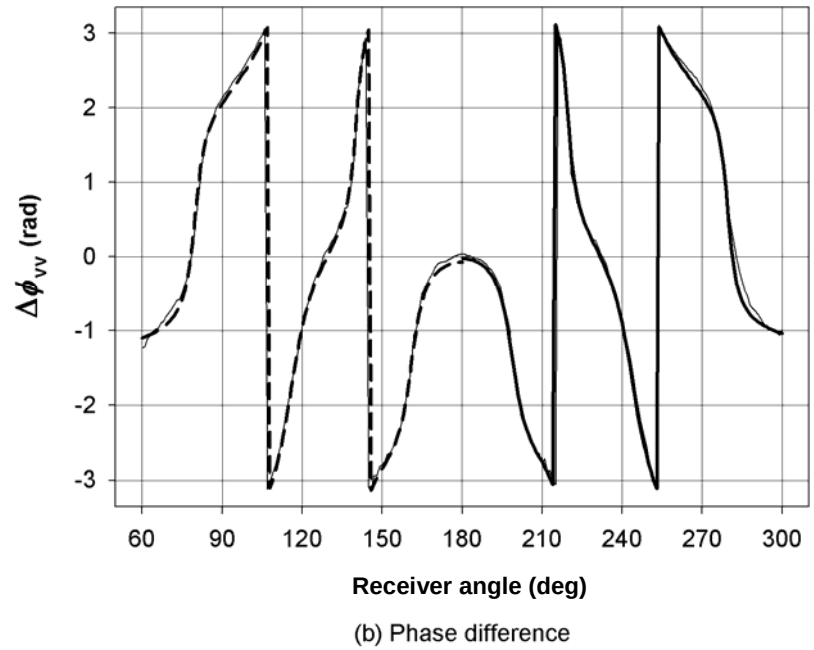

(b) Phase difference

Figure 2.17. Comparison between measurements, DDA and T-Matrix predictions for vertical polarization at 14 GHz, Case 45° [66] .

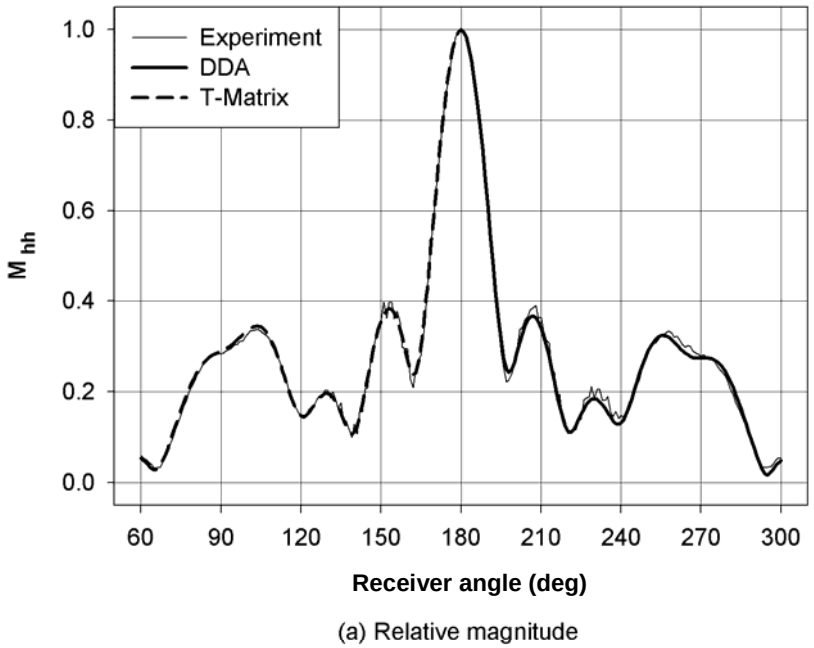

(a) Relative magnitude

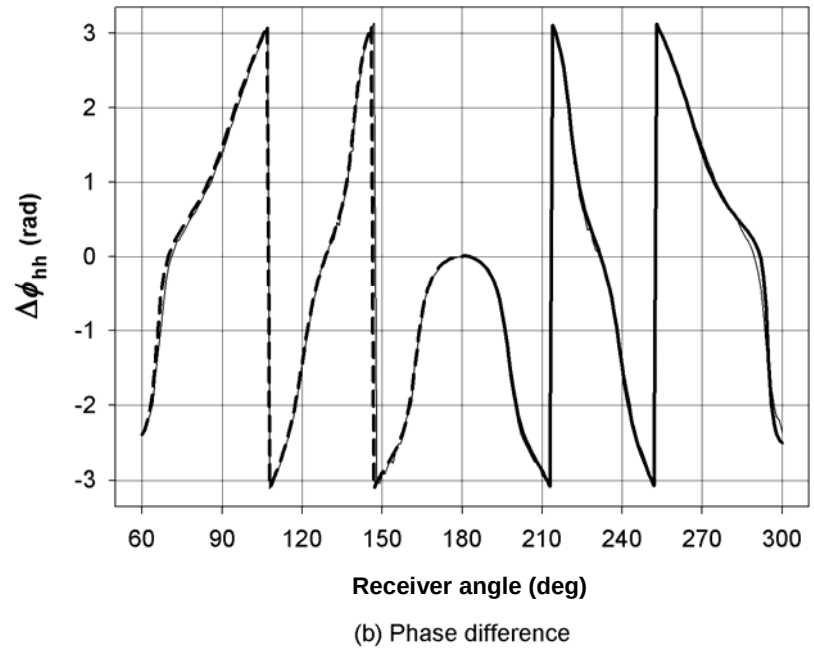

(b) Phase difference

Figure 2.18. Comparison between measurements, DDA and T-Matrix predictions for horizontal polarization at 14 GHz, Case 45° [66].

2.2.5.3. Comparison of model predictions against exact solutions for an idealized target

2.2.5.3.1. Description of test problem: Spherical aggregate

In an attempt to evaluate DDA and RDG-FA on the same test problem, a spherical aggregate problem which was utilized several times in literature for similar purposes [30, 70, 74, 109] was selected. The target displayed in Figure 2.19 is composed of 136 identical spheres arranged in cubical pitch with 6 contact points for an interior sphere. The position vectors for each primary sphere are tabulated in Appendix C. The sphere-like structure of the aggregate enables validation of radiative property predictions against Mie Theory which provides exact solutions for an equivalent sphere.

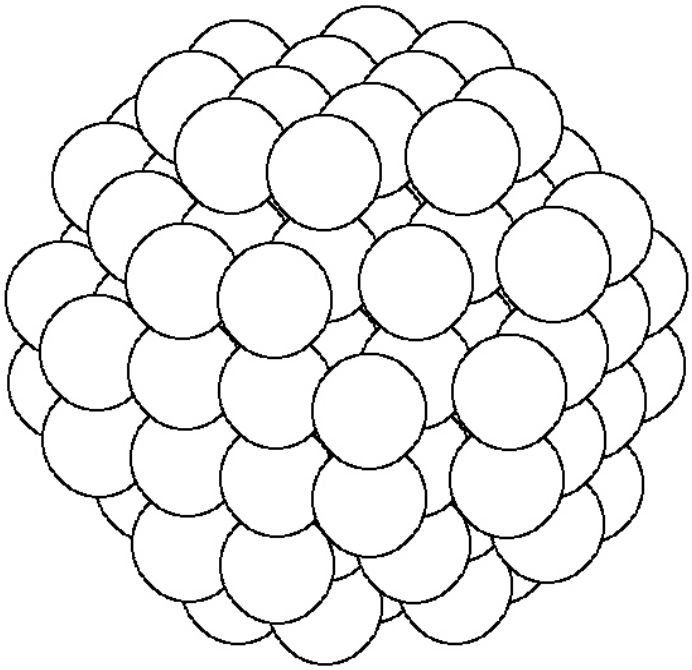

Figure 2.19. Spherical aggregate of 136 primary spheres
(coordinates tabulated in Appendix C)

The equivalent sphere (denoted by "es" different from volume equivalent sphere denoted by "eq") is the sphere which has the same volume occupied by the agglomerate including the voids and has an effective homogeneous medium with refractive index calculated from Maxwell-Garnett relation by using particle material refractive index, m_b, and volume fraction of material as follows [68]

$$G(m_{es}) = f_{v,a} \cdot G(m_b) \tag{2.60}$$

where G is the function of refractive index defined in Eq. (2.40) and $f_{v,a}$ is the volume fraction of the material within the aggregate and can be calculated as follows for the compactly packed aggregate in Figure 2.19.

$$f_{v,a} = \frac{V_{sphere}}{V_{cube}} = \frac{\pi d_p^3 / 6}{d_p^3} = \frac{\pi}{6} \tag{2.61}$$

Rearranging the above expressions, refractive index of the equivalent sphere is given by

$$m_{es} = \sqrt{\frac{1 + 2 f_{v,a} G(m_b)}{1 - f_{v,a} G(m_b)}} \tag{2.62}$$

The size parameter of equivalent sphere in terms of the volume-equivalent sphere size parameter, x_{eq} is

$$x_{es} = x_{eq} f_{v,a}^{-1/3} \tag{2.63}$$

where

$$x_{eq} = 2\pi a_{eq} / \lambda = k a_{eq} \tag{2.64}$$

a_{eq} being the radius of the volume equivalent sphere defined in Eq.(2.59). To obtain reference Mie solutions for each specified x_{eq}, x_{es} is calculated and supplied to Mie theory code (BHMIE) of Bohren and Hoffmann [68] together with m_{es}.

The specifications of the test problem at which models will be tested are determined according to the conditions of soot diagnostics practice in the present study in terms of spectral range and primary sphere diameters. The wavelength range of electromagnetic radiation under focus is in the near-infrared range between 1.18 and 1.33 μm (8500-7500 cm^{-1}). Volume-equivalent size parameters are specified to vary between 0.25 and 2.5 so that primary sphere diameters change from 2 - 200 nm for a minimum wavelength of 1.18 μm, covering experimentally reported soot spherule diameters on the order of 10-50 nm [4]. Aggregate diameters are between 12 nm to 1.2μm which represent realistic sizes for flame generated soot aggregates reported to be between 10 nm – 1 μm [110]. The refractive index of soot at 1.18 μm was calculated as m = 1.692 + i0.750 from Drude-Lorenz relation given in section 2.3.2, based on the set of dispersion constants provided by Dalzell and Sarofim [27]. Corresponding equivalent sphere refractive index for Mie calculations is m_{es}= 1.388+ i0.296.

2.2.5.3.2. Comparison against exact solutions

DDA and RDG-FA are applied to solve the scattering problem of the targer described above. For DDA, the target is subdivided into dipoles such that the extent of the target is divided into 24 dipoles resulting in 3672 occupied dipoles in cubical lattice frame of 24^3 cells . The validity criterion, $|m|kd < 0.5$ is satisfied with this subdivision for all size parameters. As RDG-FA is for fractal aggregates, it requires specification of aggregate fractal dimension as input data. The sphere-like aggregate under consideration is a compact aggregate, fractal dimension of which can be taken as 3 [111, 112]. The first validity condition of RDG approximation given in Eq. (2.35) is not satisfied as $|m-1|=1.02$ in this case. The second, Eq. (2.36) , is also violated for large size parameters.

Absorption and scattering efficiency factors predicted by DDA and RDG-FA are compared against Mie theory solutions in Figure 2.20. Absorption efficiency factor predictions of both methods are reasonably accurate for $x_{eq} < 1.5$. Beyond this size parameter limit, up to x_{eq}=2.5, both methods start to overestimate absorption efficiencies, DDA errors being less than 10% and RDG-FA errors being significantly larger. For scattering efficiency factors, DDA is in good agreement with Mie theory for all size parameters. RDG-FA predictions are in reasonable agreement for $x_{eq} < 1.5$ again and start to overestimate considerably for $x_{eq} > 1.5$. Better performance of DDA is an expected outcome as it is a more rigorous approach. For efficiency factors, it turns out that considerably simpler RDG-FA approximation can be reliably used for $x_{eq} < 1.5$ which physically correspond to aggregate size range of approximately < 460 nm and spherule diameter < 100 nm for $\lambda > 1.18$ ($\eta < 8500 cm^{-1}$).

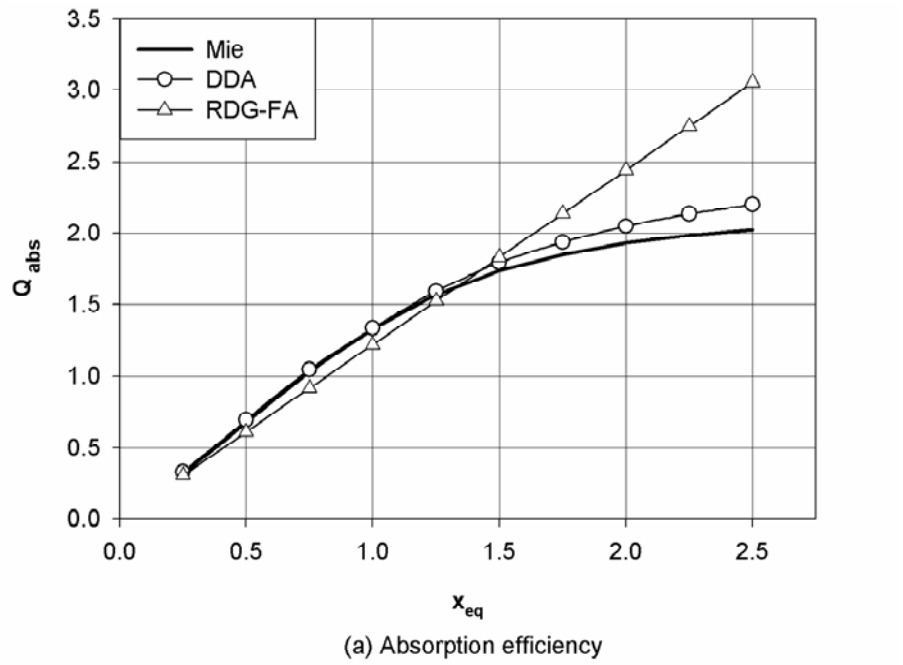

(a) Absorption efficiency

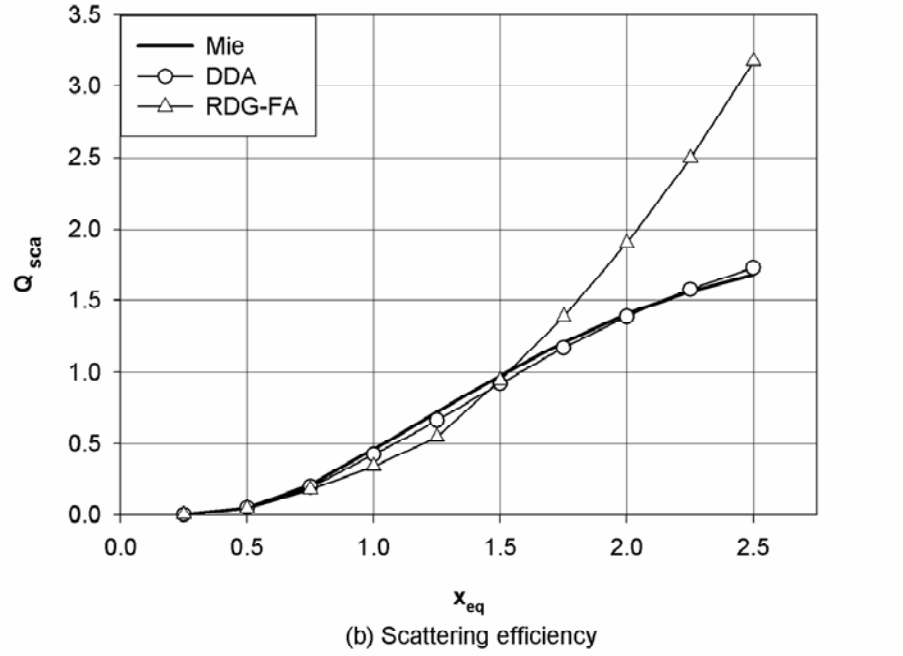

(b) Scattering efficiency

Figure 2.20. Comparison between efficiency factors predicted by DDA and RDG-FA methods against exact Mie theory solutions for spherical aggregate.

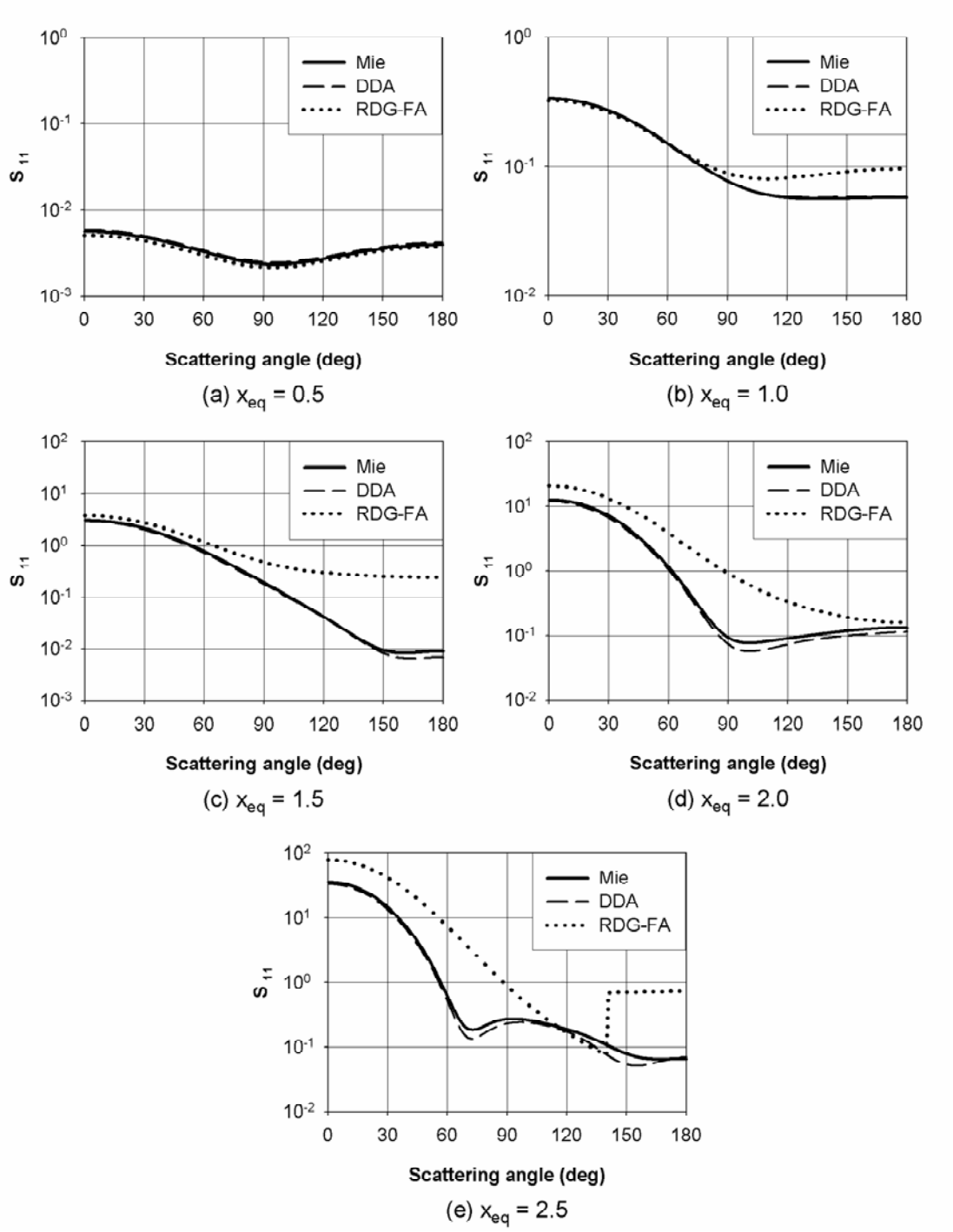

Figure 2.21. Comparison between S_{11} profiles predicted by DDA and RDG-FA methods against exact Mie theory solutions for spherical aggregate.

Figure 2.21 displays comparison between S_{11} predictions of DDA and RDG-FA with respect to Mie solutions for different volume-equivalent sphere diameters. S_{11} element of the Mueller Matrix is directly related to the scattering intensity. As the size parameter increase, the particle starts to scatter more and the scattering intensity concentrates towards the forward direction (θ near 0). At x_{eq} = 0.5 both models provide accurate predictions as expected. DDA predictions provide reasonably accurate profiles for all particle sizes. RDG-FA, on the other hand involves considerable errors starting from x_{eq} > 1.5, especially in backward directions. The discontinuity at the largest size parameter around θ=140° is due to the shift from Guinier regime to power-law regime at that point. As can be seen, power-law regime fails to capture the variation for this case.

Comparisons in this test case indicate that although the conditions are out of the theoretical validity conditions for RDG-FA, it presents a useful compromise to predict absorption and scattering coefficients of small spherical aggregates. In the next section the idealization in terms of shape is removed and radiative property models are compared for a fractal aggregate with soot-like properties.

2.2.5.4. Comparison of RDG-FA and DDA predictions for a soot-like target

2.2.5.4.1. Description of test problem: Fractal aggregate

In order to test the models on a fractal aggregate a computationally generated aggregate was taken as the target. The mass fractal aggregate that obeys the relation in Eq.(2.37) depicted on Figure 2.22 was previously generated with specified fractal dimension, number of monomers and fractal prefactor, following the procedure outlined in [113] (performed by Dr. R. Vaillon). Based on the literature review by Brasil *et* al. [113] D_f = 1.7 and k_f = 2.0 are selected as representative fractal properties of soot aggregates. The coordinates of the primary spheres in the aggregate is tabulated in Appendix D. Volume-equivalent diameters are studied in the same range as previous case, 0.25 < x_{eq} < 2.5, which leads to primary sphere diameter range from 2 to 200 nm. Refractive index is taken as m = 1.692 + i0.750, as in the previous case.

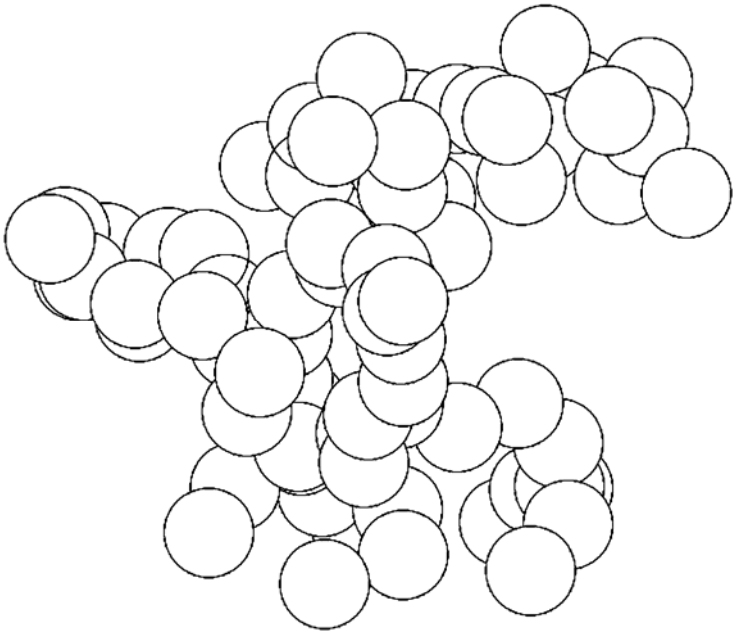

Figure 2.22. Fractal aggregate of 74 primary spheres D_f =1.7, k_f = 2.0 and R_g = 2 a_{eq} = 8.36 a_p (coordinates tabulated in Appendix D)

2.2.5.4.2. Comparison between model predictions

Based on the accuracy of DDA predictions in previous two test cases, DDA solutions are considered as reference for this test problem for which exact solutions are not available. DDA predictions were obtained by averaging resulting efficiencies over different target orientations with respect to the incident beam so that resulting properties are representative of a population of the aggregate. In this study, averaging is performed over 27 different orientations which are obtained by rotating the target at equal angle increments spanning the 4π solid angle. The selection of number of orientations is based on minimization of CPU time as much as possible. Figure 2.23 presents comparison between DDA and RDG-FA predictions for absorption and scattering efficiency factors. RDG-FA predictions for absorption efficiencies are in relatively good agreement with DDA predictions within 15% error margin for $x_{eq} < 2$. For scattering efficiencies, RDG-FA predictions overestimate DDA predictions where discrepancies become considerable beyond $x_{eq} > 1$. Scattering efficiencies are found to be negligibly small for x_{eq} less than unity with scattering albedo less than 0.1. Comparison between S_{11} predictions indicate that RDG-FA predictions are acceptable in the Guinier regime, whereas towards the backward directions, after the shift to power-law regime (visible by the discontinuity), the predictions overestimate scattering intensities.

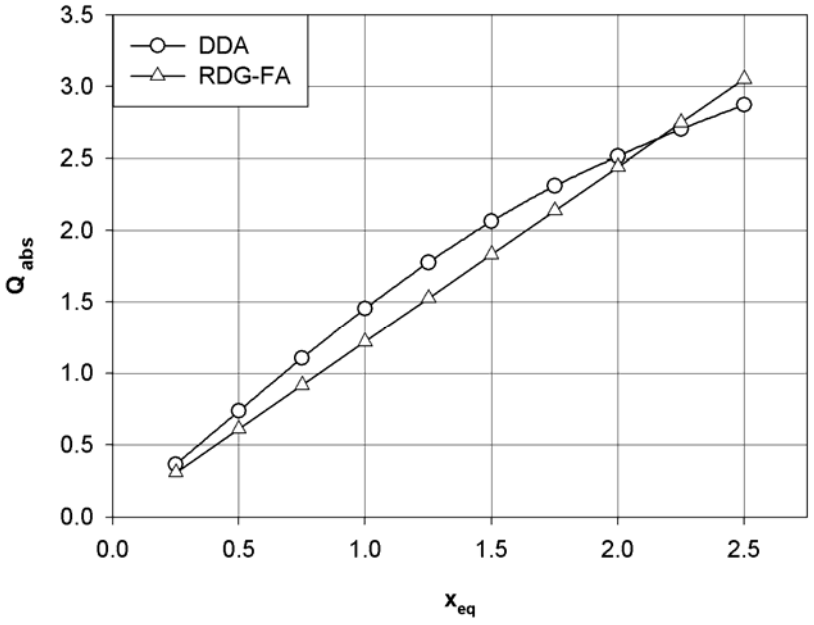

(a) Absorption efficiency

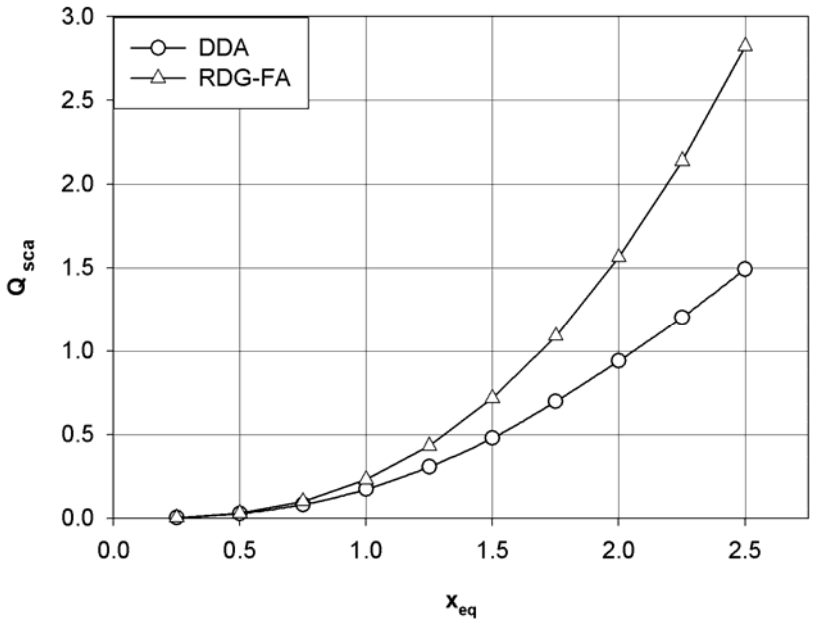

(b) Scattering efficiency

Figure 2.23. Comparison between efficiency factors predicted by DDA and RDG-FA methods for fractal aggregate.

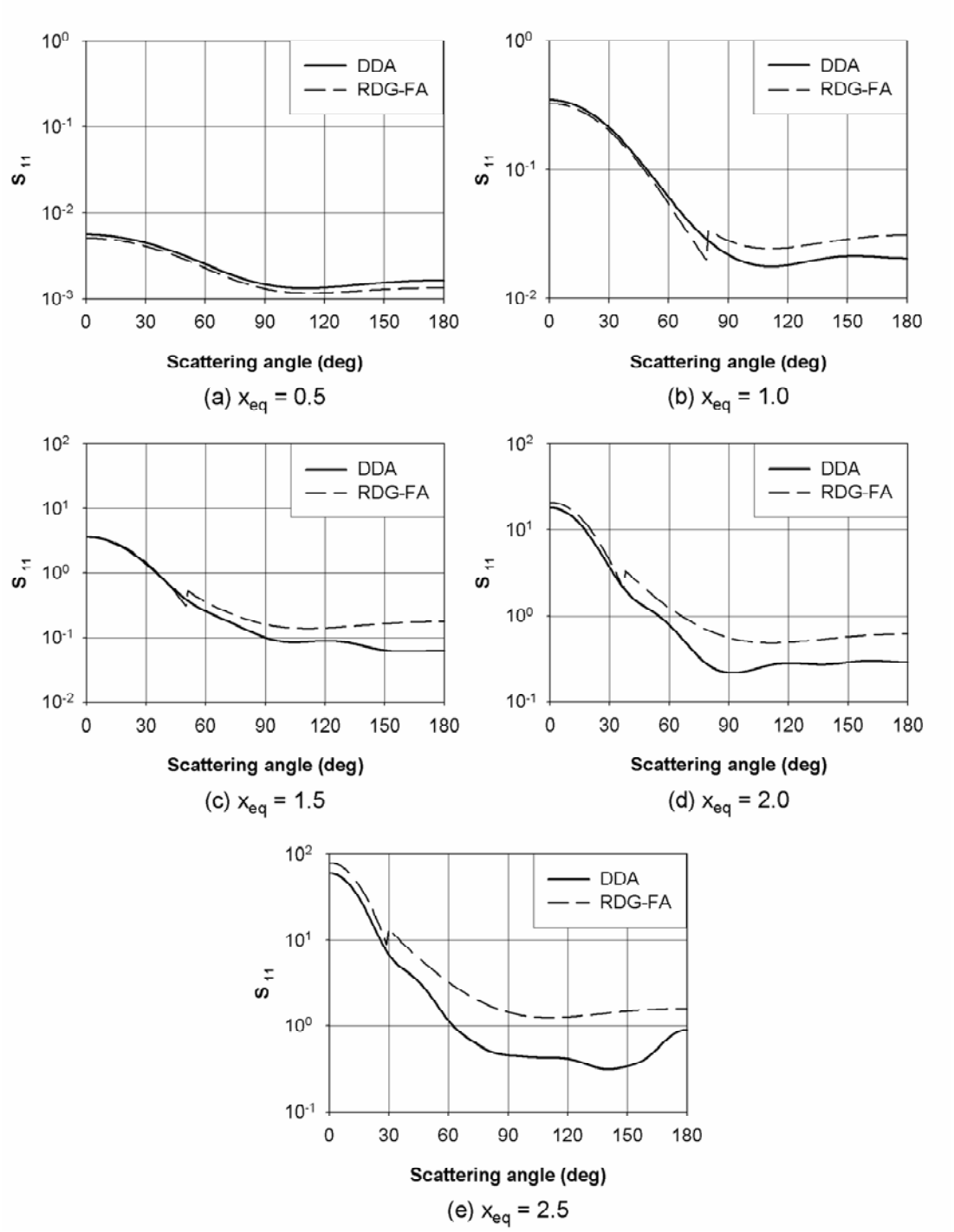

Figure 2.24. Comparison between S_{11} profiles predicted by DDA and RDG-FA methods for fractal aggregate.

When compared with the previous spherical aggregate problem, predictive performance of RDG-FA for absorption coefficient is better for the rather loosely packed fractal aggregate. This can be due to the compact layout in the spherical aggregate which may cause enhanced self-interaction and beam-shielding effects which are ignored in RDG approximation. On the other hand, scattering efficiency factor predictions of RDG-FA are better in previous compact case.

2.2.6. Conclusive remarks

Based on the presented comparisons, it can be concluded that RDG-FA, which introduces critical simplifications that enable implementation of soot property reconstruction methods, can be utilized for estimation of absorption coefficient of moderately-sized soot agglomerates ($x_{eq} < 1$) in the near-infrared range even when theoretical validity criteria of RDG approximation are violated due to large modulus of soot refractive index. Inspection of scattering albedo indicates that effect of scattering is negligible for $x_{eq} < 1$. The present study focuses on laboratory-grade flames of small optical thickness, which are expected to contain relatively small soot aggregates at early stages of agglomeration. Under these conditions, neglection of scattering and use of RDG approximation for prediction of spectral absorption coefficient are found to be acceptable approximations. These two approximations form the backbone of the proposed soot diagnostics approach and they introduce critical simplifications for the inverse model by reducing number of physically coupled unknown parameters and eliminating ill-posed inversion problems.

2.3. OPTICAL CONSTANT MODEL

2.3.1. Complex refractive index of soot

The most important limitation of optical soot characterization techniques is the uncertainty in refractive index of soot [5, 19]. Reviews on empirical and semi-empirical studies on spectrally dependent soot optical constants are available in [20, 21, 114]. Although many experimental data are available in the visible range, relatively fewer measurements were realized for the near-infrared range. Determination of refractive index for this range is most commonly realized via Drude-Lorenz semi-empirical model which is also utilized in this study for modeling refractive index of flame generated soot in both inverse and direct models.

2.3.2. Drude-Lorenz dispersion model

Variation of soot refractive index within near-infrared to visible spectral ranges can be described by the Drude-Lorenz dispersion model as practiced in previous semi-empirical studies that attempt to determine spectral optical constants of soot from measurements [23, 27, 115, 116]. Drude-Lorenz dispersion relations are based on modeling microscopic structure of matter by an assembly of harmonic oscillators which are subject to forced vibration due to electromagnetic fields [68]. The bound electrons and ions of matter are treated as simple harmonic oscillators connected by springs. Each oscillator is characterized by a damping constant, γ, a resonant frequency, ω_r and a plasma frequency ω_p which is defined as [68]

$$\omega_p^2 = \frac{e^2 N_e}{m_e \varepsilon_0} \tag{2.65}$$

where e [=1.6022×10^{-19} C] is the charge of an electron, m_e stands for the mass of the oscillator electron, ε_0 [=8.8542×10^{-12} C^{2}N^{-1}m^{-2}] is the dielectric constant and N_e represents number of oscillators per unit volume. For bound electrons, mass is taken as electron rest mass, m_e [=9.1096×10^{-31} kg] whereas free electron mass is estimated as $m_f = m_e/18$ [116]. Free electrons have a resonant frequency of zero. The constants: γ, ω_r and N_e for each oscillator are termed as dispersion constants and are characteristic properties of the material under consideration. Drude-Lorenz model provides functional dependence of complex dielectric function, $\in$, with respect to angular frequency of incident radiation, ω [=$2\pi c_0 \eta$] [68], for a given set of dispersion constants as follows

$$\in = 1 - \frac{\omega_{p,f}^2}{\omega^2 + i\gamma_f \omega} + \sum_{j=1}^{N_{be}} \frac{\omega_{p,j}^2}{\omega_{r,j}^2 - \omega^2 - i\gamma_j \omega} \tag{2.66}$$

where N_{be} stands for the number of bound electrons in the multiple oscillator model and subscripts f and j denote free electrons and bound electrons, respectively. For non-magnetic materials complex dielectric function is related directly to complex index of refraction via the following relation

$$m = \mathrm{n} + \mathrm{ik} = \sqrt{\in} \tag{2.67}$$

Implementation of Drude-Lorenz model to soot particles relies on input information from graphite models [27, 116]. To model optical constants of graphite in the visible and infrared ranges, a model with two bound and one free electron is used. Different sets of dispersion constants proposed by different researchers [23, 27, 115, 116] are given in Table 2.3. Real and imaginary parts of the complex index of refraction evaluated from these five sets of dispersion constants are plotted in Figure 2.25. Selection of one set as best representative for soot optical response in a given application is not straightforward as each of these sets involve significant uncertainties related to different factors such as experimental methodology, fuel type and temperature.

Table 2.3. Dispersion constants for Drude-Lorenz model

	Set 1	**Set 2**	**Set 3**	**Set 4**	**Set 5**	**Set 6**
	Dalzell and Sarofim (1969) [27]	Lee and Tien (1981) [116]	Charalampopoulos and Chang (1988) [115]	Habib and Vervisch (1988) [23]	Habib and Vervisch (1988) [23]	Stagg and Charalampopoulos (1993) [117]
Fuel type	Propane	Plexiglass, Polystyrene	Propane	Acetylene	Ethylene	Propane
Free electron mass	$m_f = m_b$	$m_f = m_b/18$	$m_f = m_b/18$	$m_f = m_b/18$	$m_f = m_b/18$	$m_f = m_b/18$
Resonant frequency [rad/s],						
$\omega_{r,1}$	1.25×10^{15}	1.25×10^{15}	1.25×10^{15}	1.25×10^{15}	1.25×10^{15}	1.25×10^{15}
$\omega_{r,2}$	7.25×10^{15}	7.25×10^{15}	7.25×10^{15}	7.25×10^{15}	7.25×10^{15}	7.25×10^{15}
Electron number density [#/m^3]						
$N_{e,1}$	2.69×10^{27}	4.07×10^{27}	3.88×10^{27}	1.67×10^{27}	3.34×10^{27}	3.38×10^{27}
$N_{e,2}$	2.86×10^{28}	4.47×10^{28}	4.26×10^{28}	1.83×10^{28}	3.66×10^{28}	3.717×10^{28}
$N_{e,f}$	4.06×10^{27}	4.00×10^{25}	4.82×10^{25}	7.00×10^{24}	1.40×10^{25}	0.023×10^{25}
$N_{e,t}$	3.15×10^{28}	4.88×10^{28}	4.65×10^{28}	2.00×10^{28}	4.00×10^{28}	4.00×10^{28}
Damping constant [rad/s]						
γ_1	6.00×10^{15}	5.90×10^{15}	9.80×10^{15}	7.00×10^{15}	7.00×10^{15}	7.00×10^{15}
γ_2	7.25×10^{15}	5.60×10^{15}	6.10×10^{15}	7.25×10^{15}	7.25×10^{15}	7.25×10^{15}
γ_f	6.00×10^{15}	1.20×10^{15}	1.20×10^{15}	1.20×10^{15}	1.20×10^{15}	1.20×10^{15}

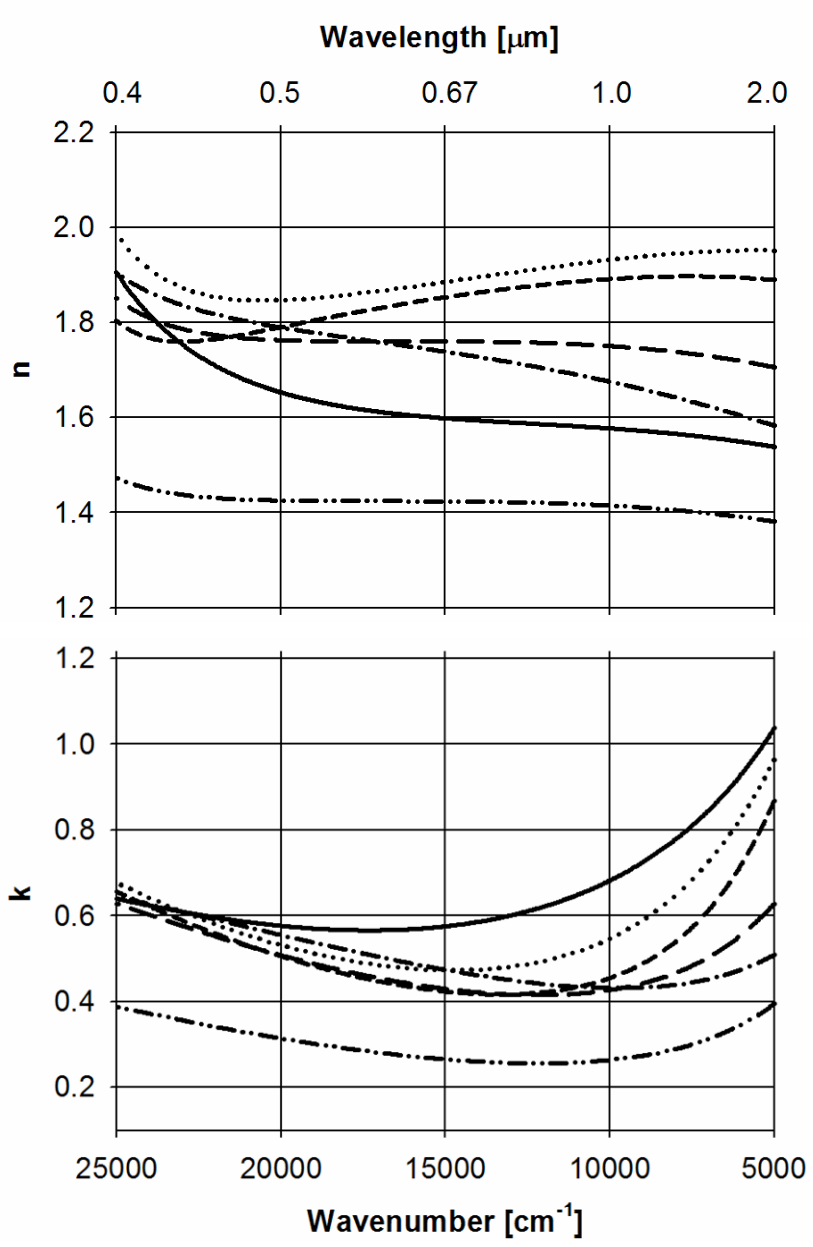

Figure 2.25. Refractive and absorptive components of soot complex index of refraction $m = n + ik$ from different sets of Drude-Lorenz dispersion constants

2.4. COUPLED MODEL FOR SIMULATION OF EXPERIMENTS

Simulation of line-of-sight near-infrared spectra emitted by a high-temperature sooty medium of prespecified profiles of soot temperature, concentration, complex index of refraction requires modeling of soot refractive index and radiative properties which are spatially varying fields required for solution of the line-of-sight radiative transfer equation. These three models for 3 different physical problems were analyzed individually in the previous sections of this chapter. In this final section, combined implementation of these sub-models is explained and utilization of this forward model for generation of synthetic measurements from Snelling *et* al.'s ethylene diffusion flame [118] for which soot temperature and concentration profiles are available by measurements. Simulation of experimental nonidealities such as noise and finite beam diameter are also elaborated for valuation of performance of the proposed reconstruction method under realistic conditions (Chapter 3).

2.4.1. Coupling procedure

The structure of the global forward model is presented in Figure 2.26. First the desired wavelength range, spectral resolution and positions of lateral nodes, x_j for simulation of line-of-sight flame emission spectra are specified together with input soot property fields. Then for each wavenumber at each lateral position, line-of-sight radiative transfer equation Eq.(2.1) is evaluated by performing line integrals along the projection chords. Line-of-sight radiative transfer model is coupled to radiative property model as chordal integration requires determination of absorption coefficient for a given position, s along the path. Radial position corresponding to s at current x_j is found from Eq.(2.3) and local temperature and volume fraction are evaluated from input radial profiles. The absorption coefficient is estimated by the RDG-FA model which inputs local volume fraction from the input profile and communicates with the optical constant model for calculation of soot refractive index function E_m at current wavenumber and position via Drude-Lorenz dispersion model and prespecified dispersion constants. Spectral line-of-sight emission intensities for each wavenumber at each lateral node are calculated by looping over the radiative transfer model.

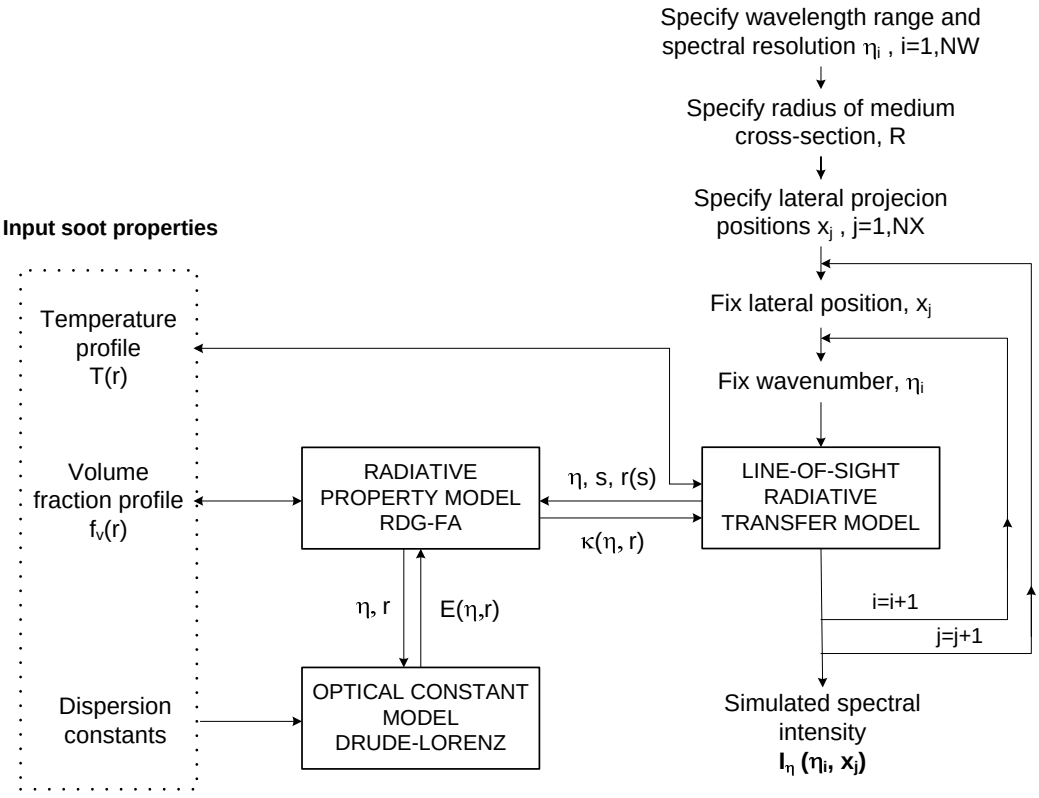

Figure 2.26. Coupling procedure for forward model

2.4.2. Description of test problem: Ethylene/air coflow diffusion flame

The problem selected as test case is based on Snelling *et* al. [118]'s laminar ethylene diffusion flame with 10.9 mm inner diameter fuel tube centered in a 10 cm diameter air nozzle and fuel and air flow rates of 194 ml/min (21°C,1atm) and 284 l/min, respectively. Temperature and volume fraction profiles of this flame were thoroughly characterized by two different measurement techniques for each property [118]. Temperature and volume fraction measurements carried out by flame emission tomography were validated against reference temperature and volume fraction measurements obtained by coherent anti-Stokes Raman scattering (CARS) nitrogen thermometry and two-dimensional line-of-sight attenuation (LOSA) corrected for scattering, respectively. Reference measurements at 30 mm height were selected as basis in the present study for generation of a realistic test case, representative of a typical optically thin, axisymmetric sooting flame in laboratory conditions. Also, steep soot volume fraction peak towards the edge poses a challenge in terms of property reconstruction.

Reference measurements (CARS and LOSA) plotted in Figure 7 of [118] were extracted and smoothing cubic splines were fitted to provide input functions to the forward model [27]. Figure 2.27 and Figure 2.28 display resulting temperature and volume fraction profiles. Refractive index of soot is also required for complete specification of the test case. Different dispersion constant sets proposed previously in the literature (see Table 2.3) were all utilized interchangeably during performance evaluation of the reconstruction method (Chapter 3). Dalzell and Sarofim's dispersion constants [27] obtained from a propane fueled diffusion flame were utilized for the intensity simulations presented in this chapter as they are usually used in the literature for soot refractive index estimation for a wide variety of flames.

2.4.3. Simulation of experimental nonidealities

The forward model described above simulates line of sight emission intensities free from any experimental restrictions. In practical application of soot property reconstruction experimental limitations, especially those due to measurement noise and finite beam diameter, can be important handicaps that substantially degrade the accuracy of inferred properties. In order to evaluate the performance of soot property reconstruction methodology proposed in this thesis under realistic experimental conditions, experimental nonidealities were also simulated.

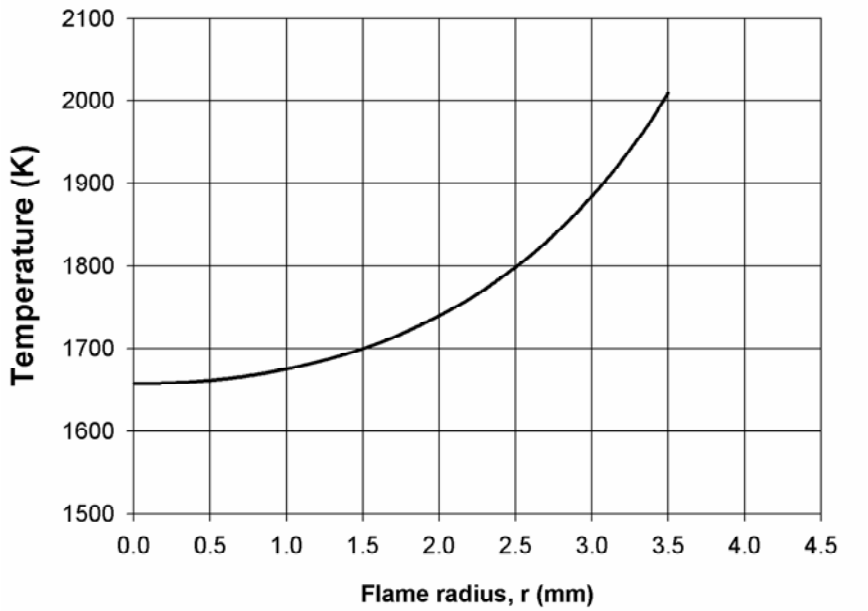

Figure 2.27. Soot temperature profile for axisymmetric coflow ethylene diffusion flame (continuous curve fitted to data by Snelling *et* al. [118])

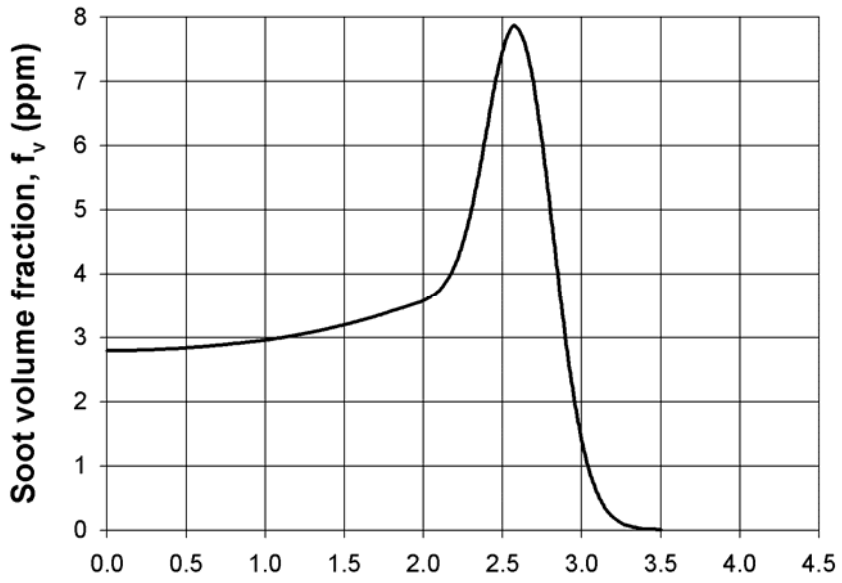

Figure 2.28. Soot volume fraction profile for axisymmetric coflow ethylene diffusion flame (continuous curve fitted to data by Snelling *et* al. [118])

2.4.3.1. Generation of artificial noise

As will be demonstrated in the experimental part of this study, noise is an inevitable component of line-of-sight flame emission measurements. To simulate this effect, random white noise was generated and superimposed on ideal intensities obtained by line integration. For this purpose a digital noise generator algorithm outlined by [119] was utilized. This algorithm enables creation of Gaussian noise signal for any given mean and specified standard deviation. The procedure starts by specification of the signal-to-noise ratio (SNR) for the desired noise level. Then, for each value of ideally simulated intensity, I_{ideal} at each wavenumber and location, 12 random numbers are generated and summed up to obtain R_{12}. Noisy intensity is then evaluated from

$$I_{noisy} = I_{ideal} \cdot \left(1 + \frac{(R_{12} - 6)}{SNR} \right) \tag{2.68}$$

The random number generator used in the present study is RNUN routine from IMSL mathematical library [25].

2.4.3.2. Modeling finite beam diameter effect

Another important and unavoidable experimental limitation is the obligation to use a finite beam diameter for detection of line-of-sight emission whereas intensity simulation via Eq. (2.1) is based on a chord of zero diameter (line) rather than a cylindrical column of finite diameter. In practice, the diameter of the beam needs to be larger than a critical diameter below which signal power becomes too low to be detected at the same time, it needs to be small enough to resolve the spatial variations within the flame.

To simulate the effect of finite beam width, a beam diameter is specified around the lateral scan location x_j. The cross-section of the beam is subdivided into NS slices as demonstrated in Figure 2.29 It is assumed that the vertical variation of soot properties negligible in the vicinity of the beam when compared to horizontal variation and line of sight emission intensity is constant within the slice, k and can be represented by the intensity projected at position x_k. Intensities for all k locations are simulated as described in section 2.4.1. The

intensity for a finite diameter beam projected on the lateral scan position, j is then evaluated by area weighted averaging of ideal intensities for the slices as follows

$$I_{j,db} = \frac{4}{(\pi . d_b^2)} \sum_{k=1}^{NS} A_{s,k} I_{k,ideal} \tag{2.69}$$

where $A_{s,k}$ stands for the area of slice k and can be geometrically evaluated from $|x_k - x_j|$, NS and d_b. In this study beam diameter effect is simulated by considering 6 strips per beam and setting d_b = 6R/14 = $6d_x$ which is close to realistic experimental conditions provided in Chapter 4.

2.4.4. Simulated flame emission measurements

The line-of-sight intensity spectra due to emission and absorption of coflow ethylene diffusion flame is simulated for equally spaced 15 lateral positions spanning the flame radius at one side. Spectral range and spectral resolution are set to [7500-8500 cm^{-1}] and 25 cm^{-1}, respectively.

Figure 2.30 to Figure 2.33 display resulting intensity profiles for 4 different cases: A – ideal case, B – noisy case with SNR=100, C – large beam diameter case, D – noisy and wide column case. Effect of noise on lateral and spectral profiles are shown in Figure 2.34a and b. Figure 2.35 shows the effect of finite beam diameter on spectral and lateral profiles. As can be seen, large beam diameter causes artificial diffusion effect by smoothing sharp lateral gradients. Figure 2.36 displays combined effect of noise and finite beam diameter.

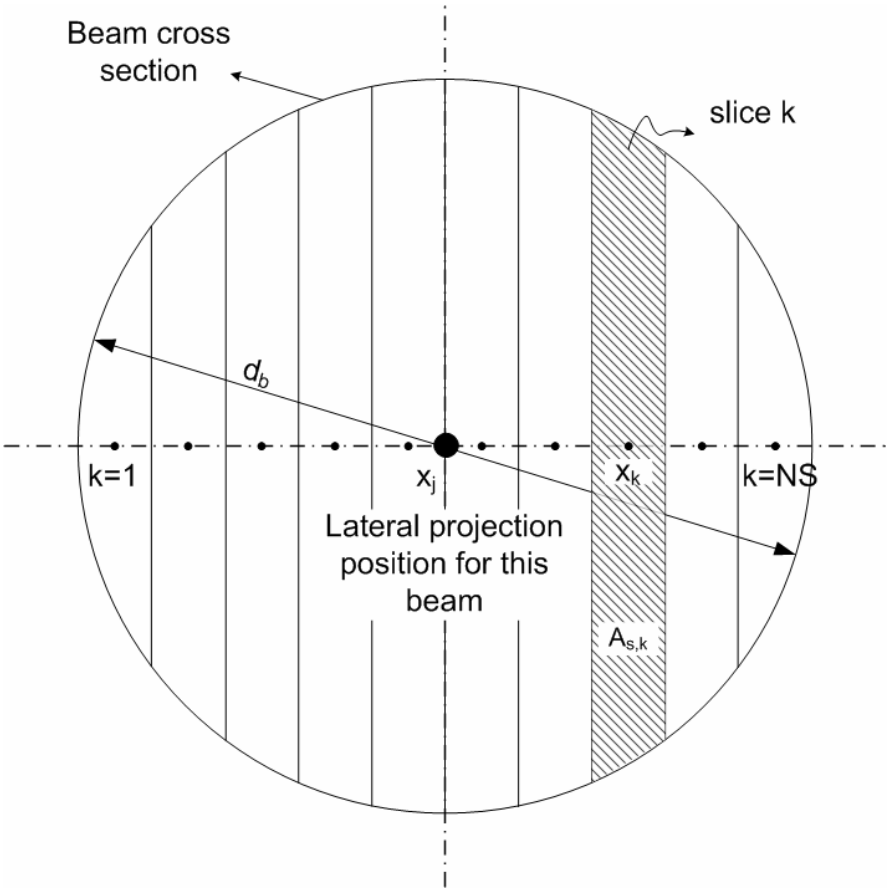

Figure 2.29. Schematic representation for modeling beam diameter effect.

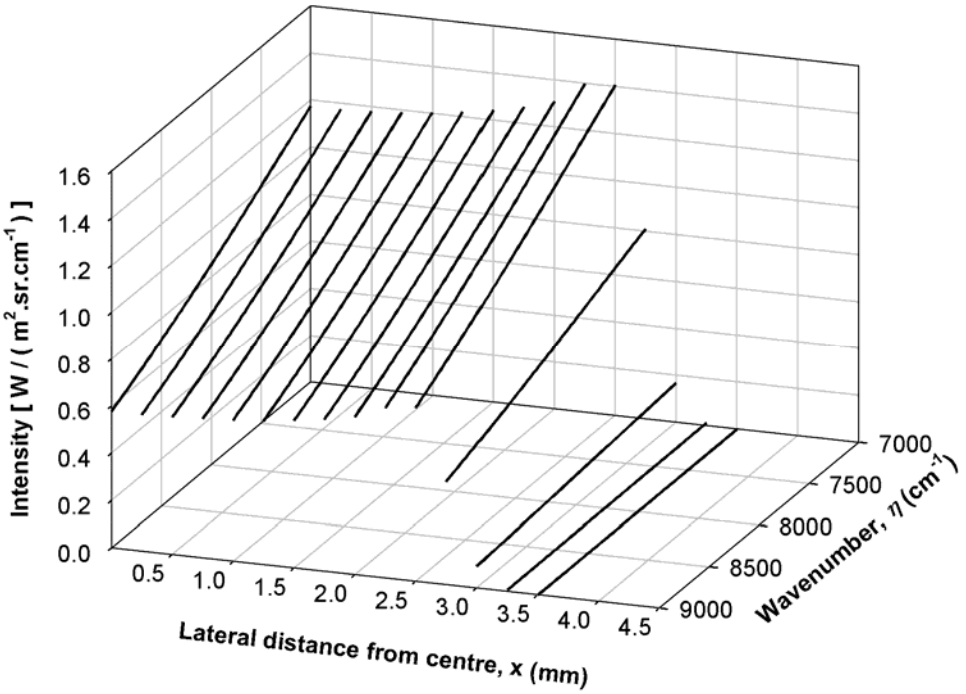

Figure 2.30. Simulated flame emission intensity spectra (Case A)

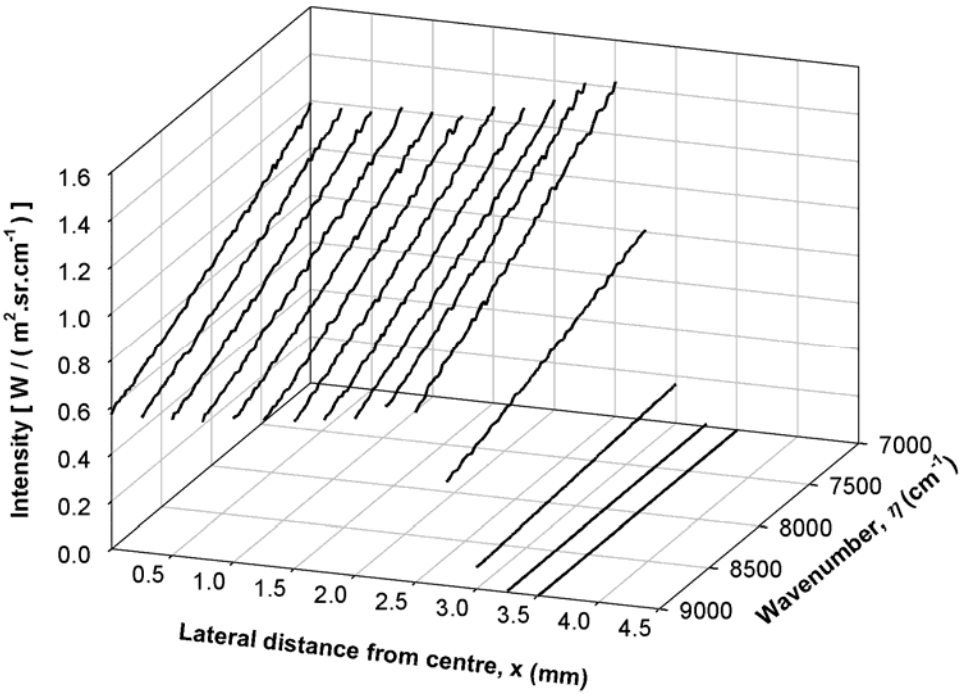

Figure 2.31. Simulated flame emission intensity spectra with noise, SNR=500 (Case B)

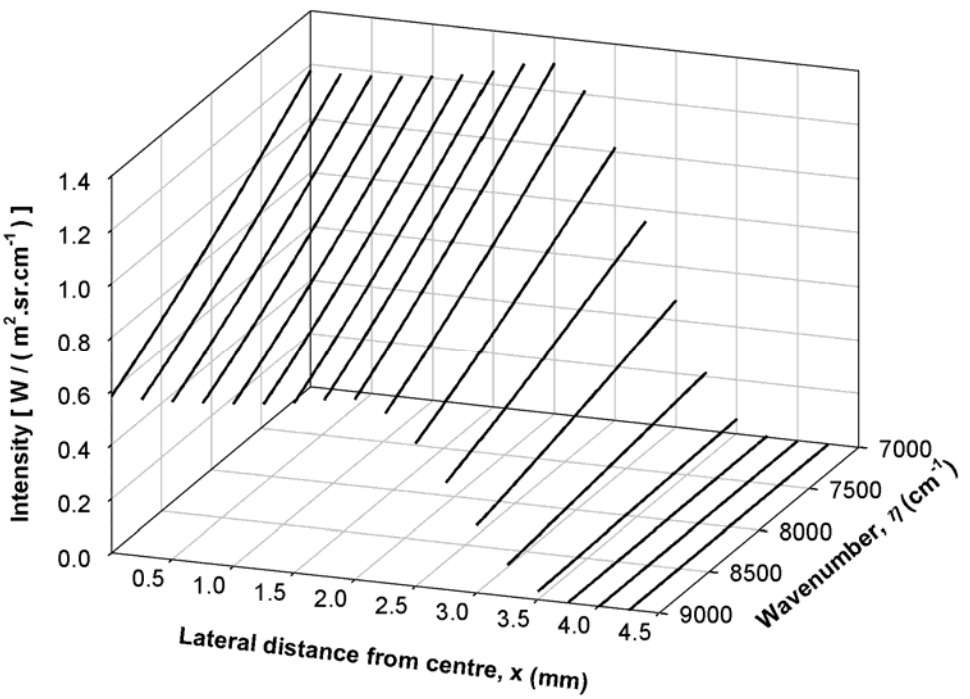

Figure 2.32. Simulated flame emission intensity spectra with finite beam diameter effect, $d_b = 6\ d_x$ (Case C)

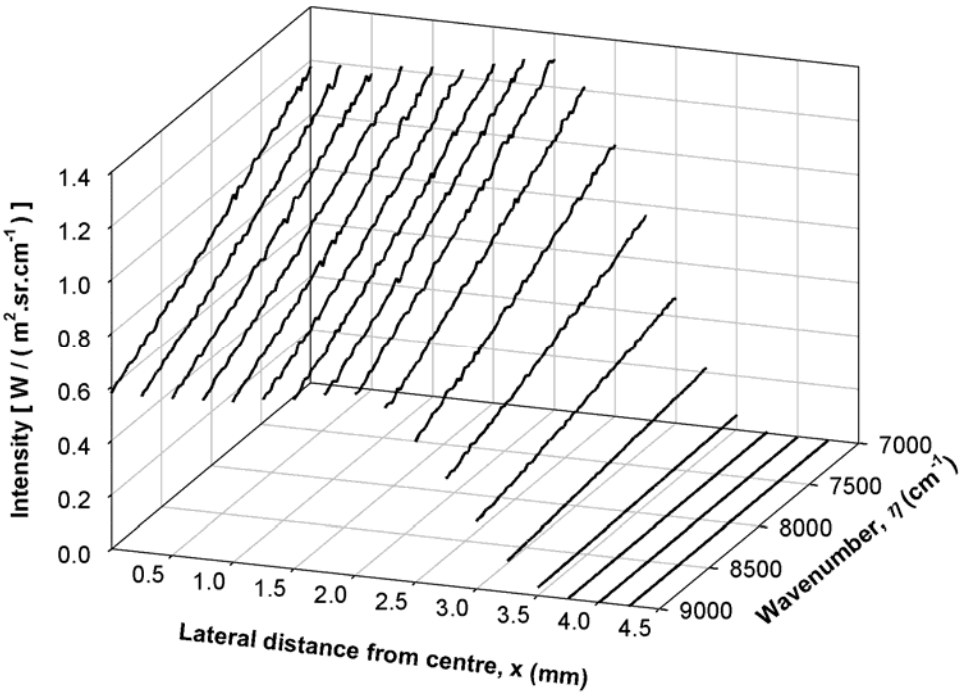

Figure 2.33. Simulated flame emission intensity spectra with noise and finite beam diameter effect, SNR=100, $d_b = 6\ d_x$ (Case D)

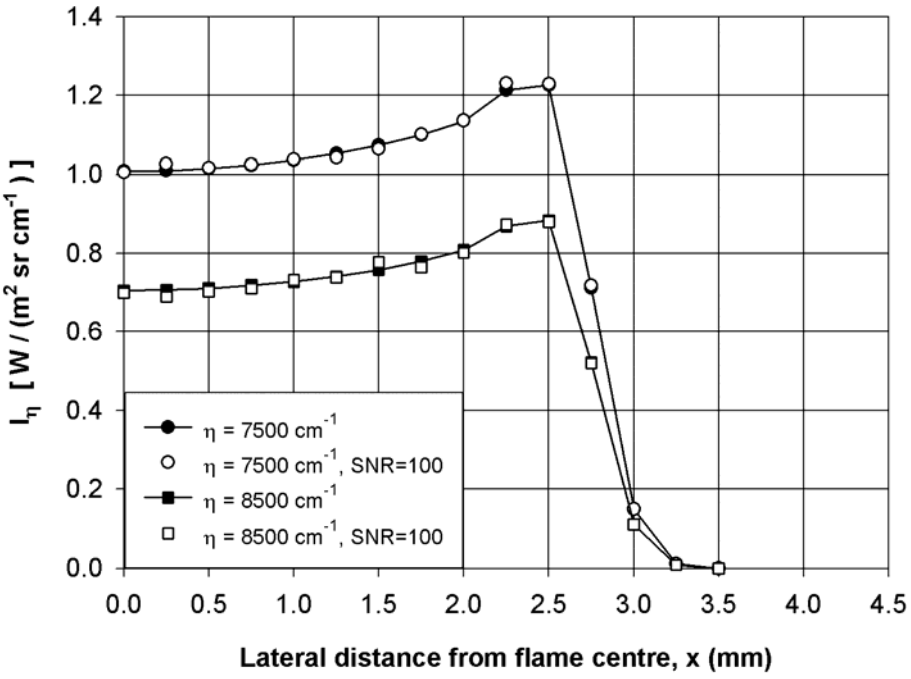

(a)

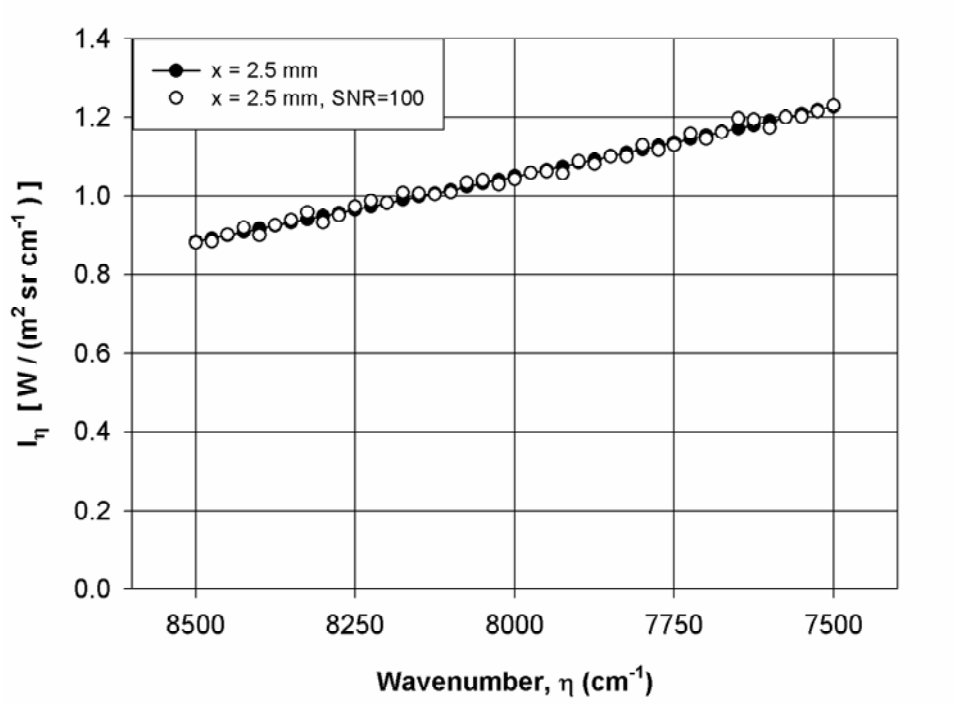

(b)

Figure 2.34. Effect of noise on (a) lateral intensity profiles, (b) intensity spectra

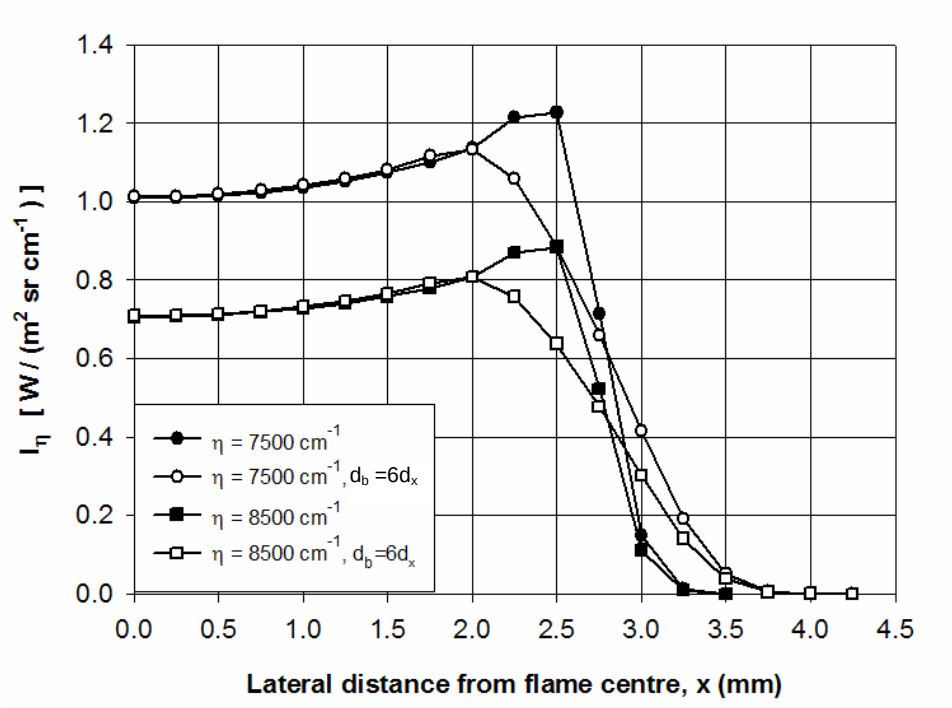

(a)

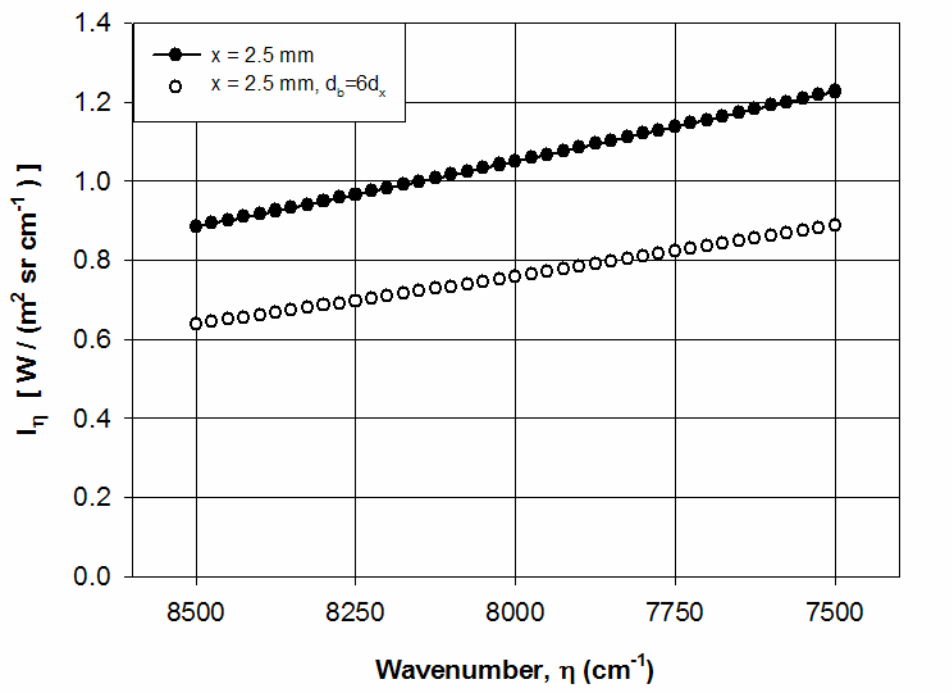

(b)

Figure 2.35. Effect of finite beam diameter on (a) lateral intensity profiles, (b) intensity spectra.

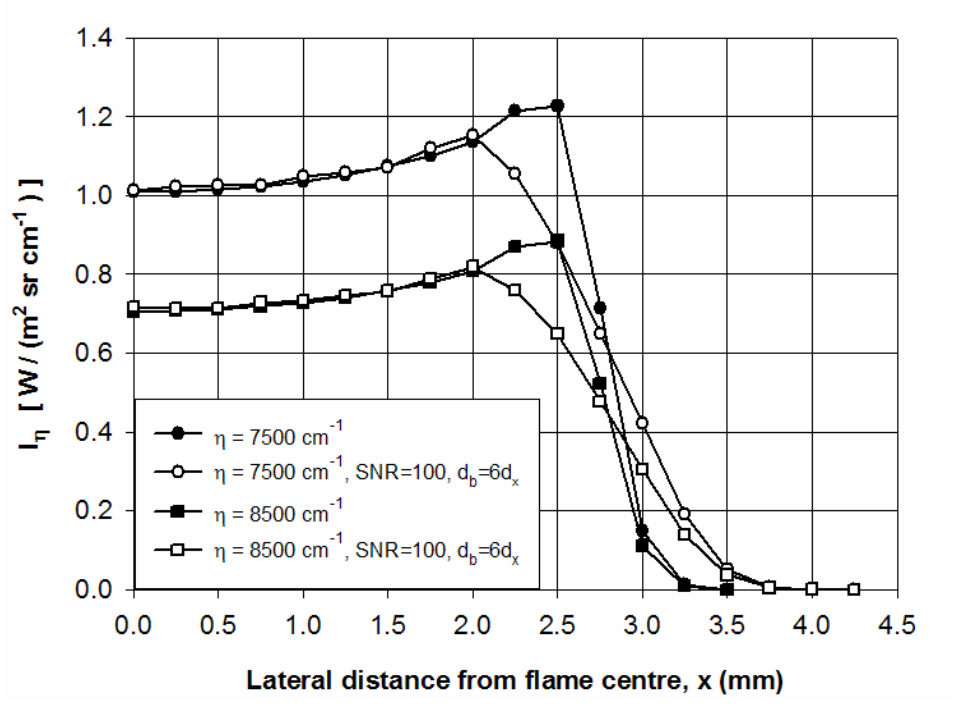

(a)

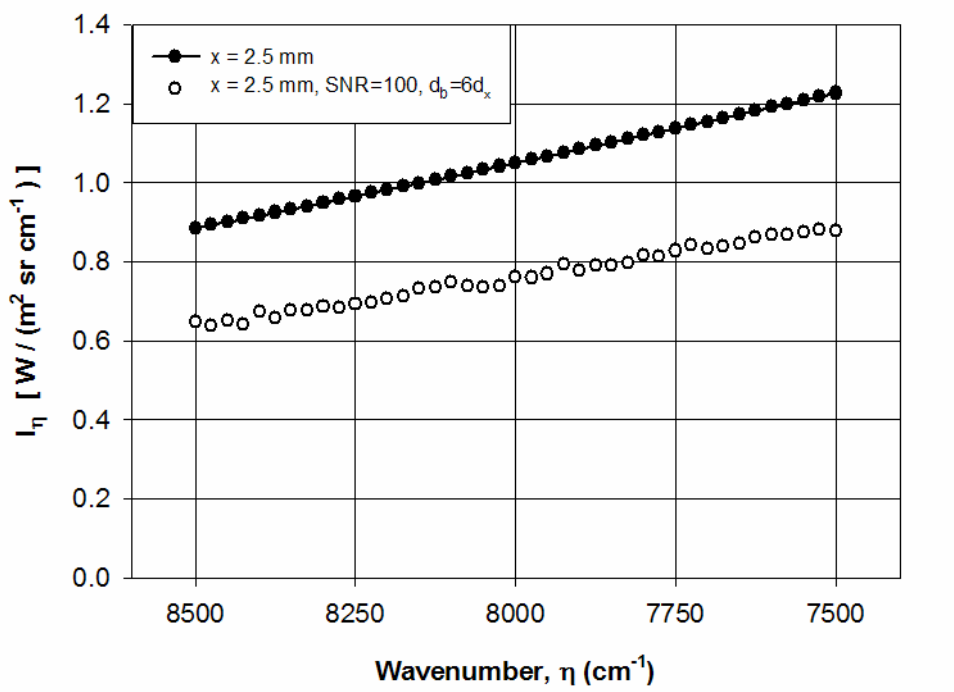

(b)

Figure 2.36. Effect of finite beam diameter and noise on (a) lateral intensity profiles, (b) intensity spectra.

CHAPTER 3

EXPERIMENTAL METHODS

The objective of the experiments is to measure spectrally resolved line-of-sight emission intensities from a laboratory grade, luminous, axisymmetric, vertical diffusion flame in still air, at different horizontal and vertical positions. Spectral measurements in the near-infrared range are performed by Fourier Transform Infrared (FT-IR) spectrometry. The spectrometer is calibrated against a blackbody to convert the spectra to physical intensities and eliminate instrument interference. This chapter starts with an introduction on laminar diffusion flames and FT-IR spectrometry followed by flame emission spectrometry. Description of experimental apparatus is followed by the experimental procedure, calibration methodologies and operating conditions of the experiments. Resulting measurements are reported and associated noise, uncertainty and reproducibility analyses are elaborated.

3.1. INTRODUCTION

3.1.1. Laminar diffusion flames

In the present study, an axisymmetric laminar diffusion flame was selected for soot characterization studies due to the following reasons *i*) diffusion flame conditions exhibit a challenging sample from the viewpoint of soot diagnostics as they enhance soot formation and cause sharp soot property gradients, *ii*) laminar flames maintain stability and reproducibility of flame conditions, *iii*) axisymmetry simplifies tomographic analysis.

In diffusion flames which are also called nonpremixed flames, the fuel and the oxidizer are supplied from separate sources and mixing takes place during the combustion process. This is why in such flames, energy release rate is primarily limited by the diffusion and mixing process rather than chemical kinetics which plays a secondary role. These flames have a complicated kinetic structure when compared to premixed flames as the flame displays sharp gradients of equivalence ratio covering the whole range from 0 to 1. Rich and lean combustion take place at the fuel and oxidizer sides, respectively. High-temperature flame front settles at stoichiometric composition regions. Soot particles are concentrated behind the

high temperature flame front, towards the fuel rich region and therefore luminosity is enhanced [8, 10].

Ethylene is selected as the fuel as ethylene diffusion flames were thoroughly studied both experimentally and theoretically and therefore present findings can be compared by the characterization studies in the literature. Soot characterization in the present study based on spectrally resolved analysis of near-infrared flame emission was carried out by using Fourier transform spectrometry which is explained in the next section.

3.1.2. Fourier transform spectrometry

Over the past two decades, Fourier Transform Spectrometry (FTS) has become the most preferred technique for measuring high quality spectra within far-infrared (λ = 25-1000 μm), mid-infrared (λ = 2.5-25 μm), near-infrared (λ = 0.7-2.5 μm) and even in visible (λ = 0.4-0.7 μm) ranges [120]. Its inherent advantages over classical dispersive instruments such as grating monochromators or spectrographs especially for the infrared, which are explained later in this section, have led to its dominant use in diverse fields including astronomy, instrumental analytical chemistry, process monitoring, combustion science, high-temperature gas dynamics, atmospheric measurements, medical diagnostics and remote sensing applications.

Spectroscopy is characterization of matter through spectrally resolved analysis of electromagnetic radiation emitted, absorbed, reflected or scattered by the sample. FT spectrometry is based on generation of an interference pattern (interferogram) from the sample wave under analysis by using an interferometer which is then digitized by the detector and Fourier transformed to construct the spectrum. The heart of any FT spectrometer is the interferometer which basically consists of a group of optical elements that generate an interference pattern from an incident beam. Optical layout of a Michelson interferometer which is the most common interferometer type is displayed in Figure 3.1. Main components of a Michelson interferometer are a beamsplitter, a fixed mirror, a movable mirror and frequently a HeNe laser.

Electromagnetic radiation beam emitted by the broadband source is collimated and directed to the beamsplitter which transmits half of the irradiation and reflects the other half, splitting

the incident beam into two beams of equal intensity. The reflected beam propagates a certain path length towards the fixed mirror from which it is reflected back to the beam splitter. The transmitted beam heads to the movable mirror which is precisely displaced back and forth along the optical axis and the beam is reflected back to the beamsplitter where it is recombined with the other half. Due to the variable path length maintained by the moving mirror, the recombined beams are no longer in phase and an interference pattern is obtained due to constructive-destructive combinations of the waves. Half of the resulting modulated beam is reflected by the beamsplitter towards the detector and the other half returns along the incident path.

The difference between the optical path lengths of two branches of the beamsplitter is called optical retardation and depending upon the wavelengths, this distance determines the amplitude of resulting interference pattern. As the mirror moves at constant velocity, the detector samples the resulting modulated signal to obtain the interferogram which is simply a plot of signal amplitude versus optical retardation. At zero path difference, all wavelengths are in phase and simultaneously interfere constructively, leading to very large peak amplitude which is called the centerburst of the interferogram. The extent of mirror movement determines the spectral resolution, i.e. the longer the scan displacement, the higher the spectral resolution. Each single data point of the interferogram carries information from full spectrum of the source radiation.

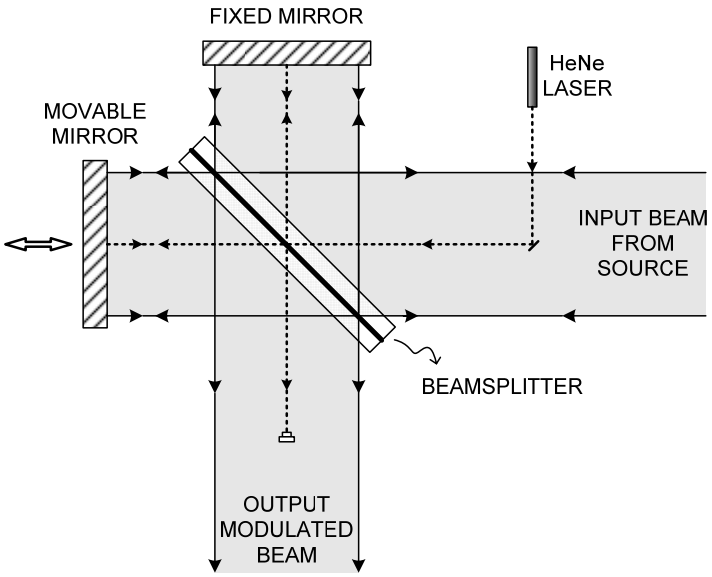

Figure 3.1. Schematic of a standard Michelson interferometer

In modern interferometers a HeNe laser beam (λ = 632.8 nm) is accompanied with the source beam as it passes through the interferometer and it is detected by a separate laser detector (Figure 3.1). As the laser is a monochromatic source, its interference pattern yields a sinusoidal interferogram with periodic constructive peaks at optical retardation distances equal to integer multiples of the laser wavelength. Such a precise pattern serves as a reference for two purposes: *i*) velocity feedback control of the mirror which needs to be kept constant to eliminate spectral artifacts, *ii*) to digitize the interferogram at precisely equal intervals of optical retardation so that spectral resolution is controlled sensitively and fast-Fourier transform algorithms can be implemented correctly at the data acquisition stage. Further information on Michelson interferometers are available by Jackson [121] and Giffiths [120].

The path followed by the modulated signal after the interferometer depends on the type of spectroscopic application under consideration. The most common mode of operation is transmission spectroscopy in which radiation from a source is modulated by the interferometer and directed to the sample substance. Transmitted interference pattern which carries signature of the sample is digitized to an interferogram and Fourier transformed to obtain the spectrum of transmitted radiation which is then normalized against the spectrum of the source to yield transmittance spectrum. This mode is used for many purposes such as elucidation of molecular structures in analytical chemistry applications and do not require calibration against reference substances. In emission spectroscopy mode, electromagnetic wave radiated by the sample substance is modulated by the interferometer and then sampled by the detector to form the interferogram. This mode of operation is commonly used for diagnosis of high temperature systems such as flames and plasmas. Quantitative emission spectroscopy analyses necessitate calibration against a reference source with known spectral emission intensity. The other less common modes are scattering and reflection spectroscopy where scattering pattern or reflection of the sample are utilized for characterization. In the present study, emission spectrometry is deployed for analysis of flame.

The critical final stage in Fourier transform spectroscopy is conversion of the sampled interferogram to a spectrum being the desired output. The interferogram is subjected to Fourier transformation which is efficiently handled via fast-Fourier transform (FFT) algorithms. This step is accompanied by several data processing procedures which are required for improvement of the quality of final spectrum and elimination of artifacts caused by instrumental imperfections and sampling limitations [120, 122, 123]. Table 3.1 presents a

condensed summary of basic data processing practices deployed in Fourier transform spectroscopy.

Inherent advantages of Fourier transform spectrometry over classical dispersive spectroscopy techniques are as follows [120, 122, 124]:

1. Throughput (Jacquinot) advantage: Optical elements of Fourier transform spectrometers are fewer and have larger area than the slits of dispersive spectrometers. This results in a higher throughput of radiation, more powerful signal and larger signal to noise ratio.

Table 3.1. Data processing techniques in Fourier transform spectroscopy

Process	Purpose	Explanation
Ensemble averaging	to improve of signal-to-noise ratio	Multiple interferograms collected at N subsequent measurements are averaged to yield a SNR improvement of $\sqrt{N}$
Zero-filling	to reduce picket-fence effect caused by using discrete form of a continuous interferogram	Zeros are added to the tails of interferogram Provides the effect of increasing resolution by interpolation
Undersampling	to eliminate aliasing overlap artifact caused by using discrete form of a continuous interferogram	Reducing data storage requirements so that sample spacing can be reduced
Apodization	to eliminate leakage artifact caused by truncation of the interferogram at finite optical retardation Artificial side lobes (feet) occur at the two sides of the interferogram peak. Available intensity unnecessarily contributes to these side lobes where it is desirable to concentrate it for the main interferogram signal.	Truncation of the interferogram less abruptly by convolution with certain apodization functions
Phase correction	to symmetrize the interferogram and to eliminate optical phase shift effects caused by instruments FT results in a spectrum of complex numbers, to obtain the real spectrum, the amplitude of the complex spectrum needs to be extracted	Finds the phasor notation amplitude of the complex spectrum Mertz method handles noise better double sided scans are favorable

2. Multiplex (Fellget) advantage: All spectral features of the source impinge on the detector simultaneously. The measurement time is determined by the time it takes to move the mirror over the displacement required for desired resolution. On the other hand, in gating spectrometers, the measurements are carried out one by one for each wavenumber. This time advantage of FTS saves time for multiple measurements which can be ensemble averaged to reduce noise. Throughput advantage and Multiplex advantage are the main reasons underlying the high spectral resolution capabilities of Fourier transform systems.
3. Connes advantage: Use of laser interference as a reference provides a built-in calibration for the FTS data acquisition system and enables high precision sampling and high wavelength reproducibility.

3.1.3. Flame emission spectroscopy for soot diagnostics

Radiative emission from flames carries characteristic information about the temperatures, concentrations and chemical compositions of flame species such as combustion gases and soot. Measurement of radiative emission has long been used for nonintrusive combustion diagnostics via well established measurement techniques such as two-color pyrometry [125]. Use of spectroscopy for measurement of flame emission introduces considerable advantages as radiative properties of combustion species are strongly wavelength dependent and spectral measurements provide useful information for selective analysis of each species. In certain spectral windows where combustion gases are transparent, continuum emission sourced by flame soot can be detected and processed to extract information on the physical variables that govern the intensity of the emission, such as, temperature, concentration and optical constants of soot. Flame emission spectroscopy[1] measurements basically consist of analyzing lateral flame radiance by sampling emitted radiative flux restricted within a narrow chord along the line-of-sight and directing it to a spectrometer which measures spectral variation of intensity. Lateral scanning of the flame from one end to another yields profiles of spectral intensities which are ready to be supplied to tomographic reconstruction for soot characterization.

---

[1] It is important to distinguish “Flame Emission Spectroscopy” (FES) term referred here, from “Flame Atomic Emission Spectroscopy” (FAES) which is also commonly called with the same name. FAES is a spectrochemical instrumental analysis technique which makes use of atomic emission for chemical characterization and deploys combustion as an agent to provide atomization and excitation to the sample delivered into the flame. On the other hand, in the present context, FES refers to the combustion diagnostics technique based on molecular emission from flame species.

Pioneering studies on spectral flame emission measurements for nonintrusive soot diagnostics was conducted by Solomon, Best and co-workers [126-128] via FTIR spectroscopy within 1.53-20 μm spectral range in combination with transmission spectroscopy to infer temperatures and relative concentrations of gaseous species, particulate matter and soot in various gas, liquid and solid fueled flames. De Iuliis *et* al. [129] measured multiwavelength soot emission intensities within 0.3-0.8 μm range by using a low resolution spectrograph and applied optical tomography to reconstruct soot volume fraction and temperature distributions in a co-annular ethylene/air diffusion flame. Bourayou *et* al. [130] performed FTIR emission spectrometry within 1.66-25 μm range to measure monochromatic radiative flux distributions emitted by a propane/air laminar diffusion flame. Snelling *et* al. [118] used a dispersive spectrometer and a charge-coupled device detector to measure line-of-sight intensity spectra within 0.3-0.945 μm range emitted by a co-annular ethylene/air diffusion flame and infer temperature and soot volume fraction profiles from tomographic reconstruction. More recently, Zheng and Gore [131] reported measurement of line-of-sight spectral emission intensities and associated statistical properties within 1.4-4.8 μm range by using a fast infrared array spectrometer (FIAS) to infer distributions of CO_2 mole fraction, temperature and soot volume fraction in a turbulent ethylene/air jet flame.

Flame emission in the NIR range, particularly in 1.18-1.33 μm (7500 – 8500 cm^{-1}) range, is a promising tool for simultaneous characterization of soot temperature, volume fraction and refractive index distributions in laboratory scale optically thin flames as combustion gases are transparent and soot refractive index displays selective spectral variation in this spectral range. Experimental investigation of this range for spectral soot diagnostics was not previously studied to date and deserves further attention. Present study focuses on the measurement methodology for line-of-sight flame emission spectrometry within 1.1-1.7 μm (9000-6000 cm^{-1}) range on an axisymmetric ethylene/air diffusion flame.

3.2. APPARATUS

Emission spectrometry measurements were realized by the experimental set-up depicted in Figure 3.2, which is located at CETHIL INSA-Lyon. Emission from the flame in the near-infrared range is scanned along its horizontal lateral axis at several altitudes above the burner. At each position, emission along a chord through the flame is collected by optical elements and directed to the FT-IR spectrometer which perceives and processes emitted

radiation to yield local line-of-sight flame emission spectra. For calibration measurements, a blackbody cavity of prespecified temperature replaces the flame. Main components of this set-up are the spectrometer, the burner, the blackbody, line-of-sight optics and the data acquisition system.

3.2.1. Burner

The burner for the laboratory grade axisymmetric laminar diffusion flame is based on the burner design used by Yousefian and Lallemand [132, 133] and it is the same burner as the one used by Bourayou *et* al. [130, 134].

The burner and its auxiliaries are schematically illustrated in Figure 3.3. Fuel flowrate is adjusted by means of a rotameter supplied by Brooks Instrument (Sho-Rate 1355). The fuel enters the mixing chamber at the bottom of the burner, crosses a porous plate and flows through a honeycomb structure for laminarization. Nozzle diameter of the burner is D_0 = 2 cm. The burner is situated on micrometric positioning stages that enable spatial exploration of the flame along vertical and horizontal directions. The flame is in quiescent air. In order to avoid flame flickering due to external air circulations, the burner is framed in a protection confinement made of polyethylene sheets as shown in the figure. As main air flow stream around the flame is in vertically upwards direction, a honeycomb structure is placed towards the bottom to stabilize air flowing through the confinement.

3.2.2. Blackbody

A vertical blackbody furnace (Pyrox, Model PY 25) of 25 mm aperture and 3 kW power was used for calibration of emission spectra. As illustrated in Figure 3.4, the blackbody furnace consists of a cylindrical cavity made of Lanthanum Chromite ($LaCrO_3$) surrounded by 4 heater rods made of the same material as the cavity. Auxiliary units for water cooling and temperature control enables stability of preset temperatures within the cavity. Blackbody is designed for operating within a temperature range of 400-1750 C°. Calibration of the blackbody for the operating temperatures was checked before the experiments by a pyrometer (LAND, M600/1600C-V type) with certified calibration provided by LNE, National Metrology and Test Laboratory of France. Combined accuracy level of blackbody temperature measurement determined by uncertainty of furnace temperature control unit (±1° C) and pyrometer uncertainty (±2° C) amounts to ±2° C.

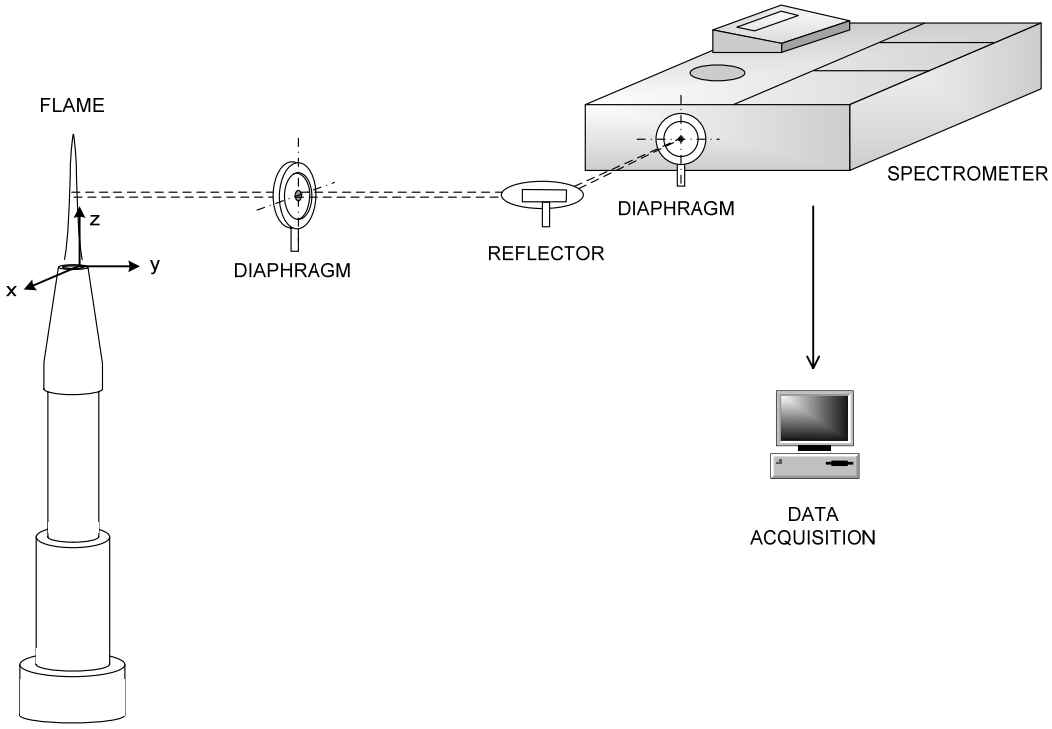

Figure 3.2. Experimental setup for line-of-sight flame emission spectra measurements

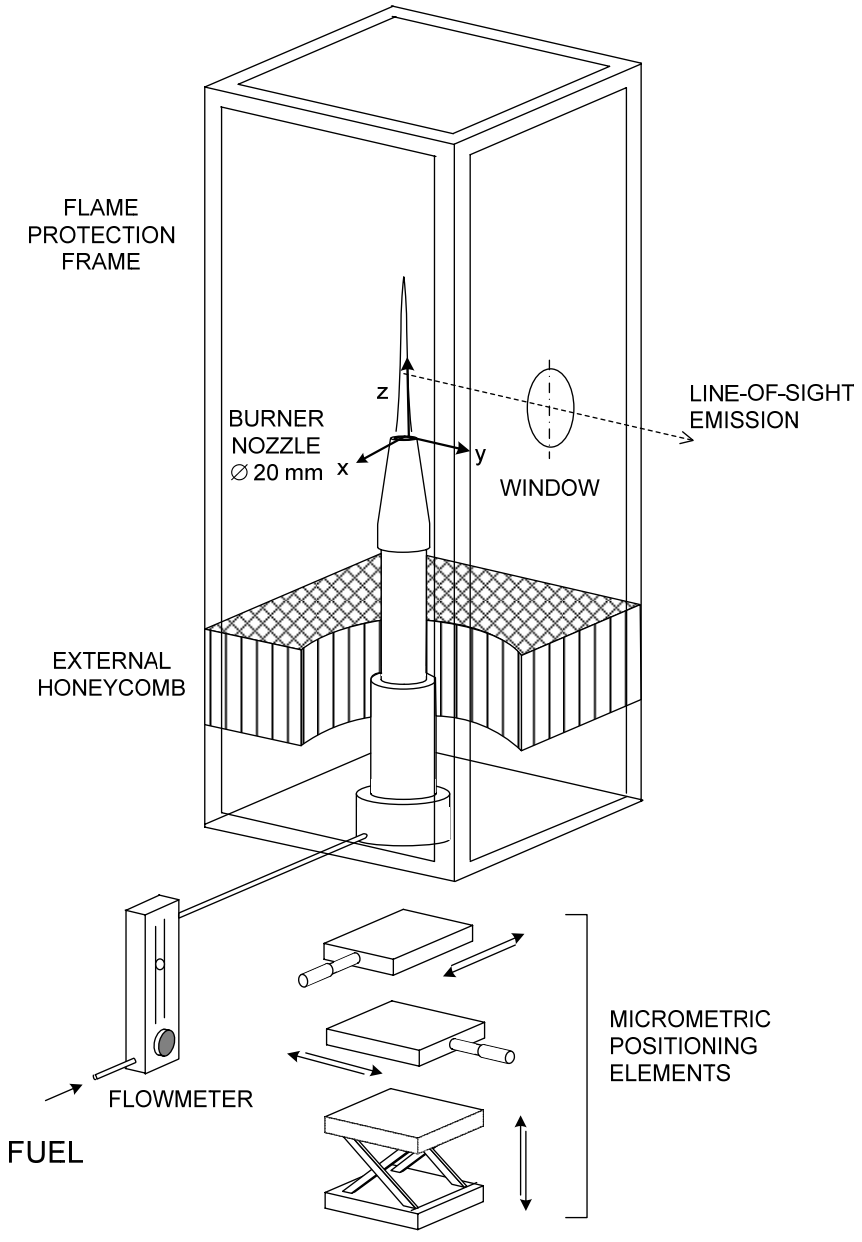

Figure 3.3. Burner and peripherals

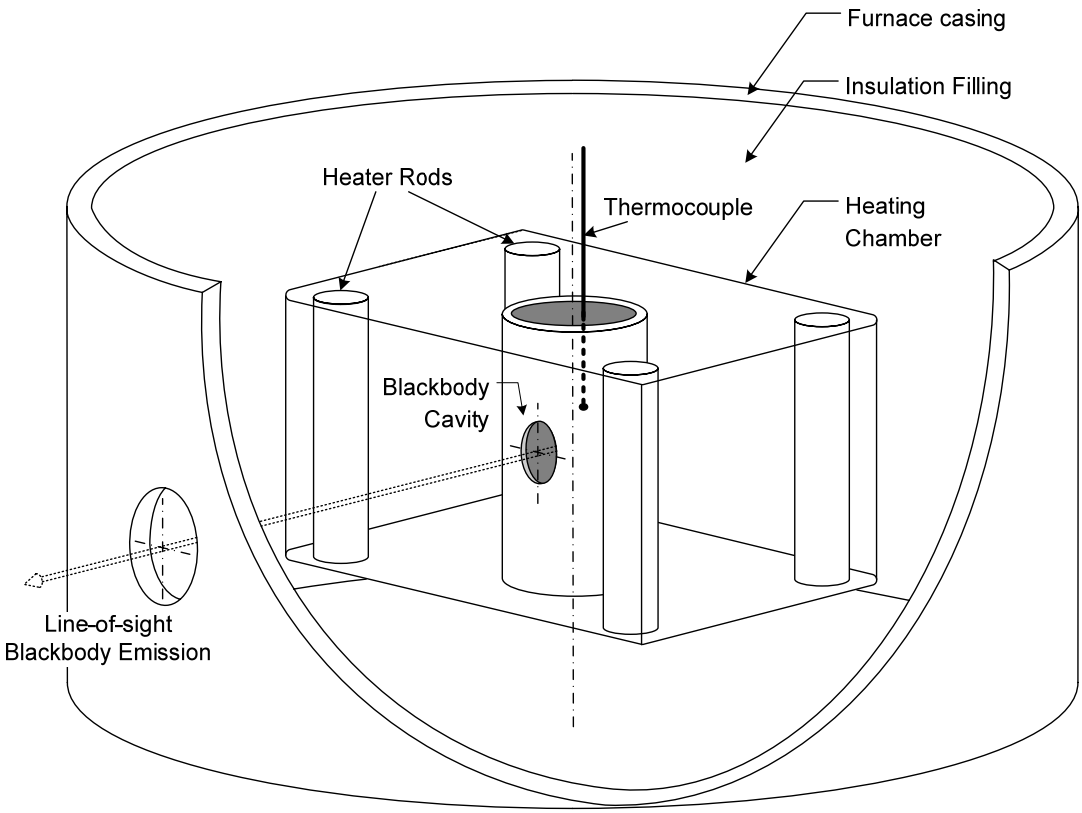

Figure 3.4. Blackbody furnace

3.2.3. Line-of-sight optics

The optical elements for collecting line-of-sight emission from a flame column consist of two iris diaphragms (Newport Corporation, Model ID-1.0) and an off-axis paraboloid reflector (Newport Corporation, Model OA-PARAB-1). Reflector wavelength range covers [0.2 – 10 μm] interval and hence it is appropriate for present experiments carried out within the near-infrared range. The elements are placed in a compartment which is mounted in line with focused source port of the spectrometer. Alignment is maintained via micrometric positioning elements.

As can be followed from the optical path illustrated in Figure 3.2 and Figure 3.5, collimated portion of the flame emission is bounded to a beam column by the Diaphragm A, the diameter of the beam being equal to the aperture. Then the beam is routed to the spectrometer by the off-axis paraboloid reflector which focuses the collimated beam to the centre of the Diaphragm B right in front of the spectrometer port. Diaphragm B is kept at smallest (pin-point) aperture so that only line-of-sight flame emission focused on the diaphragm enters the spectrometer.

3.2.4. Spectrometer

The FT-VisIR spectrometer used in this study is a Bruker IFS 66v/S system which is equipped with a high-throughput Michelson interferometer. Interior optical configuration of the spectrometer in connection with the exterior optical elements is displayed in Figure 3.5. When the focused beam enters the spectrometer, it is collimated by two mirrors and directed to the Michelson interferometer, operating principle of which is explained in 3.1.2. Modulated collimated beam is then sent to the sample compartment by a focusing mirror. The sample compartment is reserved for specimen analyses via transmission spectroscopy and remains idle for the present application of emission spectroscopy. Then the modulated beam enters the detector compartment where it is focused on the detector sensor.

The spectrometer can be configured for various spectral ranges from visible to mid-infrared ranges by using different combinations of detectors and beamsplitter. The configuration for the near-infrared region under focus in this study consists of a Germanium diode detector with a preamplifier and a CaF_2 beam splitter. Main specifications of the spectrometer configuration used in this experimental study are tabulated in Table 3.2.

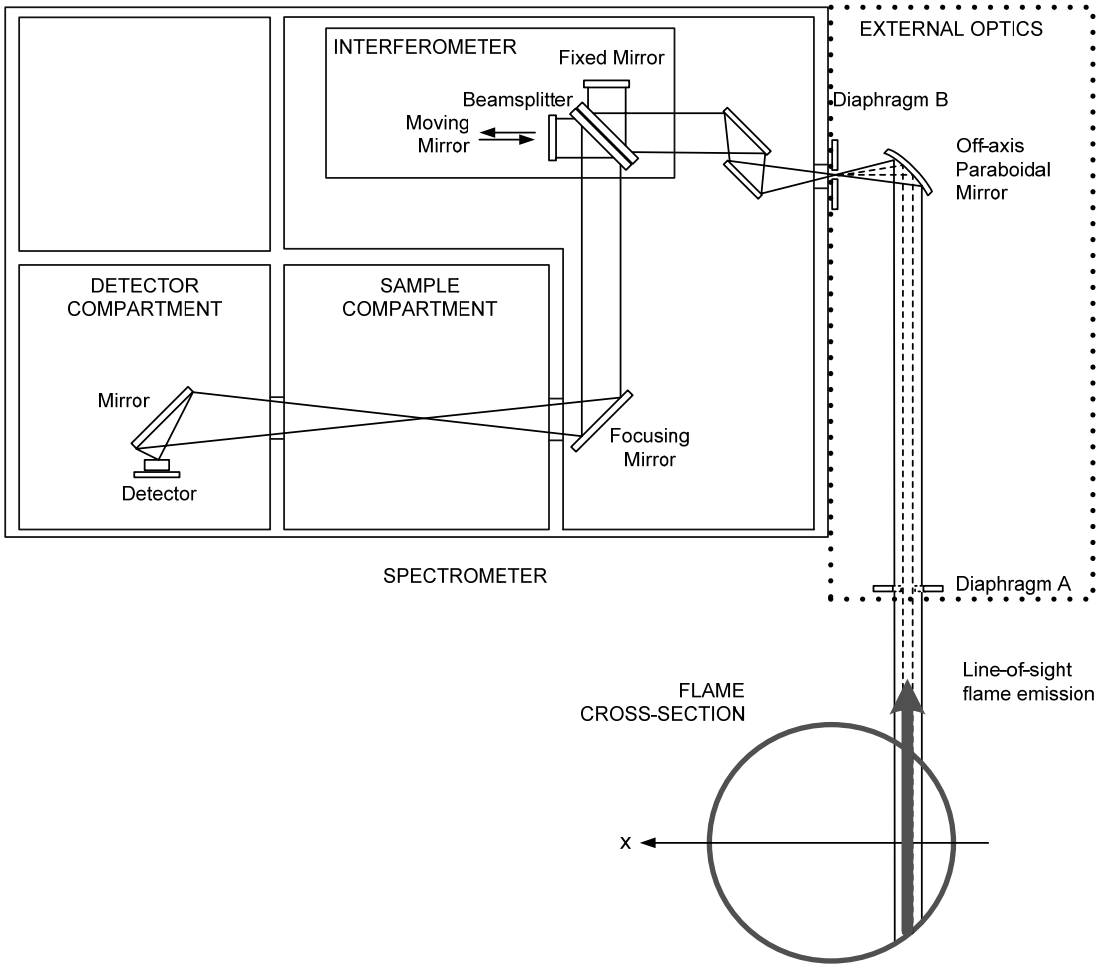

Figure 3.5. Optical path from the flame to the detector

Table 3.2. Specifications of the spectrometer configuration

Instrument	Bruker IFS66v/S extended for NIR analysis
Interferometer	High throughput Michelson interferometer with automatic alignment
Resolution	better than 0.25cm^{-1}
Beamsplitter	
Type	CaF_2 beamsplitter for UV-Vis-NIR (Model T602/6)
Design range	[55000-1500 cm^{-1}]
Detector	
Type	Germanium based photodiode (Model D425)
Design range	[15000-5300 cm^{-1}]
Alignment	Pre-aligned, mounted on dovetail slides
Sensitivity	NEP < 5×10^{-12} W Hz$^{-1/2}$
Operating temperature	Room temperature
Preamplifier gain	1-3

3.3. OPERATING CONDITIONS

The operating parameters of the spectrometer are presented in Table 3.3. Although the spectrometer is capable to achieve a spectral resolution as high as $\Delta\eta$ = 0.25 cm^{-1}, 25 cm^{-1} was determined as an optimum spectral increment as higher resolutions (smaller $\Delta\eta$) take longer recording time and they are not necessary as the study focuses on soot emission spectra which is well known to display continuum characteristics that can equally be captured by low resolution measurements. Longer measurement times required for higher resolutions pose a disadvantage from the viewpoint of possible dynamic changes in the flame. With the present settings, the measurement at each position takes approximately 1 minute for 256 scans.

Table 3.3. Spectrometer acquisition and data processing settings

Parameter	**Setting**
Effective spectral range	[12500-5200cm^{-1}]
Interferogram scan mode	Double-sided forward backward
Spectral resolution, $\Delta\underline{\eta}$	25 cm^{-1}
Number of scans	256
Scanner velocity	10 kHz
Total scan time	68 s
Apodization	Boxcar
Phase correction mode	Mertz
Phase resolution	50

Table 3.4. Burner operating parameters and flame properties

Parameter	**Value**
Fuel	Ethylene, C_2H_4
Purity	≥99.5%
Ambient temperature	22 ± 1° C
Ambient pressure	1.024 ± 0.003 bar
Fuel flow rate	18.3 ± 0.4 cm^3/s (corresponding to 65 ± 1.6 l/h air @ 20°C, 1 atm)
Exit velocity, u_0	5.8 cm/s
Re ($u_0.D_0$ / ν)	155
Visible flame height	91 mm
Visible flame width at HAB=30mm	9 mm

Table 3.5. Flame scanning parameters

Parameter	**Value**
Emission column width (diaphragm A aperture)	3 ± 0.2 mm
Horizontal spatial resolution	0.5 ± 0.2 mm
Vertical spatial increment	10 ± 0.5 mm

The fuel flow rate fixed for this study is determined by finding a compromise between flame luminosity and flame flickering. The higher the fuel flow rate, the brighter and larger the flame or in other words the higher the SNR and spatial resolution. On the other hand there is an upper limit in fuel flow beyond which the flame becomes sensitive to air circulations and further increase results in flame flickering. Although the flowrate was adjusted to same flowmeter scale during the measurements, the actual flowrate is dependent on the ambient temperature and pressure conditions. The fuel flow rate calibration procedure is given in Appendix E. It was found that the effect of ambient temperature and pressure variations cause ± 0.3 % uncertainty in flow rate which is negligible when compared to 5% instrument accuracy. Burner operating parameters and flame properties are summarized in Table 3.4 with uncertainty ranges. The flame under consideration, which is stable with these operating parameters, is pictured in Figure 3.6. Parameters associated to spatial flame scans are given in Table 3.5.

3.4. EXPERIMENTAL PROCEDURE

3.4.1. Blackbody measurements

1. Beam width is adjusted from diaphragm A in the external optics compartment (Figure 3.5).
2. The blackbody furnace is positioned at the burner location shown in Figure 3.5, in a way that the axes of the flame and blackbody will be coincident.
3. Alignment of the blackbody: The detector is replaced by a light source which comprises a horizontally mounted small light bulb. The light which follows the optical path demonstrated in Figure 3.5 in reverse direction provides a visible guide for alignment. Position of the furnace is aligned so that the circular projection of the guide beam from the spectrometer falls right at the centre of the cavity. Internal projection in the blackbody is checked by a dentist's mirror. Detector is replaced back into its compartment, spectrometer is turned on and the interferometer is aligned.
4. Furnace heating and cooling systems are turned on and blackbody temperature is raised gradually until the specified set temperature is attained.
5. Once the temperature is stabilized, blackbody spectrum is recorded.
6. Temperature is readjusted and step 5 is repeated.

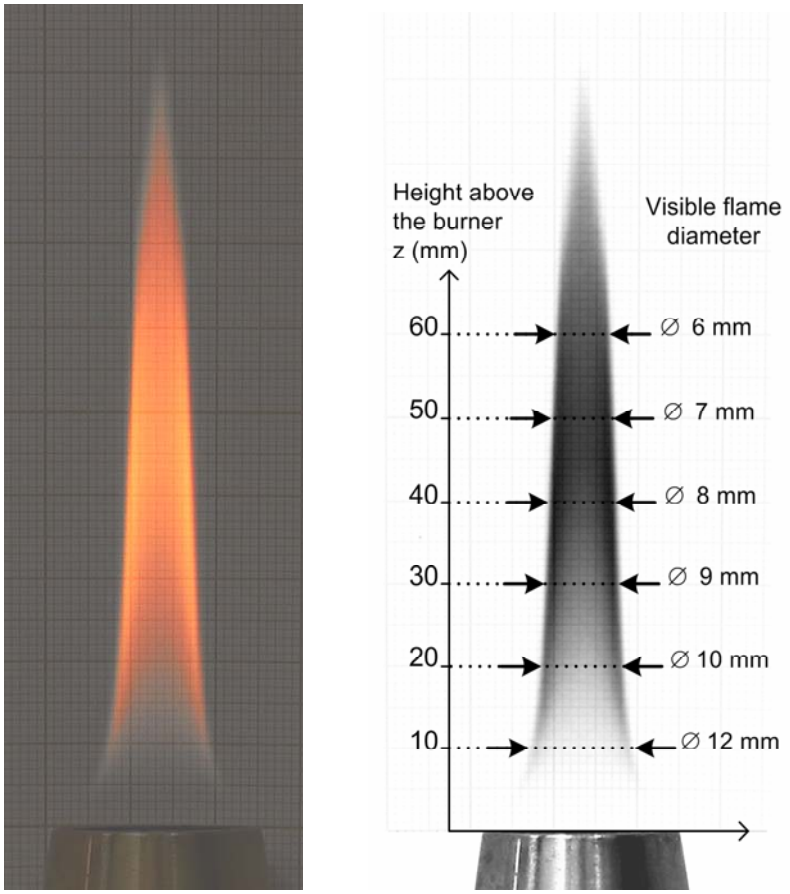

Figure 3.6. Ethylene diffusion flame analyzed in the experiments

3.4.2. Flame measurements

1. Ambient temperature and pressure conditions are recorded for fuel flow rate calculation.
2. Burner is installed at the source position same as blackbody. Aperture of Diaphragm A is left unchanged so that the flame measurements are at the same optical conditions as blackbody measurements.
3. Burner horizontal and vertical positions are aligned by using the guide beam as described in step 3 of blackbody measurements.
4. Flame is ignited; fuel flow rate is adjusted and allowed to stabilize. Flowrate and flame stability is constantly watched throughout the experiment.
5. Flame emission spectrum is recorded.
6. A consecutive measurement is realized at specific positions for noise analysis.
7. Horizontal burner position is readjusted to the adjacent position and spectrum is recorded. Flame is traversed horizontally by recording spectra at equally displaced positions.
8. Once the flame is scanned completely at one vertical position, the next altitude is adjusted and horizontal scans are repeated.
9. To validate the reproducibility, measurements at one height above the burner is independently repeated on a later experiment by setting same operating conditions and following the same procedure.

3.5. CALIBRATION OF INTENSITY SPECTRA

The spectra recorded by the spectrometer require calibration for two reasons. First, raw spectra involve emission/absorption effects of the optical elements along the path from flame to the detector and second, the spectra are recorded in instrument units by the spectrometer. In order to be able to isolate and eliminate the effects of instruments and to relate measured instrument units to physical units of intensity, calibration is carried out by recording spectra from a well-defined reference source which is a blackbody cavity in the present study. Theoretical evaluation of reference measurement from known source properties enables derivation of a calibration relation called *instrument function* which relates a raw spectrum recorded in instrument units (IU) to emission intensity spectrum in physical units.

The spectrum recorded by the spectrometer, S_η, involves emission by the optical components, G_η , as well as source emission received by the detector, which is directly dependent on the diaphragm A's aperture cross-section, A_A, spectral emission intensity of the source, I_η , and spectrometer's response function, R_η . Figure 3.7 illustrates the components of detected energy. Therefore for any emission spectrum measurement, S_η can be represented as

$$S_\eta = G_\eta + A_A \cdot R_\eta \cdot I_\eta \text{, [IU]} \tag{3.1}$$

G_η can easily be measured by blocking the source (by inserting an opaque and cold sheet between the source and diaphragm A) and recording internal emission due to optical components.

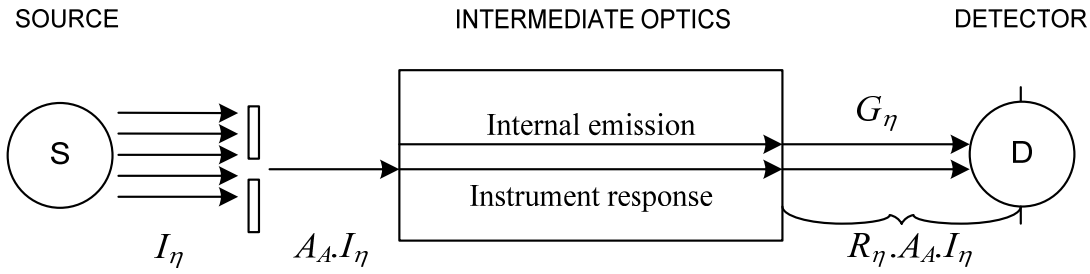

Figure 3.7. Components of detected energy

Instrument function of the spectrometer can obtained from

$$R_\eta = \frac{S_{\eta,\mathrm{b}} - G_{\eta,\mathrm{b}}}{A_{A,\mathrm{b}} \cdot I_{\eta,\mathrm{b}}} \ , \left[\frac{\mathrm{IU}}{\mathrm{W}/(\mathrm{m}^{-1} \cdot \mathrm{sr})} \right] \tag{3.2}$$

where $S_{\eta,\mathrm{b}}$ and $G_{\eta,\mathrm{b}}$ are spectra obtained from blackbody measurements, $A_{A,b}$ is the diaphragm opening during blackbody experiments and $I_{\eta,b}$ is the theoretical line-of-sight spectral emission intensity for a blackbody temperature T_b which is given by the Planck's function as follows [24]

$$I_{\eta,\mathrm{b}} = 2n^2 h c_0^2 \frac{\eta^3}{\left[\exp\left(hc_0 \eta / nkT_\mathrm{b} \right) - 1 \right]} \ , \left[\frac{\mathrm{W}}{\mathrm{m}^2 \cdot \mathrm{sr} \cdot \mathrm{m}^{-1}} \right] \tag{3.3}$$

where h, k and c_0 are Planck's constant, Boltzmann's constant and speed of light in vacuum, respectively; η stands for the wavenumber (in SI units here) and n is the refractive index of the surrounding medium which can be taken as unity for air at room temperature.

Once the instrument function is available, the intensities of arbitrary sources can be evaluated from measured spectra S_η and G_η by using the following relation

$$I_\eta = \frac{S_\eta - G_\eta}{A_A \cdot R_\eta} \ , \left[\frac{\mathrm{W}}{\mathrm{m}^2 \cdot \mathrm{sr} \cdot \mathrm{m}^{-1}} \right] \tag{3.4}$$

During the course of the flame emission measurements, raw spectra recorded at each measurement point are calibrated by the above equation to obtain line-of-sight flame emission intensities. Emission spectrum calibration presented in this section are based on the same principles as those presented by Lindermeir *et* al. [135] and Bourayou *et* al. [130].

3.6. RESULTS AND DISCUSSION

3.6.1. Blackbody measurements and instrument function

Blackbody measurements were carried out at blackbody temperatures which are expectedly close to flame temperature. T_b = 1402 °C and 1502 °C were selected working temperatures as they are exact settings at which the blackbody was calibrated by a pyrometer. Raw spectra obtained from the blackbody measurements are displayed in Figure 3.8. Superimposed on

the same plot are the theoretical blackbody intensities obtained from Planck's function in Eq. (3.3) for corresponding temperatures. Within the present spectral range, it was observed that instrument emission is not significant, resulting in $G_{\eta,b} = 0$. Evaluation of response functions from Eq. (3.2) for both temperatures yields coincident instrument functions displayed in Figure 3.9. In the present analysis, the response function obtained from T_b = 1502 °C is utilized for calibration. From the inspection of the instrument function, the spectral window that provides most suitable data for property reconstruction seems to be 8500-7500 cm^{-1} (1.33-1.18 μm) range as there is a smooth response function in this range, free from absorption bands and sharply decreasing low response levels which both degrade signal quality.

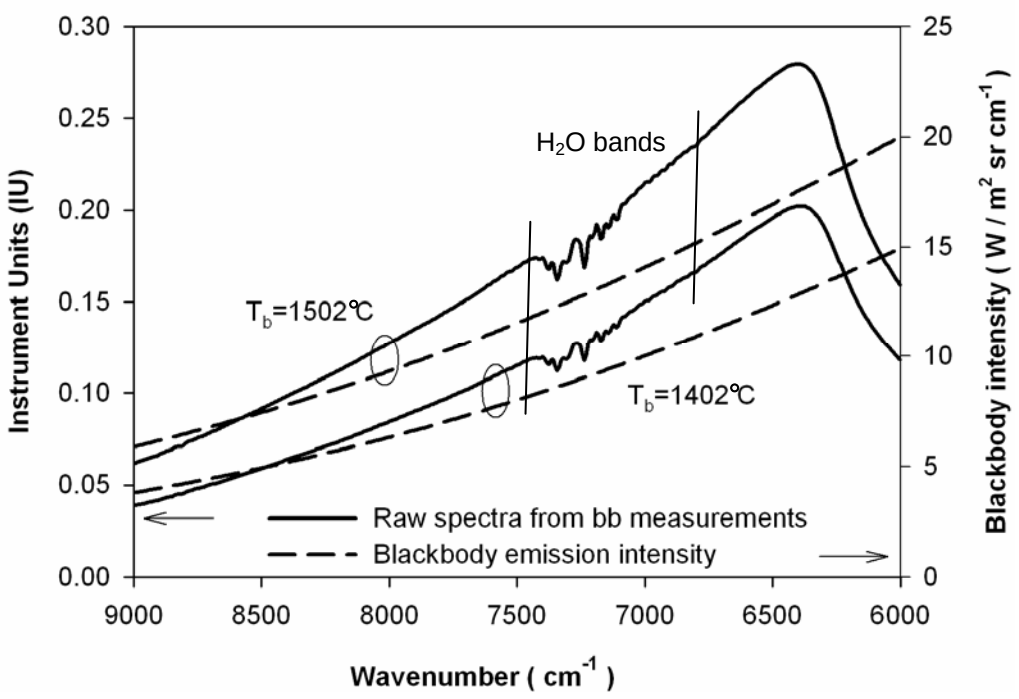

Figure 3.8. Raw spectra and theoretical intensity spectra for blackbody measurements

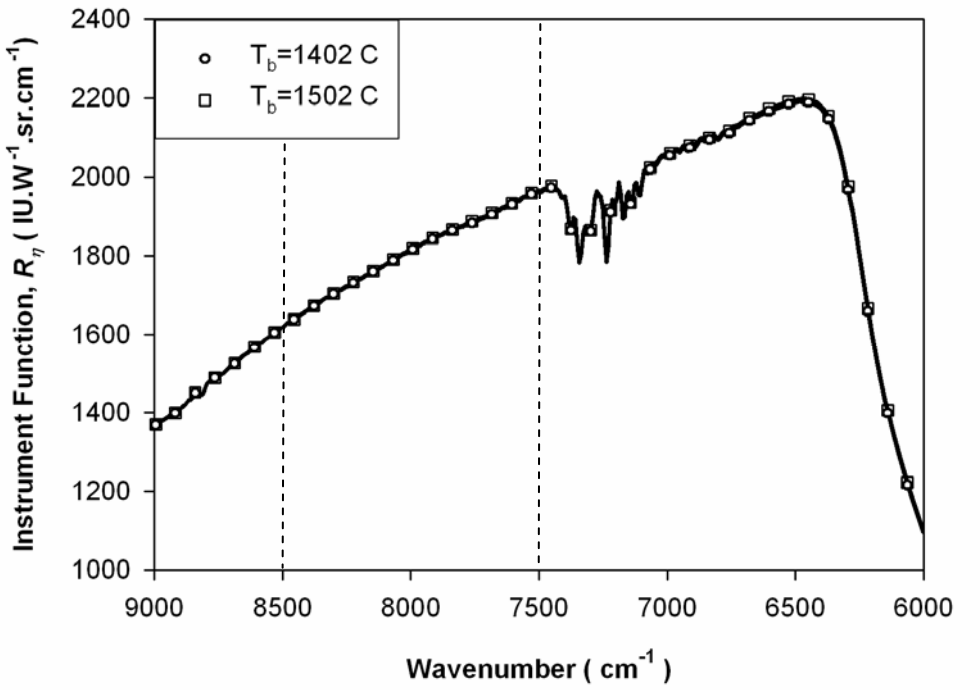

Figure 3.9. Instrument function

3.6.2. Flame emission measurements

Measurements on the flame were conducted with the procedure and operating conditions presented in previous sections. A sample raw spectrum recorded by the spectrometer in instrument units is given in Figure 3.10 for a measurement point with 30 mm height above the burner and x = 10.5 mm lateral position which corresponds to x_0 = 3 mm lateral distance from flame centre. Calibration of this raw spectrum as described before provides the absolute emission intensity spectrum corresponding to same location (Figure 3.11).

Absolute flame emission intensities for each position throughout the flame are displayed in Figure 3.12. At 10 mm above the burner the intensity profile along the lateral axis displays a minimum at the centre and two maxima next to the centre. This behavior near the nozzle exit is associated with soot concentration which is expectedly larger at the reaction zone, towards the lean zone and almost none at the centre which is the fuel rich region. The two peaks get closer and the profile evolves to a parabolic profile as we go downstream to higher positions

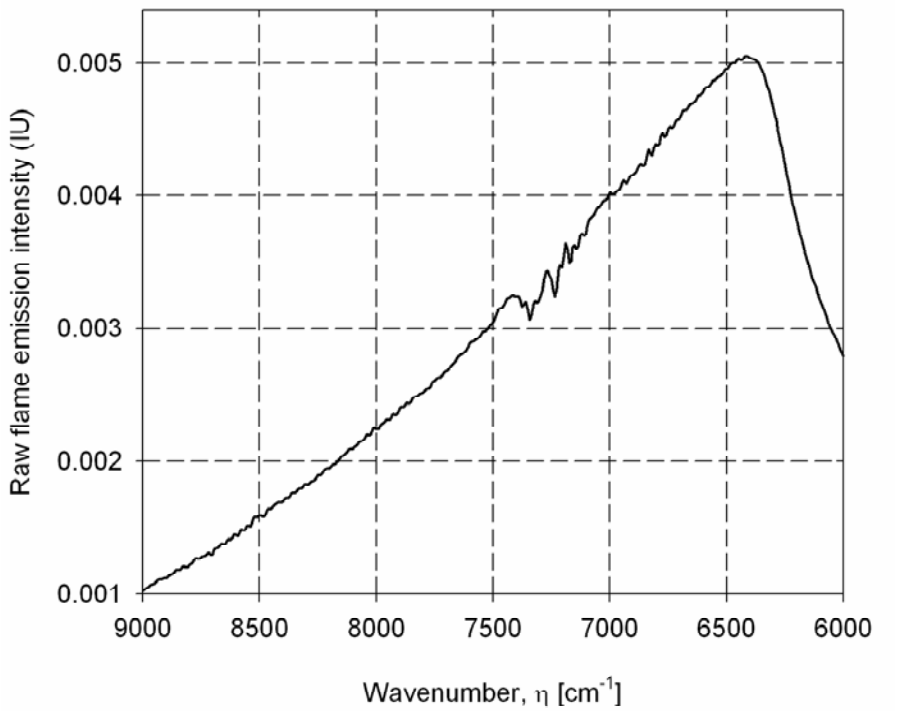

Figure 3.10. Raw data for flame emission spectrum recorded at z = 30 mm, x_0 = 3 mm

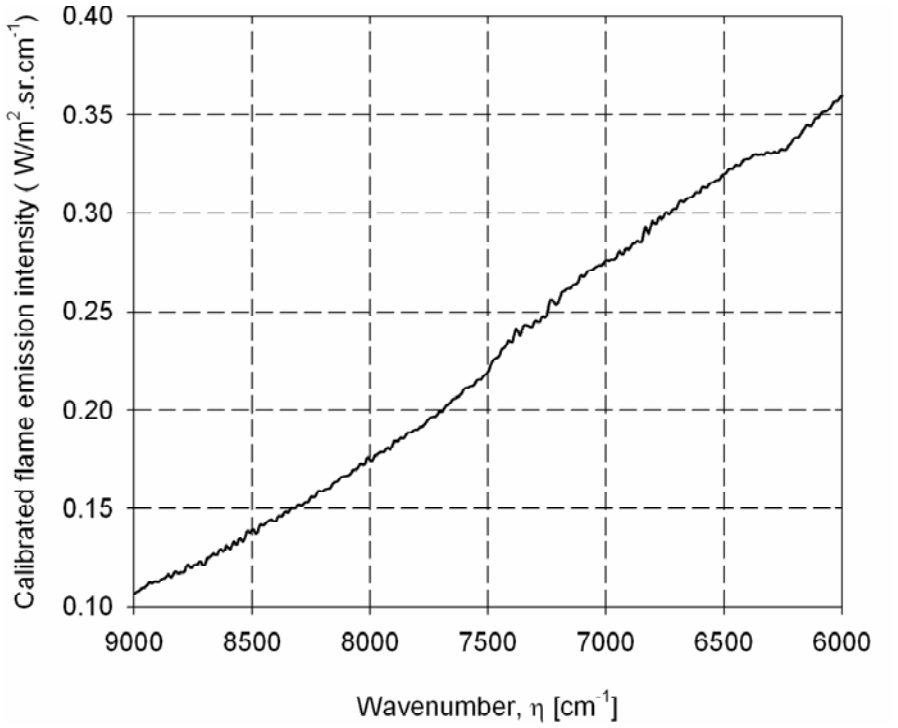

Figure 3.11. Calibrated flame emission spectrum at z = 30 mm, x_0 = 3 mm

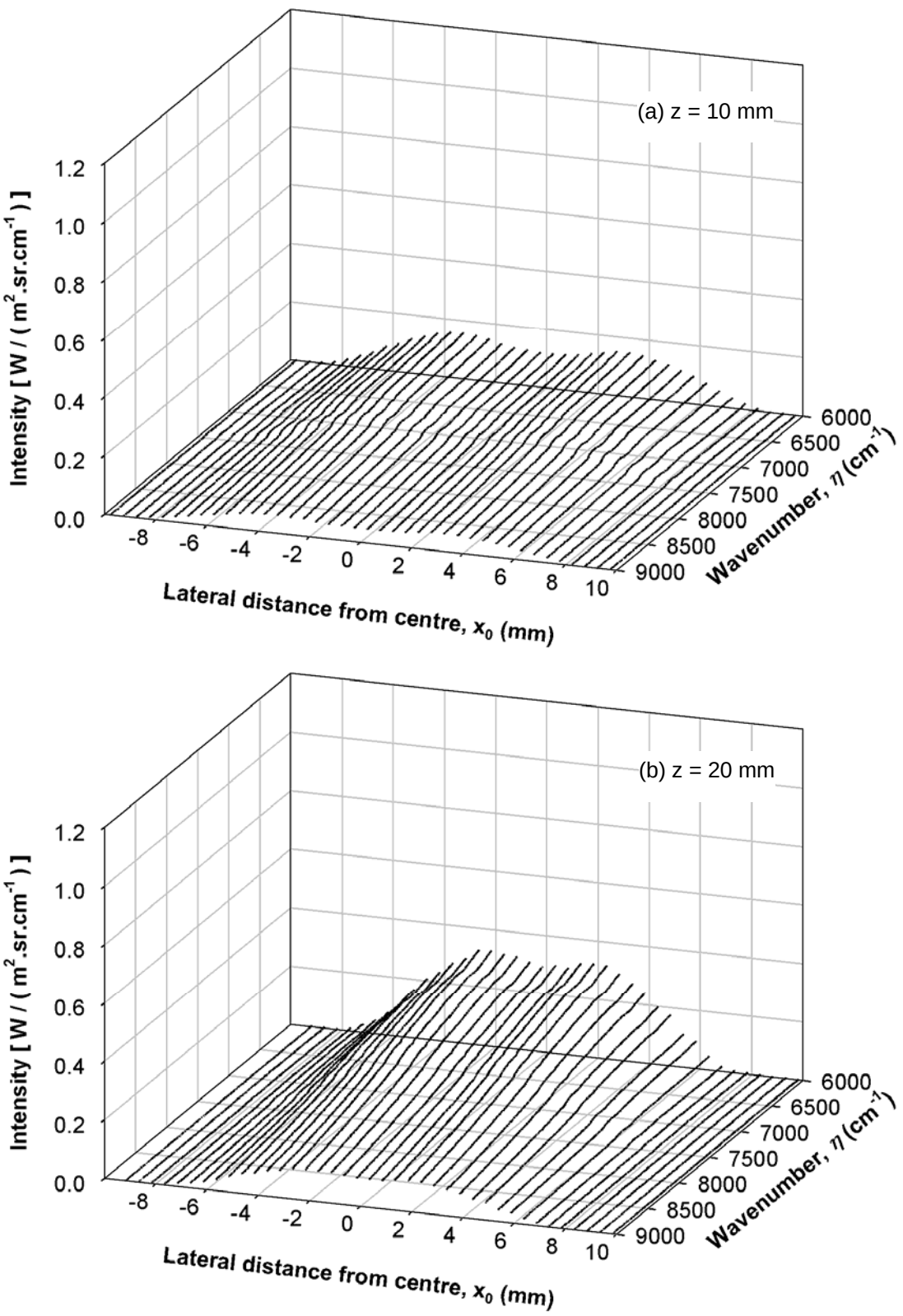

Figure 3.12. Flame emission intensity spectra throughout the flame

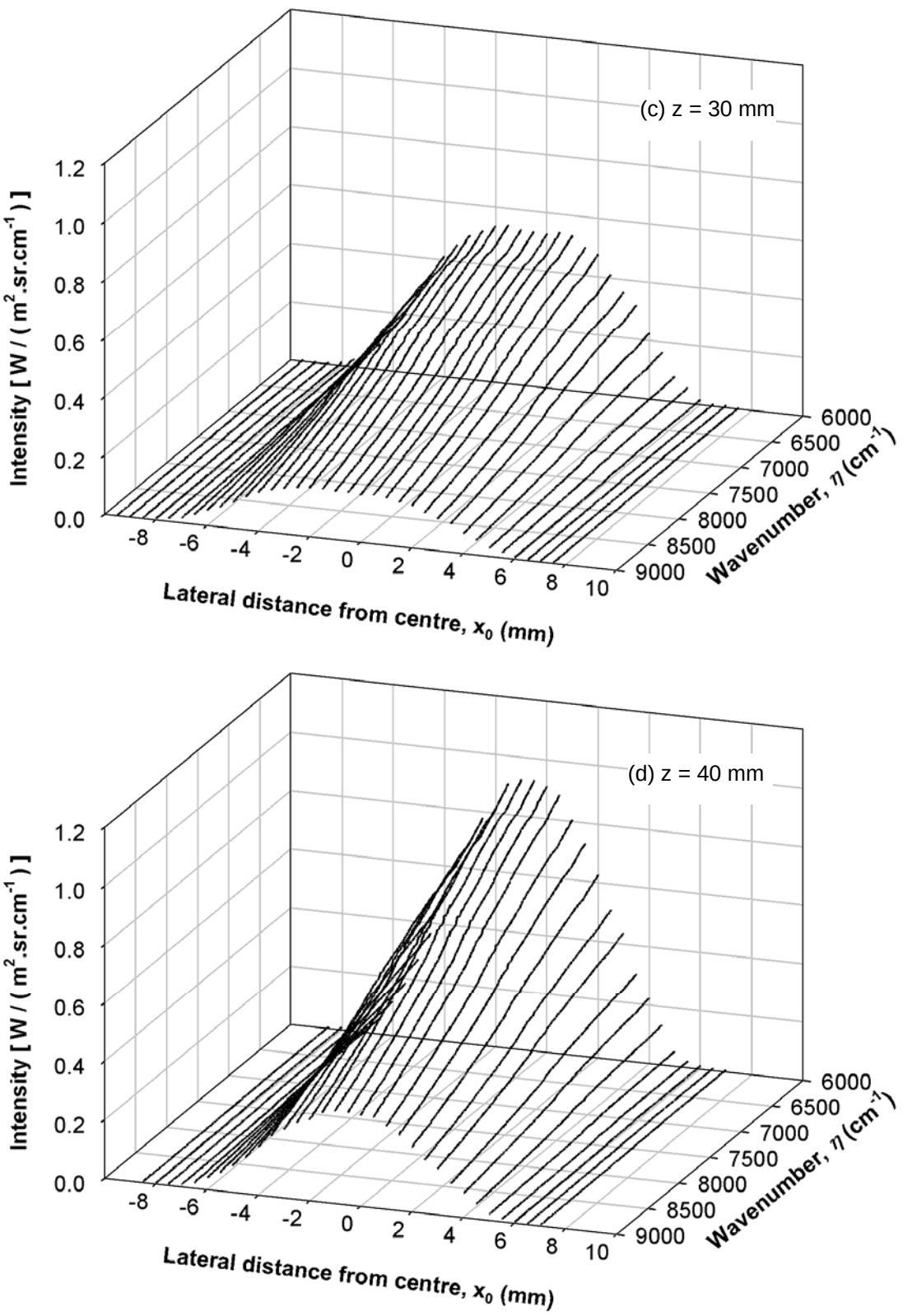

Figure 3.12. Flame emission intensity spectra throughout the flame (cont.)

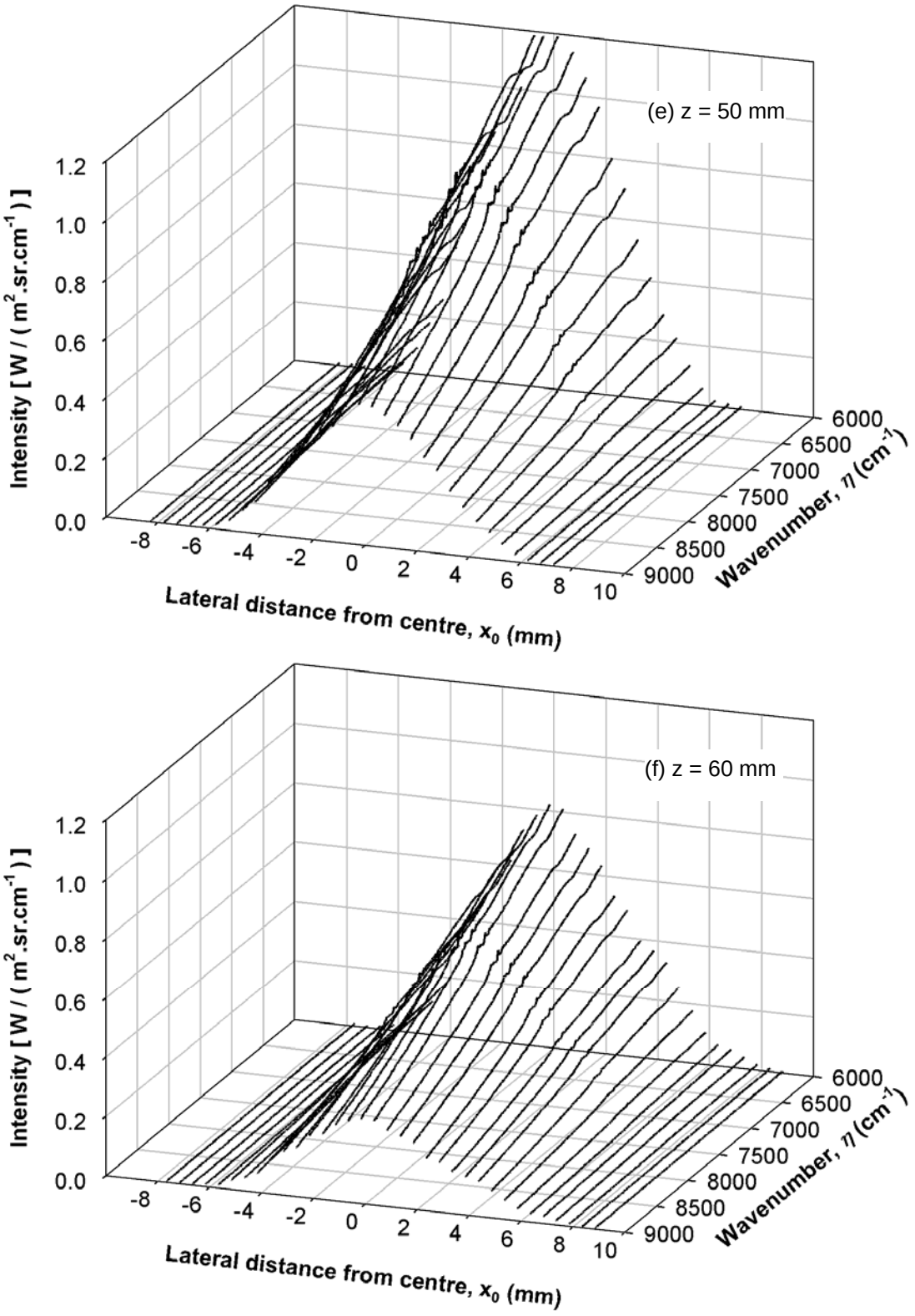

Figure 3.12. Flame emission intensity spectra throughout the flame (cont.)

probably because the reaction zone ring gets narrower and soot concentration increases. At the vertical position of z = 50 mm, the intensities are largest which is probably because this height corresponds to the high temperature region and/or high soot concentration region in the flame. Therefore, from a preliminary visual inspection it can be said that emission intensity measurements throughout the flame follow physically reasonable trends. Detailed analysis of these data to infer soot properties is to be carried out in the following chapter.

The objective of present experimental study is met by the set of intensity spectra which yields the input to the soot property reconstruction application described in the following chapters. However, for a complete experimental record, it is important to analyze and report the noise, error levels and reproducibility of the measurements, which is rarely elaborated in similar experimental studies in the literature. Following sections in this chapter are devoted to assessment of these issues.

3.6.3. Noise analysis

Noise is an unavoidable component of every instrumental measurement. It is basically composed of randomly fluctuating extraneous information embedded in the signal which constitutes the stream of desired information. Overall noise in a measurement reflects the combined effects of instrumental and environmental disturbances, as well as the uncontrollable variables that alter the properties of the sample itself. Comprehensive texts on origins of noise for instrumental analysis in general and for Fourier transform spectroscopy in particular are available by [124] and [120], respectively.

Quantification of noise is essential for a complete experimental record as it indicates the quality of the measurement. In the present study, the measurements are utilized for property reconstruction and hence characterization of noise is also required for determination of the degree of uncertainty introduced to inferred soot characteristics.

Conventional figure of merit for describing the noise level is signal-to-noise ratio (SNR). There are various methods for determination of SNR. Griffiths and de Haseth [120] describe how to forecast SNR in Fourier Transform Spectroscopy from instrument specifications. This method requires knowledge of detailed instrument and measurement properties such as efficiency, detector area and measurement time which are not all reported in standard specifications and measurement parameters provided by the manufacturers. The method is

proposed as an a priori estimate on the actual SNR as it considers only the detector noise and excludes environmental and sample effects. Combined noise can be taken into account by a statistical analysis of measured spectra.

Noise level involved in a spectroscopic measurement is commonly analyzed on the 100% line [120, 136] which is obtained by recording two single beam spectra consecutively at same controllable conditions and calculating their % ratio. Ideally, in the absence of noise the resulting spectrum would be a constant line at 100%. Standard deviation from the 100% line provides a measure of noise. Different approaches for determination of standard deviation of 100% line are reviewed by Mark and Workman [136]. First and simplest method is to compute peak to peak difference in the 100% line and assuming normal distribution for random error, one fifth of the peak to peak difference provides an estimate of the standard deviation with 99% confidence level. Upon a survey carried out among FT-IR spectrometer manufacturers, Mark and Workman [136] report that this approach as the most commonly deployed one. The second approach is the conventional definition of sample standard deviation, i.e., root mean square (RMS) of deviation from the mean. Another approach is based on fitting a line to the 100% line and estimating noise from the RMS of deviation from the fitted line. Method of successive differences proposed by Mark and Workman [136] is based on estimation of standard deviation from the RMS of differences of adjacent spectral data in the 100% line. The fifth approach, which is suggested by Mark and Workman as the most rigorous approach for SNR determination, takes possible spectral variation of noise into consideration. Different from the previous approaches which involve two consecutive measurements, this method is based on recording a larger number of spectra at same controllable conditions and computing standard deviation separately for each spectral variable to obtain a noise spectrum. For the present application this approach is not suitable as it increases the measurement time considerably and this is an important disadvantage from the viewpoint of spatial scanning of a dynamic system such as a flame.

Mark and Workman [136] compared three standard deviation estimation methods which are based on RMS of *i*) differences from mean (conventional equation), *ii*) differences from fitted line and *iii*) successive differences. They concluded that the method of successive differences which avoids inflation of noise figure by possible nonflatness of the 100% line is a more reliable way to estimate spectral noise reproducibly as the effects of systematic errors are eliminated. This finding was also confirmed by Bak and Clausen [137] who recommend use of the method of successive differences upon a comparison against conventional

standard deviation approach and the simplest method based on one-fifth of peak-to-peak difference. Under the light of these two previous analyses, method of successive differences formulated below was deployed in the present study to estimate RMS values representing spectral noise levels of each spectrum.

100 % line is evaluated by taking the ratio of two consecutive measurements, S_1 and S_2

$$X_i = \frac{S_{1,i}}{S_{2,i}} \times 100 \tag{3.5}$$

where i stands for the index for spectral variable varying between 1 and NW which is the total number of wavenumbers within the spectral range under consideration. According to the method of successive differences, RMS value which is equivalent to relative noise is calculated from [136]

$$\mathrm{RMS} = \sqrt{\frac{\sum_{i=1}^{NW-1} \left(X_{i+1} - X_i \right)^2}{2\left(NW - 1 \right)}} \tag{3.6}$$

Then the signal-to-noise ratio is obtained from [120]

$$\mathrm{SNR} = \frac{100}{\mathrm{RMS}} \tag{3.7}$$

As SNR is variable along the whole measurable spectrum, only the spectral range used for soot diagnostics is analyzed in terms of noise. A set of consecutive spectra recorded at z = 30 mm height above the burner and x_0 = 3 mm lateral distance from the flame axis is displayed in Figure 3.13 for [7500 - 8500 cm^{-1}] spectral range. Corresponding 100% line is given in Figure 3.14 where the mean, the RMS and SNR are also displayed. As can be seen from the figure, the mean of the 100% line is not exactly at 100 but there is an offset of 2.84 % caused by an uncontrollable variation (such as flame flickering) while recording the two consecutive spectra. When compared with relative RMS noise level of 0.35 %, it is evident that the unsteady disturbances that cause offset variations in spectra have considerable effect on

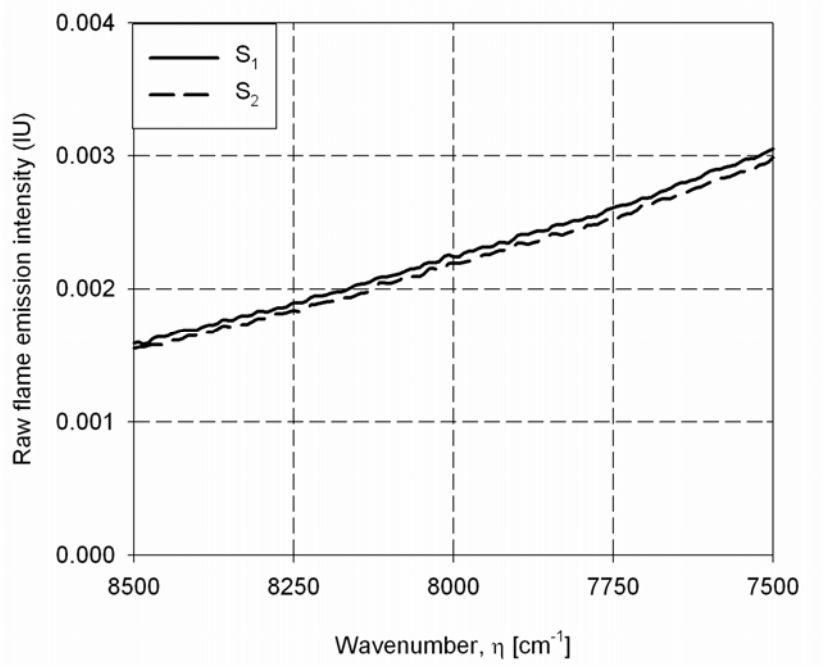

Figure 3.13. Two consecutive spectra recorded at z = 30 mm, x_0 = 3 mm

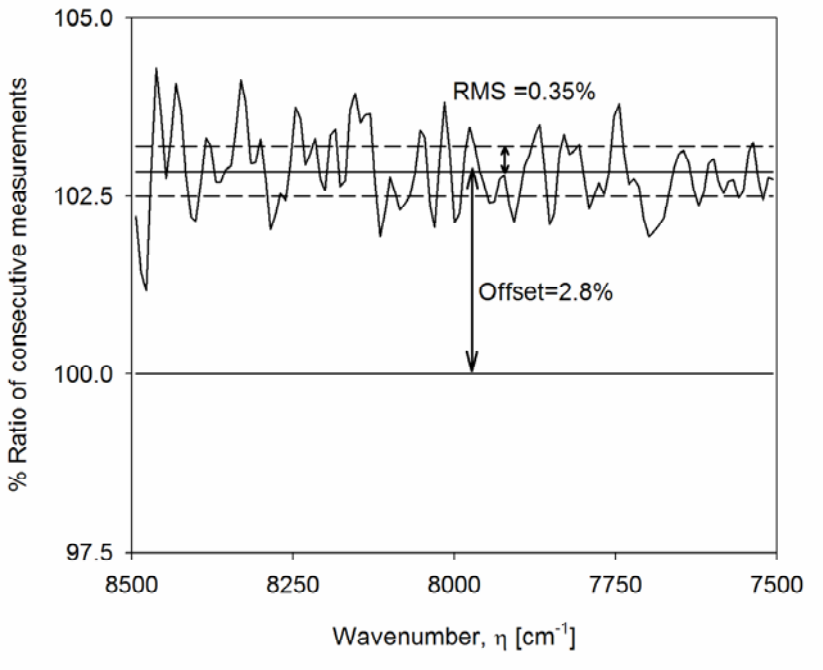

Figure 3.14. 100 % line at z = 30 mm, x_0 = 3 mm, η = 7500-8500 cm^{-1}

measured intensities and need to be taken into consideration in the error analysis. In order to report the offset level in analogy with spectral noise level, signal-to-offset ratio (SOR) is evaluated from

$$\mathrm{SOR} = \frac{100}{\left|100 - \bar{X}\right|} \tag{3.8}$$

SNR and SOR figures obtained at several lateral and vertical positions throughout the flame are plotted in Figure 3.15. Although there is not a clear functional dependence on spatial variables, general trends indicate that both figures are strongly dependent on signal level, i.e. they increase towards the flame center where signal level is higher due to more powerful emission. As can be followed from the plots, SOR levels are usually smaller than SNR values which indicate that the effect of offset is usually more than the effect of spectral noise. Therefore considering only spectral noise during error analysis would misleadingly underestimate actual noise levels.

In order to be able to deduce a general margin of noise and offset for all measurements throughout the flame, absolute noise is analyzed rather than relative noise elaborated in 100 % line. Absolute noise spectrum is obtained by evaluating difference between two consecutive measurements

$$Y_i = S_{1,i} - S_{2,i} \tag{3.9}$$

Representative absolute noise spectrum corresponding to the same spatial and spectral parameters as the 100% line above is provided in Figure 3.16. Ideally in the absence of noise, the resulting data would be a constant at zero. Standard deviation is estimated from successive differences method given in described above. The offset is obtained from the mean of the differences. The offset is linearly dependent on wavenumber and as can be followed from Figure 3.13 and Figure 3.16, it is directly proportional to the signal level. However, for the sake of simplicity, mean is considered to represent the offset level adequately.

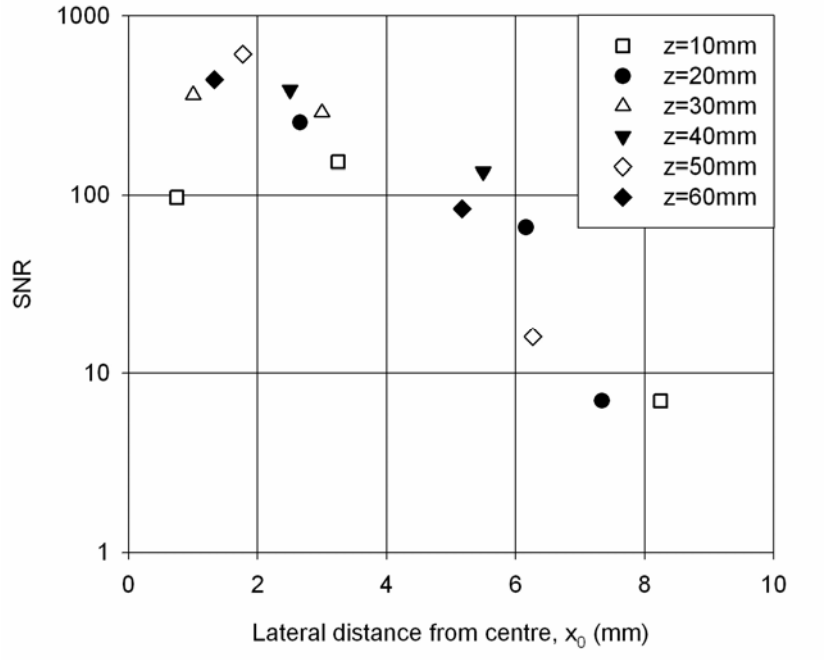

(a) Signal-to-noise ratio

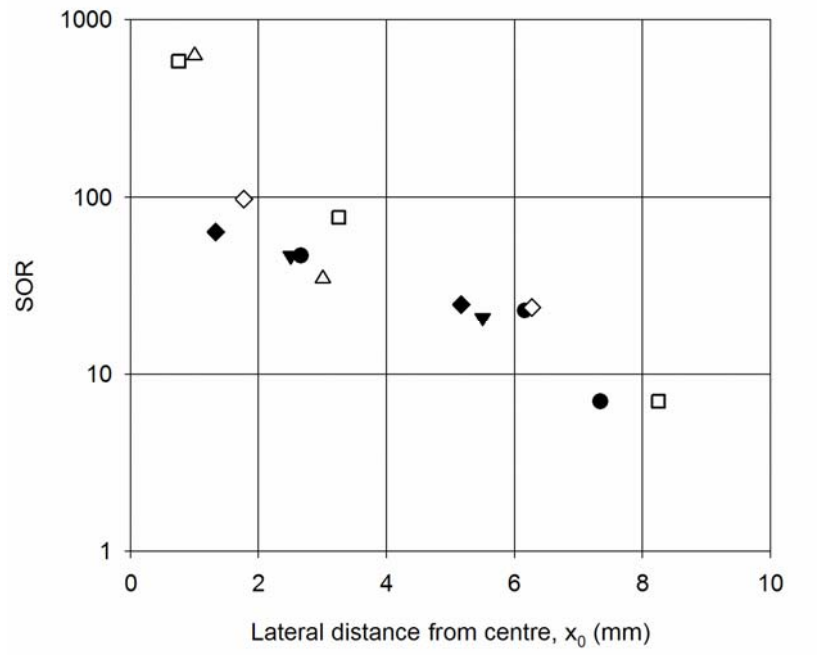

(b) Signal-to-offset ratio

Figure 3.15. SNR and SOR distributions throughout the flame

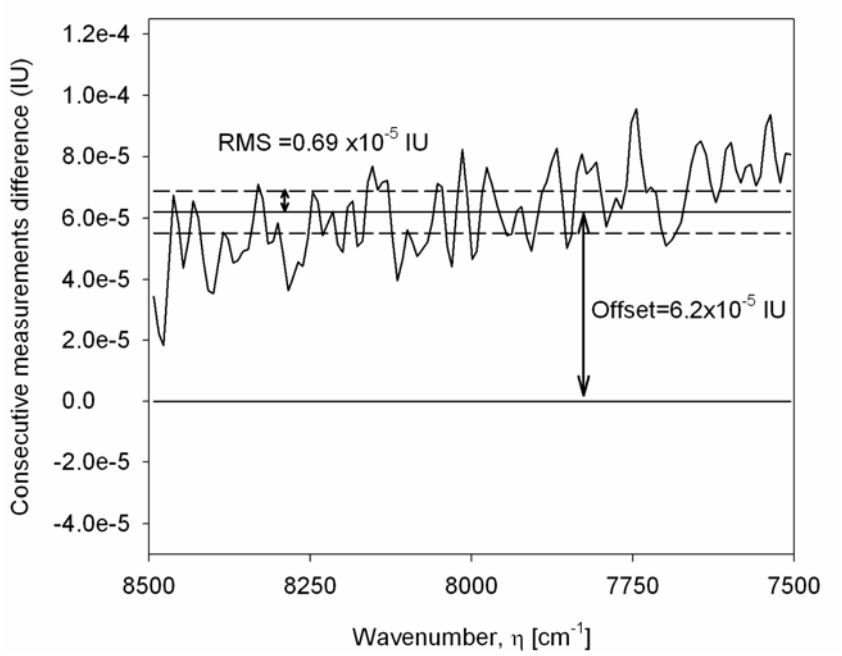

Figure 3.16. Absolute noise at z = 30 mm, x_0 = 3 mm, η = 7500-8500 cm^{-1}

The RMS values calculated for each absolute noise spectrum represent level of random errors in spectral domain. Figure 3.17 shows spectral noise and offset distributions throughout the flame. It is clear from Figure 3.17-a that spectral noise levels are of the same order of magnitude throughout the flame and can be characterized by the mean value 0.9×10^{-5}. This observation shows that spectral noise invokes a systematic effect along the spatial domain. On the other hand, the offsets are systematic errors in spectral domain, i.e., they are constant along the spectrum but they fluctuate along the spatial domain as shown in Figure 3.17-b. Similar to the previous practice deployed to characterize random error in spectral domain, standard deviation of the offsets along the lateral axis quantifies spatial noise level. As can be seen from the figure, the offset levels at $x_0 > 6$ mm region, which corresponds to the flame edge zone, are lower than the central region. To avoid overestimation of errors at flame edges, these two zones are treated separately in terms of offset noise levels. When Figure 3.17-a and b are compared, it is evident that spectral noise and spatial noise are independent from each other. This enables evaluation of their combined effect by taking root of sum of squares of their absolute standard deviations.

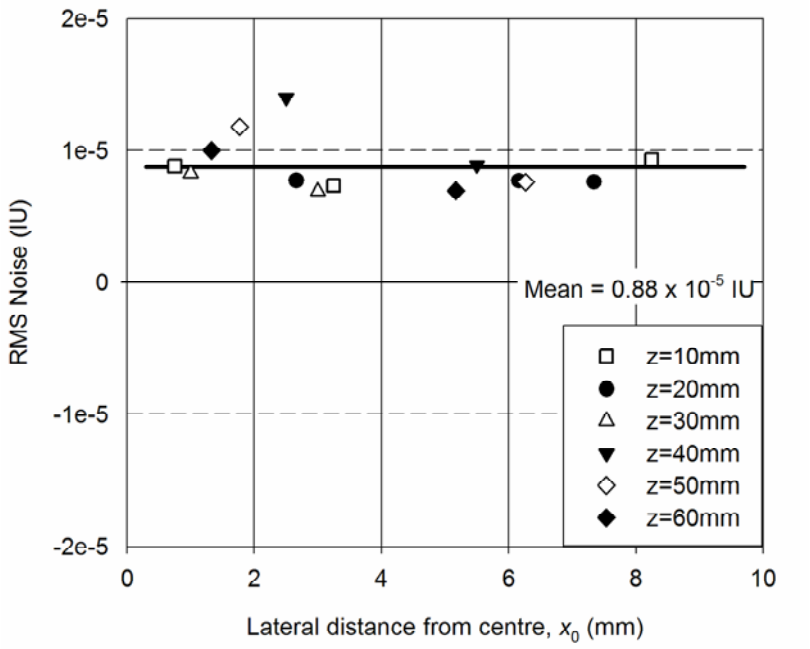

(a) Absolute spectral noise levels

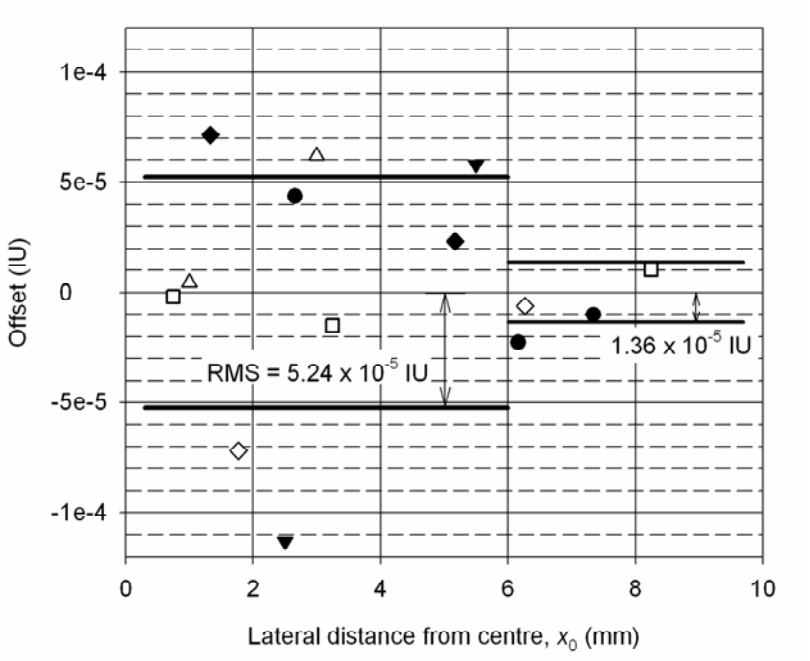

(b) Absolute offset levels

Figure 3.17. Absolute noise and offset distributions throughout the flame

Table 3.6. Noise characteristics of flame emission spectra, S_η

Spectral Noise		
SNR	7 – 609 [a]	
Mean RMS	0.88×10^{-5} IU	
Spatial Noise (offset)	$x_0 < 6$ mm	$x_0 > 6$ mm
SOR	20 – 630 [a]	7 – 20 [a]
RMS of average offset	5.24×10^{-5} IU	1.36×10^{-5} IU
Combined noise level (RMS), σ_s	5.31×10^{-5} IU	1.62×10^{-5} IU
99% confidence interval ($\Delta S_\eta = 2.58\times\sigma_s$)	$\pm 13.7\times10^{-5}$ IU	$\pm 4.18\times10^{-5}$ IU

[a] depends on signal power which is variable throughout the flame

Table 3.7. Noise characteristics of blackbody emission spectrum, $S_{\eta,b}$

Spectral Noise	
SNR	8202
RMS	1.35×10^{-5} IU
Offset	
SOR	309
Offset	37.8×10^{-5} IU
Combined noise level (RMS), σ_{sb}	37.8×10^{-5} IU
99% confidence interval ($2.58\times\sigma_{sb}$)	$\pm 97.5\times10^{-5}$ IU

Noise characteristics of the measurements with the present instrumental, environmental, flame and blackbody conditions are reported in Table 3.6 and Table 3.7 for flame emission spectra and blackbody emission spectrum, respectively. It turns out that spatial offsets which are generally overlooked in noise analyses are dominant over spectral noise for both flame and blackbody measurements. This highlights the importance of offset analysis for reliable characterization noise levels of emission spectra. The noise analysis procedure developed here in terms of absolute noise provides noise characteristics of the whole system concisely as summarized in the above tables and can easily be used in uncertainty analyses whereas conventional relative noise analysis based on SNR results in noise characteristics that are strictly dependent on measurement location.

3.6.4. Uncertainty analysis

Experimental errors which determine the uncertainty levels of flame emission intensity measurements are not limited to spectral and spatial noise involved in spectrometer recordings. As explained in section 3.5, intensities are obtained from a calibration relation equation (Eq. (3.4)) which is a function of a number of additional measured quantities. Dependence of this expression on measured quantities can be resolved by substituting Eqs. (3.2) and (3.3) in Eq. (3.4). Rearranging gives

$$I_\eta = 2hc_0^2\eta^3 \cdot \frac{A_{A,b}}{A_A} \cdot \frac{S_\eta}{S_{\eta,b}} \cdot \left[\exp\left(\frac{hc_0\eta/k}{T_\mathrm{b}} \right) - 1 \right] \tag{3.10}$$

where measured quantities are: (i) cross-sectional areas of diaphragm openings during blackbody and flame experiments, $A_{A,b}$ and A_A, (ii) blackbody and flame emission, $S_{\eta,b}$ and S_η, and (iii) blackbody temperature, T_b. As noted in the 2nd item of flame emission measurement procedure, diaphragm openings adjusted for blackbody measurements were not altered during flame emission experiments. This enables cancellation of area terms as they are equal and essentially involve the same level of uncertainty. If the apertures had been set independently even to equal openings, their error terms would be independent and it would be essential to consider uncertainties of these cross-sectional areas individually, each of which is estimated to involve about 13% error, with a combined effect of 19% error on final intensities. This emphasizes the important effect of setting the beam width once and for all throughout the whole series of measurements for improved measurement accuracy. Having eliminated the area terms, the remaining 3 measurements determine the uncertainty levels of flame emission intensity measurements.

When an instrumental analysis technique involves a number of intermediate experimental measurements, the uncertainty margins of each measurement contribute to the net indeterminate error of the final outcome. Let y represent the final result and x_i denote the intermediate measurements, where i = 1, 2, 3,…, n; n being the total number of measurements and y being a function of $x_1, x_2, x_3, \ldots, x_n$

$$y = f(x_1, x_2, ..., x_n) \tag{3.11}$$

If each measurement , x_i , involves a random error independently fluctuating with a standard deviation of σ_{xi} , standard deviation of the combined error for the final outcome is given as [124]

$$\sigma_y^2 \simeq \left(\frac{\partial y}{\partial x_1}\right)^2_{x_i, i\neq 1} \sigma_{x_1}^2 + \left(\frac{\partial y}{\partial x_2}\right)^2_{x_i, i\neq 2} \sigma_{x_2}^2 + \ldots + \left(\frac{\partial y}{\partial x_n}\right)^2_{x_i, i\neq n} \sigma_{x_n}^2 \tag{3.12}$$

The uncertainty limits of y can then be expressed as $y = y \pm \Delta y$ where Δy is the uncertainty half width estimated as $2.58\sigma_y$ for 99% confidence interval [124]. As uncertainty limit is directly proportional to standard deviation, the above equation in terms of standard deviations equally applies to uncertainty limits as follows

$$\Delta y^2 = \left(\frac{\partial y}{\partial x_1}\right)^2_{x_i, i\neq 1} \Delta x_1^{\,2} + \left(\frac{\partial y}{\partial x_2}\right)^2_{x_i, i\neq 2} \Delta x_2^{\,2} + \ldots + \left(\frac{\partial y}{\partial x_n}\right)^2_{x_i, i\neq n} \Delta x_n^{\,2} \tag{3.13}$$

Implementation of this error propagation principle to present measurements leads to the following equation for combined error limits

$$\Delta I_\eta^{\,2} = \left(\frac{\partial I_\eta}{\partial S_\eta}\right)^2_{S_{\eta,b}, T_b} \Delta S_\eta^{\,2} + \left(\frac{\partial I_\eta}{\partial S_{\eta,b}}\right)^2_{S_\eta, T_b} \Delta S_{\eta,b}^{\,2} + \left(\frac{\partial I_\eta}{\partial T_b}\right)^2_{S_\eta, S_{\eta,b}} \Delta T_b^{\,2} \tag{3.14}$$

Evaluating partial derivatives of I_η function in Eq. (3.10) yields

$$\left(\frac{\partial I_\eta}{\partial S_\eta}\right)_{S_{\eta,b}, T_b} = \frac{I_\eta}{S_\eta} \tag{3.15}$$

$$\left(\frac{\partial I_\eta}{\partial S_{\eta,b}}\right)_{S_\eta, T_b} = -\frac{I_\eta}{S_{\eta,b}} \tag{3.16}$$

$$\left(\frac{\partial I_\eta}{\partial T_b}\right)_{S_\eta, S_{\eta,b}} = -\frac{h\cdot c_0\cdot\eta}{k}\cdot\frac{I_\eta}{T_b^2}\cdot\exp\left(hc_0\eta/kT_b\right)\cdot\frac{1}{\exp\left(hc_0\eta/kT_b\right)-1} = -\frac{h\cdot c_0\cdot\eta}{k}\cdot\frac{I_\eta}{T_b^2} \tag{3.17}$$

The derivative in Eq. (3.17) is simplified by neglecting the –1 term in the denominator when compared with the exponential term. This approximation is known as Wien's approximation and its validity range covers present wavenumber and temperature levels [24]. Substituting the above expressions in Eq. (3.14) and rearranging provides the following equation which gives measurement uncertainty limits of flame emission intensities

$$\Delta I_\eta = I_\eta \cdot \sqrt{\left(\frac{\Delta S_\eta}{S_\eta}\right)^2 + \left(\frac{\Delta S_{\eta,b}}{S_{\eta,b}}\right)^2 + \left(\frac{hc_0}{k}\cdot\frac{\Delta T_b}{T_b^2}\cdot\eta\right)^2} \tag{3.18}$$

Contribution of intermediate measurement uncertainties (flame emission spectra, blackbody spectrum and blackbody temperature) to overall uncertainty of intensities are summarized in Table 3.8.. As can be seen, the effects of blackbody temperature and blackbody emission spectrum are very small when compared to the uncertainties in raw flame emission spectra. In the previous section, noise characteristics of raw flame emission spectra were elaborated and the offsets were found to be the dominant source of uncertainty. Therefore it can be concluded that the main source of uncertainty in the present intensity measurements is the spatial noise in flame spectra which is probably associated with unsteady disturbances which are more likely to occur in flames in still air rather than flames stabilized by co-flowing air. Measured flame emission intensity profiles and associated uncertainty limits at 99% confidence level are presented in Figure 3.18a-f for each vertical position and two limiting wavenumbers, η = 8500 cm^{-1} and η = 7500 cm^{-1}. These two wavenumbers are adequate to represent the results within [8500-7500 cm^{-1}] range as the intensity variation is monotonic in between these limits (see Figure 3.12a-f). Relative uncertainty levels are around 20% at weak signal intensity locations such as flame edges and z = 10 mm position. The uncertainty limits are less than 10% for the rest of the measurements which is considered as an acceptable accuracy for absolute flame emission measurements.

Table 3.8. Uncertainty budget for flame emission measurements

Measured Quantity, Q	*Uncertainty limit,* ΔQ [a]	$\frac{\partial I_\eta}{\partial Q}$	*Relative uncertainty level*
Blackbody temperature, T_b	± 2°C	$\frac{hc_0\Delta T_b}{kT_b^2}\eta$	< 0.4 %
Blackbody emission spectrum[c], $S_{\eta b}$ (η)	± 97.5×10^{-5} IU	$\frac{\Delta S_{\eta b}}{S_{\eta b}}$	< 1.1 %
Flame emission spectrum[d], S_η (η, x_0, z)	± 13.7×10^{-5} IU for x_0 < 6mm ± 4.18×10^{-5} IU for x_0 > 6mm	$\frac{\Delta S_\eta}{S_\eta}$	≤ 10 % (20-30 % at weak signal zones)
Flame emission intensity, I_η (η)	Average limits [b]: ± 0.014 W/(m^2.sr.cm^{-1}), for x_0 < 6mm ± 0.004 W/(m^2.sr.cm^{-1}), for x_0 > 6mm		≤ 10 % (20-30 % at weak signal zones)

[a] 99% confidence level

[b] see Figure 3.12 for complete spectral and spatial distribution

[c] $0.085 < S_{\eta b} < 0.16$ IU

[d] $S_\eta < 0.0083$ IU

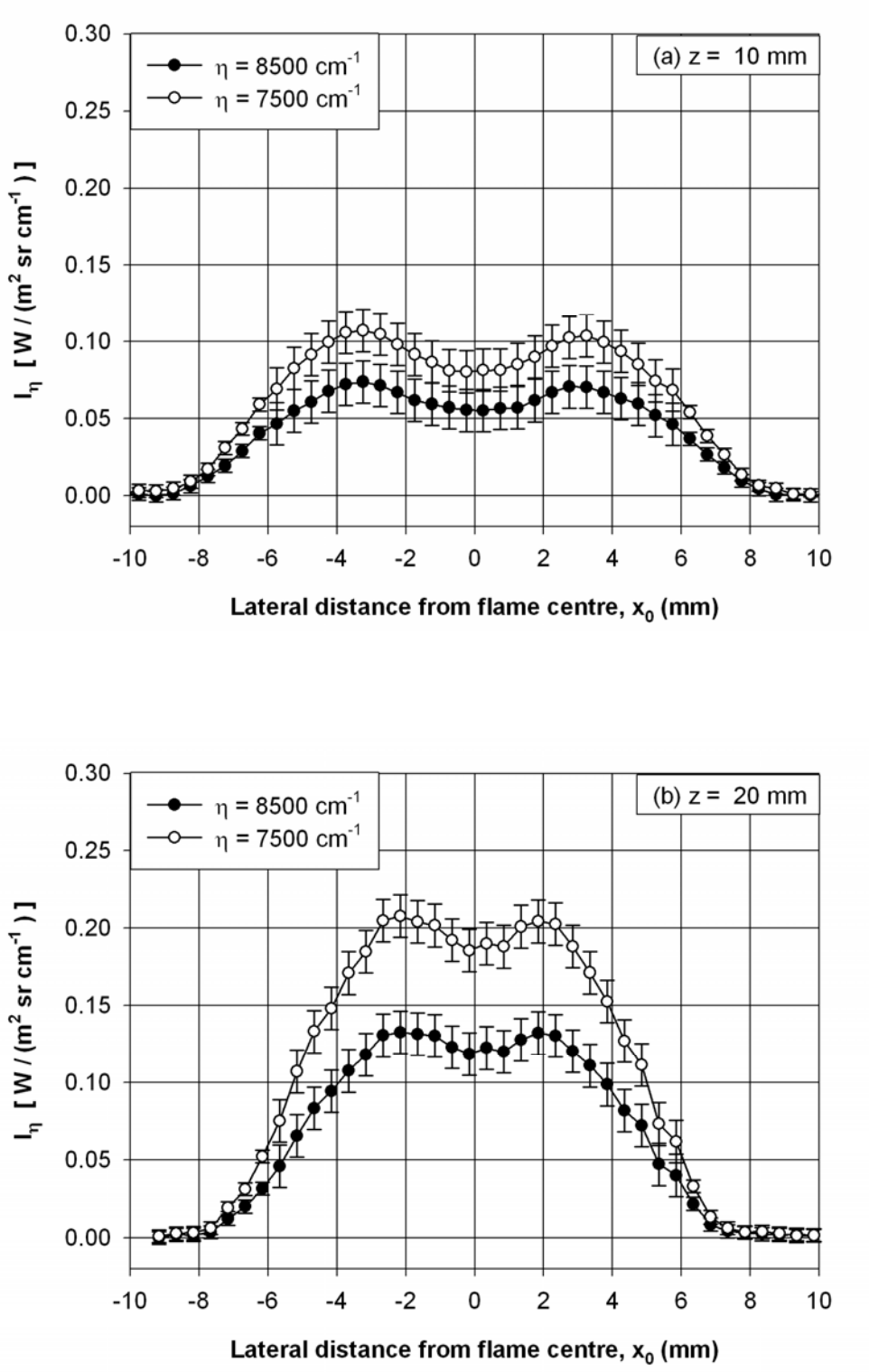

Figure 3.18. Flame emission intensity profiles with 99% confidence limits

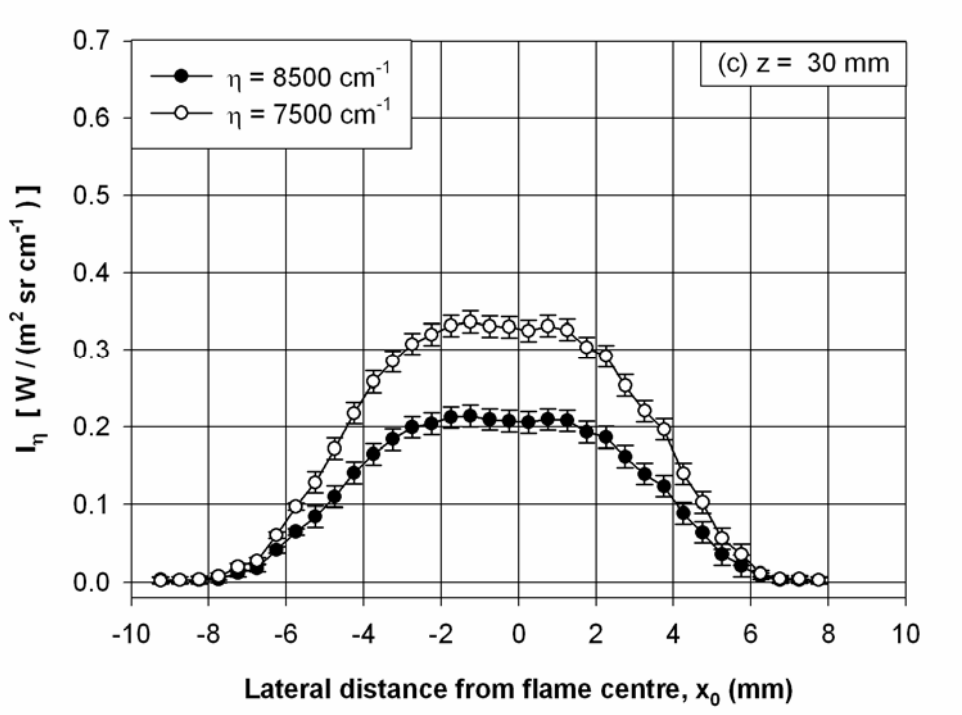

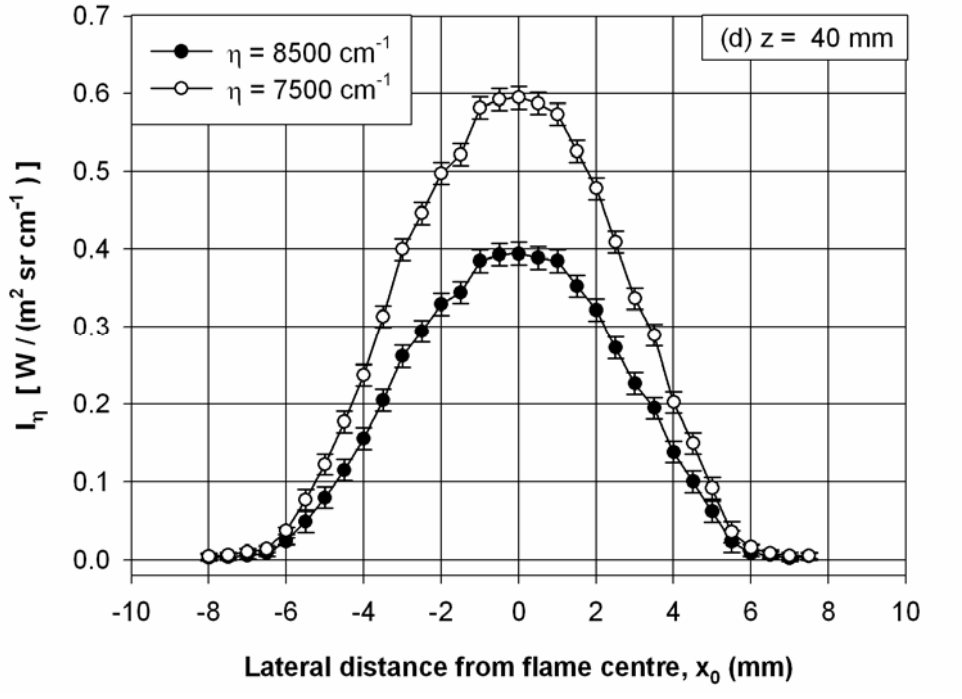

Figure 3.18. Flame emission intensity profiles with 99% confidence limits (cont.)

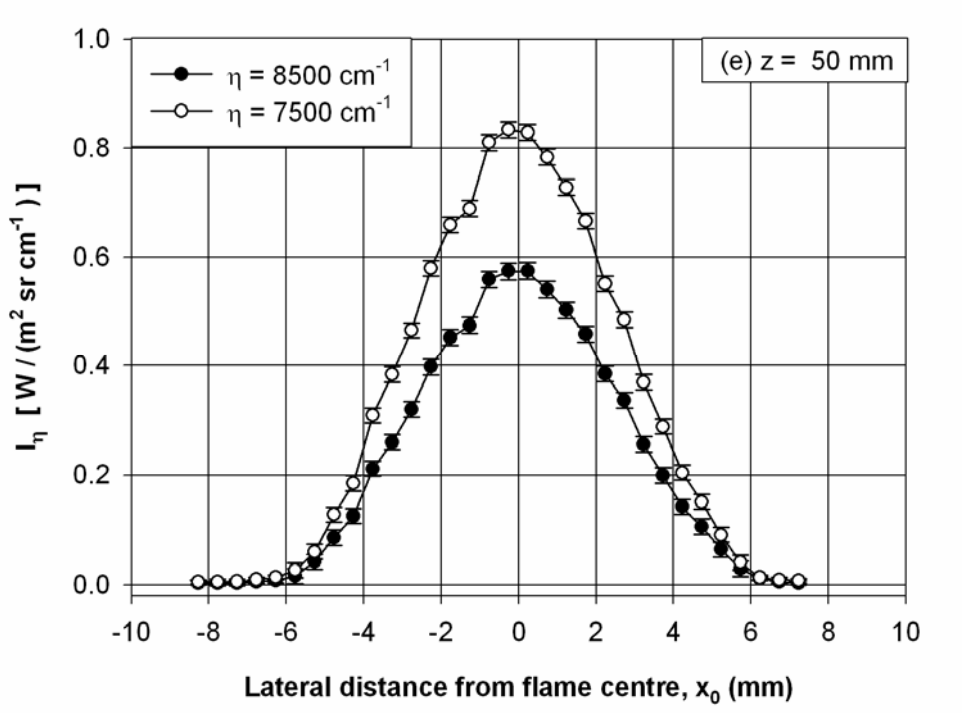

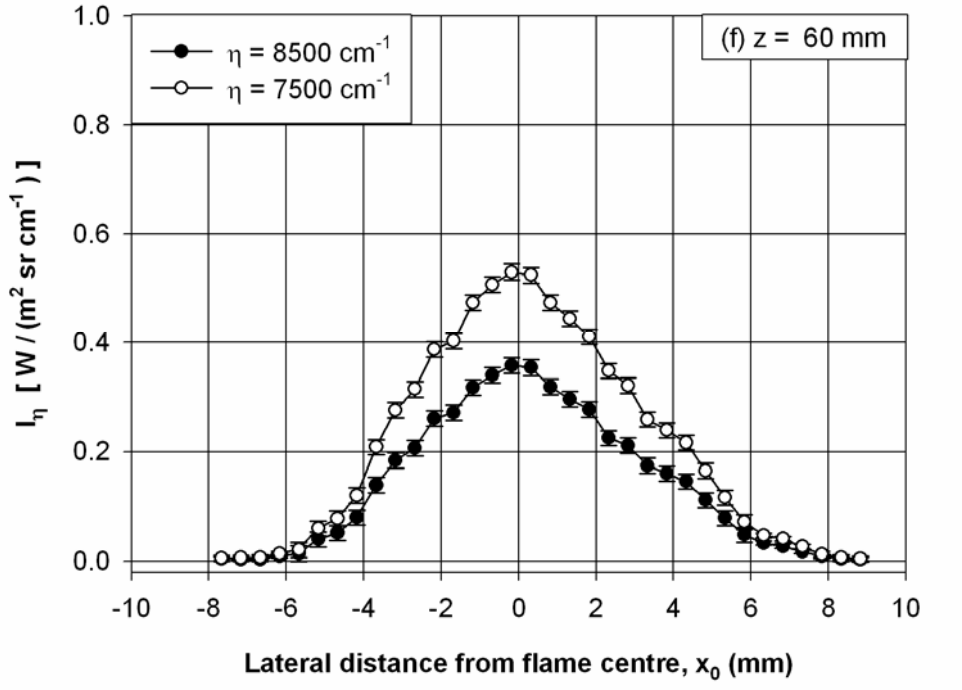

Figure 3.18. Flame emission intensity profiles with 99% confidence limits (cont.)

3.6.5. Reproducibility

In an attempt to test the reproducibility of the measurements with the present setup, flame emission measurements at z = 10 mm altitude were independently repeated by setting the same controllable operating conditions. Reproducibility of line-of-sight flame emission intensity measurements are demonstrated in Figure 3.19 where the basis flame analyzed above, is designated as Flame A and repetition flame is denoted as Flame B. It is evident that the measurements are reproducible within reported uncertainty limits.

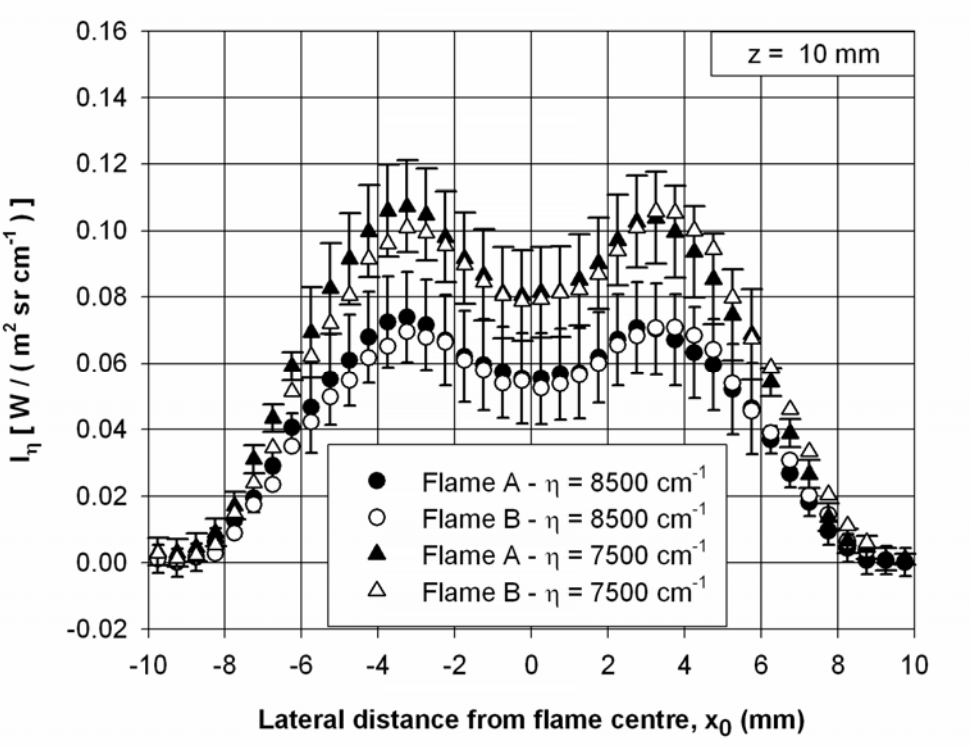

Figure 3.19. Reproducibility of flame emission intensities at z = 10 mm.

3.6.6. Conclusive remarks

Measurement of line-of-sight spectral intensities by near-infrared FTIR spectroscopy was studied on an axisymmetric, laboratory grade, ethylene/air diffusion flame within 1.1-1.7 μm (9000-6000 cm^{-1}) spectral range. Procedures for calibration, noise analysis and uncertainty assessment were presented. Reproducibility of the measurements was confirmed. It was found that spatial fluctuations dominate over spectral noise. A novel noise characterization approach which accounts for both spectral and spatial fluctuations was introduced. A paper prepared as a result of the studies presented in this chapter was presented at a Fifth International Symposium in Radiative Transfer [138] and was accepted for publication in Journal of Quantitative Spectroscopy and Radiative Transfer special issue [139].

Calibrated line-of-sight emission intensity profiles obtained in this chapter are utilized for implementation of the soot property reconstruction methodology presented in the next chapter.

CHAPTER 4

SOOT PROPERTY RECONSTRUCTION

4.1. INTRODUCTION

Soot absorption and emission in infrared range is known to be governed by Rayleigh regime for moderate size soot agglomerates (i.e. d_{eq} < 300 nm for λ > 1 μm). Line-of-sight emission intensities within Rayleigh regime depend only on soot temperature profile, volume fraction profile and refractive index function E_m in addition to flame geometry. Hall and Bonczyk [140] applied emission absorption tomography for local temperature and absorption coefficient measurement in axisymmetric flames. De Iuliis *et* al. [129] utilized emission spectra at 300-800 nm wavelength range, monochromatic emissivity formulation for homogeneous flames and applied tomographic reconstruction to infer temperature and volume fraction. More recently, Snelling *et* al. [118] have utilized tomography of line-of-sight emission spectra within 500-945 nm wavelength range for determination of soot temperature and concentration profiles by using refractive index data from literature, assumed to be constant over the wavelength range under consideration. Possible spectral variation of E_m was deduced by comparison with reference measurements.

According to the semi-empirical soot refractive index models presented in section 2.3.2, the variation of E_m with wavelength is quite considerable especially in near infrared range. Based on this common finding, present study extends existing approaches on soot diagnostics based on flame emission spectrometry by proposing an inversion scheme taking spectral variation of the refractive index function into consideration. The novelty lies in extracting characteristic information on soot refractive index model from spectral gradient of line-of-sight emission. In the sections below, description of the method and assessment of its performance are presented. Limitations of the technique and conditions of applicability are quantified by analyzing the effects of errors due to numerical methods, experimental constraints and physical approximations independently from each other.

4.2. DERIVATION AND DESCRIPTION OF SOOT PROPERTY RECONSTRUCTION METHODOLOGY

The physical problem under consideration is reconstruction of soot volume fraction, temperature and refractive index fields at horizontal cross section of a vertical, axisymmetric laboratory-scale flame from spectral line-of-sight emission intensities. Schematic representation of the problem is provided in Figure 4.1. In spectral intervals where combustion gases can be assumed to be transparent, flame soot emits, absorbs and scatters radiation continuously along the spectra. This isolated radiative activity of soot enables its characterization from emission spectrometry at certain wavelength intervals. Spectral line-of-sight emission is governed by the line-of-sight radiative transfer equation (see section 2.1) where transmitted part of radiative intensity emitted by soot is integrated along a chord s, crossing the flame at fixed lateral position, x, as follows

$$I_\eta\big|_x = \int_0^{s_f} \left[\kappa(\eta,s)\cdot I_{b,\eta}(\eta,s)\right]\cdot \exp\left[-\int_s^{s_f}\kappa(\eta,s')ds'\right]ds \tag{4.1}$$

EMISSION SELF-ABSORPTION

Restricting the analysis to optically thin flames by neglecting self-absorption term simplifies the equation to

$$I_\eta\big|_x \approx \int_0^{s_f} \underbrace{\left[\kappa(\eta,s)\cdot I_{b,\eta}(\eta,s)\right]}_{H_\eta(\eta,s)} ds \tag{4.2}$$

where the integrand in brackets is the local source term due to emission and is denoted as H_η from here onwards. The above expression now has the particular form of "line integral of local property field" which enables use of tomography to retrieve radial distribution of H_η.

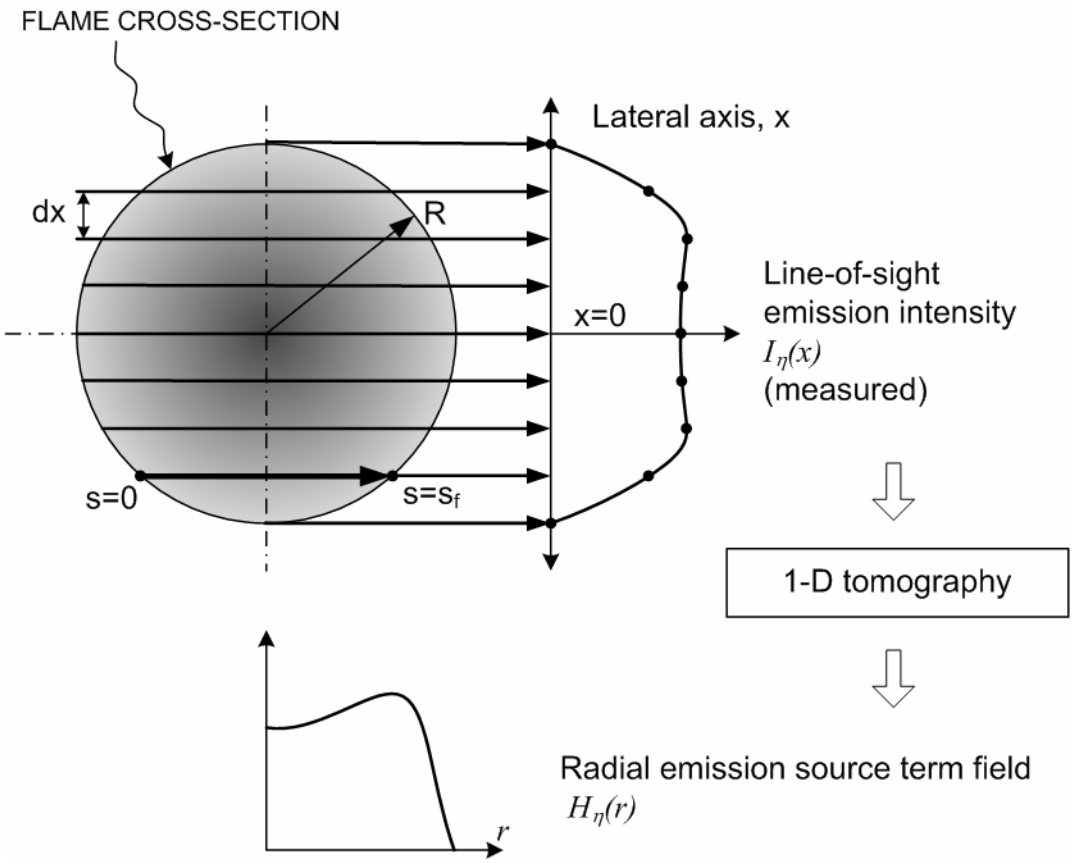

Figure 4.1. Lateral scanning of line-of-sight emission intensities along the flame cross section for tomographic reconstruction of radial emission source term field

4.2.1. Retrieval of emission source term by tomographic reconstruction

In the present study 1-D tomographic reconstruction can be conveniently implemented for determination of radial distribution of H_η within the flame from external scanning of the flame emission intensity I_η as depicted in Figure 4.1. In an axisymmetric nonhomogeneous medium such as the flame cross-section under investigation, it is possible to determine radial distribution of the axisymmetric property field, *F(r),* by scanning path integrated parallel projections of the property field along lateral axis *P(x)*. In the present problem *F(r)* and *P(x)* correspond to H_η and I_η , respectively. The relation between the projections and the property field is governed by *Abel integral equation* expressed as

$$P(x) = 2\int_{x}^{\infty} \frac{F(r)r}{\sqrt{r^2 - x^2}} dr \tag{4.3}$$

Determination of the property field from the projections requires solution of the *Abel inversion equation* (also called *Abel transform equation)* given by [141]

$$F(r) = -\frac{1}{\pi}\int_{r}^{\infty} \left(\frac{dP}{dx} \cdot \frac{1}{\sqrt{r^2 - x^2}} \right) dx \tag{4.4}$$

provided that the derivative exists.

Analytical solution of this equation is non-practical due to the singularity at $x = r$ and sensitivity of the transform to noisy data [142]. Several practical deconvolution methods that are commonly utilized to solve this inversion problem were previously compared by Dasch [143] who formulated the methods on the same grounds as weighted sums of projections. 3-point Abel inversion which was found to outperform onion-peeling and filtered back-projection techniques from the viewpoints of ease of calculation, robustness and noise amplification [143] was selected for use in the present study. 3-point Abel inversion formulations are presented in Appendix F. They are based on Dasch [143]'s formulations but presents correction of typographic errors and a modification to enable use of a lateral grid that is not necessarily coincident with the central axis of the axisymmetric system. Once radial distribution of property H_η is obtained, the next task is to isolate unknown soot properties from this field.

4.2.2. Relation between emission source term and unknown soot properties

As elaborated in Chapter 2, the optical properties of soot particles in the near-infrared range can be represented by RDG-FA theory in which absorption coefficient of soot agglomerates are equivalent to Rayleigh approximation [103] given by

$$\kappa(\eta, r) = 6\pi\eta \cdot f_v(r) \cdot E_m(\eta, r) \tag{4.5}$$

where f_v is the local volume fraction of soot and E_m is a function of wavelength dependent soot complex index of refraction, m, which may be a variable in spatial domain as well. E_m function is defined as

$$E_m(\eta,r) \equiv \mathrm{Im}\left[\frac{\left(m^2-1\right)}{\left(m^2+2\right)}\right] \tag{4.6}$$

The other component of the emission source term is the spectral blackbody intensity, $I_{b,\eta}$, that can be conveniently represented by Wien's approximation to Planck's function at flame temperatures and near-infrared to visible spectral range under consideration [24, 118].

$$I_{b,\eta}(\eta,r) = 2hc_0{}^2\eta^3 \exp\left[\frac{-hc_0}{k}\cdot\frac{\eta}{T(r)}\right] \tag{4.7}$$

Substituting Eqs. (4.5) and (4.7) in

$$H_\eta(\eta,r) = \kappa(r,\eta)\cdot I_{b,\eta}(\eta,r) \tag{4.8}$$

and grouping the constants as $B_0=12\pi hc_0{}^2$ and $B_1=hc_0/k$ gives

$$H_\eta(\eta,r) = B_0\eta^4 \cdot \boldsymbol{f_v(r)}\cdot \boldsymbol{E_m(\eta,r)}\cdot \exp\left[-\frac{B_1\eta}{\boldsymbol{T(r)}}\right] \tag{4.9}$$

where the variables in bold are desired soot characteristics.

4.2.3. Extracting spectral dependence of optical constants via the ψ-function

Rearranging the expression for H_η to isolate spectral and spatial dependencies as

$$\frac{H_\eta(\eta,r)}{\eta^4} = B_0 \cdot \boldsymbol{f_v(r)}\cdot \boldsymbol{E_m(\eta,r)}\cdot \exp\left[-\frac{B_1\eta}{\boldsymbol{T(r)}}\right] \tag{4.10}$$

shows that spectral variation of local emission source term is dependent only on spectral dependence of refractive index function E_m and temperature through the exponential term. This incepts the idea that the spectral variation of H_η is a potential source of information on E_m. The novel procedure explained in this study demonstrates how this information can be used to characterize refractive index. Having radial H_η profiles at hand from tomographic reconstruction, unknowns are eliminated one by one, yielding recovery of a function which

is only dependent on refractive index. The dependence on volume fraction can be eliminated by differentiating H_η/η^4 in spectral domain at constant radial position, r_i and dividing by itself. The convenient feature that derivative of exponential functions is equal to a factor of the function itself conveniently leads to cancellation of exponential spectrally dependent terms.

$$\gamma_{\eta,i} = \frac{\eta^4}{H_{\eta,i}} \cdot \frac{\partial}{\partial \eta}\left(\frac{H_{\eta,i}}{\eta^4}\right)\bigg|_{r=r_i} = -\frac{B_1}{T(r_i)} + \frac{1}{E_m} \cdot \frac{\partial E_m}{\partial \eta}\bigg|_{r=r_i} \tag{4.11}$$

The above function still has two unknowns: temperature and E_m. A function dependent only on E_m can be isolated by differentiating once more to cancel out temperature.

$$\Psi_i(\eta) = \frac{\partial \gamma_{\eta,i}}{\partial \eta}\bigg|_{r=r_i} = \frac{\partial}{\partial \eta}\left(\frac{1}{E_m} \cdot \frac{\partial E_m}{\partial \eta}\right)\bigg|_{r=r_i} = \left[\frac{E_m''}{E_m} - \left(\frac{E_m'}{E_m}\right)^2\right]_{r=r_i} \tag{4.12}$$

The resulting function is termed as the Ψ-function which is considered as a characteristic of the optical constants of soot as it depends only on the spectral variation of the local refractive index. Observed Ψ-function can be evaluated from H_η spectra via numerical differentiation by using LHS of Eqs. (4.11) and (4.12) as follows

$$\Psi_{r_i}(\eta) = \Gamma\left(\frac{H_\eta}{\eta^4}\right)\bigg|_{r=r_i} \tag{4.13}$$

where Γ stands for the differential operator defined as

$$\Gamma[f] \equiv \frac{\partial}{\partial \eta}\left(\frac{1}{f} \cdot \frac{\partial f}{\partial \eta}\right) \tag{4.14}$$

f being a differentiable function of η. The ψ function retrieved from Eq. (4.12) is theoretically expected to be a function of local refractive index function as follows

$$\Psi_{r_i}(\eta) = \Gamma\left[E_m(\eta, r_i)\right]\Big|_{r=r_i} \tag{4.15}$$

Determination of the ψ function from deconvolved H_η spectra was implemented and verified with simulated experiments in our recent publication [144]. However, during implementation to realistic noisy situations, it turned out that tomographic reconstruction combined with numerical differentiation for Γ operator leads to uncontrollable noise dispersion and extraneous spectral gradients that conceal characteristic spectral gradients due to refractive index. In seek of an improvement to reduce this noise vulnerability, extraction of Ψ function directly from line-of-sight emission intensity spectra, rather than reconstructed H_η spectra, was investigated. It was found that if radial variation of soot optical constants can be neglected along the line of sight, the expression for I_η can be rearranged as follows by taking E_m function out of the integral

$$I_\eta\Big|_x = B_0\eta^4 \boldsymbol{E_m(\eta)} \int_0^{s_f} \boldsymbol{f_v(r)} \cdot \exp\left[-\frac{B_1\eta}{\boldsymbol{T(r)}}\right] ds \tag{4.16}$$

Applying Γ operator to the integral expression for I_η/η^4 and rearranging by differentiation through the integrals gives the Ψ function.

$$\Gamma\left(\frac{I_\eta}{\eta^4}\right)\Big|_{x_j} = \Gamma\left[E(m)\right]\Big|_{x_j} = \Psi_{x_j} \tag{4.17}$$

Determination of observed Ψ from the above expression is suggested only under noisy conditions as it avoids noise amplifying Abel inversion step at the expense of spatially uniform E_m assumption.

Therefore it was found that Ψ function can be retrieved directly from measured line-of-sight emission intensity spectra under the following conditions:

1. thermodynamic equilibrium prevails
2. continuum emission takes place for the spectral range under consideration
3. the system is optically thin so that self-attenuation is negligible,
4. Rayleigh regime governs the absorption coefficient of the participating medium,
5. Spatial dependence of E_m function can be neglected along the path

It is noteworthy that determination of Ψ function from line-of-sight emission intensities directly does not require the emitting medium to be scanned along the lateral axis and axisymmetry assumption need not hold. This enables extension of the refractive index determination approach presented herein to characterization of more general, arbitrarily shaped, nonhomogeneous systems that satisfy the conditions listed above.

4.2.4. Determination of soot optical constants from Ψ-function

The Ψ function inferred from emission spectrometry measurements as described above is an observable quantity theoretically governed only by the spectral dependence of refractive index function, E_m. In the present approach, this function serves as a guide for determination of soot optical constants.

Previous studies on soot refractive index reviewed in [20, 114, 117] indicate that variation of soot refractive index within near infrared to visible spectral ranges is most commonly described by Drude-Lorenz dispersion relation. Previous semi-empirical studies by [23, 27, 115-117] propose different sets of dispersion constants for soot as tabulated in Chapter 2. E_m spectra obtained from Drude-Lorenz model and 6 different sets of dispersion constants from the literature are plotted in Figure 4.2a from visible to mid-infrared range. Applying the differential operator Γ to these E_m spectra returns the reference Ψ functions plotted in Figure 4.2b. As can be seen from Figure 4.2a E_m spectra evaluated from literature Drude-Lorenz constants are considerably different both in spectral variation trends and absolute values. As will be demonstrated later on in this study, uncertainties introduced by these variations may lead to considerable biases in inferred temperatures and volume fractions. Figure 4.2b demonstrates the distinctive nature of Ψ function which identifies the spectral variation character of E_m especially in 5000-10000 cm^{-1} near-infrared range which indicates that Ψ function inferred from flame emission measurements within this spectral range can be used to select the most appropriate set of dispersion constants by comparing it with reference Ψ functions from refractive index models from literature.

Determination of optical constants is realized by comparing observed Ψ function from deconvolved H_η with each of the reference Ψ functions. Comparison procedure starts with computation of sum of squared errors (SSE) and selecting the set which fit to deconvolved Ψ with minimum SSE. If two or more sets result in SSEs of same order of magnitude then a secondary comparison is necessary among these. Slope of the best line of Ψ is compared

with the slopes of best lines of reference Ψ functions, those of which with opposite signed slopes are eliminated. The final elimination is based on maximum absolute errors. The set of dispersion constants of the reference Ψ that cause the smallest maximum error is selected. Once the set of dispersion constants at the radial position under consideration is selected, Drude-Lorenz model is employed to compute local complex refractive index spectra and local E_m spectra, for use in determination of local temperature and local volume fraction explained in the next section. This selection procedure applies for ideal conditions where spectral variations are not contaminated with spatial noise. Ideally, the procedure is capable to detect possible spatial variation of refractive index however due to the noisy conditions in present experiments, radial variation of refractive index function is neglected as will be explained section 4.3.1 where further details on practical issues regarding dispersion constant selection methodology are presented. The procedure is also directly applicable to other possible physical models for spectral variation of refractive index else than Drude-Lorenz. Although limited at present, refractive index models that take effects of soot composition and temperature into account can be utilized as inputs to the proposed procedure.

4.2.5. Determination of soot temperature and volume fraction

E_m spectra determined from the selected set of dispersion constants at each radial node can now be utilized to retrieve remaining unknown properties which are radial profiles of soot temperature and volume fraction. For this purpose, the expression for local emission source term is rearranged by taking natural logarithm of both sides of Eq. (4.10)

$$\Phi_\eta(r) = \ln\left(\frac{H_\eta(r)}{\eta^4}\right) - \ln\left[E_m(r,\eta)\right] = -\frac{B_1\eta}{T(r)} + \ln(B_0 \cdot f_v(r)) \tag{4.18}$$

For each position r_i, the LHS of the above equation is computed from deconvolved $H_\eta(r_i)$ and E_m function. Performing linear regression to $\Phi_{\eta,i}$ versus η plot gives local temperature and volume fraction from the slope and intercept of the best line as follows

$$T(r_i) = -\frac{B_1}{slope} \tag{4.19}$$

$$f_v(r_i) = \frac{\exp(intercept)}{B_0} \tag{4.20}$$

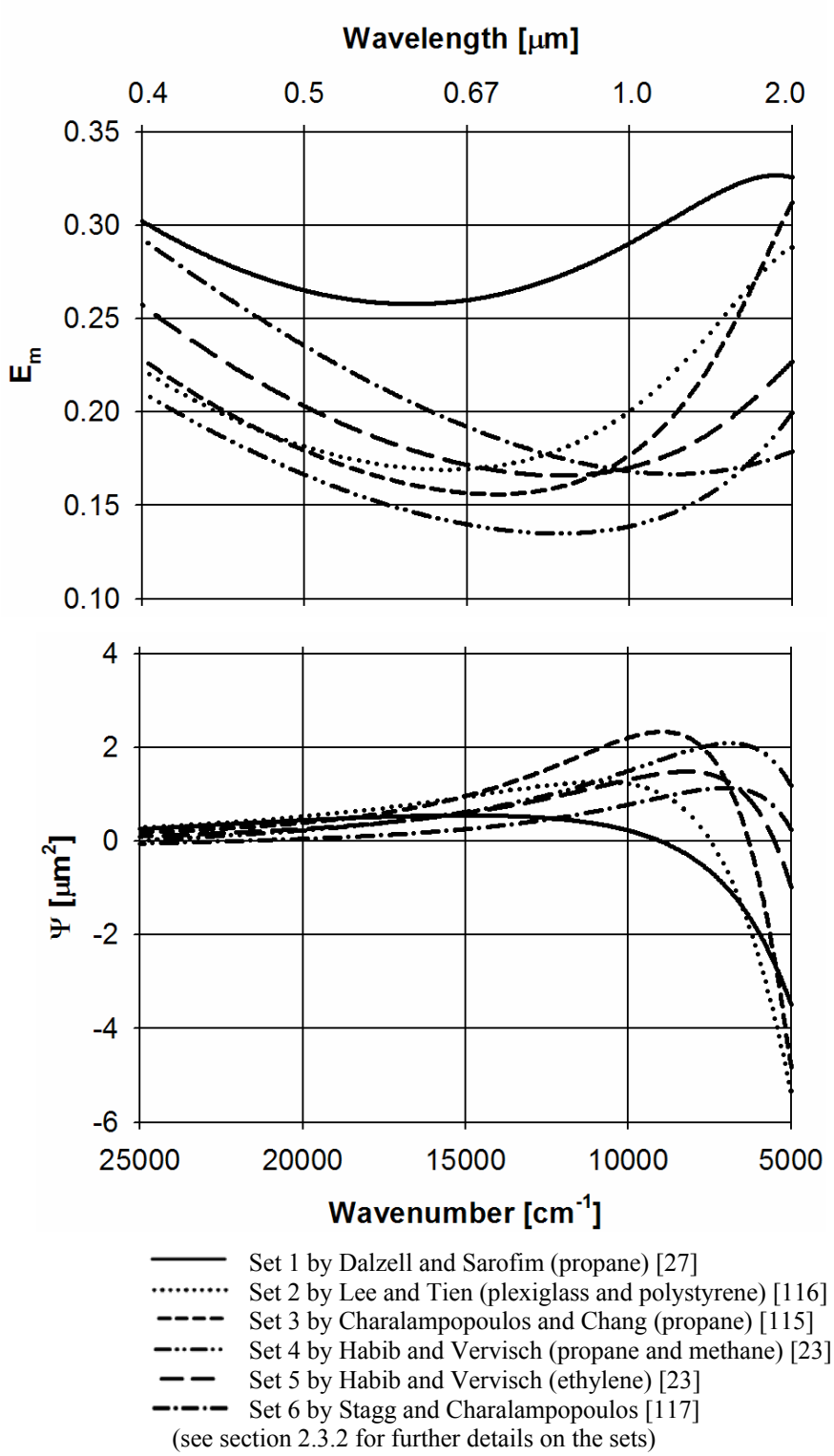

Figure 4.2. Functions of soot complex index of refraction from different sets of Drude-Lorenz dispersion constants published in the literature

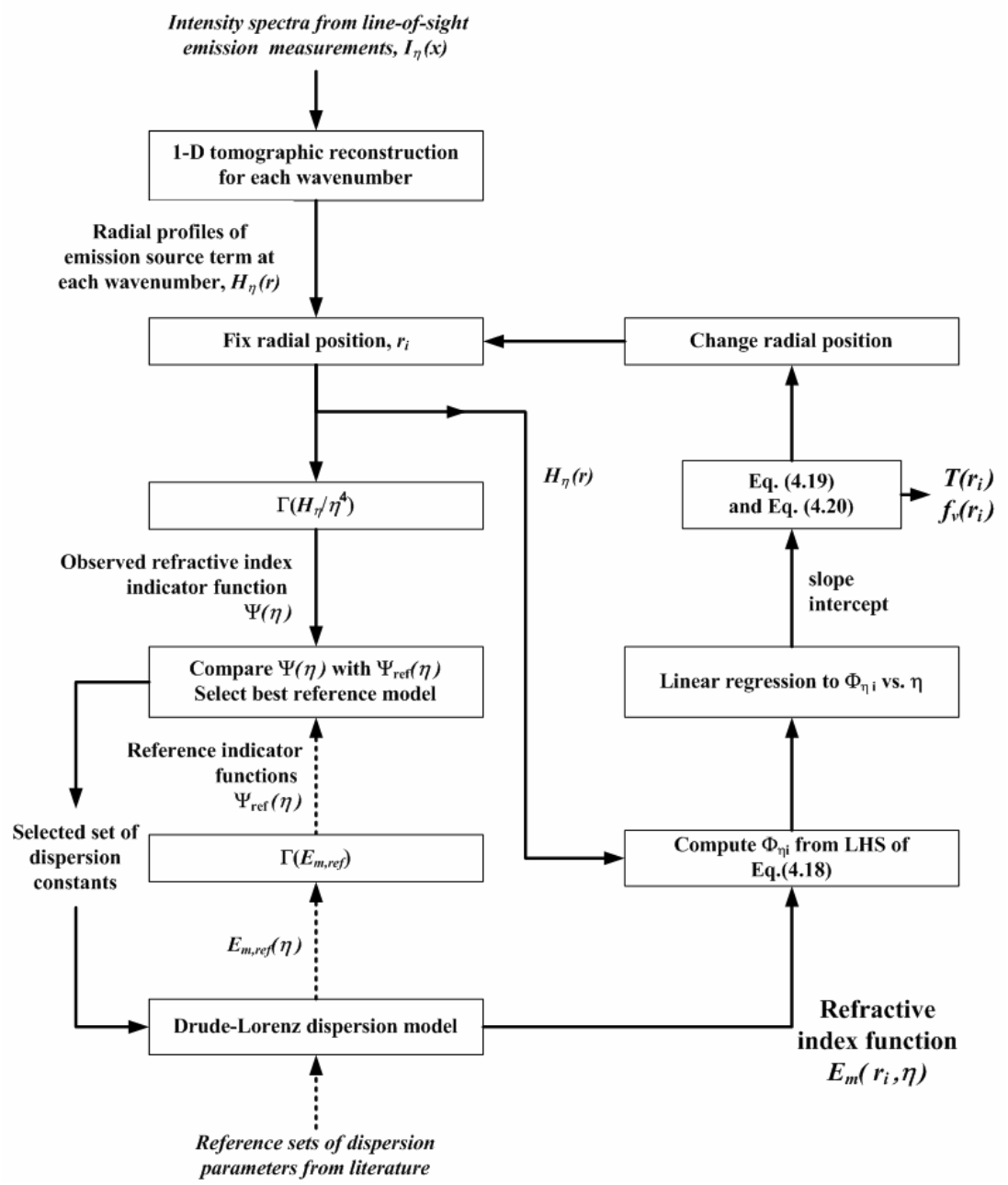

Figure 4.3. Soot property reconstruction algorithm

4.2.6. Property reconstruction procedure

Figure 4.3 outlines proposed inversion procedure starting from measurements to retrieval of soot properties. As can be followed from the scheme, the only inputs along the procedure are several reference refractive index models for comparison purposes. The reliance on external empirical data for optical constants is relatively less, as there is a selection procedure for determination of best model. The method introduces a novel approach in terms of reducing the uncertainties due to refractive index. In its present form, it does not require complementary measurements. As soot is a highly absorbing material, negligible self-absorption assumption is the most questionable aspect of the present method and its validity is assessed in section 4.4.2.

Under noisy conditions where the above procedure fails to retrieve physically meaningful Ψ functions, spatial dependence of E_m function needs to be neglected and Ψ function and refractive index determination needs to be conducted before the tomography step. Data conditioning and property retrieval procedures that need to be followed for noisy data are explained in the following section.

4.3. DATA CONDITIONING IN THE PRESENCE OF NOISE

Experimental nonidealities cause spatial and spectral noise which degrades the quality of the inferred properties. Several data conditioning steps are taken throughout the inversion procedure, starting right after the calibration step. Figure 4.4 outlines the steps taken for data conditioning alongside of the property reconstruction procedure.

4.3.1. Spectral smoothing and retrieval of Ψ variable

Spectral smoothing is a critical step for reconstruction of selective Ψ function as it involves second order differentiation in wavenumber. Calibrated line-of-sight emission intensity spectra at each lateral scan node are first subjected to moving average filter to reduce random spectral noise. Once the number of data points to be averaged in the moving window, N_f, is specified, a filter function is generated as a step function at $1/N_f$ with an area equal to unity. Convolution of the filter function and noisy emission intensity spectrum was carried out by the IMSL library routine DRCONV, resulting in smoothened spectrum.

Filtering alone is not adequate to avoid noise amplification during numerical differentiation with respect to wavenumber to get Ψ variable. After filtering, second stage in spectral

smoothing is fitting a continuous function which is in accordance with expected spectral variation. This stage is required to avoid severe oscillations after spectral differentiation. It is required to determine a model function that can mimic the spectral behavior accurately. By inspection of the expression for intensity in Eq. (4.16) a representative model function is proposed as

$$I_{fit}(\eta) = \eta^4 \cdot \exp(a_0 + a_1\eta + a_2\eta^2 + a_3\eta^3) \tag{4.21}$$

Spectral variation of I_η / η^4 is determined by the exponential temperature term and spectral variation of E_m. To test suitability of the above model function, it needs to be verified that E_m can be modeled in the form

$$E_m(\eta) = \exp(b_0 + b_1\eta + b_2\eta^2 + b_3\eta^3) \tag{4.22}$$

Fitting 3rd degree polynomials to ln(E_m) functions obtained from Drude-Lorenz dispersion model resulted in regression coefficients greater than 0.9999 for each set of dispersion constants provided in the literature (Table 2.3), confirming suitability of the proposed function in Eq. (4.21). Taking natural logarithm of both sides gives

$$\ln\left(I_\eta / \eta^4\right) = a_0 + a_1\eta + a_2\eta^2 + a_3\eta^3 \tag{4.23}$$

Model function fitting is carried out by fitting a 3rd degree polynomial to ln(I_η / η^4) vs. η data by using IMSL FORTRAN library routine RCURV [25] which performs least squares polynomial fitting to determine constants a_0, a_1, a_2, a_3 and a_4. After applying Γ operator to Eq. (4.21), Ψ variable simplifies to a line in spectral domain and can directly be obtained from

$$\Psi_{\ln I} = 2a_2 + 6a_3\eta \tag{4.24}$$

This fitting approach eliminates the requirement to implement numerical differentiation which causes noise amplification. Selection of dispersion constant sets is performed by comparing spectrally averaged Ψ_{av} variable inferred from the experiment with average reference values obtained from Drude-Lorenz model.

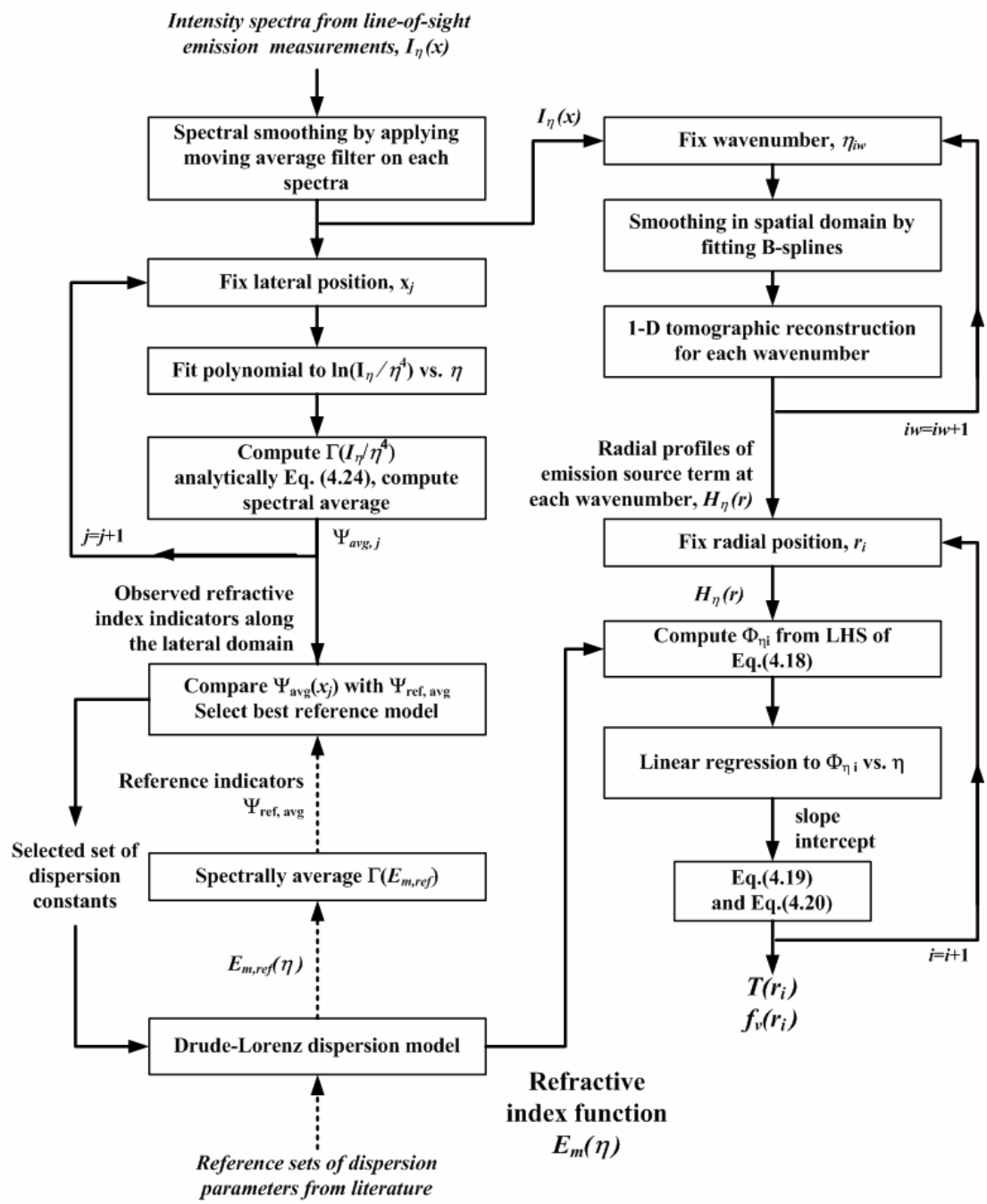

Figure 4.4. Soot property reconstruction algorithm with data conditioning

4.3.2. Determination of flame centre and smoothing in spatial domain

To determine axis of symmetry in lateral intensity profiles, a 6^{th} order polynomial is fitted to lateral profiles at fixed wavenumber. Although this polynomial does not provide an acceptable fit along the whole domain, it is successful to detect the centre of symmetry from zero derivative position. After performing the fit with RCURV routine, the points where the derivative of the fit function equals zero are determined by finding roots of the derivative of the polynomial by using ZPORC [25] routine. The real root corresponding to the central location is selected as the centre. Mean central location determined from the lateral profiles at each wavenumber is set as the origin of the lateral domain.

Spatial smoothing is an important step as present flame in still air is subject to some instabilities. The resulting spatial noise needs to be reduced to avoid accumulation of noise from the edge towards the centre during tomography process. The critical consideration in this step is to eliminate the effects of instabilities but at the same time conserve the fine variations caused by the physical radial distribution under consideration. After several trials on simulated noisy intensities, B-spline fitting was found to provide the best solution among several other methods such as moving average filtering, polynomial fitting and smoothing cubic-splines. Fitting B-splines to a given data mainly consist of fitting piecewise high order polynomials named B-splines which are connected at prespecified knots (breakpoints) where the coefficients of the splines are determined so as to provide best fit to the data while maintaining continuity of the function by matching first and second derivatives at knot positions. The fitting process requires specification of the number of knots, knot positions and order of splines which are specific to the profile's shape and it takes several trials before selection of the best combination. In the present application a smoothing B-spline interpolation was carried out by using the CONFT routine of IMSL library [25] which performs least-squares constrained spline approximation based on the algorithms by de Boor [145]. The only constraint imposed on the profiles is that the derivative is set to zero at previously determined position for centre of symmetry. 4^{th} order B-splines with 3-4 knot positions along the half profiles are generally found to result in acceptable profiles. After the smoothing, the intensity profiles are subjected to tomographical reconstruction to retrieve local emission source terms.

4.3.3. Other numerical considerations

In order to minimize possible numerical errors, overflows and underflows during computations, all fitting, smoothing and differentiation processes were carried out with

dimensionless variables. Space coordinates were normalized by radial extent of the flame, wavenumber domain was divided by the wavenumber at mid-point of the spectral range and intensities were divided by blackbody intensity at mid-point wavenumber and a reference temperature of 1100K.

4.4. RESULTS AND DISCUSSION

Performance of the proposed algorithm to infer soot characteristics is first assessed on a test problem supplying the spectral line-of-sight emission intensities simulated by using the direct model developed in Chapter 2 along a flame with pre-specified soot characteristics to the proposed inversion scheme and comparing reconstructed properties with pre-specified properties. The test problem selected for this purpose is based on Snelling *et* al. [118]'s laminar ethylene diffusion flame with 10.9 mm inner diameter fuel tube. Temperature and volume fraction profiles of this flame were thoroughly characterized by two different measurement techniques for each property. The measurements at 30 mm height were selected for the test case (see Figure 2.27 and Figure 2.28) as representative of a typical optically thin, axisymmetric sooting flame in laboratory conditions. A direct code which solves LHS of Eq. 1 by numerical integration was developed for simulation of the experiment by calculating line-of-sight emission intensity spectra. The Drude-Lorenz dispersion constant sets utilized for determination of refractive index function are outlined in section 2.3. The performance of the method is tested in 3 stages to quantify possible failures due to *i*) numerical errors *ii*) physical assumptions and *iii*) experimental limitations. Then the improvements provided by the data conditioning algorithm are demonstrated by applying it to analysis of simulated intensities with artificially generated noise. Once accuracy of the method is verified on simulated measurements, it is applied to characterization of soot properties of the ethylene diffusion flame experimentally investigated in Chapter 3.

4.4.1. Validation of proposed algorithm for ideal measurements

To assess numerical accuracy of the method, direct simulations were carried out by imposing the same physical approximations as the inversion scheme. Line-of sight emission intensity spectra at [7500-8500cm^{-1}] spectral range with 25 cm^{-1} resolution was simulated at equally spaced 35 lateral positions spanning along one half of the flame by the direct code with neglected self-attenuation. Figure 4.5*a* displays the performance of the 3-point Abel inversion approach by comparing deconvolved H_η field with actual H_η calculated from known flame properties. The agreement indicates that Abel inversion performs satisfactorily.

The capability of the Ψ function to distinguish between the dispersion constant sets is demonstrated in Figure 4.5b by comparing the function deconvolved from intensities simulated by different sets of dispersion constants with the actual Ψ functions of these models. Due to one-to-one correspondence between inferred Ψ functions and input sets of dispersion constants, the selection algorithm described in section 4.2.6 is successful to identify the refractive index model from Ψ function correctly for simulated experiments.

Figure 4.6 presents soot temperature and volume fraction profiles inferred from proposed algorithm in comparison with the properties supplied as input to the experiment simulator for the base case described above. Excellent agreement indicates that the algorithm is successful for optically thin flames with ideal line-of-sight measurements of high spatial resolution. Emission intensity spectra simulated by each refractive index model resulted in the same accuracy as in Figure 4.6.

4.4.2. Effects of physical assumptions

Limitations imposed by neglecting self-attenuation in the inverse scheme is evaluated by simulating line-of-sight intensities with self-absorption term and supplying these more realistic spectra to the inversion scheme to compare inferred properties with input profiles. To analyze the effect of this assumption, the optical thickness of the test problem under consideration ($\tau \approx 0.3$ at 7500-8500 cm^{-1}), is increased 2, 5 and 10 times by multiplying input soot volume fractions. As can be seen from Figure 4.7, self-attenuation can be neglected with confidence for the flame under consideration and reasonable accuracy is obtained for up to 5 times optically thicker conditions (≈ 1.5 at 7500-8500 cm^{-1}). At 10τ case inferred temperatures display sharp jumps due to incorrectly selected refractive index models.

An important aspect of the proposed inversion methodology is its applicability to any continuous variation of E_m function. On the other hand, constant E_m assumption is frequently used in literature, i.e. in [118], as it simplifies the inversion scheme by enabling retrieval of temperature without knowledge of E_m just from the slope of $\ln(H_\eta/\eta^4)$ vs η plot. Another common practice is selection of refractive index somewhat arbitrarily, generally just because it is widely used in literature. In order to quantify the uncertainties associated with these approximations, simulations with dispersion constant set 3 were carried out at different wavenumber ranges. Inversion was carried out via two methods, one being the proposed scheme and the other based on using a constant E_m over the spectrum which is the average value corresponding to the selected dispersion constant set.

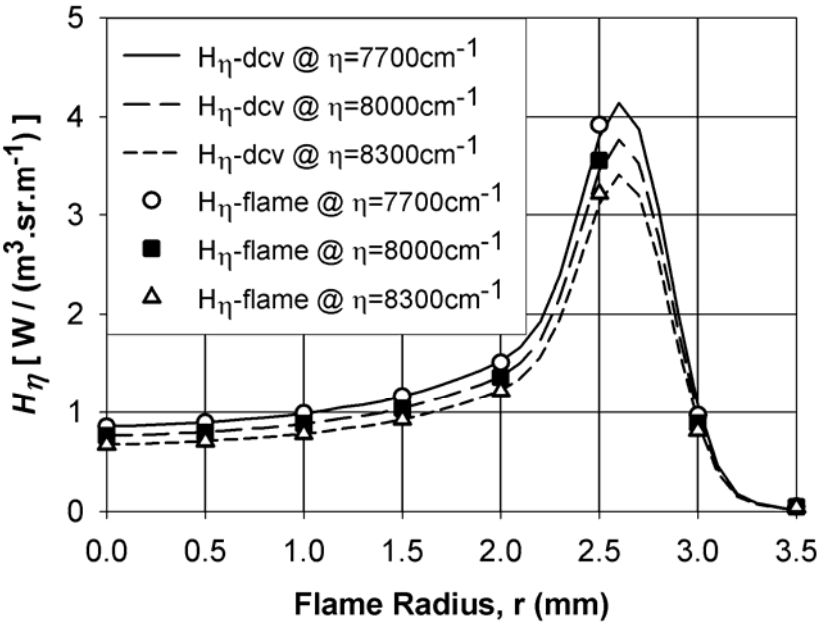

(a) H_η from flame properties vs. deconvolved H_η

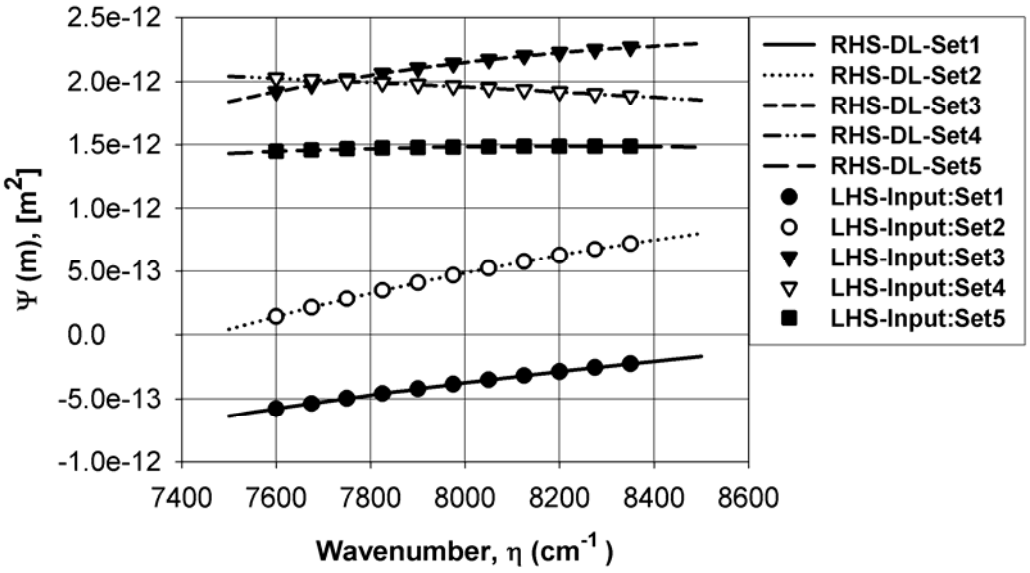

(b) Ψ function from Drude-Lorenz model vs. inferred Ψ

Figure 4.5. Isolated validation of inversion scheme modules

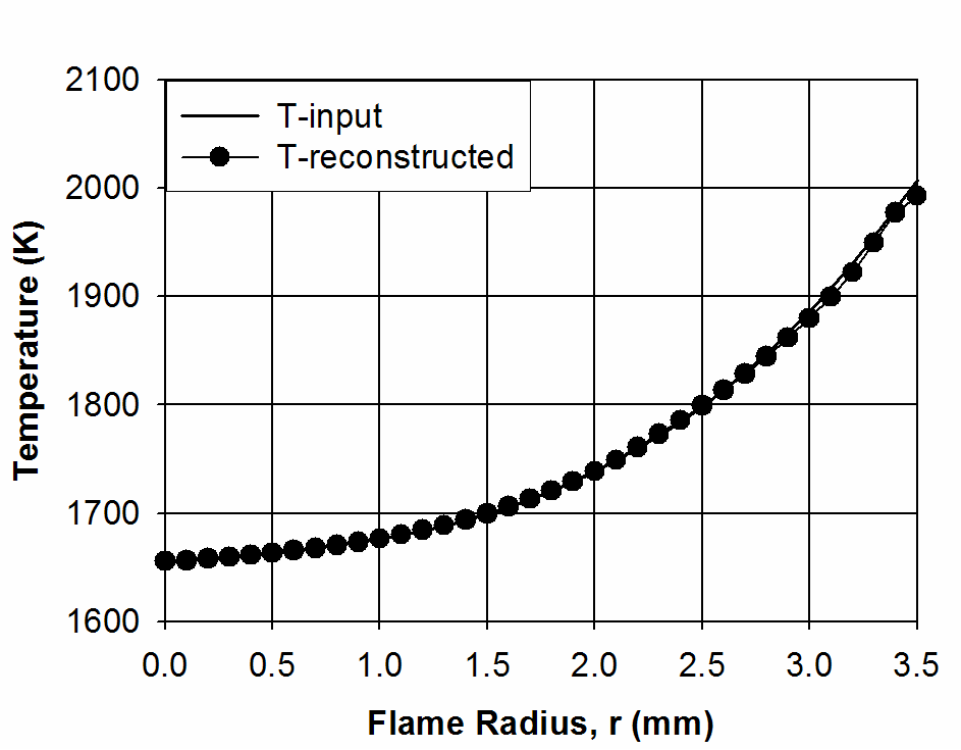

(a) Temperature

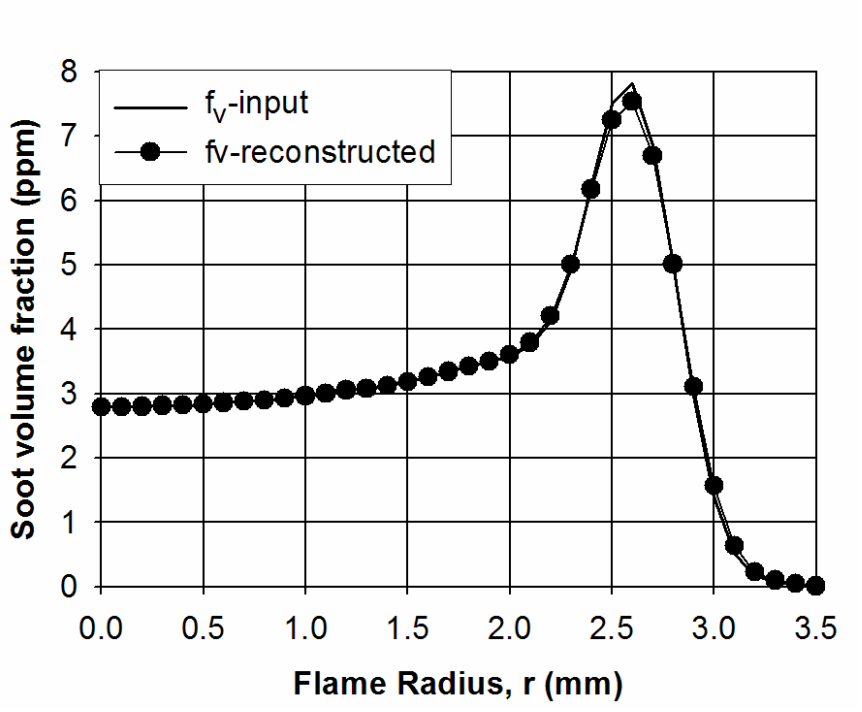

(b) Volume fraction

Figure 4.6. Comparison between reconstructed soot properties and input properties supplied to experiment simulator

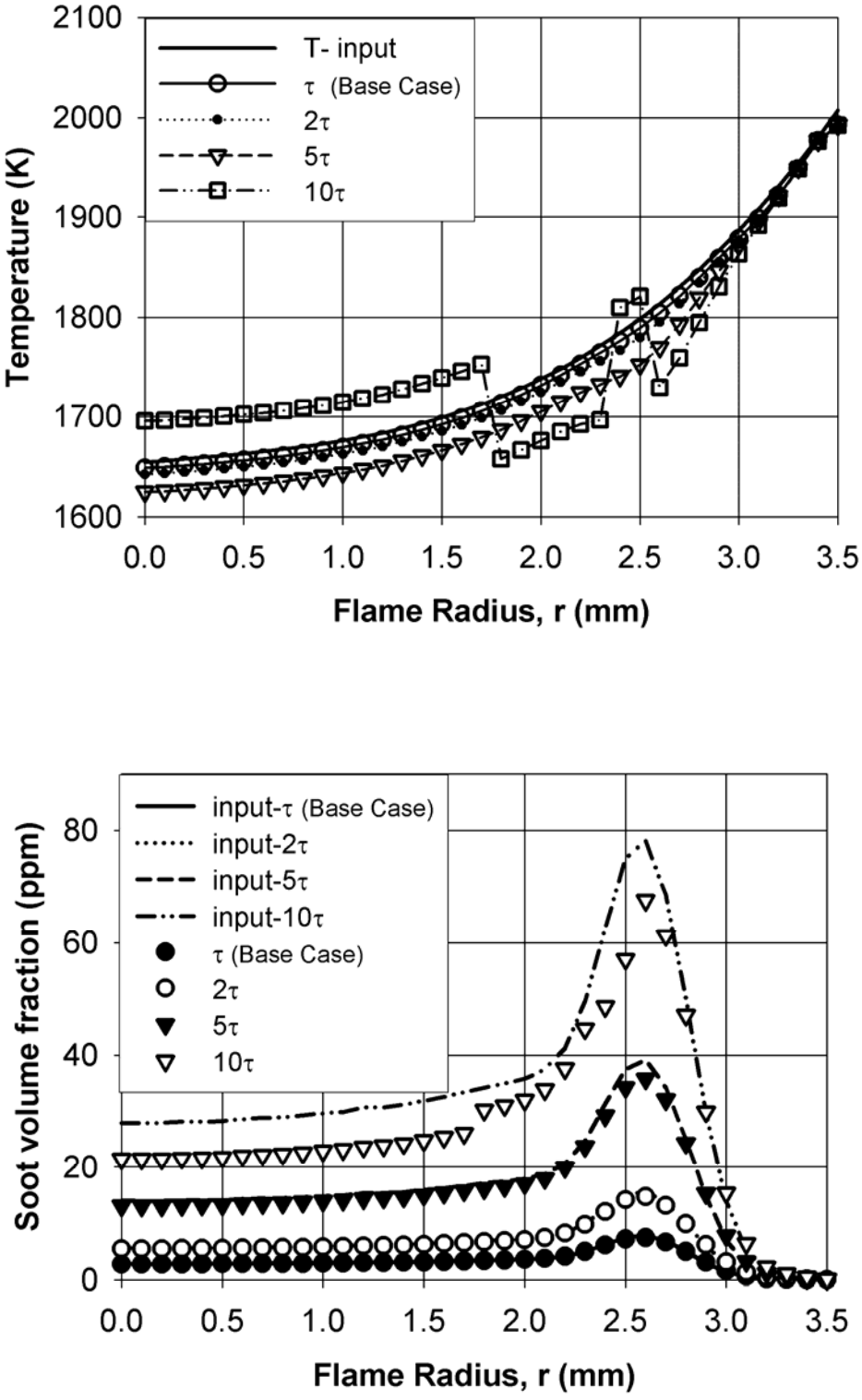

Figure 4.7. Effect of self-absorption on inferred properties

As can be seen from Figure 4.8, in the near-infrared range, neglecting spectral variation of E_m may cause 200°C underestimation in temperature. On the other hand, even when the same set of dispersion constants is used for both direct and inverse models (see set 3 case in volume fraction plot), the volume fraction can be overestimated by 100% just because spectral variation of optical constants is not considered. Moreover, if the refractive index model selection is also arbitrary, the estimated volume fractions may be up to 3 times more than the actual values. Figure 4.9 displays that the assumption of constant E_m is applicable within 667-714 nm range and the inferred volume fractions are not very sensitive to refractive index selection. However as indicated in Figure 4.10, 476-500 nm range constant E_m assumption causes around 100°C overestimation in temperature and more than 50% underestimation in volume fraction. Note that these errors due to neglecting spectral variation of E_m at different spectral ranges are related to actual spectral gradients of E_m within these ranges (Figure 4.2a). Using an average E_m towards small wavelengths in the visible spectrum causes overestimation in temperature and underestimation in volume fraction due to negative slope of E_m spectra in this region. The opposite holds in the near-infrared range as slope is positive.

4.4.3. Effects of experimental limitations

In practice, line-of-sight measurements are never ideal. In order to assess sensitivity of this approach to possible experimental limitations, the nonideal intensities simulated by the direct code and presented in 2.4.3 are supplied to the inversion algorithm and accuracy of inferred properties are investigated. One of these limitations is spatial resolution which is characterized by the increment between two adjacent line-of-sight measurements, d_x, and the diameter of the beam. Figure 4.11 displays the effect of scanning resolution on inferred properties. As can be seen, the resolution needs to be sufficiently small to capture steep gradients especially encountered in soot volume fraction profiles.

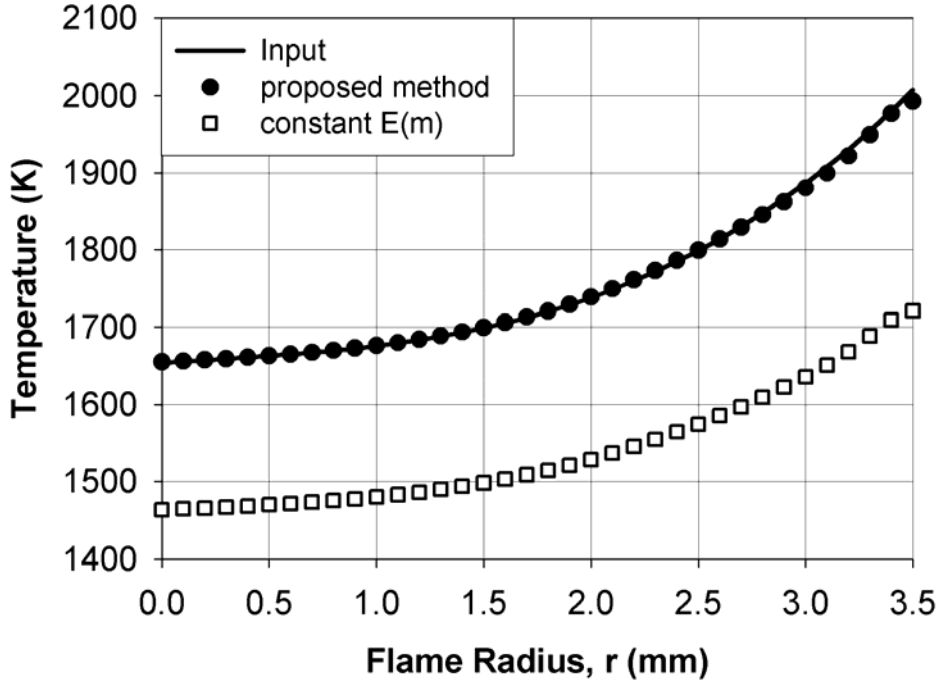

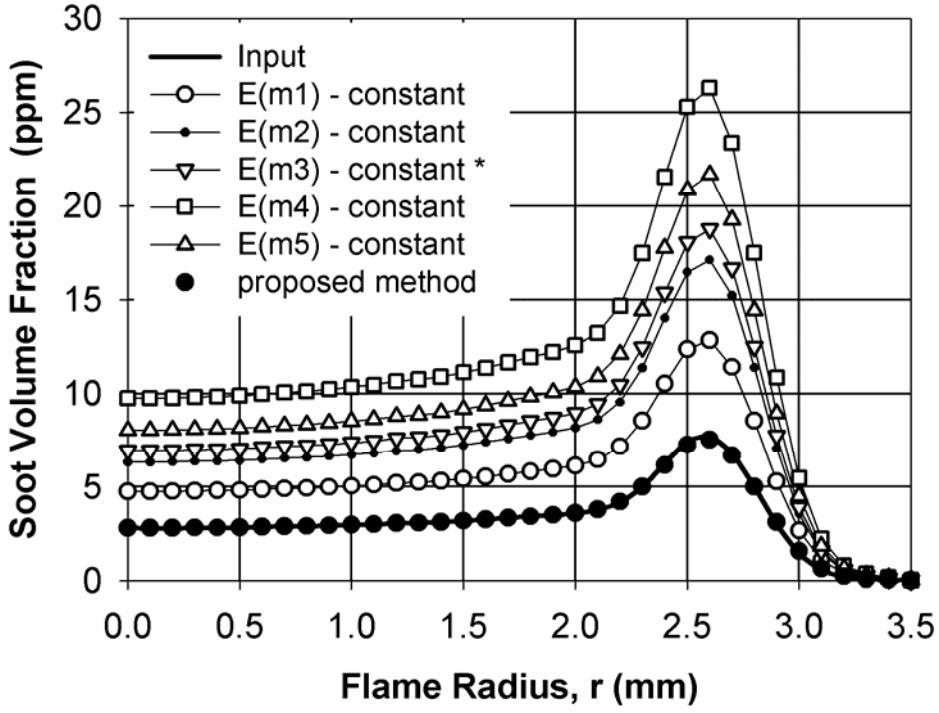

Figure 4.8. Effect of neglecting spectral variation of E_m and arbitrary selection of refractive index on accuracy of inferred properties at 7500-8500 cm^{-1} (1180-1333 nm) range

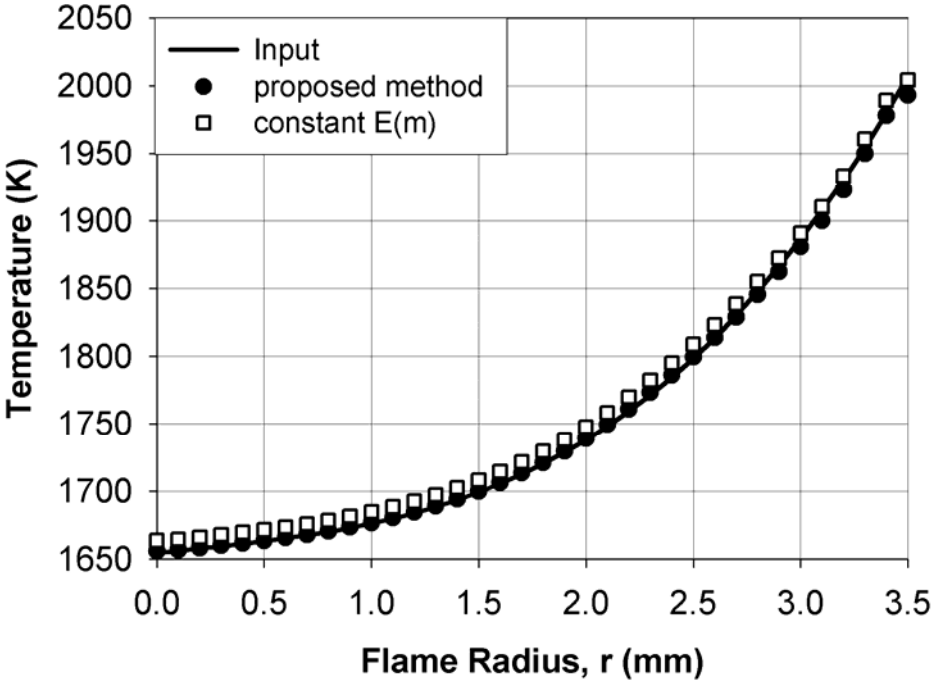

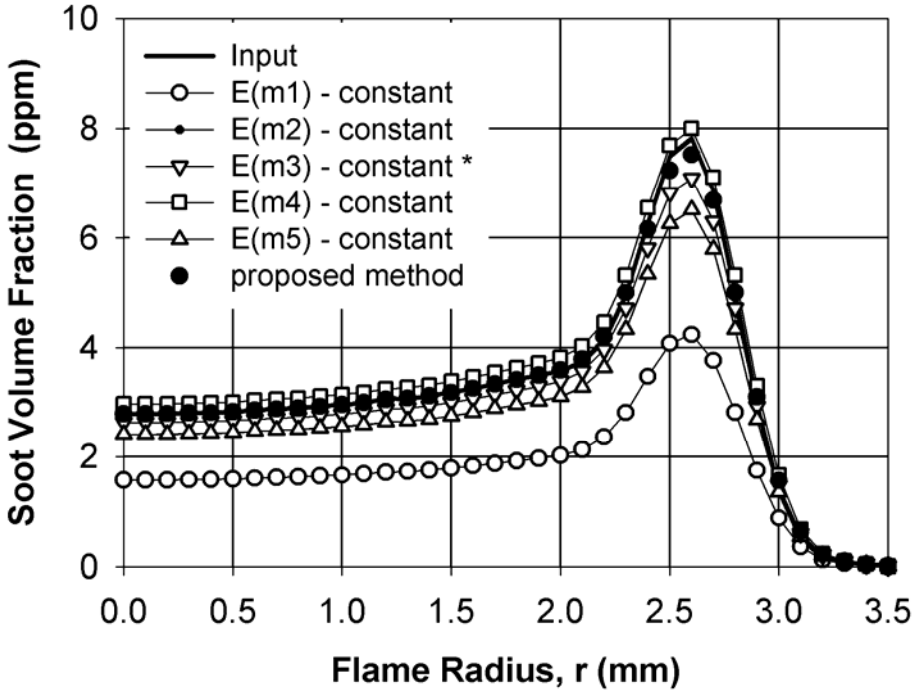

Figure 4.9. Effect of neglecting spectral variation of E_m and arbitrary selection of refractive index on accuracy of inferred properties at 14000-15000 cm^{-1} (667-714 nm) range

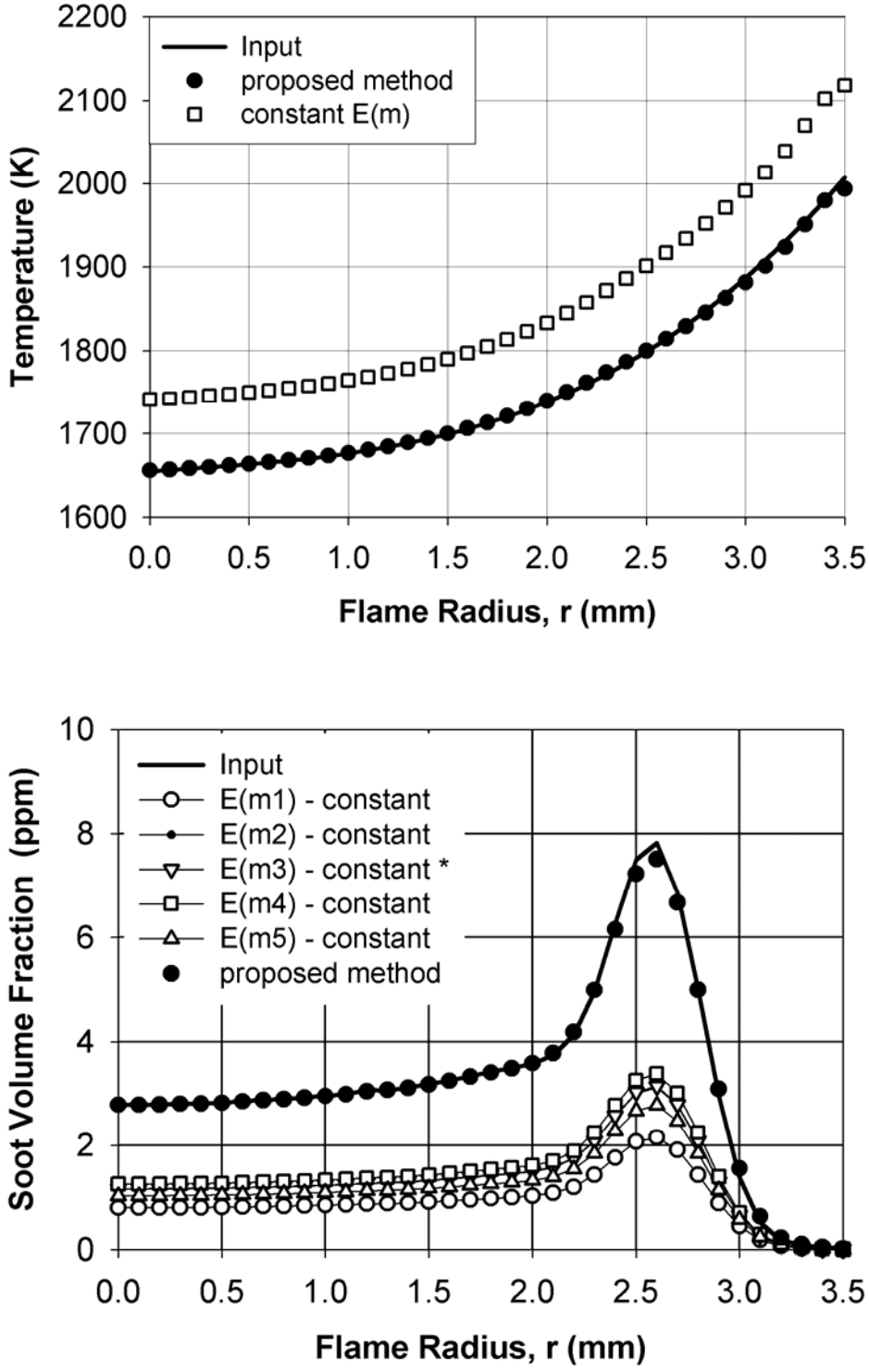

Figure 4.10. Effect of neglecting spectral variation of E_m and arbitrary selection of refractive index on accuracy of inferred properties at 20000-21000 cm^{-1} (476-500 nm) range

The effect of finite beam diameter is assessed by simulating emission intensities with beam diameter, d_b equal to d_x, $3d_x$ and $6d_x$ at two different lateral scan resolutions, the first one being a relatively fine resolution, equivalent to base case of validity analysis (d_x=R/35), the second one being a coarser resolution (d_x =R/14), equivalent to the conditions in the experimental investigation (see section 3.3) in which beam diameter was limited by the detector sensitivity and could not be reduced further. A beam diameter of d_b=$6d_x$ at coarse resolution mimic the measurement conditions and therefore are indicative of possible errors that will be encountered due to this limitation. Figure 4.12 and Figure 4.13 demonstrate effect of beam diameter limitation on performance of property reconstruction algorithm at fine and coarse scan resolutions, respectively. The results indicate that large beam diameter combined with relatively coarse scanning grid causes the inferred properties to smear out towards the edges, artificially increasing the observed flame diameter and smoothing out the soot volume fraction peaks. The large beam actually acts like a filter that smooths out the emission from soot. These results are to be taken into consideration during interpretation of the soot properties inferred from experiments.

Another experimental nonideality is noise associated with the emission spectra which is simulated by generating a Gaussian noise of specified signal to noise ratio (SNR) and superimposing it on simulated intensities as explained in section 2.4.3.1. As can be seen from Figure 4.14, the inferred properties are quite sensitive to noise. This is basically due to high sensitivity of the Ψ function to spectral variation of intensities and failure to select the correct refractive index set in the presence of noise. These results indicate that line-of-sight measurements need to be preconditioned by applying smoothing or filtering before treatment with the inversion scheme.

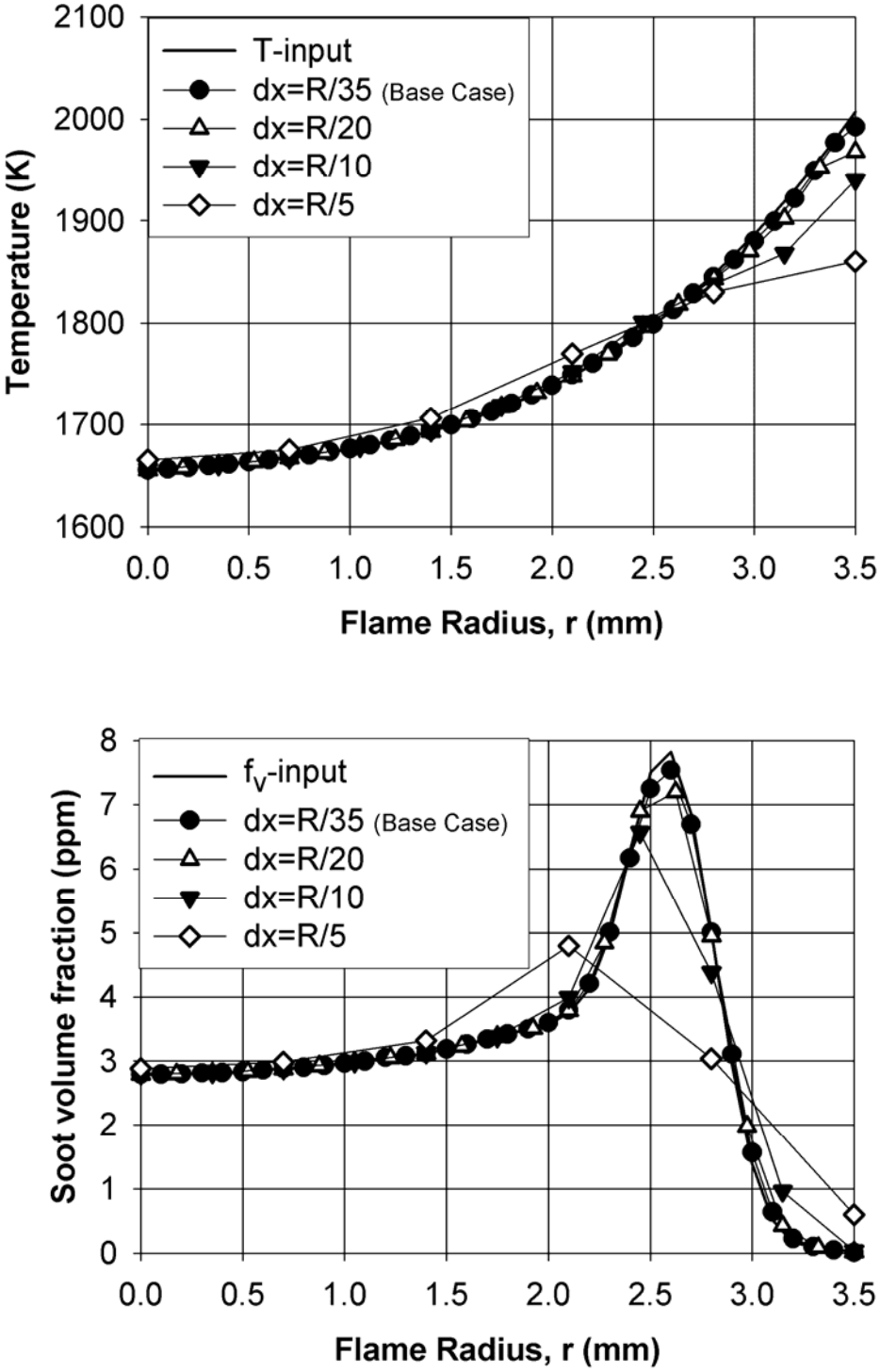

Figure 4.11. Effect of scanning resolution on inferred property profiles

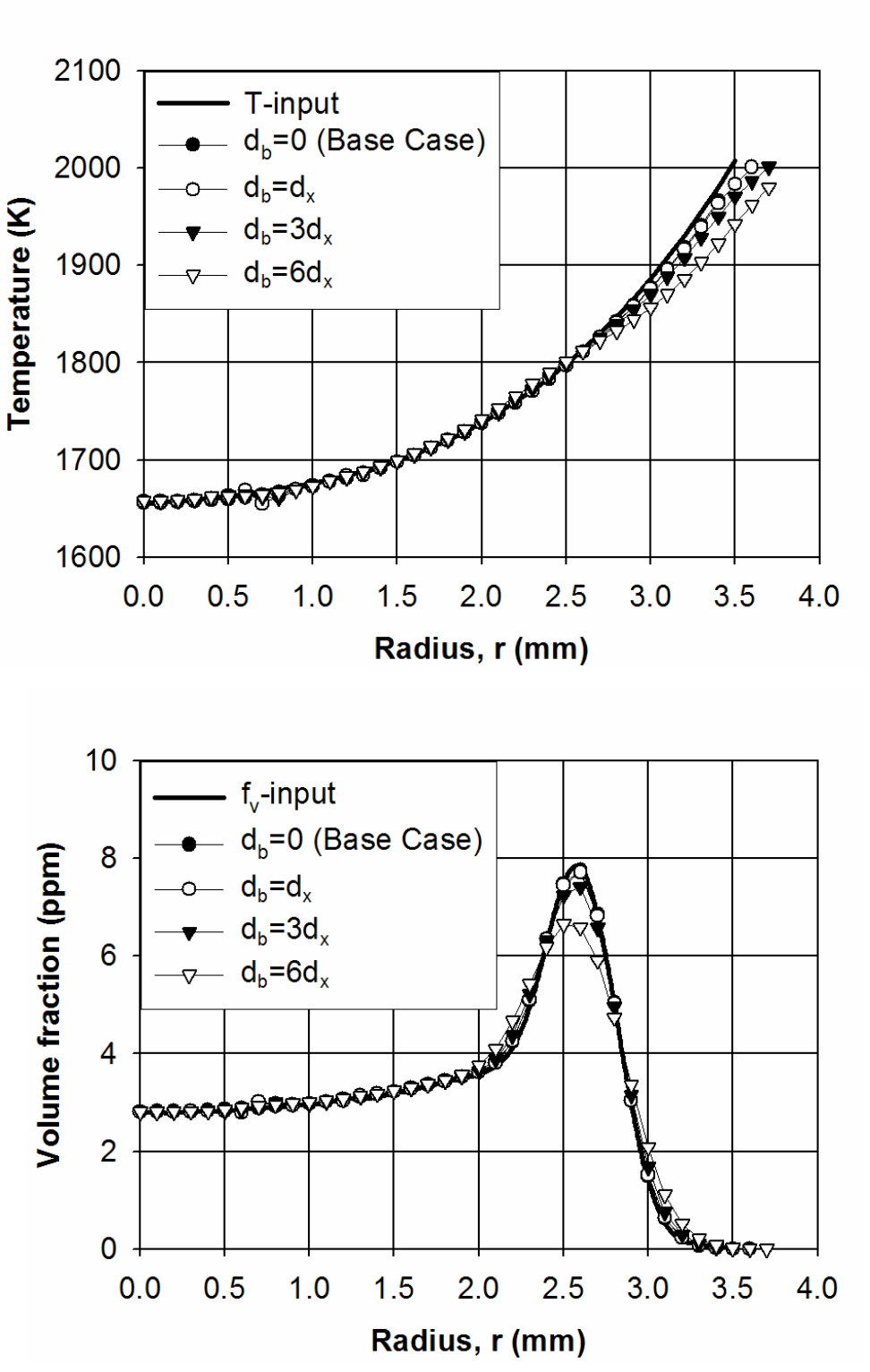

Figure 4.12. Effect of beam diameter on inferred property profiles for fine scanning resolution

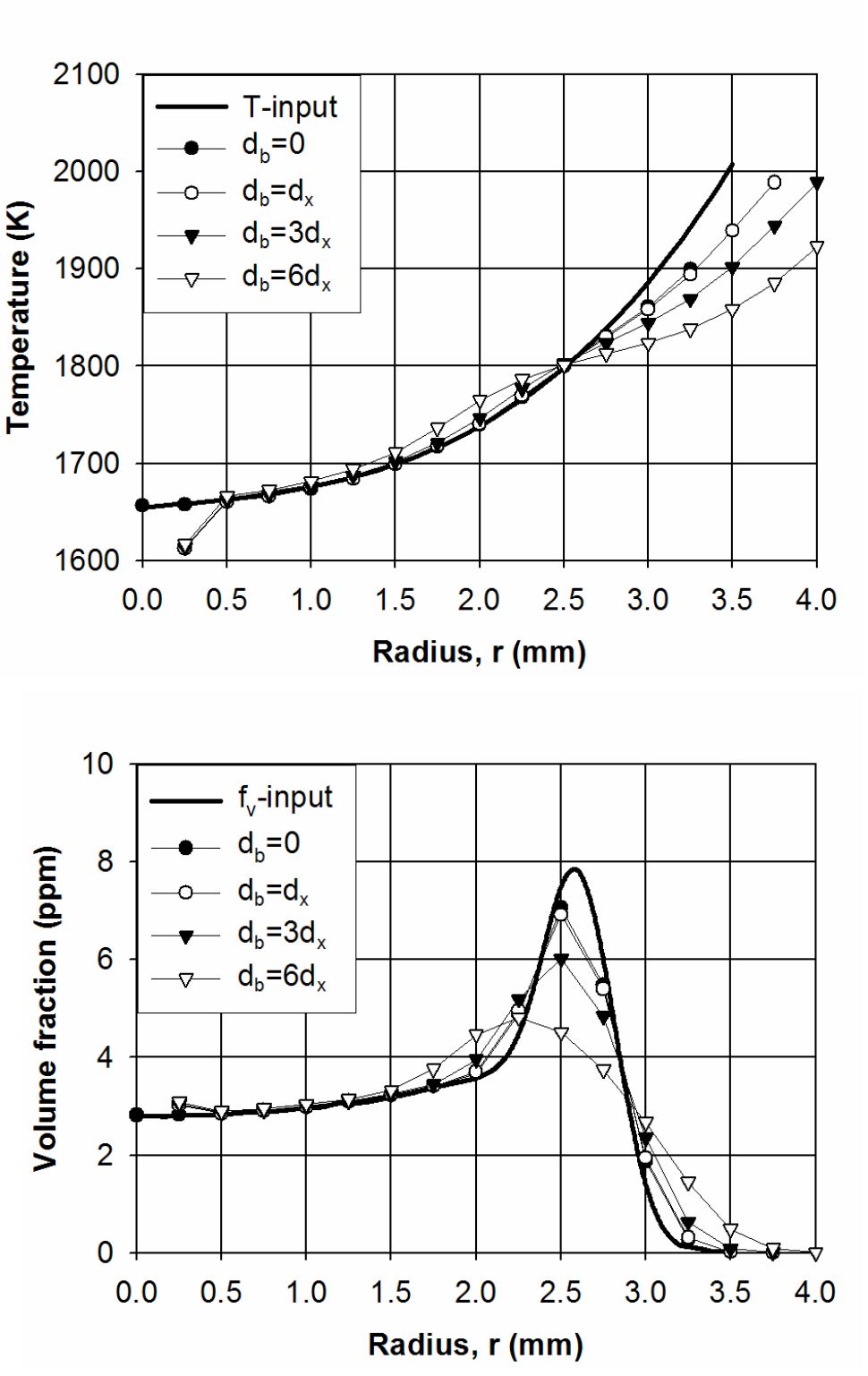

Figure 4.13. Effect of beam diameter on inferred property profiles for coarse scanning resolution

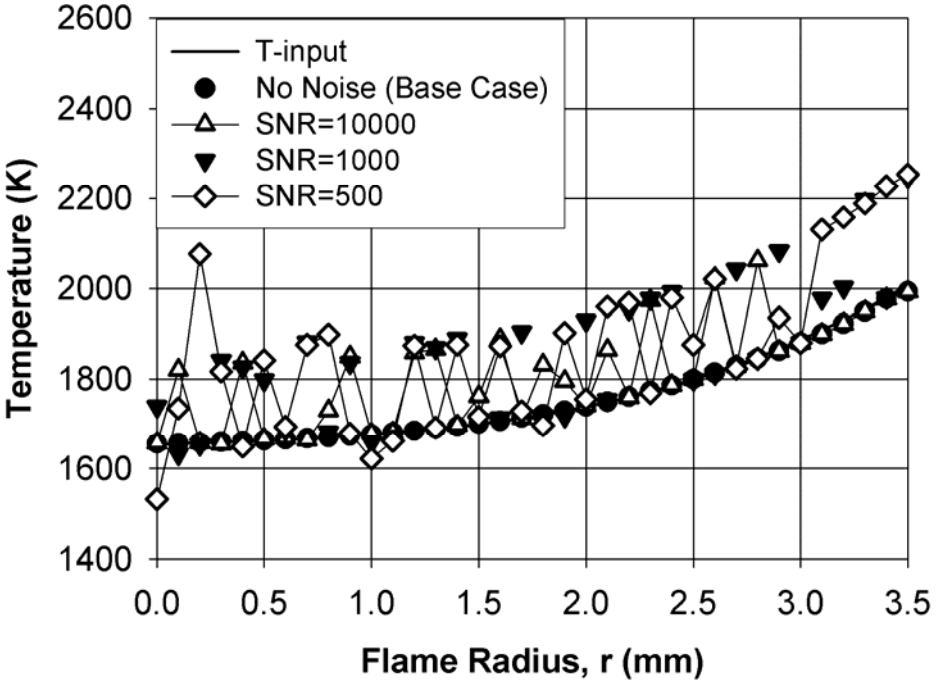

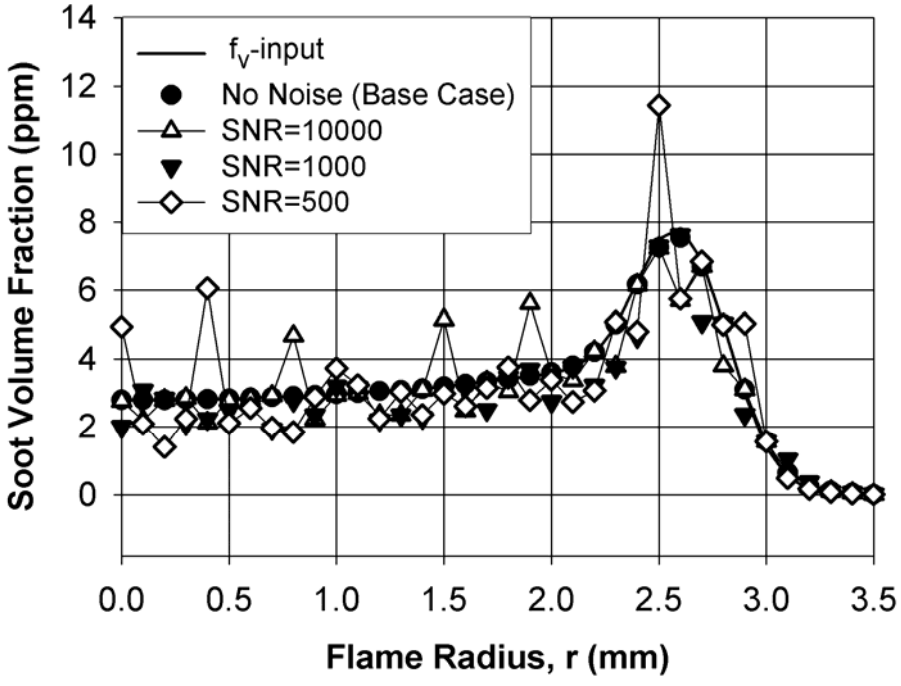

Figure 4.14. Effect of signal to noise ratio on inferred property profiles

Finally, the effect of spectral resolution of input intensity spectra on inferred properties was analyzed. It was found that $\Delta\eta$=100 cm^{-1} resolution results in equally accurate profiles as $\Delta\eta$=25 cm^{-1}, due to the continuous nature of soot emission spectra. However, it is expected that in the presence of spectral noise, high resolution spectrometry will favor stability and accuracy of retrieved of Ψ functions.

4.4.4. Performance of data conditioning algorithm

In order to test the performance of the data conditioning procedure in reducing the limitations induced by the presence of noise, intensity simulations performed with artificial noise embedded to base case simulations were processed by the data conditioning algorithm outlined in section 4.3. The observed Ψ functions which were severely oscillating, resulting in arbitrary refractive index selections without any data conditioning were found to be stabilized as a result of spectral data conditioning. Figure 4.15 displays average inferred Ψ values along the lateral axis in comparison with different average Ψ values obtained from reference sets of Drude-Lorenz dispersion constants outlined in Table 2.3. As stated before, the noisy input intensities for the base case were obtained from the direct code by using the optical constants defined by Set 1. As can be seen from the figure, although there is still some noise, the inferred Ψ functions oscillate closely around that of Set 1 and selection of correct dispersion constant set was enabled by the data conditioning algorithm.

Performance of the data conditioning procedure for inferred temperature and volume fraction profiles was illustrated in Figure 4.16 which compares inferred properties before and after data conditioning with respect to actual properties supplied as input to intensity simulation. As can be seen, data conditioning procedures has managed to filter out the negative effects of noise.

Now that the soot property reconstruction algorithm and data conditioning algorithms are proved to retrieve soot properties successfully, they will be applied to infer soot properties from real measurements.

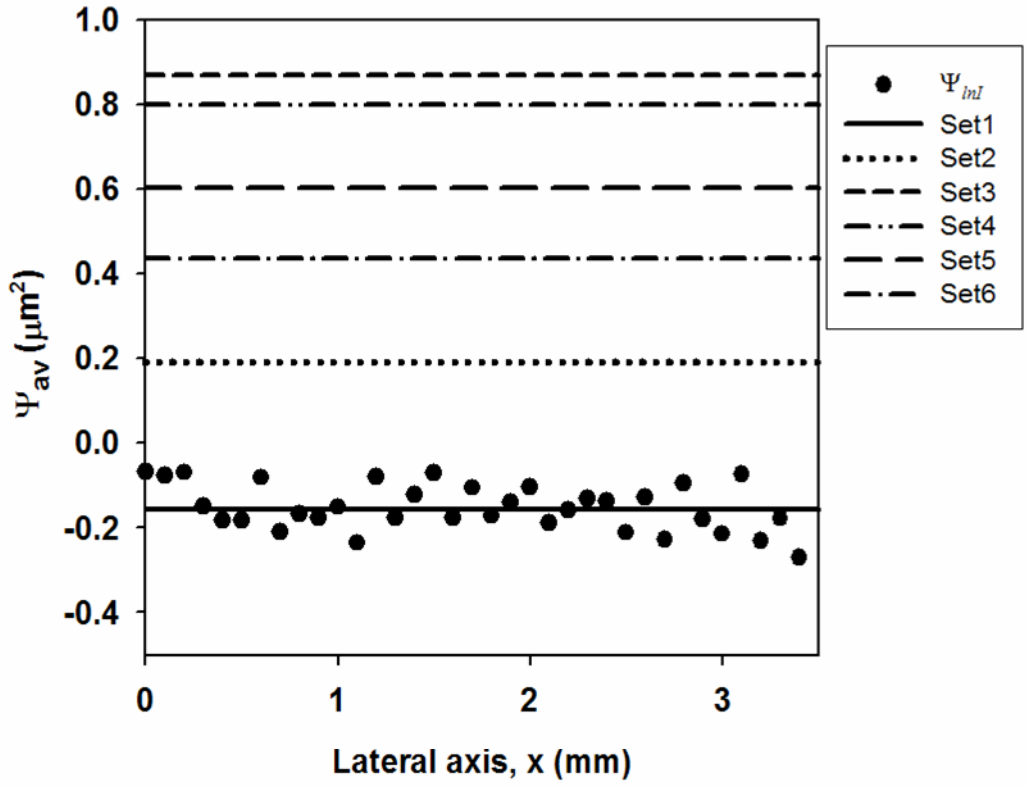

Figure 4.15. Comparison between average Ψ values inferred from conditioned noisy simulated data and reference values obtained from literature dispersion constant sets.

4.4.5. Characterization of experimentally investigated ethylene diffusion flame

Measured and calibrated intensities obtained from the experimental analysis of the ethylene diffusion flame at various levels above the burner (see Chapter 3) are supplied to the property reconstruction algorithm with data conditioning for retrieval of soot characteristics from line-of-sight emission intensities. The first output is the lateral distribution of spectrally averaged Ψ functions at different vertical locations (Figure 4.17) with respect to reference values based on literature dispersion constant sets summarized in Table 2.3. Inspection of the figure leads to selection of Set 5 which was proposed by Habib and Vervisch [23] based on experimental extinction data obtained from an ethylene fueled flame which is quite a reasonable selection as it is the only data set that was obtained for ethylene fueled flames.

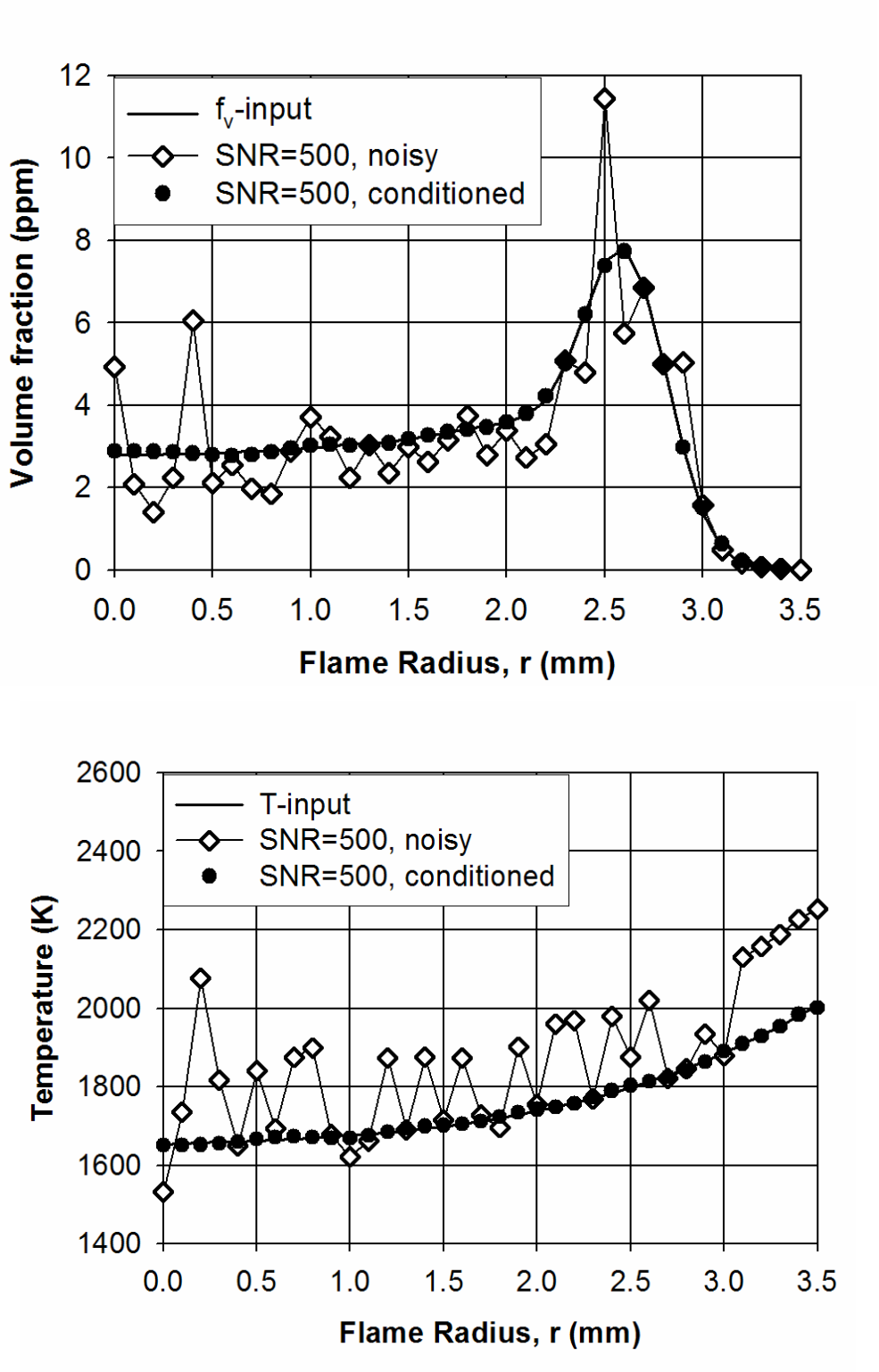

Figure 4.16. Improvement of inferred soot property profiles after implementation of data conditioning algorithm in the presence of noise

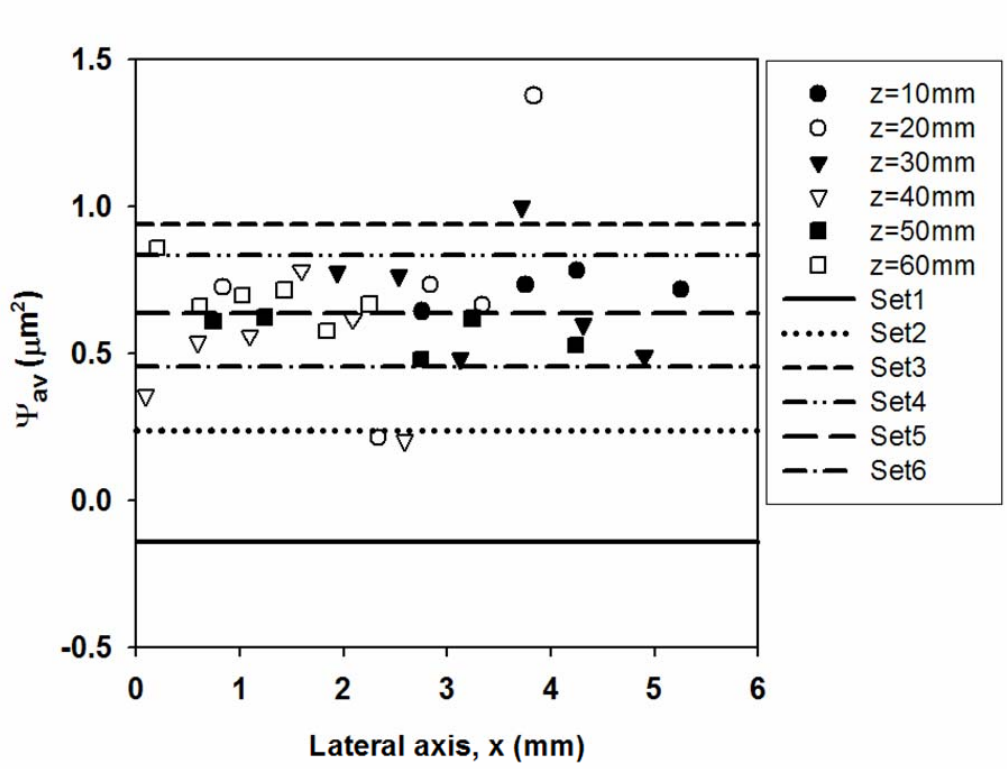

Figure 4.17. Comparison between average Ψ values inferred from measurements on the ethylene diffusion flame and reference values obtained from literature dispersion constant sets.

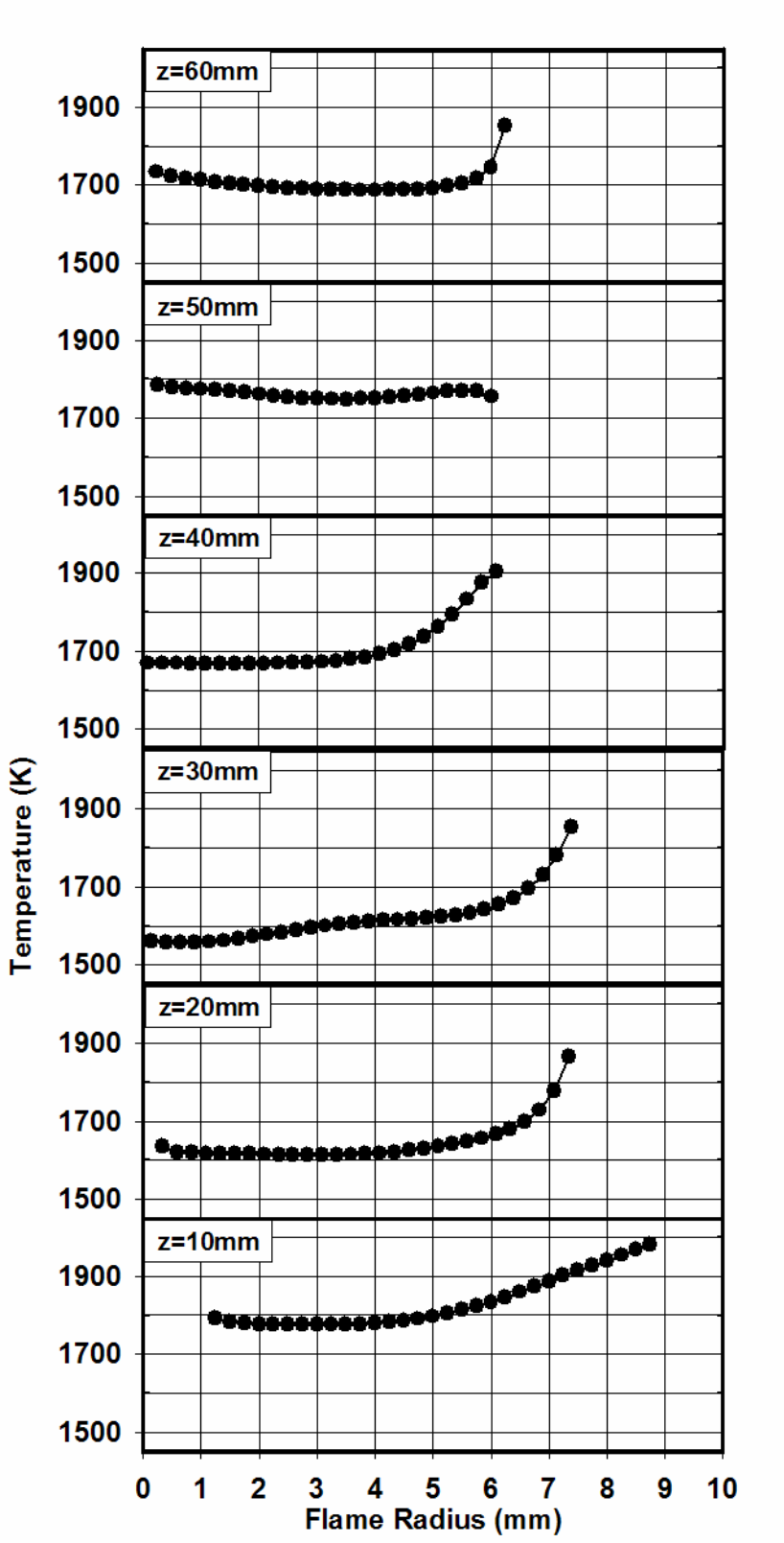

Figure 4.18. Inferred soot temperature profiles for experimentally investigated ethylene diffusion flame

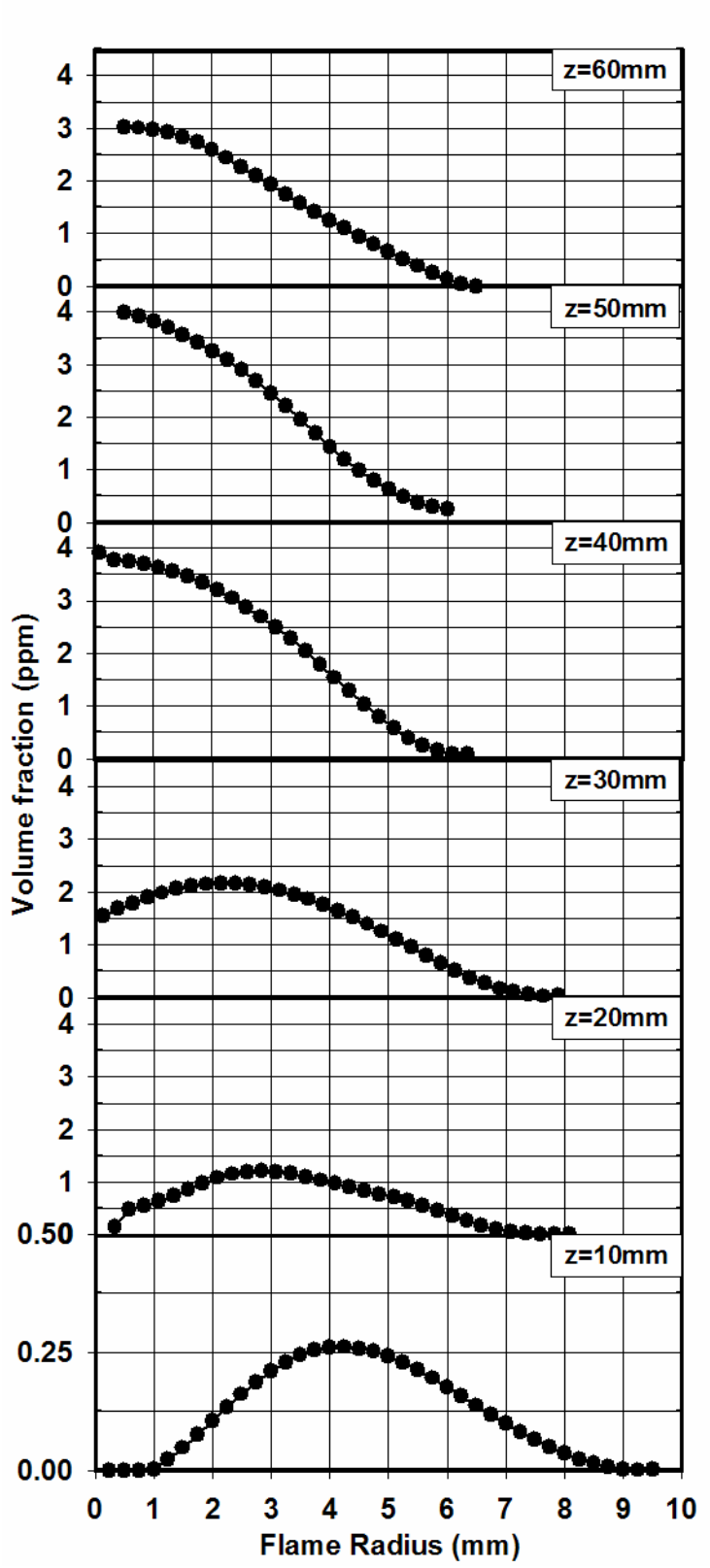

Figure 4.19. Inferred soot volume fraction profiles for experimentally investigated ethylene diffusion flame

Soot temperature and volume fraction profiles inferred using selected optical constants are presented in Figure 4.18 and Figure 4.19. Temperature profiles are nearly flat at flame centre and increase towards the flame edge. At 10 mm above the burner, volume fraction profile along the lateral axis indicates that flame contains no soot at the centre but within an annular region at 3-6 mm radius. As we go downstream to higher locations along the flame, soot concentration increases, the sooty ring narrows and the profile evolves to a parabolic shape. At z = 50 mm, both soot temperature and concentration peak and then decrease at 60 mm.

Unfortunately it is not possible to validate present results by one-to-one comparison with literature data as a study under same conditions is not available. When compared with literature data on soot properties in ethylene/air diffusion flames with close conditions to present study [118, 127, 129, 146], inferred properties are found to be of the same order of magnitude and display similar trends. Good agreement is observed both for temperature and volume fraction in the central region. However, for the profiles at the edges, sooty rings for the measurements in the literature are bounded in narrower and sharper gradients with larger peak values. Temperature gradients are also larger than those of present case. This discrepancy of the present inferred properties is mainly due to the large beam diameter with respect to flame radius dimension of which was limited by sensitivity of the detector of near-infrared FTIR measurements. As was demonstrated in section 4.4.3, Figure 2.36, this experimental limitation is expected to cause retrieved properties to be smoothened and smeared at the edges. As a result it can be said that the spatial resolution determined by combined effect of beam diameter and scan resolution was not sufficient in the present experiments for precise detection of soot properties at the edges.

4.5. CONCLUSIVE REMARKS

An inversion scheme is proposed for optically thin axisymmetric flames for *in-situ* characterization of soot temperature and volume fraction fields via 1-D tomographic reconstruction of line-of-sight flame emission spectra. It is based on reducing uncertainties in refractive index selection by extracting characteristic information on soot refractive index from spectral gradients of emission spectra. Reconstructive capabilities of the method is assessed on a realistic test case representing flame conditions by using a direct model as an experiment simulator and comparing inferred properties with simulator inputs. The effects of physical approximations on the method were analyzed. It was found that the proposed method which is based on negligible self-attenuation assumption can be confidently applied

to flames with optical thickness less than 1.5. Assuming constant refractive index within near-infrared range spectrum leads to considerable errors both in temperature and volume fraction profiles. The proposed inversion scheme was found to be especially powerful in near-infrared range for accurate prediction of flame properties where spectral variation of optical constants is significant. Regarding possible effects of experimental limitations, the refractive index selection algorithm was found to be sensitive to noise, indicating the necessity for smoothing to filter noise associated with measurements. Lateral scanning resolution needs to be adequately fine to resolve sharp soot volume fraction gradients. It was found that the beam diameter which is limited by experimental possibilities introduce considerable dispersing effects especially when the scanning resolution is coarse.

A set of data conditioning steps were developed to accommodate noisy data commonly encountered in practical soot diagnostics. Use was made of simulated noisy intensities to demonstrate effectiveness of the data conditioning procedure. Finally application of the proposed soot diagnostics methodology on the experimentally investigated ethylene diffusion flame was realized by inferring soot properties from measured intensities. Reconstructed properties at are found to be in good agreement at the flame centre when compared with properties reported in literature for similar flames. However at the edges, gradients of sooty zones are rather dispersed when compared with literature trends, due to the expected effect of relatively large beam diameter. Inferred properties are found to display expected effects of experimental limitations. Applicability of the present methodology for nonintrusive soot diagnostics in flames is promising.

A paper resulting from part of the research documented in this chapter was presented in Eurotherm Seminar N^{o}78 “Computational Thermal Radiation in Participating Media II” April 5-7 2006, held in Poitiers, France. The paper was then published in the special issue of Journal of Quantitative Spectroscopy and Radiative Transfer [144].

CHAPTER 5

CONCLUSION

In this thesis study, a novel nonintrusive soot diagnostics methodology has been developed, validated and applied for determination of temperature, volume fraction and refractive index of soot particles formed inside flames by using near-infrared emission spectrometry. The research has been conducted in three main parts which focus on direct model, measurement methodology and soot property reconstruction technique.

In the first part, theoretical analysis of radiative transfer in soot laden-media has been performed by development of a direct model for simulation of spectral line-of-sight emission intensity from axisymmetric sooty flames. Particular emphasis was devoted to estimation of radiative properties of soot agglomerates. Two popular approximate methods, first one being the discrete dipole approximation (DDA) which is a more rigorous but computationally demanding approach, and second one being Rayleigh-Debye-Gans approximation for fractal aggregates (RDG-FA) which is particularly suitable due to its simplicity but questionable regarding its validity for soot aggregates.

- Experimental validation of DDA for prediction of radiative properties of dielectric agglomerates was performed within the frame of a collaborative study, by applying it to the prediction of amplitude and phase of the electric field scattered by a cube-shaped aggregate of 27 dielectric spheres and validating its predictions against microwave measurements and T-Matrix method solutions provided by our collaborators. It was found that DDA predictions are in excellent agreement with both the measurements and T-Matrix predictions.

- In order to be able to compare DDA predictions with microwave measurements, which record scattered field in terms of amplitude and phase, publicly available DDA code, DDSCAT was modified for accurate prediction of amplitude and phase of amplitude scattering matrix elements which are primary parameters that provide complete description of the scattered field and consequently of radiative properties of the target particles. It was found that proposed modifications successfully correct

phase predictions of DDSCAT. Then the modified code was used for the assessment of dipole subdivision requirement for accurate DDA predictions and determination of applicability conditions of DDA by performing tests on single spheres of various size parameters and refractive indices. A correlation was presented to estimate the magnitude and phase errors associated with given size parameter, refractive index and cubic lattice subdivision. Assessment of computational time requirements for different optical constants demonstrated that implementation of DDA with the present specifications is unfeasible for size parameters larger than 4 when Re(m)>2 and Im(m)<0.1 at the same time, due to slow convergence rate.

- Once the validity of DDA was ensured, it was used as a reference to assess applicability of RDG-FA approximation to model near-infrared emission by soot. Two model aggregates were considered for this purpose, one having an idealized sphere-like shape and the other having a fractal structure. The targets were designed so that size of primary particles and optical constants are representative of realistic soot particles. In the first test, RDG-FA, DDA predictions and exact Mie Theory solutions for radiative properties of a compact sphere-like aggregate of 136 spheres were compared. It was found that absorption efficiency factor predictions of RDG-FA approximation are reasonably accurate for compact aggregates of $x_{eq} < 1.5$. In the second test, RDG-FA model predictions for radiative properties were compared against DDA solutions on a computationally generated soot-like fractal aggregate composed of 72 primary particles, with a fractal dimension of 1.7 and a fractal prefactor of 2. RDG-FA predictions for absorption efficiencies were found to be in relatively good agreement with DDA predictions within 15% error margin for $x_{eq} < 2$. For scattering efficiencies, RDG-FA predictions were found to overestimate DDA predictions and discrepancies become considerable beyond $x_{eq} > 1$. Scattering efficiency of this target was found to be negligibly small for x_{eq} less than unity. Under the light of these comparisons, it was concluded that RDG-FA approximation provides sufficiently accurate estimates of radiative properties of relatively small soot aggregates encountered in lab-scale flames and finds a good compromise between accuracy and simplicity. The assumption of negligible scattering under the same conditions was also justified.

- Having established the estimation method and assumptions for radiative properties of soot aggregates, modeling of spectral radiative transfer in soot-laden flames was

carried out by determination of spectral optical constants of soot from Drude-Lorenz model, estimation of radiative properties of soot aggregates from RDG-FA and solution of line-of-sight radiative transfer equation by numerical quadratures to simulate spectral radiative emission intensity emanating from the flame. The direct model was then applied to simulation of near-infrared emission spectroscopy experiments for prediction of radiative intensity emitted by soot particles in a co-flowing ethylene diffusion flame from the literature by using available experimental data on soot temperature and volume fraction.

In the second part, measurement of line-of-sight flame emission intensities was performed by Fourier Transform Infrared (FTIR) spectroscopy on an axisymmetric, laboratory grade, ethylene/air diffusion flame within 1.1-1.7 μm near-infrared range. Calibration, noise characterization, uncertainty assessment and reproducibility tests were elaborated. It was found that spatial fluctuations dominate over spectral noise. A novel noise characterization approach is proposed and demonstrated to take spatial noise into consideration.

In the third part, an inversion algorithm based on tomographic reconstruction of spectral line-of-sight intensities for inferring soot temperature, volume fraction and refractive index in small-scale flames was derived, evaluated and applied. The novelty of the method is associated with reducing uncertainties in refractive index selection by extracting characteristic information on soot refractive index from spectral gradients of emission spectra and taking spectral dependence of refractive index into consideration.

- Reconstructive capabilities of the method was assessed on a realistic test case representing flame conditions by using the direct model as an experiment simulator and comparing inferred properties with simulator inputs. The effects of physical approximations on the method were analyzed. It was found that the proposed method which is based on negligible self-attenuation assumption can be confidently applied to flames with optical thickness less than 1.5. Assuming constant refractive index within near-infrared range spectrum was found to lead to considerable errors both in temperature and volume fraction profiles. The proposed inversion scheme that accounts for spectral variation of refractive index was found to be especially powerful in near-infrared range for accurate prediction of flame properties where spectral variation of optical constants is significant. Regarding possible effects of experimental limitations, the refractive index selection algorithm was found to be

sensitive to noise, indicating the necessity for smoothing to filter noise associated with measurements. Lateral scanning resolution needs to be adequately fine to resolve sharp soot volume fraction gradients. It was also found that the beam diameter which is limited by experimental facilities introduce considerable dispersing effects especially when the scanning resolution is coarse.

- A set of data conditioning strategies was developed to accommodate noisy data commonly encountered in practical soot diagnostics. Tests with simulated noisy intensities demonstrated the success of data conditioning procedure to retrieve accurate predictions in the presence of noise.

- Finally application of the proposed soot diagnostics methodology on the ethylene diffusion flame experimentally investigated in the second part was realized by inferring soot temperature and volume fraction from measured intensities. Refractive index characteristic function inferred from spectral gradient of flame emission was found to be in agreement with reference functions obtained from Habib and Vervisch's dispersion constants reported for ethylene [23] for all locations throughout the flame. Reconstructed properties were found to display expected effects of experimental limitations. Most dominant effect was found to be due to large beam diameter. When compared with properties reported in literature for similar flames, it is concluded that present measurements with a large beam diameter fail to provide precise detection of soot volume fraction gradients near the boundaries. However, the temperatures and volume fractions at the flame centre were found to be in line with observations in the literature.

Under the light of the above investigations, it is concluded that the methodology developed in this thesis presents a promising option for nonintrusive soot diagnostics in flames.

Possible research perspectives following this study are identified as: *i*) further practical validation of the proposed methodology on different flames with improved experimental conditions, *ii*) combining present methodology with other soot diagnostics methods to improve reliability, *iii*) investigation of possibilities to extend the method to optically thick conditions and *iv*) investigation of possibilities to extract more specific information on soot refractive index from observed Ψ functions.

REFERENCES

1. Faeth, G.M. and Köylü, U.O., Soot morphology and optical properties in nonpremixed turbulent flame environments, *Combustion science and technology*, Vol.108, pp 207-229, 1995.

2. Dobbins, R.A. and Megaridis, C.M., Morphology of flame-generated soot as determined by thermophoretic sampling, *Langmuir*, Vol.3, pp 254-259, 1987.

3. Haynes, B.S. and Wagner G., H., Soot formation, *Progress in Energy and Combustion Science*, Vol.7, pp 229-273, 1981.

4. Charalampopoulos, T.T., Morphology and Dynamics of Agglomerated Particulates in Combustion Systems Using Light-Scattering Techniques, *Progress in Energy and Combustion Science*, Vol.18, pp 13-45, 1992.

5. Baillis, D. and Sacadura, J.F., Thermal radiation properties of dispersed media: theoretical prediction and experimental characterization, *Journal of Quantitative Spectroscopy & Radiative Transfer*, Vol.67, pp 327-363, 2000.

6. Manickavasagam, S. and Menguc, M.P., Scattering matrix elements of fractal-like soot agglomerates, *Applied Optics*, Vol.36, pp 1337-1351, 1997.

7. Xu, F., El-Leathy, A.M., Kim, C.H., Faeth, G.M., Soot surface oxidation in hydrocarbon/air diffusion flames at atmospheric pressure, *Combustion and Flame*, Vol.132, pp 43-57, 2003.

8. Warnatz, J., Maas, U., Dibble, R.W., *Combustion Physical and Chemical Fundamentals, Modeling and Simulation, Experiments, Pollutant Formation*, 3rd ed. Springer, Berlin, 2001.

9. Donaldson, K., Li, X.Y., MacNee, W., Ultrafine (nanometre) particle mediated lung injury, *Journal of Aerosol Science*, Vol.29, pp 553-560, 1998.

10. Borman, G.L. and Ragland, K.W., *Combustion Engineering*. McGraw-Hill, Singapore, 1998.

11. Modest, M.F., *Radiative Heat Transfer*. McGraw-Hill, Singapore, 1993.

12. Siegel, R. and Howell, J.R., *Thermal Radiation Heat Transfer*, 1st ed. McGraw-Hill, USA, 1972.

13. Smyth, K.C. and Shaddix, C.R., The elusive history of m = 1.57 - 0.56i for the refractive index of soot, *Combustion and Flame*, Vol.107, pp 314-320, 1996.

14. D'Anna, A., Rolando, A., Allouis, C., Minutolo, P., D'Alessio, A., Shaddix, C., Nano-organic carbon and soot particle measurements in a laminar ethylene diffusion flame, *Proceedings of the Combustion Institute*, 2005.

15. Shaddix, C.R., Palotas, A.B., Megaridis, C.M., Choi, M.Y., Yang, N.Y.C., Soot graphitic order in laminar diffusion flames and a large-scale JP-8 pool fire, *International Journal of Heat and Mass Transfer*, Vol.48, pp 3604-3614, 2005.

16. Yang, B., Hu, B., Köylü, U.O., Mean soot volume fractions in turbulent hydrocarbon flames: A comparison of sampling and laser measurements, *Combustion Science and Technology*, Vol.177, pp 1603-1626, 2005.

17. Neer, A. and Köylü, U.O., Effect of operating conditions on the size, morphology, and concentration of submicrometer particulates emitted from a diesel engine, *Combustion and Flame*, Vol.146, pp 142-154, 2006.

18. Shaddix, C.R. and Williams, T.C., Soot: Giver and taker of light, *American Scientist*, Vol.95, pp 232-239, 2007.

19. Widmann, J., Yang, J.C., Smith, T.J., Manzello, S.L., Mulholland, G.W., Measurement of the optical extinction coefficients of postflame soot in the infrared, *Combustion and Flame*, Vol.134, pp 119-129, 2003.

20. Fletcher, T.H., Ma, J.L., Rigby, J.R., Brown, A.L., Webb, B.W., Soot in coal combustion systems, *Progress in Energy and Combustion Science*, Vol.23, pp 283-301, 1997.

21. Chang, H. and Charalampopoulos, T.T., Determination of the Wavelength Dependence of Refractive-Indexes of Flame Soot, *Proceedings of the Royal Society of London Series A-Mathematical Physical and Engineering Sciences*, Vol.430, pp 577-591, 1990.

22. Charalampopoulos, T.T., Chang, H., Stagg, B., The Effects of Temperature and Composition on the Complex Refractive-Index of Flame Soot, *Fuel*, Vol.68, pp 1173-1179, 1989.

23. Habib, Z.G. and Vervisch, P., On the refractive index of soot at flame temperature, *Combustion Science and Technology*, Vol.59, pp 261-274, 1988.

24. Modest, M.F., *Radiative Heat Transfer*, 2nd ed., Academic Press, USA, 2003.

25. IMSL, *IMSL Math/Library Vol.1 and 2 User's Manual*. 1997, IMSL, Visual Numerics: Houston.

26. Piessens, R., deDoncker-Kapenga, E., Uberhuber, C.W., Kahaner, D.K., *QUADPACK*. Springer-Verlag, New York, 1983.

27. Dalzell, W.H. and Sarofim, A.F., Optical constants of soot and their application to heat flux calculations, *Journal of Heat Transfer-Transactions of the ASME*, Vol.91, pp 100-104, 1969.

28. Kahnert, F.M., Numerical methods in electromagnetic scattering theory, *Journal of Quantitative Spectroscopy and Radiative Transfer*, Vol.79-80, pp 775-824, 2003.

29. Mishchenko, M.I., Hovenier, J.W., Travis, L.D., *Light Scattering by Nonspherical Particles: Theory, Measurements and Applications*. Academic Press, San Diego, 2000.

30. Ku, J.C. and Shim, K.H., A Comparison of Solutions for Light-Scattering and Absorption by Agglomerated or Arbitrarily-Shaped Particles, *Journal of Quantitative Spectroscopy & Radiative Transfer*, Vol.47, pp 201-220, 1992.

31. Comberg, U. and Wriedt, T., Comparison of scattering calculations for aggregated particles based on different models, *Journal of Quantitative Spectroscopy and Radiative Transfer*, Vol.63, pp 149-162, 1999.

32. Kimura, H., Light-scattering properties of fractal aggregates: numerical calculations by a superposition technique and the discrete-dipole approximation, *Journal of Quantitative Spectroscopy & Radiative Transfer*, Vol.70, pp 581-594, 2001.

33. Köylü, U.O. and Faeth, G.M., Optical properties of soot in buoyant laminar diffusion flames, *American Society of Mechanical Engineers, Heat Transfer Division, (Publication) HTD*, 1993.

34. Krishnan, S.S., Lin, K.-C., Wu, J.-S., Faeth, G.M., Optical properties in the visible of soot emitted from turbulent pool fires, *American Society of Mechanical Engineers, Heat Transfer Division, (Publication) HTD*, 1997.

35. Van-Hulle, P., Weill, M.-E., Talbaut, M., Coppalle, A., Comparison of numerical studies characterizing optical properties of soot aggregates for improved EXSCA measurements, *Particle and Particle Systems Characterization*, Vol.19, pp 47-57, 2002.

36. Van-Hulle, P., Talbaut, M., Weill, M., Coppalle, A., Inversion method and experiment to determine the soot refractive index: Application to turbulent diffusion flames, *Measurement Science and Technology*, Vol.13, pp 375-382, 2002.

37. Eymet, V., Brasil, A.M., El Hafi, M., Farias, T.L., Coelho, P.J., Numerical investigation of the effect of soot aggregation on the radiative properties in the infrared region and radiative heat transfer, *Journal of Quantitative Spectroscopy and Radiative Transfer*, Vol.74, pp 697-718, 2002.

38. Zhu, J., Choi, M.Y., Mulholland, G.W., Gbitzo, L.A., Soot scattering measurements in the visible and near-infrared spectrum, *Symposium (International) on Combustion*, Vol.28, pp 439-446, 2000.

39. Di Stasio, S., Konstandopoulos, A.G., Kostoglou, M., Cluster-cluster aggregation kinetics and primary particle growth of soot nanoparticles in flame by light scattering and numerical simulations, *Journal of Colloid and Interface Science*, Vol.247, pp 33-46, 2002.

40. Farias, T.L., Köylü, U.O., Carvalho, M.G., Effects of polydispersity of aggregates and primary particles on radiative properties of simulated soot, *Journal of Quantitative Spectroscopy and Radiative Transfer*, Vol.55, pp 357-371, 1996.

41. Wu, J.-S., Krishnan, S.S., Faeth, G.M., Refractive indices at visible wavelengths of soot emitted from buoyant turbulent diffusion flames, *Journal of Heat Transfer*, Vol.119, pp 230-237, 1997.

42. Mulholland, G.W., Bohren, C.F., Fuller, K.A., Light scattering by agglomerates. Coupled electric and magnetic dipole method, *Langmuir*, Vol.10, pp 2533-2546, 1994.

43. Farias, T.L., Carvalho, M.G., Köylü, U.O., Faeth, G.M., Computational evaluation of approximate Rayleigh-Debye-Gans/fractal-aggregate theory for the absorption and scattering properties of soot, *Journal of Heat Transfer*, Vol.117, pp 152-159, 1995.

44. Köylü, Ü.Ö. Quantitative analysis of in situ optical diagnostics for inferring particle/aggregate parameters in flames: Implications for soot surface growth and total emissivity, *Combustion and Flame*, Vol.109, pp 488-500, 1997.

45. Krishnan, S.S., Lin, K.-C., Faeth, G.M., Optical properties in the visible of overfire soot in large buoyant turbulent diffusion flames, *Journal of Heat Transfer*, Vol.122, pp 517-524, 2000.

46. Köylü, Ü.Ö. and Faeth, G.M., Spectral extinction coefficients of soot aggregates from turbulent diffusion flames, *Journal of Heat Transfer*, Vol.118, pp 415-421, 1996.

47. Köylü, U.O. and Faeth, G.M., Radiative properties of flame-generated soot, *Journal of Heat Transfer*, Vol.115, pp 409-417, 1993.

48. Filippov, A.V., Zurita, M., Rosner, D.E., Fractal-like aggregates: Relation between morphology and physical properties, *Journal of Colloid and Interface Science*, Vol.229, pp 261-273, 2000.

49. Köylü, U.O. and Faeth, G.M., Optical properties of overfire soot in buoyant turbulent diffusion flames at long residence times, *Journal of Heat Transfer*, Vol.116, pp 152-159, 1994.

50. Sorensen, C.M., Light scattering by fractal aggregates: A review, *Aerosol Science and Technology*, Vol.35, pp 648-687, 2001.

51. Thomson, K.A., Snelling, D.R., Smallwood, G.J., Liu, F., Laser induced incandescence measurements of soot volume fraction and effective particle size in a laminar co-annular non-premixed methane/air flame at pressures between 0.5-4.0 MPa, *Applied Physics B: Lasers and Optics*, Vol.83, pp 469-475, 2006.

52. Yang, B. and Köylü, U.O., Detailed soot field in a turbulent non-premixed ethylene/air flame from laser scattering and extinction experiments, *Combustion and Flame*, Vol.141, pp 55-65, 2005.

53. Vaglieco, B.M., Monda, O., Corcione, F.E., Menguc, M.P., Optical and radiative properties of soot agglomerates at D.I. diesel engine exhaust, *American Society of Mechanical Engineers, Heat Transfer Division, (Publication) HTD*, 1993.

54. Iveziç, Z., Mengüç, M.P., Knauer, T.G., A procedure to determine the onset of soot agglomeration from multi-wavelength experiments, *Journal of Quantitative Spectroscopy and Radiative Transfer*, Vol.57, pp 859-865, 1997.

55. Hull, P., Shepherd, I., Hunt, A., Modeling light scattering from Diesel soot particles, *Applied Optics*, Vol.43, pp 3433-3441, 2004.

56. Mulholland, G.W. and Mountain, R.D., Coupled dipole calculation of extinction coefficient and polarization ratio for smoke agglomerates, *Combustion and Flame*, Vol.119, pp 56-68, 1999.

57. Iskander, M.F., Chen, H.Y., Penner, J.E., Optical-Scattering and Absorption by Branched Chains of Aerosols, *Applied Optics*, Vol.28, pp 3083-3091, 1989.

58. Manickavasagam, S. and Mengüç, M.P., Scattering matrix elements of fractal-like soot agglomerates, *Applied Optics*, Vol.36, pp 1337-1351, 1997.

59. Klusek, C., Manickavasagam, S., Mengüç, M.P., Compendium of scattering matrix element profiles for soot agglomerates, *Journal of Quantitative Spectroscopy and Radiative Transfer*, Vol.79-80, pp 839-859, 2003.

60. Iskander, M.F., Chen, H.Y., Penner, J.E., Resonance optical absorption by fractal agglomerates of smoke aerosols, *Atmospheric Environment - Part A General Topics*, Vol.25 A, pp 2563-2569, 1991.

61. Farias, T.L., Carvalho, M.G., Koeylu, U.O., Faeth, G.M., Computational evaluation of approximate Rayleigh-Debye-Gans/fractal-aggregate theory for the absorption and scattering properties of soot, *Journal of Heat Transfer*, Vol.117, pp 152-159, 1995.

62. Farias, T.L., Carvalho, M.G., Köylü, U.O., Faeth, G.M., Light scattering from soot aggregates with radially inhomogeneous primary particles, *Heat and Technology*, Vol.13, pp 27-42, 1995.

63. Lakhtakia, A. and Mulholland, G.W., On two numerical techniques for light-scattering by dielectric agglomerated structures, *Journal of Research of the National Institute of Standards and Technology*, Vol.98, pp 699-716, 1993.

64. Khlebtsov, N.G., Orientational averaging of integrated cross sections in the discrete dipole method, *Optics and Spectroscopy*, Vol.90, pp 408-415, 2001.

65. Jones, A.R., Light scattering for particle characterization, *Progress in Energy and Combustion Science*, Vol.25, pp 1-53, 1999.

66. Sabouroux, P., Stout, B., Michel Geffrin, J., Eyraud, C., Ayrancı, I., Vaillon, R., Selçuk, N., Amplitude and phase of light scattered by micro-scale aggregates of dielectric spheres: Comparison between theory and microwave analogy experiments, *Journal of Quantitative Spectroscopy and Radiative Transfer*, Vol.103, pp 156-167, 2007.

67. Ayrancı, I., Vaillon, R., Selçuk, N., Performance of discrete dipole approximation for prediction of amplitude and phase of electromagnetic scattering by particles, *Journal of Quantitative Spectroscopy and Radiative Transfer*, Vol.103, pp 83-101, 2007.

68. Bohren, C.F. and Huffmann, E.R., *Absorption and Scattering of Light by Small Particles*. Wiley, New York, 1983.

69. Kahnert, F.M., Numerical methods in electromagnetic scattering theory, *Journal of Quantitative Spectroscopy & Radiative Transfer*, Vol.79, pp 775-824, 2003.

70. Purcell, E.M. and Pennypacker, C.R., Scattering and Absorption of Light by Nonspherical Dielectric Grains, *Astrophysical Journal*, Vol.186, pp 705-714, 1973.

71. Draine, B.T. and Flatau, P.J., Discrete-Dipole Approximation for scattering calculations, *Journal of the Optical Society of America a-Optics Image Science and Vision*, Vol.11, pp 1491-1499, 1994.

72. Draine, B.T. and Goodman, J., Beyond Clausius-Mossotti - Wave-propagation on a polarizable point lattice and the discrete dipole approximation, *Astrophysical Journal*, Vol.405, pp 685-697, 1993.

73. Draine, B.T., The discrete dipole approximation for light scattering by irregular targets, in *Light Scattering by Nonspherical Particles: Theory, Measurements and Applications*, Mishchenko, M.I., et al., Editors. Academic Press, San Diego, 2000.

74. Draine, B.T., The Discrete-Dipole Approximation and its application to interstellar graphite grains, *Astrophysical Journal*, Vol.333, pp 848-872, 1988.

75. Collinge, M.J. and Draine, B.T., Discrete-dipole approximation with polarizabilities that account for both finite wavelength and target geometry, *Journal of the Optical Society of America A: Optics and Image Science, and Vision*, Vol.21, pp 2023-2028, 2004.

76. Flatau, P.J., Fast solvers for one dimensional light scattering in the discrete dipole approximation, *Optics Express*, Vol.12, pp 3149-3155, 2004.

77. Flatau, P.J., Improvements in the discrete-dipole approximation method of computing scattering and absorption, *Optics Letters*, Vol.22, pp 1205-1207, 1997.

78. Singham, S.B. and Bohren, C.F., Light scattering by an arbitrary particle: A physical reformulation of the coupled dipole method, *Optics Letters*, Vol.12, pp 10-12, 1987.

79. Singham, S.B. and Bohren, C.F., Light scattering by an arbitrary particle: the scattering-order formulation of the coupled-dipole method., *Journal of the Optical Society of America. A, Optics and image science*, Vol.5, pp 1867-1872, 1988.

80. Singham, S.B. and Bohren, C.F., Hybrid method in light scattering by an arbitrary particle, *Applied Optics*, Vol.28, pp 517-522, 1989.

81. Hoekstra, A.G., Frijlink, M., Waters, L.B.F.M., Sloot, P.M.A., Radiation forces in the discrete-dipole approximation, *Journal of the Optical Society of America A: Optics and Image Science, and Vision*, Vol.18, pp 1944-1953, 2001.

82. Hoekstra, A.G., Grimminck, M.D., Sloot, P.M.A., Large scale simulations of elastic light scattering by a fast discrete dipole approximation, *International Journal of Modern Physics C*, Vol.9, pp 87-102, 1998.

83. Gutkowicz-Krusin, D. and Draine, B.T., *Propagation of electromagnetic waves on a rectangular lattice of polarizable points*, 2004, <http://xxx.arxiv.org/abs/astro-ph/0403082>, last date accessed: 09.07.2007.

84. Draine, B.T. and Flatau, P.J., *User guide for the discrete dipole approximation code DDSCAT.6.1,* 2004, <http://arxiv.org/abs/astro-ph/0409262>, last date accessed: 09.07.2007.

85. Temperton, C., A generalized prime factor FFT algorithm for any $N=2^p3^q5^r$, *SIAM Journal on Scientific and Statistical Computing*, Vol.13, pp 676-686, 1992.

86. van der Vorst, H.A., BI-CGSTAB: a fast and smoothly converging variant of BI-CG for the solution of nonsymmetric linear systems, *SIAM Journal on Scientific and Statistical Computing*, Vol.13, pp 631-644, 1992.

87. da Cunha, R.D. and Hopkins, T., *Parallel Iterative Methods (PIM) package*, 2003, <http://euler.mat.ufrgs.br/~rcunha/pim.html>, last date accessed: 09.07.2007.hy

88. van de Hulst, H.C., *Light Scattering by Small Particles*. Dover Publications, New York, 1981.

89. Kerker, M., *The scattering of light, and other electromagnetic radiation*. Academic Press, New York, 1969.

90. Forrest, S.R. and Witten, T.A., Long-Range Correlations in Smoke-Particle Aggregates, *Journal of Physics A-Mathematical and General*, Vol.12, pp L109-L117, 1979.

91. Martin, J.E. and Hurd, A.J., Scattering from Fractals, *Journal of Applied Crystallography*, Vol.20, pp 61-78, 1987.

92. Jullien, R. and Botet, R., *Aggregation and Fractal Aggregates*. World Scientific Publishing Co., Singapore, 1987.

93. Dobbins, R.A. and Megaridis, C.M., Absorption and Scattering of Light by Polydisperse Aggregates, *Applied Optics*, Vol.30, pp 4747-4754, 1991.

94. Sorensen, C.M., Cai, J., Lu, N., Light-Scattering Measurements of Monomer Size, Monomers Per Aggregate, and Fractal Dimension for Soot Aggregates in Flames, *Applied Optics*, Vol.31, pp 6547-6557, 1992.

95. Sorensen, C.M., Cai, J., Lu, N., Test of static structure factors for describing light scattering from fractal soot aggregates, *Langmuir*, Vol.8, pp 2064-2069, 1992.

96. Sorensen, C.M., Lu, N., Cai, J., Fractal Cluster-Size Distribution Measurement Using Static Light-Scattering, *Journal of Colloid and Interface Science*, Vol.174, pp 456-460, 1995.

97. Wang, G. and Sorensen, C.M., Experimental test of the Rayleigh-Debye-Gans theory for light scattering by fractal aggregates, *Applied Optics*, Vol.41, pp 4645-4651, 2002.

98. Köylü, U.O. and Faeth, G.M., Optical-properties of soot in buoyant laminar diffusion flames, *Journal of Heat Transfer-Transactions of the ASME*, Vol.116, pp 971-979, 1994.

99. Farias, T.L., Köylü, U.O., Carvalho, M.G., Range of validity of the Rayleigh-Debye-Gans theory for optics of fractal aggregates, *Applied Optics*, Vol.35, pp 6560-6567, 1996.

100. Mandelbrot, B.B., *The Fractal Geometry of Nature*. W. H. Freeman, New York, 1982.

101. Nelson, J., Test of a Mean Field-Theory for the Optics of Fractal Clusters, *Journal of Modern Optics*, Vol.36, pp 1031-1057, 1989.

102. Chen, H.Y., Iskander, M.F., Penner, J.E., Light-Scattering and Absorption by Fractal Agglomerates and Coagulations of Smoke Aerosols, *Journal of Modern Optics*, Vol.37, pp 171-181, 1990.

103. Köylü, U.O. and Faeth, G.M., Optical-Properties of Overfire Soot in Buoyant Turbulent- Diffusion Flames at Long Residence Times, *Journal of Heat Transfer-Transactions of the ASME*, Vol.116, pp 152-159, 1994.

104. Köylü, U.O. and Faeth, G.M., Radiative Properties of Flame-Generated Soot, *Journal of Heat Transfer-Transactions of the ASME*, Vol.115, pp 409-417, 1993.

105. Puri, R., Richardson, T.F., Santoro, R.J., Dobbins, R.A., Aerosol Dynamic Processes of Soot Aggregates in a Laminar Ethene Diffusion Flame, *Combustion and Flame*, Vol.92, pp 320-333, 1993.

106. Sorensen, C.M., Cai, J., Lu, N., Test of Static Structure Factors for Describing Light-Scattering from Fractal Soot Aggregates, *Langmuir*, Vol.8, pp 2064-2069, 1992.

107. Ku, J.C. and Shim, K.H., Optical Diagnostics and Radiative Properties of Simulated Soot Agglomerates, *Journal of Heat Transfer-Transactions of the ASME*, Vol.113, pp 953-958, 1991.

108. Berry, M.V. and Percival, I.C., Optics of Fractal Clusters Such as Smoke, *Optica Acta*, Vol.33, pp 577-591, 1986.

109. Farias, T.L., Carvalho, M.G., Köylü, U.O., Faeth, G.M., Computational Evaluation of Approximate Rayleigh-Debye- Gans/Fractal-Aggregate Theory for the Absorption and Scattering Properties of Soot, *Journal of Heat Transfer-Transactions of the ASME*, Vol.117, pp 152-159, 1995.

110. Köylü, U.O., Faeth, G.M., Farias, T.L., Carvalho, M.G., Fractal and projected structure properties of soot aggregates, *Combustion and Flame*, Vol.100, pp 621-633, 1995.

111. Bunde, A. and Havlin, S., *Fractals and Disordered Systems*. Springer-Verlag, 1991.

112. Gouyet, J.-F., *Physics and Fractal Structures*. Springer Verlag, 1996.

113. Brasil, A.M., Farias, T.L., Carvalho, M.G., Evaluation of the fractal properties of cluster-cluster aggregates, *Aerosol Science and Technology*, Vol.33, pp 440-454, 2000.

114. Mullins, J. and Williams, A., The optical properties of soot: a comparison between experimental and theoretical values, *Fuel*, Vol.66, pp 277-280, 1987.

115. Charalampopoulos, T.T. and Chang, H., In-situ optical properties of soot particles in the wavelength range from 340 nm to 600 nm, *Combustion Science and Technology*, Vol.59, pp 401-421, 1988.

116. Lee, S.C. and Tien, C.L., Optical constants of soot in hydrocarbon flames, *Eighteenth Symposium (International) on Combustion*, The Combustion Institute, 1981.

117. Stagg, B.J. and Charalampopoulos, T.T., Refractive-Indexes of Pyrolytic-Graphite, Amorphous-Carbon, and Flame Soot in the Temperature-Range 25-Degrees-C to 600-Degrees-C, *Combustion and Flame*, Vol.94, pp 381-396, 1993.

118. Snelling, D.R., Thomson, K.A., Smallwood, G.J., Gulder, O.L., Weckman, E.J., Fraser, R.A., Spectrally resolved measurement of flame radiation to determine soot temperature and concentration, *AIAA Journal*, Vol.40, pp 1789-1795, 2002.

119. Smith, S.W., *Digital Signal Processing: A Practical Guide for Engineers and Scientists*. Newnes, Elsevier, USA, 2003.

120. Griffiths, P.R. and de Haseth, J.A., *Fourier Transform Infrared Spectrometry*. John Wiley and Sons, New York, 1986.

121. Jackson, R.S., Continuous Scanning Interferometers for Mid-Infrared Spectroscopy, in *Handbook of Vibrational Spectroscopy*, Chalmers, J.M., Griffiths, P.R., Editors. John Wiley & Sons Ltd, USA, 2002.

122. Herres, W. and Gronholz, J., Understanding FT-IR Data Processing, Part 1: Data acquisition and Fourier transformation, *Instruments and Computers (Reprint)*, Vol.1, pp, 1984.

123. Gronholz, J. and Herres, W., Understanding FT-IR Data Processing, Part 2: Details of the spectrum calculation, *Instruments and Computers (Reprint)*, Vol.3, pp, 1985.

124. Skoog, D.A., Holler, F.J., Nieman, T.A., *Principles of Instrumental Analysis*, 5th ed. Saunders College Pub., Philadelphia, 1998.

125. Copalle, A. and Joyeux, D., *Combustion Science and Technology*, Vol.93, pp 375-386, 1993.

126. Solomon, P.R., Best, P.E., Carangelo, R.M., Markham, J.R., Chien, P.L., Santoro, R.J., Semerjian, H.G., *Twenty-first symposium (international) on combustion,* Pittsburgh, The Combustion Institute, 1987.

127. Best, P.E., Chien, P.L., Carangelo, R.M., Solomon, P.R., Danchak, M., Ilovici, I., Tomographic Reconstruction of FT-IR Emission and Transmission Spectra in a Sooting Laminar Diffusion Flame - Species Concentrations and Temperatures, *Combustion and Flame*, Vol.85, pp 309-318, 1991.

128. Solomon, P.R. and Best, P.E., Fourier transform infrared emission/transmission spectroscopy in flames, in *Combustion Measurements*, Chigier, N., Editor. Hemisphere, USA, 1991.

129. De Iuliis, S., Barbini, M., Benecchi, S., Cignoli, F., Zizak, G., Determination of the soot volume fraction in an ethylene diffusion flame by multiwavelength analysis of soot radiation, *Combustion and Flame*, Vol.115, pp 253-261, 1998.

130. Bourayou, R., Vaillon, R., Sacadura, J.-F., FTIR low resolution emission spectrometry of a laboratory-scale diffusion flame: experimental set-up, *Experimental Thermal and Fluid Science*, Vol.26, pp 181-187, 2002.

131. Zheng, Y. and Gore, J.P., Measurements and inverse calculations of spectral radiation intensities of a turbulent ethylene/air jet flame, *Proceedings of the Combustion Institute*, Vol.30, pp 727-734, 2005.

132. Yousefian, F., Sakami, M., Lallemand, M., Recovery of temperature and species concentration profiles in flames using low-resolution infrared spectroscopy, *Journal of Heat Transfer-Transactions of the ASME*, Vol.121, pp 268-279, 1999.

133. Yousefian, F., Application des techniques radiatives inverses à la métrologie thermique par voie spectrométrique infrarouge (Application of inverse radiative techniques in heat transfer metrology by using spectrometric infrared data), *PhD*, ENSMA, 1998.

134. Bouryaou, R., Etude spectrométrique du rayonnement infrarouge des suies dans les flammes de diffusion laminaires, *PhD*, CETHIL, 2002.

135. Lindermeir, E., Haschberger, P., Tank, V., Dietl, H., Calibration of a Fourier-Transform Spectrometer Using 3 Blackbody Sources, *Applied Optics*, Vol.31, pp 4527-4533, 1992.

136. Mark, H. and Workman, J., *Statistics in Spectroscopy*. Academic Press, USA, 1991.

137. Bak, J. and Clausen, S., Signal-to-noise ratio of FT-IR CO gas spectra, *Applied Spectroscopy*, Vol.53, pp 697-700, 1999.

138. Ayrancı, I., Vaillon, R., Selçuk, N., Near-Infrared Emission Spectrometry Measurements for Nonintrusive Soot Diagnostics in Flames, *The Fifth International Symposium on Radiative Transfer,* June 17-23 Bodrum, Turkey, 2007.

139. Ayrancı, I., Vaillon, R., Selçuk, N., Near-Infrared Emission Spectrometry Measurements for Nonintrusive Soot Diagnostics in Flames, *Journal of Quantitative Spectroscopy & Radiative Transfer*, (accepted for publication) 2007.

140. Hall, R.J. and Bonczyk, P.A., Sooting Flame Thermometry Using Emission Absorption Tomography, *Applied Optics*, Vol.29, pp 4590-4598, 1990.

141. Dong, J.Y. and Kearney, R.J., Symmetrizing, Filtering and Abel Inversion Using Fourier-Transform Techniques, *Journal of Quantitative Spectroscopy & Radiative Transfer*, Vol.46, pp 141-149, 1991.

142. Woodbury, K.A., *Inverse Engineering Handbook*. CRC Press, Boca Raton, 2003.

143. Dasch, C.J., One-Dimensional Tomography - A Comparison of Abel, Onion-Peeling, and Filtered Backprojection Methods, *Applied Optics*, Vol.31, pp 1146-1152, 1992.

144. Ayrancı, I., Vaillon, R., Selçuk, N., Andre, F., Escudie, D., Determination of soot temperature, volume fraction and refractive index from flame emission spectrometry, *Journal of Quantitative Spectroscopy & Radiative Transfer*, Vol.104, pp 266-276, 2007.

145. de Boor, C., *A Practical Guide to Splines*. Springer-Verlag, New York, 1978.

146. Honnery, D.R. and Kent, J.H., Soot Formation in Long Ethylene Diffusion Flames, *Combustion and Flame*, Vol.82, pp 426-434, 1990.

147. Air Liquide, *Gas Encyclopaedia*. Elsevier, Paris, 2005.

148. Perry, R.H. and Green, D. eds., *Perry's Chemical Engineering Handbook*. 5th ed. 1984, McGraw-Hill.

APPENDIX A

Modifications on DDSCAT v.6.1 Code

Modifications implemented on the original DDSCAT code to enable correct predictions of phases of ASM elements are outlined below [67].

Subroutine EVALE:

- New variables NXMIN,NXMAX,NYMIN,NYMAX,NZMIN,NZMAX declared as integers
- Following lines inserted at the beginning of the executable statements:

```
C Find minimum limits of dipole position array IXYZ0
      NXMIN=IXYZ0(1,1)
      NYMIN=IXYZ0(1,2)
      NZMIN=IXYZ0(1,3)
      DO IA=2,NAT0
         IF(IXYZ0(IA,1).LT.NXMIN)NXMIN=IXYZ0(IA,1)
         IF(IXYZ0(IA,2).LT.NYMIN)NYMIN=IXYZ0(IA,2)
         IF(IXYZ0(IA,3).LT.NZMIN)NZMIN=IXYZ0(IA,3)
      ENDDO
C Subtract phase difference from origin (centre of target) to corner from
incident E field
            CXE00=CXE00*CEXP(CXI*(AKD(1)*(NXMIN-1)*DX(1)+
     &                            AKD(2)*(NYMIN-1)*DX(2)+
     &                            AKD(3)*(NZMIN-1)*DX(3)))
```

Subroutine EXTEND:

- Following lines are inserted at the end of the executable statements:

```
C Move origin of dipole positions from corner back to original origin
      DO JA=1,NAT0
         IX(JA)=IX(JA)-1+IXMIN
         IY(JA)=IY(JA)-1+IYMIN
         IZ(JA)=IZ(JA)-1+IZMIN
      ENDDO
```

Once these corrections are implemented, the magnitudes and phases of ASM elements are obtained from CXS1, CXS2, CXS3, and CXS4 parameters calculated in the subroutine GETMUELLER.

APPENDIX B

Applicability Conditions of DDA for Prediction of ASM Elements

Accuracy of DDA depends on the number of dipoles used for representation of the target. Different physical specifications require different dipole subdivisions. For example a small size parameter sphere with small refractive index requires less number of dipoles than a large size parameter/large refractive index combination. In any given problem, the target needs to be discretized so as to satisfy the following two criteria [71]: *i*) the dipole size represented by the lattice spacing d is small compared with the wavelength within the target material, *ii*) the dipole size is small enough to represent the required target shape satisfactorily. The first criterion is met when ratio of dipole size to wavelength of the beam within the target medium, represented by the dimensionless parameter $|m|kd$, is less than unity. In contrast to this well defined first criterion, the second one is strongly problem dependent. Numerical experiments are necessary to determine the lattice subdivision that ensures DDA to be a valid approximation for the specific target shape, size parameter and refractive index under consideration. Naturally, the first stage of numerical experiments comprises tests on single spheres to determine effects of size parameter and refractive index on discretization requirements. As exact solutions are not available for most irregularly shaped targets, the validity criteria derived for single spheres provide a basis for the validity criteria for complex shaped particles which are, in fact, the problems where DDA is particularly advantageous as it can flexibly be applied to any target shape.

Validity criteria for application of DDSCAT was previously analyzed on single sphere problems based on a series of numerical computations and error analysis of predicted efficiency factors with respect to exact Mie theory solutions for $x < 12$ and various refractive indices; m =1.1+i0.001, m =1.33+i0.01, m =1.7+i0.1 , m =2+i, m = 3+i4 [72, 74]. Based on these studies, Draine and Flatau recommend to set the resolution so that $|m|kd < 1$ to obtain reasonably accurate efficiency factor predictions from DDSCAT and to keep $|m|kd < 0.5$ if the parameter of interest is a variable with angular dependence such as phase function [84]. It was also reported that DDA works well for materials with $|m-1| \leq 3$ and target dimension $D_d \leq 5\lambda$ [8].

The above mentioned validity criteria were established in terms of secondary scattering properties such as efficiency factors, differential cross sections as they are the conventionally measurable quantities. The objective of the present analysis is to quantify the predictive performance of DDA and to determine applicability conditions for accurate prediction of the primary variables i.e. magnitude and phase of the ASM elements which inherently provide a complete description to the scattering phenomena under consideration.

To achieve this objective, a parametric study is carried out to evaluate accuracy, computational efficiency and convergence performance of the modified DDSCAT code at different physical conditions and target discretizations. Variable parameters are the size parameter of the target ($x_D = \pi D/\lambda$, where D is target diameter), real and imaginary parts of refractive index and order of the cubic lattice subdivision represented by the number of dipoles along the characteristic dimension of the target (D/d). Systematic successive runs were carried out for 4 different lattice resolutions for each of 180 physical situations obtained by combination of the parameters summarized in Table B.1.

Table B.1. Physical and computational variables of the parametric study

Re(m)	1.1	1.5	1.75	2.0	2.25	2.5
Im(m)	0	0.1	0.25	0.5	0.75	1
x_D	0.5	1	2	4	8	
D/d	8	16	32	64		

The ASM elements, S_1 and S_2, which are the only nonzero elements for single spheres are calculated by the modified DDSCAT code and Bohren and Huffmann's Mie Theory code [68]. Then percent errors for magnitudes are evaluated relative to the maximum magnitude value in the whole angular domain which is the forward direction magnitude for dielectrics as follows

$$\Delta|S_i|(\theta)=\left|\frac{|S_i|_{DDA}(\theta)\ -\ |S_i|_{Mie}(\theta)}{|S_i|_{Mie}(\theta=0)}\right|\times 100 \tag{B.1}$$

where subscript i stands for the index of the ASM element. As the domain of variance of magnitudes display several orders of magnitude difference depending upon the physics of the problem (i.e., compare magnitudes at x = 2 and x = 8 in Figure 2.7a and b in section 2.2.5.1.3), normalization of error with maxima enables meaningful comparisons of magnitude errors among different problems. On the other hand, the domain of variance for phase is always within [-π,π] and there is no need for normalization to compare errors on the same scale. Absolute phase errors are evaluated from

$$\Delta\delta_i(\theta)=\left|\delta_{i,DDA}(\theta)-\delta_{i,Mie}(\theta)\right| \tag{B.2}$$

In order to be able to analyze variation of degree of accuracy of the present DDA implementation with respect to physical variables and discretization parameters, for each individual run, average and maximum magnitude and phase errors are calculated over the angular variation of the errors of both S_1 and S_2 from following relations

$$\Delta|S|_{avg}=\frac{1}{2\pi}\left(\int_0^{\pi}\Delta|S_1|(\theta)\cdot d\theta+\int_0^{\pi}\Delta|S_2|(\theta)\cdot d\theta\right) \tag{B.3}$$

$$\Delta|S|_{\max}=\max\left[\left(\max\Delta|S_1|(\theta)\right),\left(\max\Delta|S_2|(\theta)\right)\right] \tag{B.4}$$

$$\Delta\delta_{avg}=\frac{1}{2\pi}\left(\int_0^{\pi}\Delta\delta_1 d\theta+\int_0^{\pi}\Delta\delta_2 d\theta\right) \tag{B.5}$$

$$\Delta\delta_{\max}=\max\left[\left(\max\Delta\delta_1(\theta)\right),\left(\max\Delta\delta_2(\theta)\right)\right] \tag{B.6}$$

In order to test the validity criteria reported in the literature, variation of these errors is analyzed with respect to $|m|kd$. Figure B.1a-d display variations of average and maximum errors for magnitude and phase in log-log scale. Although a linear trend is evident from the plot, the standard deviation is quite large. For instance, for the same $|m|kd$ value of 0.5, the average and maximum magnitude errors can vary between 10^{-4}-0.1% and 0.1-10%. Best lines of these plots, which may serve for rough error estimates are evaluated via linear regression of $|m|kd<1$ data and displayed on the plots. With regard to the previously reported criterion of $|m|kd<0.5$, it is observed that magnitude errors can be suppressed below the reasonable limit of 10% with this condition. For phase predictions, although $|m|kd<0.5$ ensures average errors to be less than only 0.3 degrees (0.005rad), considerable maximum errors can be encountered depending upon the physics and discretization of the problem. Evidently, the accuracy of a DDA implementation can not be related solely to $|m|kd$.

The parameter $|m|kd$ is actually a combination of the 3 factors that affect the accuracy of DDA: lattice subdivision, size parameter and refractive index. It can be expressed in terms of these parameters as follows

$$|m|kd = \frac{2|m|x_D}{(D/d)} \tag{B.7}$$

where D is the characteristic dimension of the target (sphere diameter in this case), D/d stands for the number of discrete dipoles along the characteristic dimension axis and x_D ($=\pi D/\lambda$) is the size parameter of the target in terms of its characteristic dimension. The large variances in Figure B.1 imply the necessity to consider each parameter as separate factors that determine the level of accuracy of DDA.

Firstly, the effect of lattice subdivision on amplitude and phase is demonstrated in Figure B.2 and Figure B.3 on a sphere of $x_D = 4$ and $m = 1.75+i0.5$. As can be seen from the figures, the parameter S_2 that determine scattering at parallel polarized incidence is more susceptible to errors than S_1. The results obtained from $D/d=8$ illustrate typical nature of errors caused by inadequate target discretization. For these specific physical conditions under consideration, $D/d=32$ provides grid independent solutions however in other cases i.e. for larger particles, it is necessary to represent the target with more dipoles.

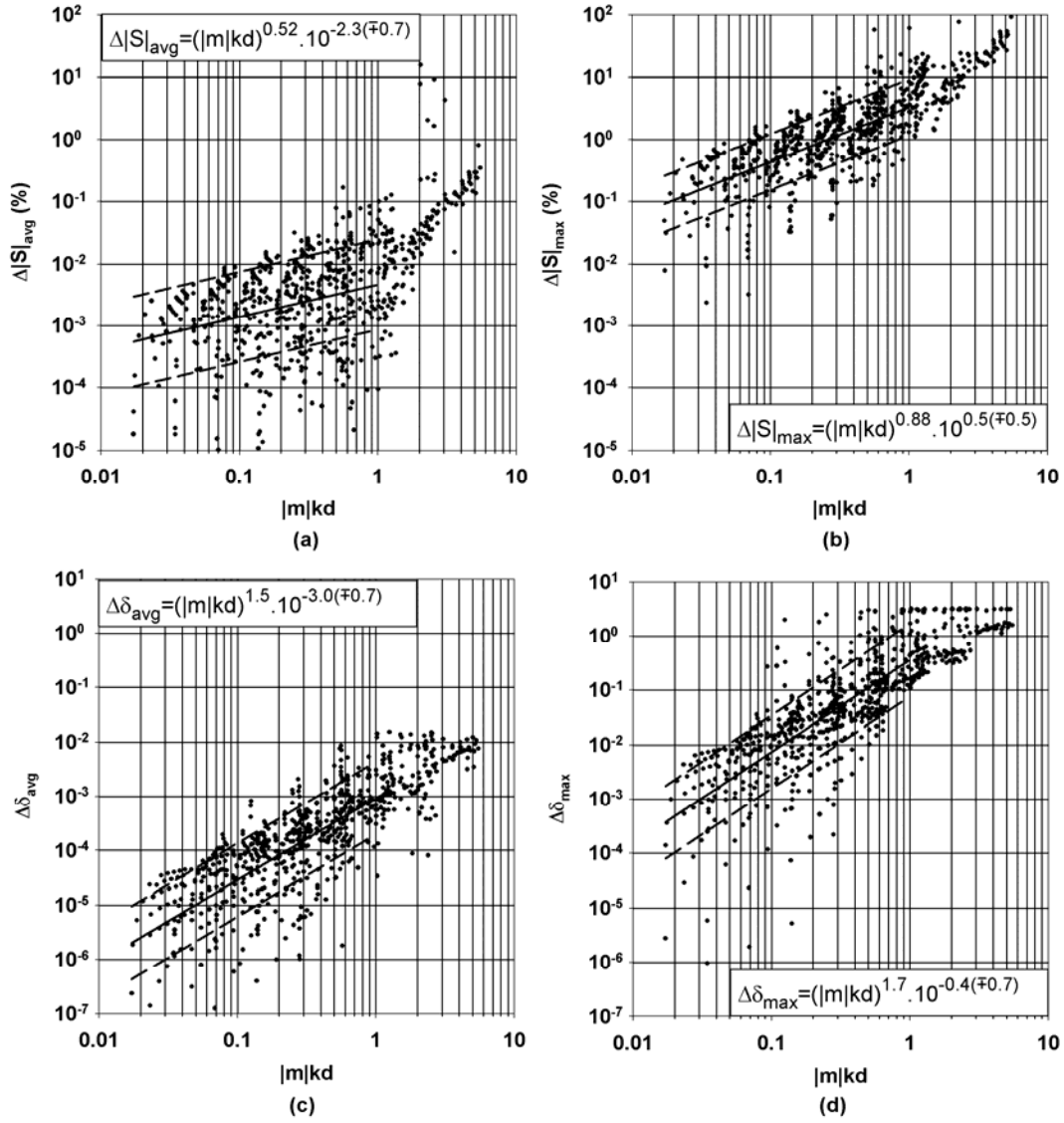

Figure B.1. Dependence of amplitude and phase errors of DDA on $|m|kd$ for systematic numerical experiments on single sphere problem within the size parameter ranges x_D = 0.5-8, D/d=8-64, Re(m)=1.1-2.5, Im(m)=0-1. Solid lines stand for the best lines for $|m|kd$<1 domain, dashed lines display the standard deviations.

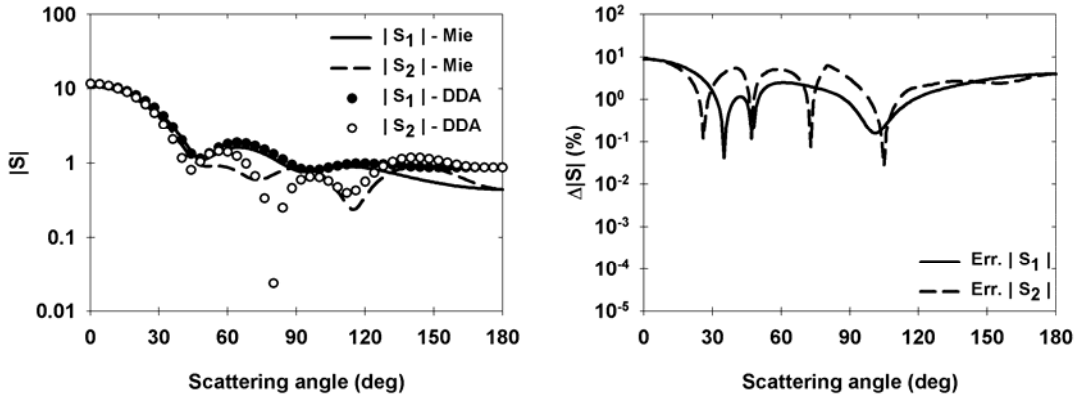

(a) D/d=8, Number of dipoles=251 , $|m|kd$=1.86

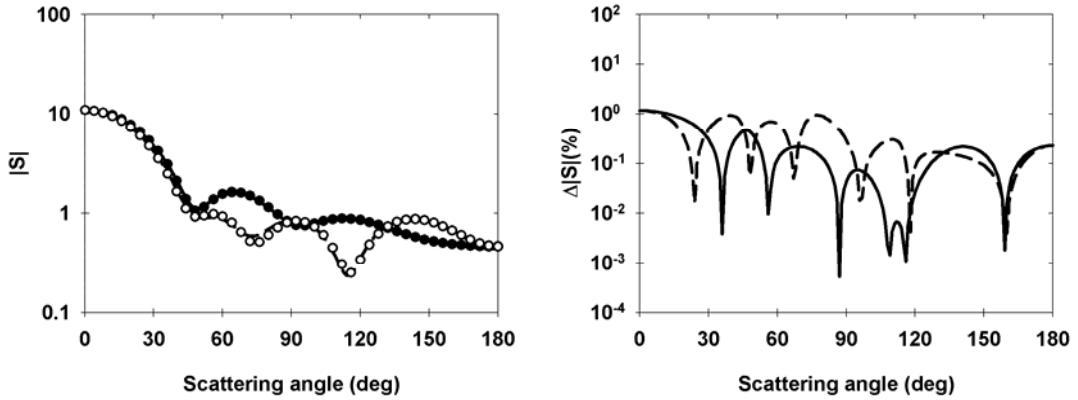

(b) D/d=32, Number of dipoles=17071 , $|m|kd$=0.46

Figure B.2. Effect of lattice subdivision on magnitude of ASM elements predicted by DDA for a sphere of x_D = 4 and m = 1.75+ i0.5.

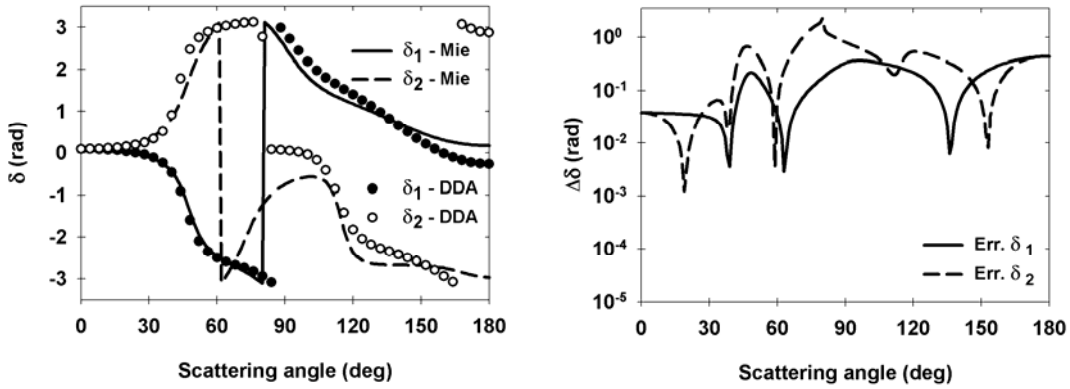

(a) D/d=8, Number of dipoles=251 , $|m|kd$=1.86

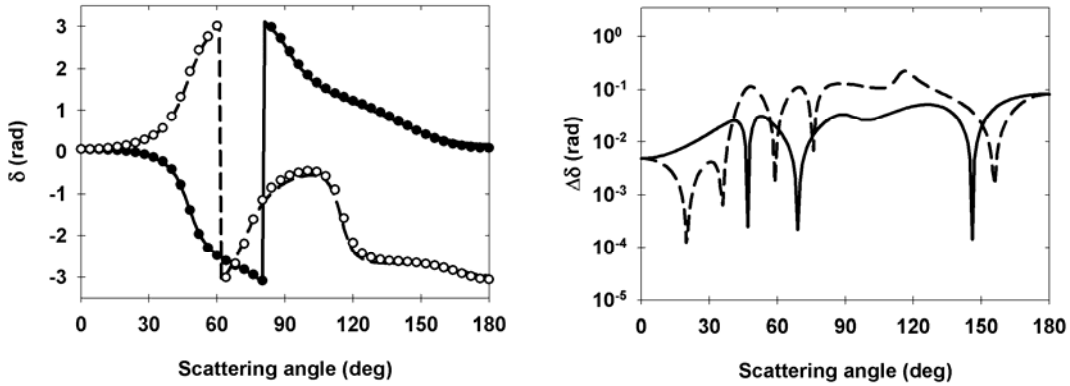

(b) D/d=32, Number of dipoles=17071 , $|m|kd$=0.46

Figure B.3. Effect of lattice subdivision on phase of ASM elements predicted by DDA for a sphere of x_D = 4 and m=1.75+0.5i.

The effect of size parameter and D/d on the accuracy of predicted magnitude and phase is analyzed at constant refractive index. Variation of average and maximum magnitude and phase errors with size parameter and lattice subdivision is plotted in log-log-log scale on Figure B.4 for refractive index of m=1.75+i0.5 and in Figure B.5 for refractive index of m=2.5+i0.1. The plots are found to fit a plane yielding a correlation between the errors, x_D and D/d as follows

$$\log \Delta = a + b \log x_D + c \log(D/d) \tag{B.8}$$

or equivalently

$$\Delta = 10^a \cdot {x_D}^b \cdot \left(D/d\right)^c \tag{B.9}$$

where a, b and c are constants for fixed refractive index. Analyses on other refractive indices covering n=1.1-2.5 and k=0-1 range resulted in similar planar variation of errors with x_D and D/d in each of the 36 cases. The constants determined via surface fitting for all complex refractive indices under consideration are reported in Table B.2-Table B.5 together with the standard errors associated with regression of each plane. As can be followed from the tables, the real and imaginary parts of the refractive index have considerable effects on the errors.

As a result of the above analysis, a correlation that relates accuracy of the present DDA implementation to optical constants, size parameter and lattice subdivision is proposed in Table B.2-Table B.5. These correlations can either be used to estimate errors for given target properties and lattice subdivision, or to determine the degree of dipole discretization required to attain a prespecified order of accuracy. The discretization criterion to ensure an accuracy of Δ for a target of characteristic dimension D is

$$\frac{D}{d} \geq \left(\frac{\Delta}{10^a \cdot {x_D}^b} \right)^{1/c} \cdot 10^{\pm \sigma / c} \tag{B.10}$$

where parameters a, b, c and σ are constants for a given complex index of refraction and can be determined by interpolation from one of the tables depending upon the type of the error specification. Note that these relations are based on single sphere targets and can be considered as a guide to determine optimum lattice subdivision for irregularly shaped targets.

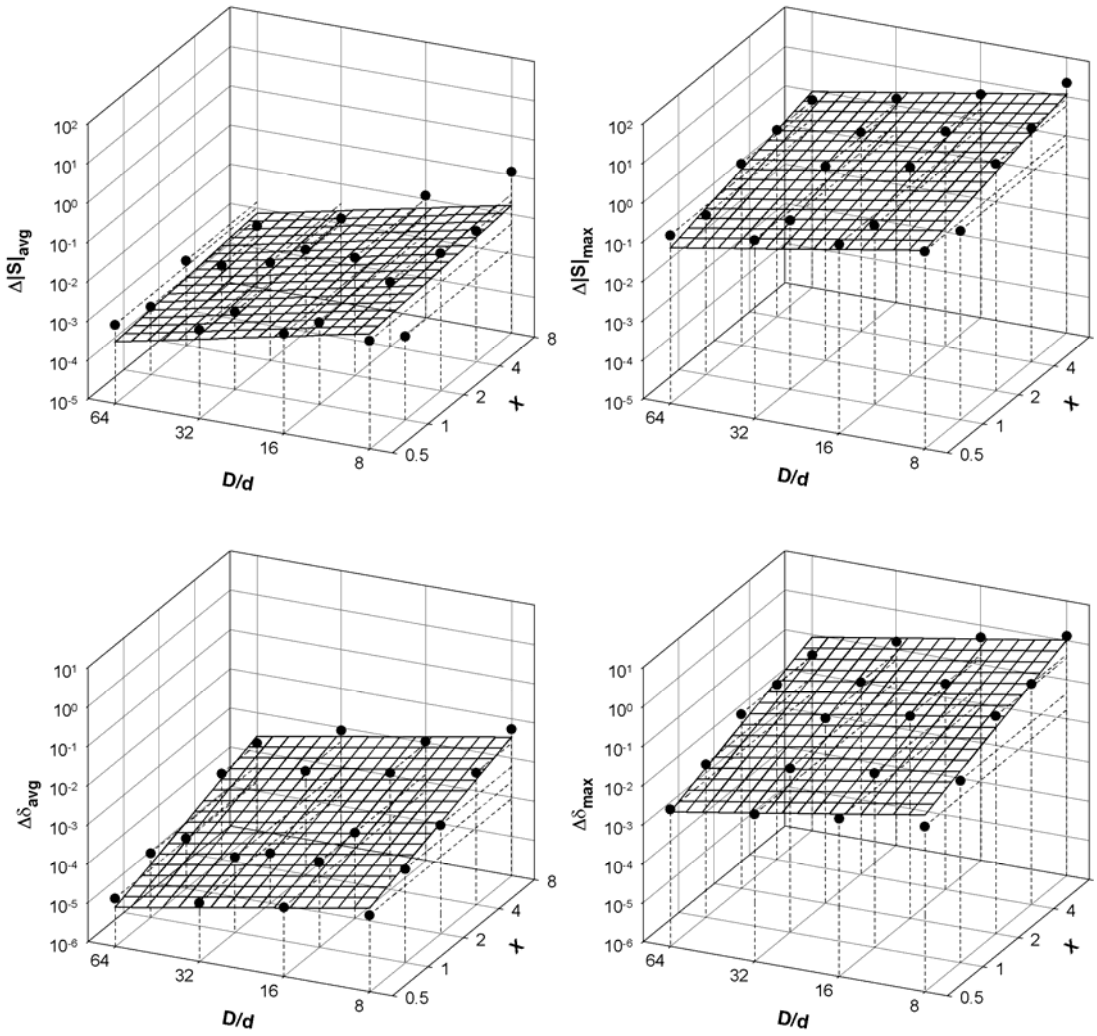

Figure B.4. Combined effects of lattice subdivision and target size parameter on average and maximum errors of the magnitudes and phases of the ASM elements predicted by DDA for m=1.75+i0.5.

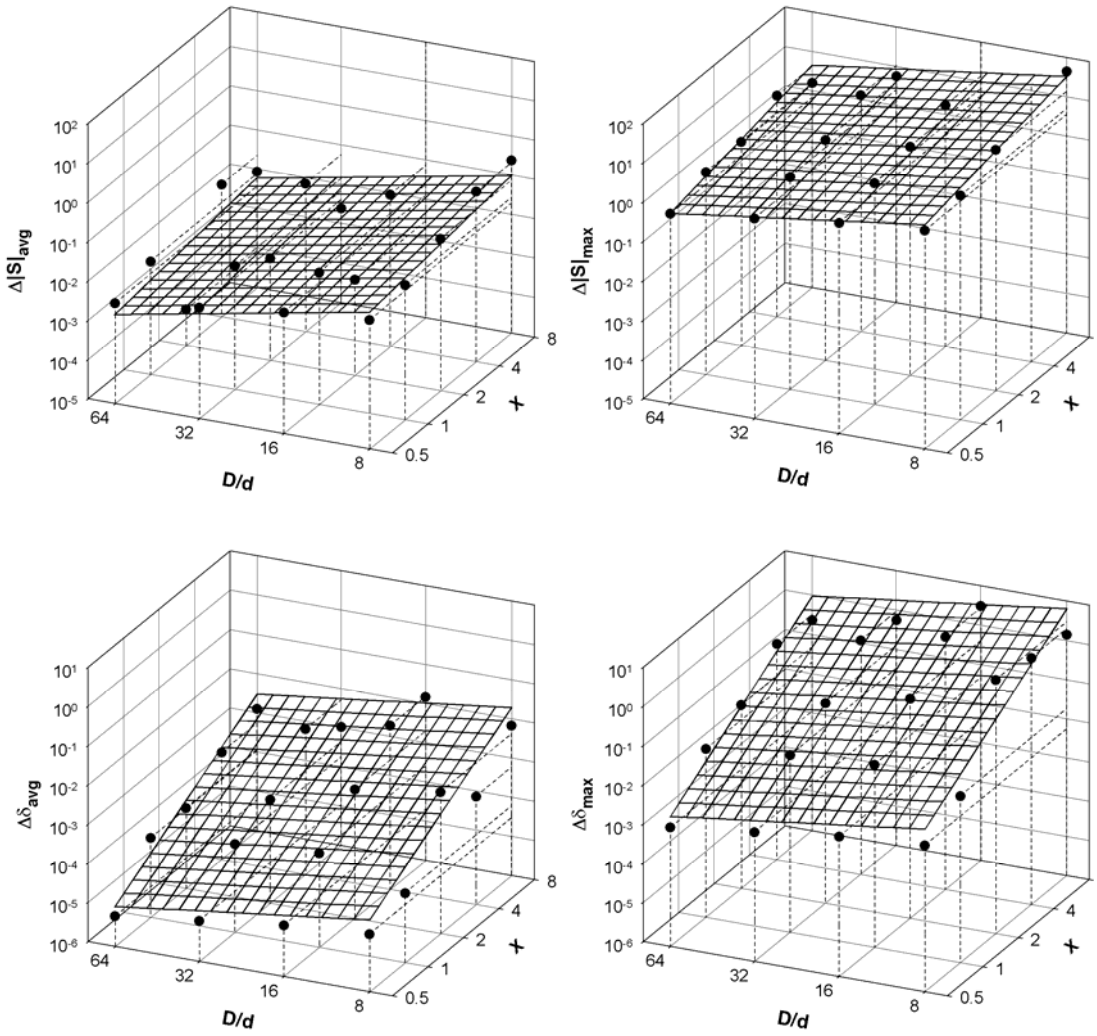

Figure B.5. Combined effects of lattice subdivision and target size parameter on average and maximum errors of the magnitudes and phases of the ASM elements predicted by DDA for m=2.5+i0.1.

Table B.2. Fitted constants and standard errors for $\Delta |S|_{avg} = 10^{a} x_D{}^{b} \left(D/d\right)^{c} \cdot 10^{\pm\sigma}$ [%] for each complex index of refraction m = n + ik

Fitted parameter, a						
	k = 0	k = 0.1	k = 0.25	k = 0.5	k = 0.75	k = 1
n = 1.1	-0.91	-1.27	-0.57	-0.49	-0.25	0.39
n = 1.5	-1.16	-1.34	-0.82	-0.66	-0.99	-0.36
n = 1.75	-1.43	-1.16	-0.54	-0.66	-0.43	-0.23
n = 2	-0.28	-0.65	-0.15	-0.25	-0.31	0.24
n = 2.25	-0.50	-0.93	-0.79	0.21	0.51	0.10
n = 2.5	-0.80	-0.20	-0.34	0.06	0.19	0.18
Fitted parameter, b						
	k = 0	k = 0.1	k = 0.25	k = 0.5	k = 0.75	k = 1
n = 1.1	1.03	1.18	0.31	-0.01	-0.14	-0.15
n = 1.5	1.36	0.61	0.36	0.53	0.75	0.41
n = 1.75	0.84	0.41	0.17	0.25	0.27	0.37
n = 2	0.53	0.37	-0.38	-0.05	0.38	0.20
n = 2.25	1.04	0.32	-0.06	-0.13	0.15	0.04
n = 2.5	0.73	0.42	-0.02	-0.25	0.00	-0.24
Fitted parameter, c						
	k = 0	k = 0.1	k = 0.25	k = 0.5	k = 0.75	k = 1
n = 1.1	-2.15	-1.93	-2.09	-1.70	-1.68	-2.12
n = 1.5	-1.16	-1.02	-1.46	-1.73	-1.51	-1.70
n = 1.75	-0.71	-0.97	-1.41	-1.49	-1.65	-1.77
n = 2	-1.26	-1.13	-1.52	-1.59	-1.82	-2.05
n = 2.25	-1.09	-0.84	-1.11	-1.90	-2.42	-1.90
n = 2.5	-0.76	-1.33	-1.26	-1.70	-2.02	-1.95
Standard deviation, σ						
	k = 0	k = 0.1	k = 0.25	k = 0.5	k = 0.75	k = 1
n = 1.1	0.48	0.57	0.52	0.46	0.45	0.80
n = 1.5	0.60	0.32	0.43	0.47	0.66	0.44
n = 1.75	0.37	0.38	0.32	0.50	0.43	0.37
n = 2	0.50	0.29	0.58	0.48	0.60	0.51
n = 2.25	0.53	0.42	0.93	0.42	0.62	0.53
n = 2.5	0.24	0.63	0.50	0.46	0.67	0.75

Table B.3. Fitted constants and standard errors for $\Delta |S|_{\max} = 10^{a} x_D{}^{b} \left(D/d\right)^{c} \cdot 10^{\pm\sigma}$ [%] for each complex index of refraction m = n + ik

Fitted parameter, a						
	k = 0	k = 0.1	k = 0.25	k = 0.5	k = 0.75	k = 1
n = 1.1	0.86	0.67	1.10	1.47	1.48	1.50
n = 1.5	1.65	1.26	1.28	1.31	1.43	1.48
n = 1.75	1.06	1.32	1.50	1.38	1.45	1.59
n = 2	2.10	1.84	1.84	1.60	1.53	1.70
n = 2.25	1.73	1.69	1.75	1.77	1.62	1.84
n = 2.5	1.45	1.75	1.95	1.87	2.08	1.83
Fitted parameter, b						
	k = 0	k = 0.1	k = 0.25	k = 0.5	k = 0.75	k = 1
n = 1.1	1.15	1.53	0.74	0.28	0.23	0.23
n = 1.5	1.73	0.72	0.67	0.94	0.87	0.57
n = 1.75	1.10	0.69	0.63	0.84	0.80	0.62
n = 2	0.98	0.50	0.55	0.76	0.82	0.76
n = 2.25	1.36	0.56	0.48	0.73	0.81	0.85
n = 2.5	0.91	0.68	0.60	0.74	1.05	0.90
Fitted parameter, c						
	k = 0	k = 0.1	k = 0.25	k = 0.5	k = 0.75	k = 1
n = 1.1	-1.56	-1.58	-1.52	-1.41	-1.18	-1.03
n = 1.5	-1.50	-1.24	-1.30	-1.40	-1.40	-1.25
n = 1.75	-0.83	-1.05	-1.21	-1.20	-1.21	-1.18
n = 2	-1.32	-1.24	-1.28	-1.16	-1.12	-1.18
n = 2.25	-0.94	-1.01	-1.10	-1.16	-1.08	-1.18
n = 2.5	-0.68	-0.95	-1.17	-1.17	-1.33	-1.11
Standard deviation, σ						
	k = 0	k = 0.1	k = 0.25	k = 0.5	k = 0.75	k = 1
n = 1.1	0.35	0.39	0.22	0.24	0.18	0.13
n = 1.5	0.70	0.21	0.24	0.23	0.27	0.29
n = 1.75	0.27	0.17	0.18	0.23	0.19	0.12
n = 2	0.47	0.23	0.20	0.18	0.20	0.19
n = 2.25	0.36	0.20	0.18	0.16	0.19	0.23
n = 2.5	0.18	0.18	0.14	0.16	0.31	0.17

Table B.4. Fitted constants and standard errors for $\Delta\delta_{avg} = 10^{a} x_D{}^{b} \left(D/d\right)^{c} \cdot 10^{\pm\sigma}$ [rad] for each complex index of refraction m = n + ik

Fitted parameter, a						
	k = 0	k = 0.1	k = 0.25	k = 0.5	k = 0.75	k = 1
n = 1.1	-4.52	-3.25	-3.46	-3.11	-2.95	-2.71
n = 1.5	-3.53	-2.74	-2.37	-2.48	-2.17	-2.66
n = 1.75	-2.99	-2.74	-2.55	-2.40	-2.72	-2.88
n = 2	-2.89	-2.42	-2.80	-2.35	-2.36	-2.38
n = 2.25	-4.23	-2.77	-2.38	-1.76	-2.25	-2.22
n = 2.5	-3.10	-2.76	-1.98	-1.97	-1.97	-2.16
Fitted parameter, b						
	k = 0	k = 0.1	k = 0.25	k = 0.5	k = 0.75	k = 1
n = 1.1	4.59	2.48	1.87	1.58	1.28	0.99
n = 1.5	3.48	2.26	1.38	1.20	0.97	0.75
n = 1.75	2.72	2.13	1.71	1.16	0.94	0.81
n = 2	2.57	1.96	1.37	0.77	0.85	0.83
n = 2.25	3.36	2.28	1.60	0.97	0.69	0.78
n = 2.5	2.66	2.04	1.31	1.09	0.98	0.77
Fitted parameter, c						
	k = 0	k = 0.1	k = 0.25	k = 0.5	k = 0.75	k = 1
n = 1.1	-1.43	-1.36	-0.99	-1.12	-1.14	-1.19
n = 1.5	-1.20	-1.28	-1.41	-1.23	-1.50	-1.05
n = 1.75	-1.40	-1.17	-1.10	-1.24	-0.95	-0.80
n = 2	-1.29	-1.25	-0.86	-1.18	-1.08	-1.04
n = 2.25	-0.48	-1.02	-1.08	-1.51	-1.09	-1.09
n = 2.5	-0.86	-0.89	-1.31	-1.24	-1.24	-1.10
Standard deviation, σ						
	k = 0	k = 0.1	k = 0.25	k = 0.5	k = 0.75	k = 1
n = 1.1	0.88	0.75	0.58	0.45	0.50	0.51
n = 1.5	0.38	0.35	0.35	0.15	0.54	0.44
n = 1.75	0.66	0.46	0.35	0.28	0.31	0.40
n = 2	0.65	0.57	0.40	0.39	0.19	0.22
n = 2.25	0.64	0.38	0.30	0.47	0.36	0.25
n = 2.5	0.50	0.49	0.46	0.30	0.21	0.24

Table B.5. Fitted constants and standard errors for $\Delta\delta_{\max} = 10^{a} x_D{}^{b} \left(D/d\right)^{c} \cdot 10^{\pm\sigma}$ [rad] for each complex index of refraction m = n + ik

Fitted parameter, a						
	k = 0	k = 0.1	k = 0.25	k = 0.5	k = 0.75	k = 1
n = 1.1	-2.18	-0.87	-0.73	-0.40	-0.23	-0.13
n = 1.5	-1.42	-0.58	-0.22	-0.08	-0.03	-0.01
n = 1.75	-0.88	-0.59	-0.13	-0.06	0.07	0.11
n = 2	-0.35	-0.40	-0.08	0.05	0.16	0.26
n = 2.25	-0.96	-0.38	0.03	0.24	0.24	0.29
n = 2.5	-0.57	-0.38	0.23	0.28	0.39	0.35
Fitted parameter, b						
	k = 0	k = 0.1	k = 0.25	k = 0.5	k = 0.75	k = 1
n = 1.1	4.93	2.83	2.23	1.72	1.40	1.12
n = 1.5	3.81	2.52	1.72	1.29	1.09	0.96
n = 1.75	3.47	2.47	1.80	1.25	1.02	0.92
n = 2	2.97	2.35	1.57	1.11	0.98	0.96
n = 2.25	3.22	2.42	1.63	1.20	0.98	0.97
n = 2.5	3.05	2.21	1.52	1.14	1.06	1.07
Fitted parameter, c						
	k = 0	k = 0.1	k = 0.25	k = 0.5	k = 0.75	k = 1
n = 1.1	-1.31	-1.33	-1.29	-1.37	-1.33	-1.23
n = 1.5	-1.00	-1.02	-1.25	-1.27	-1.24	-1.18
n = 1.75	-1.02	-0.99	-1.04	-1.18	-1.23	-1.20
n = 2	-1.28	-0.91	-1.10	-1.19	-1.23	-1.26
n = 2.25	-0.77	-0.97	-1.14	-1.28	-1.23	-1.24
n = 2.5	-0.92	-0.91	-1.24	-1.23	-1.29	-1.24
Standard deviation, σ						
	k = 0	k = 0.1	k = 0.25	k = 0.5	k = 0.75	k = 1
n = 1.1	0.71	0.61	0.43	0.32	0.24	0.21
n = 1.5	0.44	0.64	0.36	0.19	0.17	0.17
n = 1.75	0.73	0.39	0.72	0.20	0.17	0.16
n = 2	0.69	0.79	0.57	0.26	0.19	0.19
n = 2.25	0.40	0.45	0.42	0.32	0.19	0.18
n = 2.5	0.46	0.50	0.39	0.28	0.21	0.23

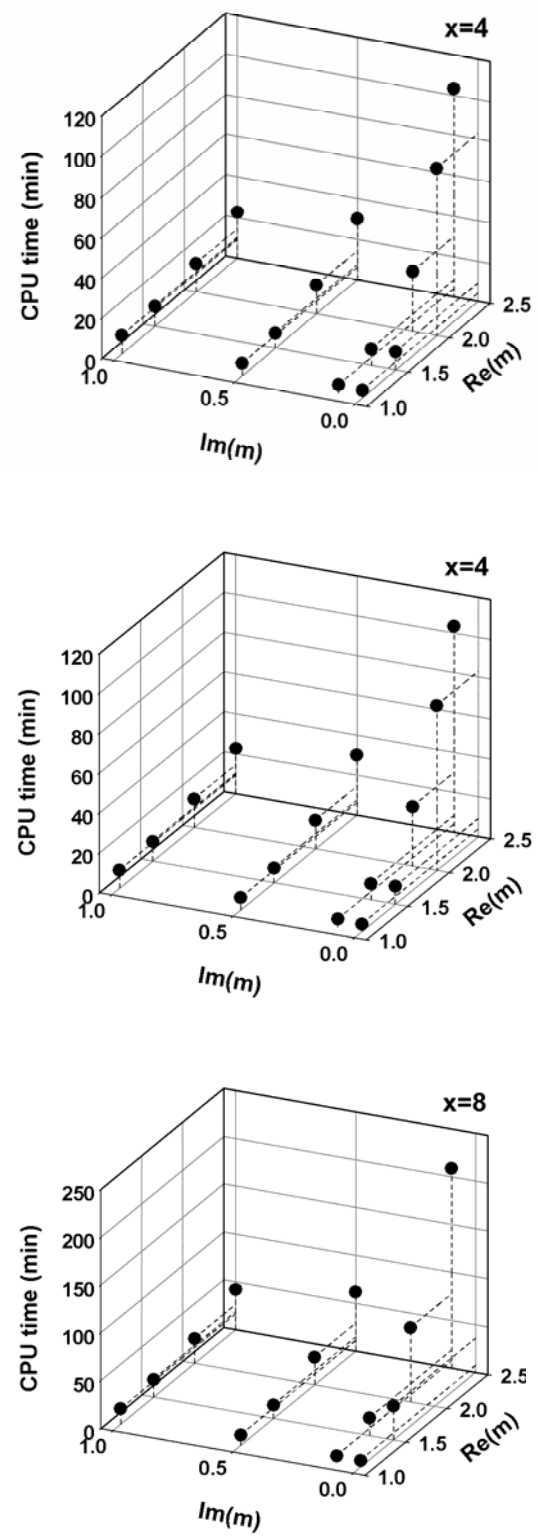

Figure B.6. Variation of computational time with real and imaginary parts of complex index of refraction for D/d=64 (CPU times are due to a PC with 2.4GHz Pentium 4 processor).

The errors in irregularly shaped targets are expected to be larger than those for spheres. Eq. (B.10) gives the number of dipoles along the target characteristic length. The cubic lattice grid that is to be used to approximate a complex shaped particle should be at least as fine as D/d evaluated from Eq. (B.10).

Another factor that determines the applicability of DDA is the computational load. The effect of lattice subdivision on CPU time and memory requirements of DDSCAT was previously reported [73, 84]. In the present analysis the effect of refractive index on the CPU time is assessed. As iterations for polarizability vectors are the dominant CPU time consumers, CPU time analysis is equivalent to convergence rate analysis. The convergence tolerance of the conjugate gradients routine was set to 10^{-5} for every run. The resulting CPU times for D/d=64 and x=2, 4, 8 are displayed in Figure B.6. It was found that the number of iterations required to achieve the same level of convergence increases with increasing modulus of refractive index. However when Re(m) ≥ 2 the convergence rate is considerably faster for large absorptive index whereas it is slow for small or zero absorptive index. Some of the problems with large |m|, large x and small Im(m) combinations were found to yield divergence, i.e., the iterations finalized with irrelevant results or did not converge at all for extremely long periods of time. Note that the cases that resulted with divergence are excluded from Figure B.6 (m = 2.5 for x = 4 and m = 2.5 and m = 2 for x = 8). Convergence problems for large targets of highly polarizable materials with slight or no absorption are due to the strong sensitivity of dipole moments to neighboring dipoles within the target which leads to a strongly coupled system of equations. As a result, it was found that use of DDSCAT with the present specifications is unfeasible when Re(m)>2 and Im(m)<0.1 for large targets with x > 4.

Contents of this section were published in [67].

APPENDIX C

Position Data for Primary Particles of the Spherical Aggregate

No	x	y	z
1	3	3	3
2	4	3	3
3	5	3	3
4	3	4	3
5	4	4	3
6	5	4	3
7	3	5	3
8	4	5	3
9	2	3	3
10	1	3	3
11	0	3	3
12	2	4	3
13	1	4	3
14	0	4	3
15	2	5	3
16	1	5	3
17	3	2	3
18	4	2	3
19	5	2	3
20	3	1	3
21	4	1	3
22	5	1	3
23	3	0	3
24	4	0	3
25	2	2	3
26	1	2	3
27	0	2	3
28	2	1	3
29	1	1	3
30	0	1	3
31	2	0	3
32	1	0	3
33	3	3	2
34	4	3	2
35	5	3	2
36	3	4	2
37	4	4	2
38	5	4	2
39	3	5	2
40	4	5	2
41	2	3	2
42	1	3	2
43	0	3	2
44	2	4	2
45	1	4	2
46	0	4	2
47	2	5	2
48	1	5	2
49	3	2	2
50	4	2	2
51	5	2	2
52	3	1	2
53	4	1	2
54	5	1	2
55	3	0	2
56	4	0	2
57	2	2	2
58	1	2	2
59	0	2	2
60	2	1	2
61	1	1	2
62	0	1	2
63	2	0	2
64	1	0	2
65	3	3	4
66	4	3	4
67	5	3	4
68	3	4	4
69	4	4	4
70	3	5	4
71	2	3	4
72	1	3	4
73	0	3	4
74	2	4	4
75	1	4	4
76	2	5	4
77	3	2	4
78	4	2	4
79	5	2	4
80	3	1	4
81	4	1	4
82	3	0	4
83	2	2	4
84	1	2	4
85	0	2	4
86	2	1	4
87	1	1	4
88	2	0	4
89	3	3	1
90	4	3	1
91	5	3	1
92	3	4	1
93	4	4	1
94	3	5	1
95	2	3	1
96	1	3	1
97	0	3	1
98	2	4	1
99	1	4	1
100	2	5	1
101	3	2	1
102	4	2	1
103	5	2	1
104	3	1	1
105	4	1	1
106	3	0	1
107	2	2	1
108	1	2	1
109	0	2	1
110	2	1	1
111	1	1	1
112	2	0	1
113	3	3	5
114	4	3	5
115	3	4	5
116	2	3	5
117	1	3	5
118	2	4	5
119	3	2	5
120	4	2	5
121	3	1	5
122	2	2	5
123	1	2	5
124	2	1	5
125	3	3	0
126	4	3	0
127	3	4	0
128	2	3	0
129	1	3	0
130	2	4	0
131	3	2	0
132	4	2	0
133	3	1	0
134	2	2	0
135	1	2	0
136	2	1	0

Particle diameter =1 unit

APPENDIX D

Position Data for Primary Particles of the Fractal Aggregate

No	x	y	z	No	x	y	z
1	5.6132	4.4608	4.4300	38	6.8548	4.1277	9.3983
2	5.2708	4.3599	5.3641	39	8.7265	6.1900	7.6476
3	6.3672	3.9575	4.8520	40	6.3725	1.3068	2.0038
4	6.3617	3.9581	5.8520	41	3.0976	2.7344	8.4035
5	7.1605	4.4288	5.4775	42	7.0323	3.1517	1.1768
6	6.9670	3.7398	4.0820	43	5.8058	2.8030	0.9369
7	5.6200	3.9340	3.5799	44	5.3738	2.9889	9.6744
8	6.4822	4.8192	6.3459	45	3.5422	2.8375	9.2933
9	6.0548	3.9362	6.8035	46	2.1099	3.4568	8.2577
10	4.9183	3.3619	4.0044	47	9.9122	5.8267	6.4925
11	4.3424	3.0518	4.7609	48	6.1561	3.7107	10.3241
12	7.5240	4.4783	6.4078	49	4.6395	1.2095	1.7434
13	7.2548	5.4425	6.4668	50	1.3977	3.5397	7.5606
14	6.9414	3.7511	3.0824	51	3.1852	1.9756	9.6533
15	4.9152	2.3619	4.0002	52	5.5303	2.7565	10.6343
16	8.1019	5.3283	5.9477	53	2.7122	3.2236	9.6957
17	5.5723	3.5052	7.5661	54	3.8277	1.6645	10.3536
18	5.5418	1.6207	4.2412	55	4.6196	2.4305	10.8877
19	7.8068	4.6707	7.3474	56	10.0887	5.9408	7.4702
20	3.4374	3.4681	4.8481	57	2.8163	1.0462	9.6460
21	6.7310	4.4776	2.4282	58	7.1804	0.8074	1.6911
22	3.4034	3.5144	3.8498	59	6.8173	1.5706	1.1479
23	6.9213	3.5387	2.1054	60	5.4399	3.2968	11.4709
24	5.3991	1.2093	3.3409	61	0.5000	3.5009	7.9995
25	2.9303	3.1821	5.6612	62	2.4102	3.2346	10.6490
26	4.7432	3.1476	7.9957	63	4.2974	1.2365	11.1257
27	8.9421	4.8530	6.2091	64	5.5644	3.6695	0.5000
28	5.7801	3.2407	8.5078	65	1.9926	0.5000	9.4937
29	6.3261	2.7993	1.7908	66	2.6532	2.4325	11.1945
30	2.6543	3.2413	6.6205	67	2.7992	0.8074	10.6170
31	4.0438	3.7717	8.3440	68	1.8332	4.0090	10.9085
32	8.8024	4.9575	7.1937	69	1.6568	2.3485	11.2043
33	6.2843	4.8057	1.5958	70	4.4829	1.5552	12.0553
34	8.9427	5.8363	6.7376	71	3.1366	0.7267	11.5548
35	2.8428	3.2753	7.6020	72	1.6793	1.3526	11.2919
36	5.9274	3.7566	9.3517	73	4.4046	1.6347	0.8694
37	5.4400	1.1806	2.3422	74	10.7559	5.4615	6.9001

Particle diameter =1 unit

APPENDIX E

Calibration of Fuel Flow Rate

For a given flowmeter scale reading, a certified calibration curve provides corresponding volumetric flowrate of air at 20° C and 1 atm. Conversion of this value to the fuel flow rate at experiment's temperature and pressure conditions can be done based on the fact that the drag force exerted on the float by the fuel at T_{exp} and P_{exp} must be equal to that of air at 20°C and 1 atm. Drag force for a rotameter float is given as

$$F_D = A_f \cdot C_D \cdot \rho \cdot \left(\frac{u_{\max}^2}{g_c} \right) \tag{E.11}$$

where A_f, C_D and g_c stand for the cross-sectional area of the float, drag coefficient and gravitational constant, respectively. ρ is the density of the fluid and u_{max} represents the maximum velocity of the fluid passing around the float which is equal to volumetric flow rate divided by the minimum cross-sectional area between the float and the tube ($u_{max} = Q/A_{min}$). Equating the drag forces exerted by air at normal conditions and by the fuel at experiment conditions and canceling the constants yields

$$\left(Q^2 \cdot \rho\right)_{air@NC} = \left(Q^2 \cdot \rho\right)_{fuel@T_{exp},P_{exp}} \tag{E.12}$$

Ethylene, which is the fuel in this study, can be assumed to follow ideal gas behavior. Substituting ideal gas law ($P.M_{wt} = \rho.RT$) into the above equation and rearranging yields

$$\frac{Q_{air@NC}^2}{Q_{fuel@T_{exp},P_{exp}}^2} = \frac{\rho_{fuel@T_{exp},P_{exp}}}{\rho_{air@NC}} = \frac{\rho_{fuel@NC}}{\rho_{air@NC}} \cdot \frac{293.15\ \text{K}}{T_{exp}} \cdot \frac{P_{exp}}{1\ \text{atm}} \tag{E.13}$$

Gas densities are generally reported in terms of specific gravity (*SG*) which is the ratio of gas density at specified temperature and pressure to air density at same conditions. It can be shown from ideal gas law that the ratio of densities of two ideal gases is independent of

temperature and pressure. If both the fuel and air are assumed to follow ideal gas behavior, SG_{fuel} reported at T_{sg} and P_{sg} is equal to the ratio of densities at normal conditions.

$$SG_{fuel@T_{sg},P_{sg}} = \frac{\rho_{fuel@T_{sg},P_{sg}}}{\rho_{air@T_{sg},P_{sg}}} = \frac{\rho_{fuel@NC}}{\rho_{air@NC}} \tag{E.14}$$

Substituting the above equation into Eq.(3.3) provides the following calibration equation that relates the air flow rate found from calibration curve to actual fuel flow rate.

$$Q_{fuel@T_{exp},P_{exp}} = Q_{air@NC} \cdot \left(SG_{fuel} \cdot \frac{293.15\ \mathrm{K}}{T_{exp}} \cdot \frac{P_{exp}}{1\ \mathrm{atm}} \right)^{-1/2} \tag{E.15}$$

Table E.1 lists the thermophysical properties of ethylene used to evaluate the fuel flow rate reported in the section 4.5 together with other operating parameters.

Table E.1. Thermophysical properties of ethylene

Parameter	**Value**
Specific gravity, SG_{fuel}	0.974 @ 0° C, 1 atm [147]
Density, ρ	1.2644 g/l @ 0° C, 1 atm [148]
Viscosity, μ	0.951×10^{-4} poise @ 0° C, 1 atm [147]
Kinematic viscosity, ν (= μ / ρ)	7.521×10^{-6} m^2/s

APPENDIX F

Formulations for Three-Point Abel Inversion

This section presents equations for 3-point Abel inversion which are modified from Dasch's formulations [143]. Projection data *P(x)* at lateral nodes x_j with spacing d_x is deconvolved to give the field distribution *F(r)* at radial grid nodes r_i as follows

$$F(r_i) = \frac{1}{d_x} \sum_{j=0}^{\infty} \mathbf{D_{ij}} P(x_j) \tag{E.1}$$

For 3-point Abel inversion, deconvolution operator is given as follows

$$\mathbf{D_{ij}} = \begin{cases} 0 & j < i - 1 \\ \mathbf{I_{i,j+1}}^{(0)} - \mathbf{I_{i,j+1}}^{(1)} & j = i - 1 \\ \mathbf{I_{i,j+1}}^{(0)} - \mathbf{I_{i,j+1}}^{(1)} + 2\mathbf{I_{i,j}}^{(1)} & j = i \\ \mathbf{I_{i,j+1}}^{(0)} - \mathbf{I_{i,j+1}}^{(1)} + 2\mathbf{I_{i,j}}^{(1)} - \mathbf{I_{i,j-1}}^{(0)} - \mathbf{I_{i,j-1}}^{(1)} & j \geq i + 1 \\ \mathbf{I_{i,j+1}}^{(0)} - \mathbf{I_{i,j+1}}^{(1)} + 2\mathbf{I_{i,j}}^{(1)} - 2\mathbf{I_{i,j-1}}^{(1)} & i = 0, j = 1 \end{cases} \tag{F.2}$$

Defining decimal ratios for radial and lateral position nodes as $s_i = r_i / d_x$, $t_j = x_j / d_x$. Dasch's formulations limit these ratios to integers which require the positions of field and projection nodes to be arranged to start from 0, incrementing by d_x. By defining the ratios as decimals, the formulations apply for any series of equally distributed positions, not necessarily coincident with the origin.

$$A_{i,j} = \sqrt{\left(2t_j + 1\right)^2 - 4{s_i}^2} \tag{F.3}$$

$$B_{i,j} = \sqrt{\left(2t_j - 1\right)^2 - 4{s_i}^2} \tag{F.4}$$

$$\mathbf{I_{ij}^{(0)}} = \begin{cases} 0 & j = i = 0 \text{ or } j < i \\ \dfrac{1}{2\pi} \ln\left(\dfrac{A_{i,j} + 2t_j + 1}{2t_j} \right) & j = i \neq 0 \\ \dfrac{1}{2\pi} \ln\left(\dfrac{A_{i,j} + 2t_j + 1}{B_{i,j} + 2t_j - 1} \right) & j > i \end{cases} \tag{F.5}$$

$$\mathbf{I_{ij}^{(1)}} = \begin{cases} 0 & j < i \\ \dfrac{A_{i,j}}{2\pi} - 2t_j \mathbf{I_{ij}^{(0)}} & j = i \\ \dfrac{\left(A_{i,j} - B_{i,j} \right)}{2\pi} - 2t_j \mathbf{I_{ij}^{(0)}} & j > i \end{cases} \tag{F.6}$$

Performing the algebraic operation defined in Eq.(F.1) at each radial node by substituting the above equations grid provides radial field distribution.

CURRICULUM VITAE

Surname, Name: Ayrancı Kılınç, Işıl
e-mail: ayranci.kilinc@gmail.com

PERSONAL INFORMATION

Nationality: Turkish
Date and Place of Birth: 1978, Ankara
Maiden Name: Ayrancı

EDUCATION

PhD (co-supervised)	METU Chemical Engineering *supervisor* : Prof. Dr. Nevin Selçuk INSA-Lyon Thermal and energy science *supervisors* : Dr. Rodolphe Vaillon Prof. Dr. Jean-François Sacadura	2007
MSc	METU Chemical Engineering *supervisor* : Prof. Dr. Nevin Selçuk	2001
BSc	METU Chemical Engineering	1999
BSc	METU Food Engineering (Double Major)	1999
High School	TED Ankara Collage	1995

WORK EXPERIENCE

2000 – 2006	METU, Dept. Chem. Eng.	Research Assistant
June – Sept. 1999	Kırıkkale Refinery	Practicing Process Engineer
June – Sept. 1998	ANSAN A.Ş., Ankara Coca-Cola Beverage Factory	Practicing Process Engineer

ACADEMIC EXPERIENCE

Teaching Assistance:

Graduate Courses
- Transport Phenomena (3 semesters)
- Chemical Engineering Mathematics (2 semesters)
- Advanced Chemical Engineering Thermodynamics

Undergraduate Courses
- Heat Transfer in Radiating and Combusting Systems
- Chemical Engineering Laboratory
- Thermodynamics I
- Industrial Organization and Management
- Chemical Engineering Economics

Training Course: Attended ICS (International Centre for Science and High Technology) Training Course on Laser Diagnostics of Combustion Processes, National Institute of Laser Enhanced Sciences, Cairo, Egypt, June 22-26, 2002.

Conferences : Presented a paper at Fifth International Symposium on Radiative Transfer, June 17-22, 2007, Bodrum, Turkey.

Presented a paper at Eurotherm Seminar 78 - Computational Thermal Radiation in Participating Media, April 5-7, 2006, Poitiers, France.

Participated Fourth International Symposium on Radiative Transfer, June 20-25 2004, Istanbul, Turkey as co-author of 3 papers.

Presented a paper in Eurotherm Seminar 73 - Computational Thermal Radiation in Participating Media, April 15-17, 2003, Mons, Belgium.

Presented poster in 12th International Heat Transfer Conference, August 18-23, 2002, Grenoble, France.

Presented a paper in Third International Symposium on Radiative Transfer, June 17-22, 2001, Antalya, Turkey.

Attended Heat Transfer in Gas Turbine Systems, August 13-18, 2000, Çeşme, İzmir, Turkey.

Peer Review:
- Journal of Quantitative Spectroscopy and Radiative Transfer
  Reviewer of 3 papers, August-December 2006
- Fifth International Symposium on Radiative Transfer
  Reviewer of 2 papers, January 2007

EXPERIMENTAL EXPERIENCE

Radiative heat flux measurements on a fluidized bed combustor test rig
Fourier Transform Visible - Infrared Spectroscopy (FT-VisIR)
Laser Doppler Anemometry (LDA)
Combustion diagnostics measurements on a diffusion flame
Spectrometric calibration with a high temperature blackbody furnace

LANGUAGE SKILLS

English: Advanced
French: Intermediate

COMPUTER SKILLS

Programming Language:	Fortran 77/90
Operating Systems:	MS Windows (98,2000,XP), Unix, DOS
Other:	MS Office Applications, Matlab, Tecplot, Visio, Sigmaplot

AWARDS

June 2007	Young Scientists' Award in Radiative Transfer presented by Journal of Quantitative Spectroscopy and Radiative Transfer, Elsevier.
April 2007	ICHMT Grant for attendance to Fifth International Symposium on Radiative Transfer, June 17-23 2007, Bodrum, Turkey.
2003 - 2005	French Government Scholarship for co-supervised PhD studies in France
1997 - 2001	Turkish Petroleum Foundation, undergraduate and masters education grants

CITATIONS RECEIVED

Number of citations received (as of June.2007, Source: www.scopus.com)
Self-citations excluded: 23
Total: 33

RESEARCH PROJECTS

1. Selçuk N., Vaillon R., Ayrancı, I., Escudié D., Sacadura J-F., André F., Embassy of France in Turkey, Turkish-French University and Scientific Cooperation Project, 2003-2006.
2. Selçuk N., Ayrancı I., Comparison of radiation/complex-shape particles interaction models for characterization of soot particles in combustion chambers, TÜBİTAK MİSAG-263, Project No: 103M037, September 2004, Ankara.
3. Selçuk N., Tarhan T., Göğebakan Y., Batu A., Erşahin C., Ayrancı I. and Harmandar, H., Clean and Efficient Energy Production from Turkish Lignites Using Fluidized Bed Combustion Technologies, TÜBİTAK MİSAG-159, Project No: 100M049, September 2002, Ankara.

DISSERTATIONS

1. Ayrancı Kılınç I., A nonintrusive diagnostics technique for flame soot based on near-infrared emission spectrometry, Ph. D. Thesis, Middle East Technical University, Ankara and INSA-Lyon, Villeurbanne, 2007.
2. Ayrancı I., The method of lines solution of discrete ordinates method for radiative heat transfer in 3-D rectangular enclosures containing scattering media, M.Sc. Thesis, Middle East Technical University, Ankara, 2001.

PUBLICATIONS

10 publications in science citation index journals
9 papers in international conference proceedings

1. Ayrancı I., Vaillon R., Selçuk N., Near-infrared emission spectrometry measurements for nonintrusive soot diagnostics in flames, Journal of Quantitative Spectroscopy and Radiative Transfer, (accepted for publication), 2007. (Also in Proceedings of Fifth International Symposium on Radiative Transfer, June 17-23 2007, Bodrum, Turkey.)
2. Ayrancı I., Vaillon R., Selçuk N., André F. and Escudié D., Determination of soot temperature, volume fraction and refractive index from flame emission spectrometry, Journal of Quantitative Spectroscopy and Radiative Transfer, Vol. 104 (2), p. 266-276, 2007. (Also printed in Proceedings of Eurotherm Seminar No: 78 - Computational Thermal Radiation in Participating Media II, 5-7 April 2006, Poitiers, France, p.307)
3. Ayrancı I., Pinguet G., Escudié D., Selçuk N., Vaillon R. and André F., Effect of particle polydispersity on particle concentration measurement by using laser Doppler anemometry, Experimental Thermal and Fluid Science (in press), 2007.
4. Ayrancı I., Vaillon R., Selçuk N., Performance of discrete dipole approximation for prediction of amplitude and phase of electromagnetic scattering by particles, Journal of Quantitative Spectroscopy and Radiative Transfer, Vol. 103 (1), p. 83-101, 2007.

5. Sabouroux P., Stout B., Geffrin J. M., Eyraud C., Ayrancı I., Vaillon R., Selçuk N., Amplitude and phase of light scattered by micro-scale aggregates of dielectric spheres: Comparison between theory and microwave analogy experiments, Journal of Quantitative Spectroscopy and Radiative Transfer, Vol. 103 (1), p. 156-167, 2007.

6. Selçuk N., Ayrancı I., Gogebakan Y., Effect of recycle on radiative heat transfer in the freeboard of a fluidized bed combustor, Proceedings of 18th International Conference on Fluidized Bed Combustion, May 22-25 2005, Toronto, Ontario, Canada, FBC2005-78069.

7. Selçuk N., Uygur A.B., Ayrancı I. and Tarhan T., Transient simulation of radiating flows, Journal of Quantitative Spectroscopy and Radiative Transfer, Vol. 93 (1-3), p.151-161, 2005. (Also in Proceedings of Fourth International Symposium on Radiative Transfer, June 20-25, 2004, Istanbul, Turkey, p.327)

8. Demirkaya G., Arınç F., Selçuk N. and Ayrancı I., Comparison between performances of Monte Carlo method and method of lines solution of discrete ordinates method, Journal of Quantitative Spectroscopy and Radiative Transfer, Vol 93. (1-3), p. 115-124, 2005. (Also in Proceedings of Fourth International Symposium on Radiative Transfer, June 20-25, 2004, Istanbul, Turkey, p.435)

9. André F., Vaillon R., Ayrancı I., Escudié D. and Selçuk N., Radiative Transfer Diagnostic Technique of Sooting Flames from Emission Spectroscopy, Proceedings of Fourth International Symposium on Radiative Transfer, June 20-25, 2004, Istanbul, Turkey, p.97.

10. Ayrancı I., Selçuk N., MOL solution of DOM for transient radiative transfer in 3-D scattering media, J. of Quantitative Spectroscopy and Radiative Transfer, Vol. 84 (4), p. 409-422, 2004. (Also in Proceedings of Eurotherm Seminar 73 - Computational Thermal Radiation in Participating Media, April 15-17, 2003, Mons, Belgium, Elsevier, p. 47)

11. Selçuk N., Ayrancı I., The method of lines solution of discrete ordinates method for radiative heat transfer in enclosures containing scattering media, Numerical Heat Transfer Part B, Vol. 43, p.179-201, 2003.

12. Ayrancı I., Selçuk N., Effect of spatial differencing schemes on the performance of MOL solution of DOM in anisotropically scattering medium, Proceedings of 12th International Heat Transfer Conference, August 18-23, 2002, Grenoble, France (in CD-ROM).

13. Selçuk N., Batu A., Ayrancı I., Performance of method of lines solution of discrete ordinates method in the freeboard of a bubbling fluidized bed combustor, Journal of Quantitative Spectroscopy and Radiative Transfer, Vol. 73, 2-5, p.503-516, 2002. (Also in Proceedings of Third International Symposium on Radiative Transfer, June 17-22, 2001, Antalya, Turkey, p. 527)

FOLIO ADMINISTRATIF

THESE SOUTENUE DEVANT

L'INSTITUT NATIONAL DES SCIENCES APPLIQUEES DE LYON

NOM : AYRANCI KILINÇ Prénom : Işıl	DATE de SOUTENANCE 17 juin 2007
TITRE : A nonintrusive diagnostics technique for flame soot based on near-infrared emission spectrometry	
NATURE : Doctorat	Numéro d'ordre : 2007-ISAL-0037
Ecole doctorale : Mécanique, Energétique, Génie civil et Acoustique de Lyon (MEGA) Spécialité : Thermique et Energétique	
Cote B.I.U. - Lyon : et bis	CLASSE :

RESUME :

A novel nonintrusive soot diagnostics methodology was developed, validated and applied for *in-situ* determination of temperature, volume fraction and refractive index of soot aggregates formed inside flames by using near-infrared emission spectrometry. Research was conducted in three main parts, first one addressing development and validation of a comprehensive "direct" model for simulation of line-of-sight radiative emission from axisymmetric sooty flames by coupling sub-models for radiative transfer, radiative properties and optical constants. Radiative property estimation for soot agglomerates was investigated by experimentally validating discrete dipole approximation against microwave measurements and using it as reference to assess applicability of simpler Rayleigh-Debye-Gans approximation for fractal aggregates (RDG-FA). Comparisons between predictions of two methods for soot-like model aggregates demonstrated that radiative property predictions of RDG-FA are acceptably accurate for relatively small soot aggregates encountered in small-scale flames.

Part two concerns experimental investigation of an axisymmetric ethylene/air diffusion flame by Fourier Transform Near-Infrared spectroscopy. Measurement of line-of-sight emission intensity spectra was performed along with analyses on calibration, noise, uncertainty and reproducibility. A noise characterization approach was introduced to account for spatial fluctuations which were found to dominate over spectral noise.

Final part focuses on development, evaluation and application of an inversion methodology that inputs spectral emission intensity measurements from optically thin flames, removes noise, identifies soot refractive index from spectral gradients and retrieves soot temperature and volume fraction fields by tomographic reconstruction. Validation with simulated data and favorable application to measurements indicate that proposed methodology is a promising option for nonintrusive soot diagnostics in flames.

MOTS-CLES : Combustion diagnostics, *in-situ*, radiative properties, tomography, diffusion flame, soot aggregates

Laboratoires de recherche : Centre de Thermique (CETHIL) de l'Institut National des Sciences Appliquées (INSA) de Lyon –UMR CNRS 5008 et Département de Génie Chimique de l'Université Technique du Moyen-Orient, Ankara, Turquie

Directeurs de thèse: M^{r} VAILLON Rodolphe (CR1 CNRS), M^{r} SACADURA Jean-François (Pr), Mme Nevin SELÇUK (Pr.)

Président de jury: F. ARINÇ
Composition du jury: F. ARINÇ, G. GÜRÜZ, J-F. SACADURA, N. SELÇUK, R. VAILLON, J-P. VANTELON